Order Number 9419754

Principal stress orientations inferred from inversion of focal mechanism data in Hawaii and Iran

Gillard, Dominique Gérard, Ph.D.

University of Alaska Fairbanks, 1993

U·M·I
300 N. Zeeb Rd.
Ann Arbor, MI 48106

PRINCIPAL STRESS ORIENTATIONS INFERRED FROM INVERSION OF FOCAL MECHANISM DATA IN HAWAII AND IRAN

A

THESIS

Presented to the Faculty

of the University of Alaska Fairbanks

in Partial Fulfillment of the Requirements

for the Degree of

DOCTOR OF PHILOSOPHY

By

Dominique Gillard, M.S.

Fairbanks, Alaska

December 1993

PRINCIPAL STRESS ORIENTATIONS INFERRED FROM INVERSION OF FOCAL MECHANISM DATA IN HAWAII AND IRAN

By

Dominique Gillard

RECOMMENDED:

Advisory Comittee Chair

Department Head

APPROVED:

Dean of Natural Sciences

Dean of the Graduate School

7 December 1993

Date

ABSTRACT

Fault plane solutions were inverted to estimate stress tensor directions in Hawaii and Iran. These directions were compared to the seismically released strain tensor obtained by summing the moment tensors of the same earthquakes. Attempts were made to determine which of the nodal planes was the fault plane. Regional seismotectonic models were constructed based on these results.

The seismotectonic model for west Hawaii explains the seaward motion of the upper crust along a near-horizontal plane under a near-vertical greatest principal stress. The focal mechanism of the 1951 M=6.9 Kona earthquake in west Hawaii was modeled as a decollement based on a synthesis of teleseismic body waves using a new method designed for sparse data sets.

In southeast Hawaii, a single stress tensor orientation is compatible with a complex mixture of decollement, reverse, and normal faults. However, the stress field varies as a function of space and time. The differences between stress and strain orientations are caused by rotations of stress or strain directions, respectively, while the other remains constant. A rotation of the greatest principal stress in 1979 suggests magma movements within the aseismic part of Kilauea's southeast rift zone. Strain directions rotate due to the shifting of seismic activity from one fault to another in a volume of diverse faulting. These results show that the decollement plane at 10 km depth is weak and can slip in response to greatest principal stresses oriented near-perpendicular, sub-parallel or at 45° to it.

In Iran, stress directions, as estimated from major earthquakes, are homogeneous over areas several hundred kilometers long and mostly coincide with strain directions, suggesting that the strength of the crust is uniform.

The quality of the stress inversion results, measured by the size of the average misfit, is similar in Hawaii and Iran, although the dimensions of the study areas vary from tens to several hundreds of kilometers, and the magnitudes of the earthquakes from M=3.5±0.5 to M=6±0.5, respectively. Average misfits between 2° and 6° were obtained in both studies and are interpreted as characteristic of crustal volumes with homogeneous stress fields.

TABLE OF CONTENTS

LIST OF FIGURES

Figure

CHAPTER 2

CHAPTER 3

CHAPTER 4

CHAPTER 5

LIST OF TABLES

Table

CHAPTER 2

CHAPTER 3

ACKNOWLEDGEMENTS

I want to thank my adviser Professor Max Wyss who, through his excellent scientific guidance and constant encouragement, helped me to achieve this work. As a friend I thank him and his family for having made my life in America, from Colorado to Alaska, so enjoyable and exciting. I will never forget.

I am grateful to my committee members, Profs. Douglas Christensen, Stephen McNutt, Hans Pulpan, and William Harrison for their helpful comments which helped improve this manuscript.

My life in Alaska would not have been as enjoyable without the exceptional working atmosphere on the third floor of the Geophysical Institute. I want to thank all my friends and colleagues from the GI who helped me during these two years in Fairbanks. Special thanks to Vicki McConnell, Stefan Wiemer, Hilary Fletcher, and Guy Tytgat for their moral support and hands on help in making figures.

Most of my scientific education was accomplished at the University of Colorado at Boulder, where all my class work and most of my PhD work was done. There, I benefitted of the teaching and advice of Profs. Carl Kisslinger, Roger Bilham, John Wahr, and Max Wyss, to whom I am thankful. I want to thank also Drs. Frank Scherbaum and Martin Beisser with whom I collaborated and who patiently taught me the use of their computer codes. Special thanks to Paul Bodin with whom I spent endless hours talking about science, art, literature, and life, and who always had the right words whenever I needed moral support. My gratitude also to Carol

Finn, Ellen Franconi, and Bruce Kindel for their encouragement throughout these years of hard work. Thanks also to Barbara Sloan for her help in formatting this thesis.

Finally, I want to thank my parents and my sisters who always believed in me and supported me without hesitation.

Many computer codes were kindly provided by their authors to whom I am grateful: John Gephart (stress inversion), Martin Beisser (waveform modeling), Beiyuan Liang (strain calculation), Frank Scherbaum and James Johnson (PITSA).

Data were collected at the Hawaiian Volcano Observatory (HVO). I thank Dr. Paul Okubo and the staff of HVO for their help and hospitality. Funding for parts of this thesis was provided by grants from the National Science Foundation (EAR 8916252, EAR 9116722, and EAR 9118086) and the Wadati endowment at the Geophysical Institute of the University of Alaska to M. Wyss.

CHAPTER 1

INTRODUCTION

Earthquake focal mechanisms can be used to infer the orientation of the principal stresses that cause earthquakes along faults and at plate boundaries. From a variety of different focal mechanisms within a crustal volume of uniform stress, the directions of the principal stresses can be calculated if one assumes that, on each fault plane, slip occurs in the direction of the resolved shear stress. This assumption is justified by the fact that faults are planes of weakness, which implies that the greatest and least principal stresses can be oriented anywhere in the extensional and compressional quadrants, respectively. Based on these assumptions, *Gephart and Forsyth* [1984] have developed a method to estimate the stress orientations from groups of focal mechanisms. This method had not been used extensively and still needed to be tested in different tectonic environments and at different scales. In this thesis, I tested this method in two different tectonic environments, Hawaii and Iran, where the orientation of the stress field was unknown and where such a technique had never been applied. In Hawaii, the volumes analyzed typically had dimensions of 10 km and contained one hundred to several hundred earthquakes, with focal mechanisms, whereas in Iran the dimensions where several hundred kilometers and the number of earthquakes with focal mechanisms was between 20 and 30. The magnitudes of the events used in Hawaii were mostly 3.5±0.5, and 6.0±0.5 in Iran. Surprisingly, I found that the assumption of homogeneity of the stress directions

seems to be fulfilled at both of these scales to within a few degrees.

Another approach of understanding seismotectonic processes is to compute the strain orientation by summing the moment tensor of the earthquakes as described by *Kostrov* [1974]. The resulting moment tensor is then proportional to the average strain released by the earthquakes within a volume of the crust. I hypothesize that the principal stress axes and the principal strain axes must be coaxial if the strength of the crust is uniform. However, if in a crustal volume, some of the earthquakes occur on a fault which is weak, the strain and stress orientations may differ. The reason for this difference comes from the fact that a fault will always slip in a direction which is at 45° from the greatest principal strain but the stress resolved on this fault may be very small if the greatest principal stress is almost perpendicular or parallel to the the fault. This hypothesis was tested in Hawaii, Iran and southern California.

This thesis is a collection of four papers (Chapters 2-5). Each chapter was written as an individual contribution. However they are linked by the similarity of the problem they address: the inference of the stress field from focal mechanisms and its comparison to the strain field released by the earthquakes.

Chapters 2 and 4 are studies of the stress field in western Hawaii (chapter 2) and in the south flank of Kilauea volcano in Hawaii (chapter 4). In these two chapters, the relationship between the orientation of the principal stresses and the volcanos and their rift zones is investigated and a seismotectonic model for western Hawaii is proposed.

Chapter 3 is not directly related to inversion of stress. It presents the modelling of the 1951, M=6.9, Kona earthquake in western Hawaii, using a method developed by *Beisser et al.* [1990] to retrieve the source parameters (strike, dip, rake, and depth) of sparsely recorded events. This method was tested on a well recorded earthquake and then applied to a large but sparsely recorded event in western Hawaii. By defining the fault plane orientation of this largest earthquake in western Hawaii, I showed that the most significant faulting occurs on a decollement plane. By this finding I added a new fundamental piece of evidence to validate the seismotectonic model derived in Chapter 2 for western Hawaii.

Chapter 5 is a study of the comparison of stress and strain orientations in Iran and southern California. In the seismological field, there are virtually no studies comparing strain with stress directions, both derived from fault plane solutions. It appears that authors believe in the benefits of one or the other method exclusively. For example, *Jackson and McKenzie* [1984; 1988], and *Ekstroem and England* [1989] have exclusively used the strain method to study the kinematics of plate motions, whereas *Gephart and Forsyth* [1984], *Michael* [1987], *Jones* [1988], and *Zoback and Beroza* [1993] have studied stress orientations in California and ignored the possibility of computing the strain orientations. It is only in the field of structural geology that such comparisons are made in applying both of these methods mainly to field observations of fault slip data instead of focal mechanisms [e.g. *Marrett and Allmendinger*, 1990]. In chapter 5, I show that comparisons of the two types of results (stress and strain) can add to the understanding of faulting processes.

Chapter 2 (a seismotectonic model for western Hawaii based on stress tensor Inversion from fault plane solutions) was published in the Journal of Geophysical research in 1992 and was coauthored by Max Wyss and Jennifer Nakata. Chapter 3 (inversion for source parameters from sparse data sets: test of the method and application to the 1951 (M=6.9), Kona, Hawaii, earthquake) was submitted to the Journal of Geophysical Research and accepted for publication in 1993. The first author of this paper is Martin Beisser, but the paper was written by me. Martin Beisser designed the method, implemented it in the computer and performed the test of the method with the Kaoiki earthquake. With his aid, I modelled the 1951, Kona earthquake after digitizing the historical records. Our coauthor is Max Wyss, who helped in the writing of the manuscript. Chapter four (stress tensor orientations in the south flank of Kilauea, Hawaii, estimated from fault plane solutions) has been submitted for publication to the Journal of Geophysical research, and is coauthored by Max Wyss and Paul Okubo. Invitations for co-authorship were extended to two U.S. Geological Survey (USGS) staff members (J. Nakata and P. Okubo) of the Hawaiian Volcano Observatory (HVO) because the first motion polarities necessary to calculate the fault plane solutions were gathered at HVO. Chapter 5 (comparison of strain and stress tensor orientation: application to Iran and southern California) has been submitted to the Journal of Geophysical Research and is coauthored by Max Wyss.

CHAPTER 2

A SEISMOTECTONIC MODEL FOR WESTERN HAWAII BASED ON STRESS TENSOR INVERSION FROM FAULT PLANE SOLUTIONS[1]

1. ABSTRACT

For 57 fault plane solutions of earthquakes with magnitude $M_L \geq 3.0$ located west of the southwest rift zone of Mauna Loa volcano in Hawaii, which occurred between 1972 and 1988, the dominant focal mechanisms (44 events) are decollement type with one nodal plane nearly horizontal (dip $\leq 30°$). The average slip vector of the upper crust on the decollement plane points in an azimuth of 260° toward the ocean, away from Mauna Loa's southwest rift zone at an angle of about 150° with respect to the NE-SW oriented rift. Two other types of focal mechanisms are present: normal faults (4 events) and strike-slip faults with normal component (9 events).

The orientation of the principal stresses was derived by minimizing the sum of the misfits between the theoretical and observed fault geometry for each focal mechanism. After subdividing the data set into three different regions we found

---

[1] Chapter 2 contains the complete text and figures of the manuscript, *A seismotectonic model for western Hawaii based on stress tensor inversion from fault plane solutions,* by D. Gillard, M. Wyss, and J.S. Nakata, as published in the *Journal of Geophysical Research, Vol. 97, Pages 6629-6641, 1992.*

that the stress tensor is not homogeneous in west Hawaii. The orientation for the stress tensor is best resolved in the area located between latitude 19.27°N and 19.4°N and longitude 155.7°W and 155.9°W where the greatest principal stress directions within the 95% confidence limits are nearly vertical with some spreading to the West. Their plunge varies between 53° and 85°. The intermediate and least principal stresses are mostly horizontal and have similar magnitudes. Their plunge varies between 1° and 36°. The area between latitudes 19.4° and 19.6°N and longitude 155.7° and 156°W is characterized partly by near-vertical and partly by east-west oriented greatest principal stresses. The least principal stresses are approximately horizontal and have magnitudes similar to the intermediate principal stresses.

In the two areas where the stress tensor was well resolved, the principal strain directions differed from the principal stress directions by 30° in the plunge, suggesting that the faulting in western Hawaii takes place on a weak plane, but this result could not be established at the 95% confidence level.

The tectonic model proposed for west Hawaii is similar to the model for the Kalapana region. The strain is accumulated through magmatic intrusions in the southwest rift zone of Mauna Loa, and the earthquakes occur along a zone of weakness composed of oceanic sediment at about 10 km depth. The west flank of Mauna Loa slips in the direction away from the rift.

2. INTRODUCTION

An earthquake of magnitude M=6.9 occurred on the west flank of Mauna Loa volcano, Hawaii, on August 21, 1951 (Figure 2.1). Its location was along the west coast near Kealakekua (Kona district). The earthquake caused considerable damage [*Wyss and Koyanagi*, 1992] and was followed by an aftershock sequence that lasted several months with an M=6 event on May 23 1952. Nine hundred and sixty five earthquakes were recorded by instruments from the time of the mainshock until the end of September [*Macdonald and Wentworth*, 1952]. The mechanism of this earthquake could be inferred if we had a tectonic model for the west flank of Mauna Loa volcano. A model exists for the southern part of the island east of the southwest rift zone of Mauna Loa but is lacking for west Hawaii. The purpose of this paper is to develop a seismotectonic model for west Hawaii.

On the basis of focal mechanisms and other seismological and geodetic evidence, several authors [*Swanson et al.*, 1976; *Furomoto and Kovach*, 1979; *Ando*, 1979; *Endo*, 1985; *Lipman et al.*, 1985; *Wyss and Kovach*, 1988] have shown that the November 29, 1975, M_S=7.2 Kalapana earthquake (Figure 2.1) was caused by the accumulation of strain energy by magmatic intrusion in Kilauea volcano and its rift zones. The upper part of the crust slipped perpendicularly away from the rift on a near horizontal plane. The hypocentral depth of this earthquake was between 8 and 11 kilometers. The proposed tectonic model states that the buried sediment layer of the sea floor, upon which the edifice of the volcanoes is deposited, acts as a near horizontal plane of weakness. The evidence for this comes from refraction

data [*Hill and Zucca*, 1987], from the concentration of relocated crustal earthquakes at the depth of this layer [*Savage and Meyer*, 1987; *Thurber and Gripp*, 1988], and from fault plane solutions [*Crosson and Endo*, 1981; *Bryan and Johnson*, 1991].

For the Kaoiki area (Figure 2.1), where the November 16, 1983, M_S=6.6 earthquake occurred, two types of focal mechanisms have been observed [*Endo*, 1985], near-vertical strike-slip and near horizontal decollement types. *Endo* [1985] interpreted the latter type as a mechanism by which the southeast flank of Mauna Loa can slip away from the summit caldera and rift zones in a similar way as described for the south flank of Kilauea volcano. Also, *Wyss et al.* [1992] showed that in an inversion for the stress tensor orientation in the Kaoiki area, the decollement plane is chosen as the probable fault plane in 84% of the focal mechanisms.

In the Hilea area, which is located south of Kaoiki (Figure 2.1), only decollement solutions exist [*Endo*, 1985], suggesting that Mauna Loa's south flank slips to the south-east away from its rift zone. The stress tensor inversion by *Liang and Wyss* [1991] confirmed the idea that Mauna Loa's southwest rift zone is the source of stress causing earthquakes in this area. Slip of the upper crust to the SE is more easily possible here than further north, because there is no mass like that of Kilauea offering resistance. *Wyss* [1988] used this model as the basis for a source model for the great Hawaiian earthquake of April 2, 1868.

An oceanic sediment layer must be present everywhere at the base of the island, except where it may have been eroded by the magmatic intrusions, including the western part of the island, as shown in the refraction profile 7 of *Hill and Zucca*

[1987]. We propose that the stress, which caused the 1951 Kona earthquake, accumulated by magma intrusions in the southwest rift zone of Mauna Loa volcano, and that the near horizontal oceanic sediment layer located at a depth of approximately 11 kilometers acts as a zone of weakness in this part of the island also.

To test this hypothesis, we have examined focal mechanisms of M_L=3.5±0.5 earthquakes that occurred between 1972 and 1988 in the west part of Hawaii (Figure 2.2). If our hypothesis is correct, these focal mechanisms should show greatest principle stress directions and slip vectors oriented approximately perpendicular to the southwest rift, and the events located at a depth of about 11 kilometers should have mostly decollement-type focal mechanisms.

The focal mechanisms show a variety of fault plane solutions (Figure 2.2). If they are produced by a single stress tensor, then this variation may be the result of the presence of planes of weakness with different orientations to accommodate the slip. On the other hand, the variation could reflect the inhomogeneity of the stress tensor within the crust. In order to test the hypothesis that the stress tensor may be homogeneous throughout Kona, we will use the method developed by *Gephart and Forsyth* [1984] to infer the orientation of the stress tensor and its relative magnitude. This method, contrary to other stress inversion techniques [*Angelier*, 1979; *Angelier et al.*, 1982; *Michael*, 1984; 1987a], allows one to determine the orientation of the stress tensor by inverting focal mechanism data without prior knowledge of the fault plane. From a variety of different focal mechanisms within a crustal volume of uniform stress, the directions of the principal stresses and the relative

stress magnitudes can be calculated because on each fault plane, slip occurs in the direction of the resolved shear stress [*Gephart and Forsyth*, 1984; *Gephart*, 1990b]. This implies that a variety of focal mechanisms may offer a good constraint on the orientation of the stresses that produced the slip on the faults. As a first step, we will test the validity of the main assumption that all the focal mechanisms are produced by a single homogeneous tensor by applying the inversion to three separate data sets from different regions. If the 95% confidence limits around the best stress tensor solutions do not overlap, we will conclude that the stress tensor is not homogeneous throughout the crustal volume considered. If they overlap, we will define criteria of comparison based on the goodness of fit and the distribution of relative magnitudes between the different sets in order to resolve any possible differences in the stress tensors. The same procedure will be applied to subsets of the data as a function of depth in order to check if the stress tensor changes with depth.

Finally, we compared the regional stress tensor with the seismic strain tensor following the procedure proposed by *Wyss et al.* [1992]. The regional stress tensor is the tectonic stress which causes the earthquakes. The seismic strain tensor results from the application of the tectonic stress which will produce slip on particular faults. In relatively isotropic material, the principal axes of stress and strain should be the same or close to each other. If a dominant zone of weakness is present in a volume, it is possible that the principal strain directions are significantly different than the principal stress directions because the angle between the principal strain directions and the slip direction of the fault is always 45°, while the greatest principal stress can lie anywhere in the dilatational quadrant [*McKenzie*, 1969; *Kostrov*,

1974].

3. DATA

The data set consists of all relatively well-recorded events of magnitude $M_L \geq 3.0$ located in an area defined by latitudes 19.1°-19.8°N and longitudes 155.6°-156.1°W (Figure 2.3) for the period from January 1969 through December 1988 as listed in the catalog of Hawaiian earthquakes published by the Hawaiian Volcano Observatory (HVO). The criteria of selection were that each event had to have at least 15 first motion readings made by the HVO staff and that the takeoff angles had to be well distributed and not clustered around the same value. Because this part of the island is not well covered by seismograph stations (Figure 2.3), this condition was difficult to fulfill. Eighty-three earthquakes with M≥3.0 were selected for study, with an average of 29 first motions per event. We added 14 more events with magnitude M≥2.5 from the preliminary catalog covering the period 1986-1988. The magnitude threshold used for this period was lower because a magnitude shift of -0.5 had been detected in a previous study of the catalog; thus we believe that M=2.5 after 1985 is equivalent to M=3.0 before the new method was introduced in 1986 to calculate magnitudes.

The focal mechanisms were calculated using a computer program [*Whitcomb et al.*, 1973] that determines focal mechanisms from P wave first motion data by testing a grid of trial mechanisms with a resolution of 5°. It chooses the best mechanism as the one which minimizes the number of first motion readings in error. As an output, the program gives a minimum score (Sc) which is equal to half

the sum of the quality ratings of the readings in error. The quality ratings are equal to 2 for impulsive first motion and 1 for emergent first motion. The stations near the nodal planes are linearly tapered from 0 to 1 within a distance of 3° from the nodal plane. This download from tapering is also added in the calculation of the score. The quality of the fault plane solutions was evaluated on a scale from A to D based on Sc and the number of first motions in error (Ninc). The quality factor was used in the stress inversion program as a weight for each solution. The scale was defined as: A= Sc≤1.5, Ninc≤4; B= 1.5≤Sc≤2.6, 3≤Ninc≤6; C=2.7≤Sc≤4.5, 6≤Ninc≤9; D=4.5 < Sc, 9 < Ninc. In addition, we used some subjective judgment to downgrade poorly constrained solutions. Solutions with one plane not constrained to better than ± 45° were assigned D quality and rejected regardless of other scores. In most solutions the uncertainty of the slip vector was less than or equal to 5°, with only three solutions that had uncertainties larger than 25° (Figure 2.4).

We first computed the focal mechanisms using the data as they are listed in the catalog. For correcting polarity reversals we used the HVO list of reversals, which is an expansion of the list compiled by *Endo* [1985]. We added to this list reversals that have been compiled by *Wyss et al.* [1992] for 1977-1988 and some noted by F.W. Klein (personal communication, 1989).

The quality of focal mechanisms is controlled by the accuracy of the takeoff angles and their distribution on the focal sphere. The velocity structure is an important factor to assess the accuracy of the takeoff angle. If one uses a horizon-

tally layered structure, even with linear gradient, the takeoff angles for the stations located further than the crossover distance for direct and refracted waves will all be the same. If the azimuthal coverage of the stations is good, their projections on the stereographic net will appear along the same small circle. If the stations have similar azimuths, then the first motions will be clustered on the focal sphere. In both cases, it becomes difficult to fit nodal planes through the data (Figure 2.5a). This situation appears often in the data from the west flank of Mauna Loa, if the velocity model that was developed for the area around Kilauea is used.

The hypocenters in the Hawaiian catalog have been calculated with the velocity model HG50 [*Klein*, 1981]. This model has given good results for locating earthquakes and computing their focal mechanisms in the southern and eastern parts of Hawaii [*Klein*, 1981] (Table 2.1). On the west flank of Mauna Loa, the network is sparse (Figure 2.3). Only five stations are located within the studied area, seven additional stations are within 15 km and most of the rest of the stations are located to the east at distances greater than or equal to 50 km. From the refraction survey of *Hill and Zucca* [1987] and *Zucca et al.* [1982] we concluded that the Moho below the Kona coast of Mauna Loa is substantially deeper than in the model HG50. They have estimated the depth of the Moho at about 18 km beneath the high, subaerial flank of Mauna Loa, allowing that it could be about 2 km deeper due to poorly constrained velocities in the crust. Using a model with the Moho at a depth that is too shallow has the effect of artificially compressing stations from a range of distances into the small circle where all refracted wave paths are projected on the stereo net. To avoid this error, we increased the depth of the Moho in our

model. In order to determine at what depth we should put the Moho, we calculated the takeoff angles of all the focal mechanisms for different depth of the Moho starting at 16.5 km as in HG50 and increasing it by 1 km up to 26.5 km without relocating the events. We compared the resulting focal mechanisms and observed that the improvement was substantial at a Moho depth of 21.5 km (Figure 2.5c), because compressions and dilations, which were mixed at the refraction angle of HG50, became separated when a model with a deeper Moho was used. With the Moho at 21.5 km, the average number of stations in error dropped from 5 to 4, while the score stayed stable around an average of 2. The difference in velocity model did not significantly change the fault plane solutions of some events, but it affected that of others considerably (Figure 2.5).

The final focal mechanisms were calculated with the modified HG50 model with the Moho at 21.5km (Table 2.1) keeping the same location as in the catalog. These focal mechanisms were graded with quality factors ranging from A to D as described above. Out of a total of 97 events, 21 received a quality factor of A, 18 a B, 22 a C, and 36 of quality D were rejected. The focal mechanisms of the remaining 61 events selected for the inversion are given in Table 2.2. The average number of stations used to calculate the focal mechanisms is 30 with a minimum of 18 and a maximum of 47 stations. The average number of stations in error is 4 per event and the average score is 1.9.

The uncertainty of the fault plane parameters (strike, dip, and rake) is estimated from the range of angles which the slip vectors may occupy without

introducing an additional (unnecessary) violation of a first-motion reading. This range is part of the output when finding fault plane solutions [*Whitcomb et al.*, 1973]. For our data set the average uncertainty was 9° with 84% of the solutions having uncertainties of less than 15° (Figure 2.4). Based on this observation, we expect that in inversions for stress orientations of homogeneous data sets, the misfits for individual solutions should not exceed 15°.

The new Moho depth is deeper than the one determined by *Hill and Zucca* [1987] even if we add the 2 km that they allow. For that reason, we have compared the focal mechanisms computed with the Moho at 21.5 km with the fault plane solutions obtained with the Moho at 18.5 km. The average of the absolute difference in strike, dip and rake between the two data set is 19°, 7° and 14° with 72%, 88% and 76% of the differences below 15°, respectively. This comparison was possible because for more than 90% of the events, the fault plane solutions were similar enough that the nodal planes were directly comparable. We conclude that these differences are not significant and we maintain our decision to keep the Moho at 21.5 km.

To test if our decision of keeping the same location as in the catalog was reasonable, we relocated the events using the Joint Hypocenter Determination (JHD) method [*Dewey*, 1972] with the Kaoiki mainshock of 1983 as calibration event. The choice of the Kaoiki event as calibration event is not ideal because this event is 60 km east of the studied area which means that the waves leaving its source do not have the same path as the seismic waves produced by the earthquakes on the west

flank of Mauna Loa. On the other hand, it is difficult to get accurate locations independently of the choice of the calibration event because the earthquakes occur in a poorly instrumented part of the network and one may argue that heterogeneities in the shallow layers below the receivers will be corrected for by the method used. We propose that if the focal mechanisms of the relocated events are similar to the focal mechanisms of the non relocated ones, one can assume that the mechanisms are robust and not significantly dependent on the location.

The average difference between the Hawaiian Volcano Observatory (HVO) locations and the new locations is 3.5 km with a maximum of 9.5 km and a minimum of 0.2 km. The relocated events moved north by about 1.1 km in the average and east by about 1.1 km relative to the HVO locations. The depth of the relocated events are on the average deeper by about 0.6 km. The depth distribution of the relocated events is scattered, possibly because we did not use any S wave first arrivals and because there are only five stations close enough to the events to control the depth. The average depth of the relocated events is 10.4 km with a standard deviation of 3.6 km.

The difference in the orientation of the P axes between the relocated events and the nonrelocated ones is on the average 22° with 56% of the focal mechanisms showing a difference of less than 15° and 73% less than 30°. In the case of the T axes, the average difference is 26° with 54% of the focal mechanisms showing a difference of less than 15° and 76% less than 30°. As for the fault plane solutions of the nonrelocated events, the solutions of the relocated events have uncertainties

of about 15°. Within that range of uncertainty, one concludes that the focal mechanisms based on the new locations did not vary significantly from those using the original locations.

4. METHOD

4.1. Inversion of stress

The basic assumption in the stress inversion method by *Gephart and Forsyth* [1984] is that the deviatoric stress tensor is uniform in the crustal volume of study. The second assumption is that, on each fault plane, slip occurs in the direction of resolved shear stress [*Bott*, 1959; *Gephart and Forsyth*, 1984; *Gephart*, 1990b]. In order to invert successfully the focal mechanism data for the direction of principal stresses, one must have a crustal volume with faults representing zones of weaknesses with different orientations in an homogeneous stress field. This stress field will produce earthquakes on these faults with a variety of focal mechanisms. Each of these focal mechanism types acts as a constraint under the second assumption. If only one type of focal mechanism is observed, then the direction of the principal stresses would be as poorly constrained as in the case of a single fault plane solution. *McKenzie* [1969] showed that, for one focal mechanism, with well-determined nodal planes, the direction of the greatest principal stress can be anywhere in the dilatational quadrant of the fault plane solution.

In the inversion algorithm of *Gephart* [1990a], the model parameters are the directions of the three principal stresses σ_1, σ_2, σ_3 (where $\sigma_1>\sigma_2>\sigma_3$) and the ratio

R which is defined as

$$R = \frac{\sigma_2 - \sigma_1}{\sigma_3 - \sigma_1} \quad (1)$$

In order to determine these three unknown parameters, one has to minimize the difference between the prediction of the model and the observations. This difference is called a misfit and is defined as the minimum rotation about any arbitrary axis that brings the fault plane geometry into coincidence with a new fault plane geometry (prediction of the model) that satisfies the second assumption and $0 \leq R \leq 1$ [*Gephart and Forsyth*, 1984]. Since there are two nodal planes for each observed focal mechanism, there will also be two misfits; one for each nodal plane. The plane with the smallest misfit is assumed to be the fault plane. The smaller misfit of the two nodal planes of each earthquake are added to give the sum of the misfits. The best model of direction of principal stresses is found by a grid search over the focal sphere. The model with the smallest sum of misfits is chosen as the best solution.

In addition to the best model we also need its confidence limits. Gephart and Forsyth used the one-norm misfit described by *Parker and McNutt* [1980] to compute the limit of confidence level because the distribution of misfits is exponential and in that case the one-norm misfit is more appropriate than the two-norm misfit [*Menke*, 1984].

This inversion technique is objective in the sense that it does not require knowledge of the fault plane. If data are in sufficient quantity, it can pick the fault

planes with a fairly good percentage of success as tested by *Michael* [1987a]. He also pointed out that if two data sets of focal mechanisms, generated by two different stress fields, are mixed, then this inversion technique will produce a solution which is an average of the two stress fields. This implies that it can be difficult to decide whether a data set of focal mechanisms is produced by one single stress field or many. The only way around this problem is to divide the data set into different subsets according to spatial, temporal, or tectonic criteria and to calculate the inversion for every subset. If more than one subset yields the same result within the 95% confidence limits, then the stress direction may be considered homogeneous within those subsets and within the resolution afforded by the data.

Criteria for preferring the inversion result of a subset of the data over that of the entire data set include (1) reduction of the average misfit, (2) reduction of the number of fault plane solutions that are incompatible, or have misfits substantially larger than the errors of the fault parameters, and (3) change from a bimodal distribution of R values to a single (modal) distribution. We define as inconsistent with an inversion result those solutions for which both misfits are larger than 20° because the uncertainties in the the fault geometry are less than 15°. The relationship between the errors in the fault plane solutions and the minimum misfit is not clear, but it is reasonable to assume that individual solutions for which the minimum misfit is larger than these errors are not compatible with the assumption of a homogeneous stress tensor. The size of the 95% confidence limits will not be a criterion for preferring an inversion result, because it does not measure the quality of the result but the degree to which it is constrained. These criteria will also help

to resolve differences between regions with overlapping 95% confidence regions. As *Michael* [1987b] pointed out, if two 95% confidence regions overlap, that does not mean that these two results cannot be different because the distribution of models within the 95% confidence region can still be described by different distributions at the 95% confidence level. The criteria mentioned above will be applied to resolve any difference more in a qualitative way rather than quantitative because we do not know the distribution of the models within the 95% confidence region.

4.2. Strain calculation

It is possible to compute the strain released in a crustal volume due to slip on faults with a variety of orientations. *Kostrov* [1974] showed that the averaged released strain and the moment tensors of the earthquakes located within a volume V are related as follows:

$$\varepsilon_{ij} = \frac{1}{2\mu V} \sum_{K} M_{ij}^{K} \tag{2}$$

where μ is the shear modulus.

M_{ij}^{K} is the moment tensor of the kth earthquake and is related to the scalar seismic moment by

$$M_{ij}^{K} = M_0^{K} \ (u_i^{K} n_j^{K} + u_j^{K} n_i^{K})_j \tag{3}$$

where n_i^{K} is a unit vector normal to the fault plane and u_j^{K} is a unit vector parallel to the slip direction. The scalar moment can be obtained from the moment-magnitude relation and the vectors n and u from fault plane solutions. The shear

modulus and the volume are scalar values that do not affect the orientation of the strain tensor. The scalar moments were derived from the moment-magnitude relation for Hawaii proposed by *Zuñiga et al.* [1988].

In order to compare the direction of principal strains with the direction of principal stresses within a region of homogeneous stress field, one has to determine the uncertainty of the principal strain directions. The 95% confidence ellipses of the principal strain directions were calculated using the error analysis described by *Wyss et al.* [1992]. We used 10° as the uncertainty of the strike and the dip since this is approximately the average slip vector uncertainty (Figure 2.4). The error on the scalar moment is 1.9 multiplied by the average moment as proposed by *Wyss et al.* [1992]. In order for the strain tensor to be considered significantly different from the stress tensor, the 95% confidence ranges should not overlap. Even if the best solutions for the stress and strain tensor differ by tens of degrees, we cannot claim that the tensor directions are significantly different if the 95% ranges overlap.

5. RESULTS

It is difficult to verify that the assumption of homogeneity in the volume and for the period containing the data is fulfilled. Our data sample a period of about seventeen years which is small compared to the time it may take to rotate the stress tensor by tectonic processes. Also, our data set does not contain any earthquake with magnitudes larger than 5 and no major intrusions occurred in Mauna Loa's south rift during this time. For that reason, it is reasonable to assume that the stress direction has not changed over the period covered by the data.

We divided our data set spatially into three areas which seemed to be separated naturally by lack of activity between them (Figure 2.3). Area 1 is located between 19.4°-19.6°N latitude and 156.0°-155.7°W longitude. Area 2 is located between 19.27°-19.40°N latitude and 155.90°-155.7°W longitude. The separation of the data into area 1 and area 2 is also justified tectonically because the southwest rift zone changes orientation at about latitude 19.36°N, and most of the events in area 2 are located south of this latitude. Area 1 is north of the bend in the orientation of the rift, and it is also closer to the Hualalai volcano. Area 3 was defined separately from the others because the earthquakes are closer to Mauna Loa than the rest of the events and consequently more likely to occur in a locally different stress field. We first inverted the data set containing all events and subsequently the subsets corresponding to the different areas.

The procedure used to invert a data set of focal mechanisms was to start with several initial values for σ_1 and σ_3 axes and to search over the entire focal sphere with a 10° grid for the models with the smallest average misfit. The best result was then used as a starting value in the search with a 5° grid over a smaller range of the focal sphere (about 30°). The model with the smallest average misfit resulting from this second search was called the best model and the 95% confidence limit was then computed.

5.1. Inversion of the entire data set

This data set comprises all the events (57) located inside the areas defined in Figure 2.3. The four events outside these areas were not used in the analysis

because they are isolated and distant from the other earthquakes. We classified the focal mechanisms having one plane dipping at an angle smaller or equal to 30° as decollement-type focal mechanisms. Three types of focal mechanisms are present in this data set: 44 events are decollement type with an average slip on the decollement plane oriented at an azimuth of 260°±12° and a plunge of 6° ± 1°, 4 are normal faults, and 9 are strike slip with a normal fault component (Figure 2.2). The inversion of the entire data set resulted in an average misfit of 6.0° (Table 2.3). The 95% confidence region is small (Figure 2.6a) thanks to the number of events (57) and their variety of focal mechanisms. Three inconsistencies were detected with misfits equal to 23°, 26°, and 28°.

The distribution of R values (Figure 2.6a) shows a concentration of models below R=0.4 and above R=0.6. This may be an indication that this data set is not homogeneous but composed of subsets. We would expect that if a set is homogeneous, then the R values would concentrate around one value and not around two different values. Below we will examine whether subsets of the data in smaller regions will furnish a smaller average misfit, fewer inconsistencies, and a distribution of R values concentrated around one value. If so, the subsets may be more homogeneous than the mixed set.

5.2. Area 1

In area 1 we observe two types of focal mechanisms: the decollement type (26 events) and normal faults (3 events, Figure 2.2a). The average slip vector for the upper crust in the decollement type has an azimuth of 243°±19° and a plunge of

7°±1°. The average depth of the events having a decollement-type of focal mechanism is 10.3 km. The normal fault events have an average depth of 10.0 km.

The inversion for this data set gave as best result σ_1 almost vertical with a plunge of 83° (Table 2.3, Figure 2.7a). σ_2 and σ_3 are horizontal, and the R value of 0.9 suggests that σ_2 is approximately equal to σ_3. The 95% confidence region (Figure 2.7a) shows that σ_2 and σ_3 overlap. Only one inconsistency was detected with misfit equal to 25°. None of the rest of the focal mechanisms in the inversion of this data set showed a misfit larger than 17° for the preferred plane. Also the average misfit (4.5° , Table 2.3) shows an improvement compared to the inversion of the entire set. We assume that the plane with the smaller misfit may be chosen as the fault plane if the difference between the misfit of the two nodal planes is larger than 15°. If the difference is less than 15°, then a choice is not possible, both planes could be the fault plane. The value of 15° was chosen because 84% of the fault plane solutions have slip vector uncertainties smaller than 15° with an average around 10°. The algorithm was able to pick 6 fault planes: 2 were decollement planes, 3 were the vertical planes from a decollement type and 1 was the plane of a normal type. In 23 cases a choice was not possible.

5.3. Area 2

In area 2, there are 16 decollement-type focal mechanisms and only one normal fault out of a total of 17 events (Figure 2.2b). The average depth of the earthquakes studied in this area is 10.8 km. The distribution of slip vectors for the decollement type is similar to that in area 1, with an average azimuth of 259°±18°

and a plunge of 6°±1°.

The inversion also gives a best result with σ_1 near-vertical (plunge of 82°) and both σ_2 and σ_3 are horizontal and exchangeable (R=0.9) (Figure 2.7b and Table 2.3). The average misfit is low (2.3°) compared to the average misfit of the entire set (6.0°) or in area 1 (4.5°) (Table 2.3). No inconsistent focal mechanisms have been found (maximum misfit for the preferred plane is 9.5°). The 95% confidence region is small (Figure 2.7b) and the R values (Figure 2.7b) are concentrated around values greater than 0.8. The fault planes selected by the method described above included 1 decollement plane and 1 vertical plane out of 2 cases in which a choice was possible.

5.4. Area 3

Area 3 presents different characteristics than the other regions. The average depth of the events is about 7.5 km, which is substantially shallower than the average for areas 1 and 2. These depths are probably better constrained than the depths of the events located in regions 1 and 2, because area 3 is closer to the center of the seismograph network. The focal mechanisms are well constrained with many first motions, few inconsistencies, and good distribution on the focal sphere. Two types of focal mechanisms are recognizable: strike slip with normal faulting component (nine events) and decollement type (two events) (Figure 2.2c).

The inversion of the 11 events in area 3 gives an average misfit of 2.3° (Table 2.3) and the highest misfit for the preferred planes is 5.7°, which is an indication that this data set is homogeneous. On the other hand, the best result is poorly

resolved because most of the earthquakes have similar mechanisms and the number of events used is small. Consequently, the 95% confidence region is very broad (Figure 2.7c). Most of the models within the 95% confidence region have R values around 0.6 (Figure 2.7c).

5.5. Area 1, depth ≥ 10 km

We investigated the depth dependency of the stress tensor within area 1 in order to see if we could improve the inversion result, because the average misfit was still high compared to the values for areas 2 and 3. We inverted separately the focal mechanism data of the earthquakes with depth greater than or equal to 10 km (23 events). The average misfit decreased slightly from 4.5 for area 1 to 4.0 (Table 2.3). The best fitting model, the R values, and the 95% confidence region stayed the same as for area 1 (Table 2.3 and Figure 2.6b). The same fault plane solution as in area 1 received a misfit of 25°. The program chose 3 vertical planes, 1 decollement plane, and 1 normal fault as fault planes. The limitation in the number of events available for inversion in area 1 prevented further investigation of spatial and depth dependency of the stress tensor.

6. STRAIN CALCULATION

The strain tensor was calculated (Table 2.4) for areas 1 and area 2 because the best results of the stress inversion are well resolved in these regions providing a way of comparing the principal stress and strain directions. We did not compare the strain and stress tensor in area 3 because of the lack of resolution of the stress

tensor inversion in this region.

The directions of principal strain are the same in areas 1 and area 2 (Figure 2.8 and Table 2.4). In both areas, the plunge of the greatest and least principal strain direction is close to 45° (Table 2.4) which is what we expect if most of the earthquakes are of decollement type on a horizontal plane. The 95% confidence ellipse of the strain tensor partially overlaps the 95% confidence range of the stress tensor in both areas (Figure 2.8), but the plunge of the best results of the stress inversion differs by about 30° in the average from the plunge of the principal strain directions.

7. DISCUSSION AND CONCLUSIONS

The first question is whether the stress tensor is homogeneous throughout the crust in the west part of Hawaii. To answer this question, we compared the results for the different regions according to the criteria we defined in the previous section. After subdividing the entire data set into three different subsets, the average misfits decreased substantially (Table 2.3). Furthermore the distribution of R values becomes simpler and more reasonable for the subdivided data sets, and the number of inconsistencies decreased. Consequently, we conclude that the stress tensor is not homogeneous in the west of Hawaii. It seems probable that the stress tensor is homogeneous within area 2 because of the low average misfit (2.3°) and the absence of inconsistencies. In area 1 it is more doubtful that the stress tensor is homogeneous because the average misfit is equal to 4.5°, twice that of area 2. This result could not be improved significantly by subdivision with respect to depth

because the average misfit improved only by 0.6° and the single inconsistency remained. This may be interpreted as suggesting that the assumption of homogeneity may not be fulfilled. Unfortunately it was not possible to make more subdivisions because not enough events were available.

The average misfits for areas 1, 2, and 3 are the same or smaller than the 4.5° misfits obtained for the Kaoiki area [*Wyss et al.*, 1992, their Table 3]. In the Kaoiki area the fault plane solutions were better defined because the epicenters are located near the center of the seismograph network. Also, in the southeastern part of the Kaoiki area, the stress tensor in several spatial subsets had the same orientation. Thus *Wyss et al.* [1992] argued that the stress orientations in the southeastern part of Kaoiki were homogeneous and that the average misfit of about 4.5° was linked to the uncertainties of the fault plane parameters, which was 5° in the average. Comparing the Kaoiki results with the misfits of less than and equal to 4.5° in west Hawaii, we propose that the quality of stress inversions in west Hawaii is as good as that in Kaoiki. Therefore it is reasonable to assume that the stress directions in the three areas of Figure 2.3 are homogeneous, because it was shown that in Kaoiki a homogeneous data set yielded the same average misfit.

The most homogeneous set of fault plane solutions is that of area 3, but because of this the stress orientations are poorly defined. Although we believe that the orientation of the stress tensor here is different than in areas 1 and 2, this cannot be resolved at the 95% confidence level (Figure 2.7c).

The only region where we have a tight definition of the stress tensor direction

is area 2 (Figure 2.7b). The greatest principal stress is almost vertical, and σ_2 and σ_3 are horizontal and interchangeable because their magnitudes are similar (R > 0.6). The azimuth of the greatest principal stresses for the models within the 95% confidence region varies between 230° and 293° and their plunge between 53° and 85° (Figure 2.7b). We interpret this orientation as being due to stress accumulated through forceful magma intrusion in the rift of Mauna Loa between latitudes 19.3°-19.4°N. If the fault plane is the decollement plane, it may be possible for the flank of Mauna Loa to slip over this plane under a near-vertical greatest principal stress if high pore pressure exists at the depth of the decollement plane. This possibility is plausible because Hawaii is an island and water may be trapped in the buried oceanic sediment layer which forms the decollement plane. The San Andreas fault and the Calaveras fault are other examples of weak faults where the greatest principal stress is almost perpendicular to them [*Zoback et al.*, 1987; *Jones*, 1988; *Oppenheimer et al.*, 1988].

In area 1 it is more difficult to correlate the orientation of the stress tensor with the orientation of the southwest rift of Mauna Loa because the area is more distant and we are not completely sure if the stress tensor is invariant spatially within this area. The distribution of the greatest principal stresses within the 95% confidence region range from a north-south to an east-west orientation. The reason for the more southerly strike of σ_1 compared to that in area 2, may be that, in area 1, magma intrusions in Hualalai could contribute to building up the stress field.

A choice of fault plane was possible in seven events in the separate inversions

for areas 1 and 2. Of these, three decollements and four near-vertical planes were chosen as probable fault planes. The reason choices are difficult to make is that for both areas the best fitting stresses are nearly axially symmetric ($\sigma_2 = \sigma_3$) and many B axes are coplanar with the equal principal stresses. *Gephart* [1985] showed that for axially symmetric stresses the choice between the two nodal planes is not possible because the shear stress and slip directions will match on both nodal planes. The number of available data is too small in this study to accept the suggestion than both nodal planes may be active in separate earthquakes or to reject the hypothesis that the decollement plane is an important plane of weakness. We believe that one needs a large data set and an overwhelming majority, as in the Kaoiki area [*Wyss et al.*, 1992], to be convinced that the method yields significant choices of fault planes. The current data set is thus not strong enough to allow identification of the preferred fault plane.

The average slip vector in the decollement plane is almost horizontal and points toward the ocean away from Mauna Loa's south rift zone at an angle of about 150° with respect to the NE-SW oriented rift. The orientation of the average slip vector indicates the average direction in which the west flank of Mauna Loa has moved during these earthquakes (Figure 2.1). It is also the most likely direction of slip because the flank of the volcano is free to move in this direction as there is no other edifice to stop it. Northwest of Mauna Loa the volcano Hualalai acts as a buttress. The earthquakes in area 1 and 2 are located at depth between 8 and 12 km which correspond to the depth expected for the oceanic sediment layer [*Hill and Zucca*, 1987; *Savage and Meyer*, 1987; *Thurber and Gripp*, 1988; *Thurber et al.*,

1989]. Because the depth estimates of the earthquakes are not very accurate, one may propose that the four kilometers interval in which they all occur is due entirely to errors; they may occur on a thin horizontal plane at a depth of 10±2 km. These observations support the model of a layer of oceanic sediment underlying the island of Hawaii, which provides a zone of weakness along which slip can occur in earthquakes as proposed by many authors [*Swanson et al.*, 1976; *Nakamura*, 1977; *Furomoto and Kovach*, 1979; *Ando*, 1979; *Nakamura*, 1982; *Endo*, 1985; *Hill and Zucca*, 1987; *Dieterich, 1988; Wyss and Kovach*, 1988]. They are also in agreement with the results of *Bryan and Johnson* [1991], who carefully analyzed 14 focal mechanisms of events located on the Mauna Loa West flank and proposed a similar tectonic model.

The comparison of the strain with the stress directions offers a way to discriminate between a tectonically isotropic crust and a crust with a zone of weakness [*Wyss et al.*, 1992]. In an isotropic crust, the directions of principal stresses are identical to the directions of principal strain. In the presence of a zone of weakness, the strain and stress directions may differ substantially because even small shear stress components resolved on a weak fault plane may induce slip on that plane, while the strain direction will be at 45° to the plane of weakness [*Kostrov*, 1974; *Wyss et al.*, 1992]. The difference of 30° in the plunge between the principal stress and strain directions suggests that in western Hawaii, sliding may occur on a weak horizontal plane at the base of the volcano Mauna Loa. However, this difference is not significant at the 95% confidence level.

On the basis of these results, we cannot be certain that the focal mechanisms for the Kona earthquake of 1951 and any major earthquake which could happen in the west flank of Mauna Loa in the future, are decollement types. However, if the decollement plane is the fault plane, then we expect a strike of about 140° and a SW-NE dip of approximately 12° (Figure 2.9). This orientation of the fault plane was calculated by computing the average strike and dip of the decollement-type focal mechanisms for areas 1, and 2. The average slip on these decollement planes gave the pole of the auxiliary plane. We also calculated the predicted slip on the proposed fault plane for the stress tensor models within the 95% confidence region of area 2, because in this area we believe that the stress tensor is homogeneous. The predicted slip on the decollement plane is oriented between azimuths 277° and 228° with the upper crust moving in the direction away from the rift (Figure 2.9). Whether this proposed focal mechanism is correct has to be verified by inversion of the seismograms recorded for the 1951 mainshock.

One notices that the proposed decollement plane is dipping toward the west, while the dip of the zone of weakness made of oceanic sediments is oriented toward the east according to the refraction profile of *Hill and Zucca* [1987]. This apparent discrepancy comes from the fact that for a nearly horizontal nodal plane, the dip will vary between west and east within the range of errors. If we apply an error of 15° to the proposed fault plane solutions, we get a plane dipping eastward at about 3° which is in accordance with the model of Hill and Zucca. This ambiguity is due to the fact that the first motions have takeoff angles near 90° which implies that a small change in this angle will make the plane dip either westward or eastward.

West Hawaii has geomorphological and tectonic features similar to those in the Kalapana region in southeast Hawaii (Figure 2.1) [*Nakata et al.*, 1990]. In both regions, normal faults are mapped at the surface, and traces of large landslides have been identified both on land and on the ocean floor (Figure 2.1) [*Lipman, 1980*; *Lipman et al.*, 1988; *Moore et al.*, 1989]. It is likely that the normal faults along the Kona coast become activated during major and large Kona earthquakes, as the Hilina faults did during the Kalapana 1975 earthquake [*Tilling et al.*, 1976].

Along the southern and western coasts the focal mechanisms of earthquakes of magnitude $M_L \geq 3.0$ allow slip perpendicular to the coasts along decollement planes, and both regions have experienced earthquakes near magnitude 7. If the strain accumulation in the Kona area could be monitored by geodetic means, one would have the possibility to test our expectation that major earthquakes with fault plane characteristics as depicted in Figure 2.9, are to be expected along the Kona coast.

Acknowledgments. We thank John Gephart for his computer codes and advice, and we thank J. Dvorak, R.Y. Koyanagi and F.W. Klein for helpful comments on the manuscript. Andy Michael and Carl Johnson made very thorough reviews which helped improve the manuscript. This work was supported by NSF grant EAR 8916252.

8. REFERENCES

Ando, M., The Hawaii earthquake of November 29, 1975: low-angle normal fault due to forceful injection of magma, *J. Geophys. Res., 84*, 7616-7626, 1979.

Angelier, J., Determination of the mean principal direction of stresses for a given fault population, 1, *Tectonophysics, 56*, 717-726, 1979.

Angelier, J., A. Tarantola, B. Valette, J. Manoussis, Inversion of field data in fault tectonics to obtain a regional stress - I. Single phase fault populations: a new method of computing the stress tensor, *Geophys. J. R. Astron. Soc., 69*, 607-621, 1982.

Bott, M. H. P., The mechanics of oblique slip faulting, *Geol. Mag., 96*, 109-117, 1959.

Bryan, C. J., and C. E. Johnson, Block tectonics of the island of Hawaii from a focal mechanism analysis of basal slip, *Bull. Seismol. Soc. Am., 81*, 491-507, 1991.

Crosson, R. S., and E. T. Endo, Focal mechanisms of earthquakes related to the 29 November 1975 Kalapana, Hawaii, earthquake: the effect of structure models, *Bull. Seismol. Soc. Am., 71*, 713-729, 1981.

Dewey, J. W., Seismicity and tectonics of western Venezuela, *Bull. Seism. Soc. Am., 62*, 1711-1751, 1972.

Dieterich, J. H., Growth and persistence of Hawaiian volcanic rift zones, *J. Gophys. Res., 93*, 4258-4270, 1988.

Endo, E. T., *Seismotectonic framework for the southeast flank of Mauna Loa, Hawaii,* Ph.D. thesis, Univ. of Wash., Seattle, 1985.

Furomoto, A. S., and R. L. Kovach, The Kalapana earthquake of November 29, 1975; an intraplate earthquake and its relation to geothermal processes, *Phys. Earth Planet. Int., 18,* 197-208, 1979.

Gephart, J. W., and D. W. Forsyth, An improved method for determining the regional stress tensor using earthquake focal mechanism data: application to the San Fernando earthquake sequence, *J. Geophys. Res., 89,* 9305-9320, 1984.

Gephart, J. W., Principal stress directions and the ambiguity in fault plane identification from focal mechanisms, *Bull. Seismol. Soc. Am., 75,* 621-625, 1985.

Gephart, J. W., FMSI: A Fortran program for inverting fault/slickenside and earthquake focal mechanism data to obtain the original stress tensor, *Computer and Geosciences, 16,* 953-989, 1990a.

Gephart, J. W., Stress and the direction of slip on fault planes, *Tectonics, 9,* 845-858, 1990b.

Hill, D. P., and J. J. Zucca, Geophysical constraints on the structure of Kilauea and Mauna Loa volcanoes and some implications for seismomagmatic processes, *U. S. Geol. Surv. Prof. Pap., 1350,* 903-917, 1987.

Jones, L. M., Focal mechanisms and the state of stress on the San Andreas fault in southern California, *J. Geophys. Res. 93,* 8869-8891, 1988.

Klein, F. W., A linear gradient crustal model for south Hawaii, *Bull. Seismol. Soc. Am., 71*, 1503-1510, 1981.

Kostrov, B. V., Seismic moment and energy of earthquakes and seismic flow of rock, *Izv. Acad. Sci., USSR Phys. Solid Earth, 1*, 23-44, 1974.

Liang, B., and M. Wyss, Estimates of orientations of stress and strain tensors based on fault plane solutions in the epicentral area of the great Hawaiian earthquake of 1868, *Bull. Seis. Soc. Amer., 81*, 2320-2334, 1991.

Lipman, P. W., The southwest rift zone of Mauna Loa: Implications for structural evolution of Hawaiian volcanoes, *Amer. J. Sci., 280-A*, 752-776, 1980.

Lipman, P. W., J. P. Lockwood, R. T. Okamura, D. A. Swanson, and K. M. Yamashita, Ground deformation associated with the 1975 magnitude 7.2 earthquake and resulting changes in activity of Kilauea volcano, Hawaii, *U. S. Geol. Surv. Prof. Pap., 1276*, 1-45, 1985.

Lipman, P. W., W. R. Normark, J. G. Moore, J. B. Wilson, and C. E. Gutmacher, The giant submarine Alika Debris Slide, Mauna Loa, Hawaii, *J. Geophys. Res., 43*, 4279-4299, 1988.

Macdonald, G. A., and C. K. Wentworth, The Kona earthquake of August 21, 1951, and its aftershocks, *Pac. Sci., 6*, 269-287, 1952.

McKenzie, D. P., The relation between fault plane solutions for earthquakes and the direction of the principal stresses, *Bull. Seismol. Soc. Am., 59*, 591-601, 1969.

Menke, W., *Geophysical Data Analysis: Discrete Inverse Theory*, 260 pp., Academic Press, Orlando, 1984.

Michael, A. J., Determination of stress from slip data: faults and folds, *J. Geophys. Res., 89*, 517-526, 1984.

Michael, A. J., Use of focal mechanisms to determine stress: a control study, *J. Geophys. Res., 92*, 357-368, 1987a.

Michael, A. J., Stress rotation during the Coalinga aftershock sequence, *J. Geophys. Res., 92*, 7963-7979, 1987b.

Moore, J. G., D. A. Clague, R. T. Holcomb, P. W. Lipman, W. R. Normark, and M. E. Torresan, Prodigious submarine landslides on the Hawaiian Ridge, *J. Geophys. Res., 94*, 465-484, 1989.

Nakamura, K., Volcanoes as possible indicators of tectonic stress orientation - principle and proposal, *J. Volcanol. Geotherm. Res., 2*, 1-16, 1977.

Nakamura, K., Why do long rift zones develop better in Hawaiian volcanoes: a possible role of the thick oceanic sediments, *in Proc. International Symp. Activity of oceanic volcanoes, Ser. Cienc. Nat. 3, Universidade dos Acores, Ponta Delgada*, 59-73, 1982.

Nakata, J., W. Tanigawa, and J. J. Dvorak, Comparison of earthquake activity along the west flank of Mauna Loa volcano and the south flank of Kilauea Volcano, Hawaii, *EOS, Trans. AGU, 71*, 1561, 1990.

Oppenheimer, D. H., P. A. Reasenberg, and R. W. Simpson, Fault plane solutions for the 1984 Morgan Hill, California earthquake sequence: evidence for the state of stress on the Calaveras fault, *J. Geophys. Res., 93*, 9007-9026, 1988.

Parker, R. L., and M. K. McNutt, M.K., Statistics for the one-norm misfit measure, *J. Geophys. Res., 85*, 4429-4430, 1980.

Savage, M. K., and R. P. Meyer, A new model for tectonics of the south flank of Kilauea volcano, Hawaii and for the 1975 M=7.2 Kalapana earthquake: rupture and slide zones in the old oceanic sediment layer, *Eos, Trans. AGU, 68*, 1353, 1987.

Swanson, D. L., W. A. Duffield, and R. S. Fiske, Displacement of the south flank of Kilauea volcano: the result of forceful intrusion of magma into the rift zones, *U. S. Geol. Surv. Prof. Pap., 963*, 39 pp, 1976.

Thurber, C. H., and A. E. Gripp, Flexure and Seismicity beneath the south flank of Kilauea volcano and tectonic implications, *J. Geophys. Res., 93*, 4271-4278, 1988.

Thurber, C. H., Y. Li, and C. Johnson, Seismic detection of a low-velocity layer beneath the southeast flank of Mauna Loa, Hawaii, *Geophys. Res. Lett., 16*, 649-652, 1989.

Tilling, R. I., R. Y. Koyanagi, P. W. Lipmann, J. P. Lockwood, J. G. Moore, and D. A. Swanson, Earthquake and related catastrophic events, Island of Hawaii, November 29, 1975: A preliminary report, *Geol. Surv. Circular 740*, 1976.

Whitcomb, J. H., C. R. Allen, J. D. Garmany, and J. A. Hileman, San Fernando earthquake series, 1971, focal mechanisms and tectonics, *Rev. Geophys. Space Phys., 11*, 693-730, 1973.

Wyss, M., A proposed source model for the Great Kau, Hawaii, earthquake of 1868, *Bull. Seismol. Soc. Am., 78*, 1450-1462, 1988.

Wyss, M., and R. L. Kovach, Comment on "A single-force model for the 1975 Kalapana, Hawaii, earthquake" by Eissler, H.K. and Kanamori, H. *J. Geophys. Res., 93*, 8078-8082, 1988.

Wyss, M., and R. Y. Koyanagi, Isoseismal maps, macroseismic epicenters and estimated magnitudes of historic earthquakes in the Hawaiian Islands, *U.S. Geol. Surv. Bull., 2006*, 1992.

Wyss, M., B. Liang, W. R. Tanigawa, and X. Wu, Comparison of orientations of stress and strain tensors based on fault plane solutions in Kaoiki, Hawaii, *J. Geophys. Res., 97*, 4769-4790, 1992.

Zoback, M. D., M. L. Zoback, V. S. Mount, J. Suppe, J., J. P. Eaton, J. H. Healy, D. Oppenheimer, P. Reasenberg, L. Jones, C. B. Rayleigh, I. G. Wong, O. Scotti, and C. Wentworth, New evidence on the state of stress of the San Andreas fault system, *Science, 238*, 1105-1111, 1987.

Zucca, J. J., D. P. Hill, and R. L. Kovach, Crustal structure of Mauna Loa volcano, Hawaii, from seismic refraction and gravity data, *Bull. Seis. Soc. Amer., 72*, 1535-1550, 1982.

Zuñiga, F.R., M. Wyss, and F. Scherbaum, A moment-magnitude relation for Hawaii, *Bull. Seis. Soc. Amer., 78*, 370-373, 1988.

Table 2.1. Velocity Models Used for Locating Earthquakes in West Hawaii.

	Depth, km		Velocity
	HG 50	Modified HG 50	[km/sec]
Layer 1	0.0	0.0	1.9
Layer 2	4.6	4.6	6.5
Layer 3	15.0	20.0	6.9
Mantle	16.5	21.5	8.3

Table 2.2. Fault Plane Solutions for West Hawaii.

Date	Latitude [deg]	Longitude [deg]	Q	F	Depth [km]	Mag	Az1 [deg]	Dip1 [deg]	Az2 [deg]	Dip2 [deg]	Nsta	Ninc	Score
721221	19.468	-155.939	B	2	12.0	3.2	59.028	4.164	187.629	87.399	19	5	2.42
740113	19.486	-155.739	B	1	10.0	3.0	318.818	89.261	59.028	4.162	28	4	2.76
740523	19.336	-155.742	B	1	11.0	3.5	120.973	4.164	310.514	85.893	22	5	1.06
741117	19.441	-155.844	B	1	11.0	3.6	78.687	10.938	271.745	79.339	34	8	2.22
750318	19.496	-155.651	B	1	8.0	3.0	124.226	68.839	357.408	32.859	26	5	2.62
750417	19.493	-155.648	C	2	7.0	3.1	59.028	4.164	249.654	85.907	25	9	3.47
750418	19.483	-155.697	C	1	10.0	3.3	73.309	80.318	281.315	10.937	28	9	3.35
750605	19.322	-155.799	C	1	11.0	3.5	120.973	4.164	294.272	85.864	29	5	3.50
750620	19.498	-155.655	B	2	6.0	3.2	59.028	4.164	277.950	86.758	27	4	2.41
751010	19.494	-155.879	C	1	9.0	3.0	28.874	76.184	171.976	17.093	23	4	2.50
751108	19.297	-155.867	B	1	14.0	3.6	.000	37.118	210.400	56.865	32	1	1.00
751127	19.563	-155.952	C	1	11.0	3.6	18.429	34.389	254.425	69.054	30	12	2.67
751209	19.345	-155.809	C	1	11.0	3.0	62.095	73.655	251.399	16.551	26	4	1.96
760213	19.512	-155.929	C	1	10.0	3.5	170.000	20.000	350.000	70.000	24	4	2.50
760910	19.469	-155.861	A	1	10.0	3.0	105.648	58.072	281.167	32.007	29	3	1.24
770518	19.504	-155.827	C	1	10.0	3.3	75.575	85.020	193.033	10.701	33	6	4.90
770606	19.511	-155.934	C	2	11.0	3.0	130.631	70.224	284.875	21.763	32	7	3.50

Date	Latitude [deg]	Longitude [deg]	Q	F	Depth [km]	Mag	Az1 [deg]	Dip1 [deg]	Az2 [deg]	Dip2 [deg]	Nsta	Ninc	Score
770812	19.327	-155.798	C	1	12.0	3.4	120.973	4.164	331.983	86.429	31	7	3.91
770905	19.448	-155.727	B	2	9.0	3.0	139.096	76.423	303.037	14.107	29	8	2.45
780527	19.643	-156.025	C	1	10.0	3.0	86.353	72.232	276.846	18.051	21	9	1.50
780112	19.520	-155.925	C	1	10.0	3.0	359.779	83.442	120.973	12.514	30	8	5.29
781231	19.532	-155.699	A	2	10.0	3.0	29.046	7.357	231.062	83.174	28	3	1.03
790514	19.279	-155.786	B	2	9.0	3.5	59.028	4.164	177.445	88.016	26	4	1.89
790626	19.476	-155.867	B	1	10.0	3.4	92.644	47.840	267.117	42.293	26	3	1.99
790904	19.744	-156.014	C	1	9.0	3.2	7.715	84.992	120.973	12.513	28	4	2.00
790914	19.349	-155.821	A	1	12.0	3.9	109.806	19.058	345.835	79.074	37	2	1.29
790926	19.542	-155.923	A	1	11.0	3.2	209.047	7.357	341.363	85.032	23	2	1.00
791130	19.582	-155.991	B	2	11.0	3.1	147.710	79.809	261.047	24.408	24	1	.48
800507	19.734	-155.746	C	2	13.0	3.4	144.473	18.509	277.487	77.136	36	8	4.24
800907	19.449	-155.819	A	1	10.0	3.0	171.401	7.963	305.609	84.429	29	4	2.00
801009	19.383	-155.825	A	1	13.0	3.3	353.942	73.751	144.473	18.509	30	1	.50
801201	19.514	-155.920	A	1	12.0	3.4	161.572	11.310	314.754	79.880	34	2	.64
801230	19.300	-155.777	C	2	10.0	3.9	180.000	86.000	0.000	4.000	43	5	1.86
810208	19.351	-155.850	A	2	11.0	3.0	208.494	86.445	109.481	21.631	22	2	1.50
810521	19.206	-155.696	B	2	7.0	3.5	44.990	15.192	308.490	88.239	32	11	1.89

Date	Latitude [deg]	Longitude [deg]	Q	F	Depth [km]	Mag	Az1 [deg]	Dip1 [deg]	Az2 [deg]	Dip2 [deg]	Nsta	Ninc	Score
810531	19.489	-155.773	B	1	10.0	3.2	94.871	89.270	186.839	20.366	23	4	1.50
811101	19.487	-155.880	B	1	11.0	3.1	348.000	70.000	168.000	20.000	26	3	1.00
830412	19.494	-155.667	A	1	7.0	3.7	95.414	72.985	358.456	68.403	35	1	1.00
830521	19.590	-155.699	B	1	7.0	3.1	96.846	18.051	328.051	78.460	23	2	.74
830622	19.489	-155.863	C	1	11.0	3.3	161.617	11.351	331.512	78.821	32	6	2.50
830906	19.511	-155.657	A	1	8.0	3.3	123.887	56.146	19.789	70.044	39	3	1.50
830909	19.506	-155.661	A	1	6.0	3.1	99.481	80.050	358.747	43.285	26	2	1.00
830912	19.503	-155.664	C	1	8.0	3.3	120.973	51.930	10.495	65.931	32	1	.50
830914	19.507	-155.658	A	1	8.0	3.7	120.973	66.062	350.471	34.354	45	5	2.07
830916	19.496	-155.650	A	1	8.0	4.1	130.059	56.746	21.444	64.043	47	1	.50
830916	19.503	-155.653	A	1	8.0	4.0	132.017	60.468	20.967	57.625	45	2	1.00
830926	19.304	-155.758	B	1	11.0	3.0	15.736	86.662	120.973	12.513	36	3	1.54
831005	19.504	-155.658	A	1	7.0	3.2	123.090	46.474	355.805	57.472	31	3	1.00
840924	19.326	-155.888	A	1	11.0	4.2	83.155	18.051	344.914	87.325	45	2	.83
850323	19.421	-155.828	A	1	11.0	2.9	161.572	11.310	306.351	80.721	36	4	1.56
850610	19.299	-155.796	C	1	11.0	3.1	120.973	4.164	309.991	85.887	37	1	.04
851010	19.314	-155.876	C	1	11.0	3.4	78.687	10.938	287.191	80.362	45	8	4.50
851212	19.516	-155.908	B	1	12.0	4.0	198.430	11.310	345.982	80.420	45	4	1.95

Date	Latitude [deg]	Longitude [deg]	Q	F	Depth [km]	Mag	Az1 [deg]	Dip1 [deg]	Az2 [deg]	Dip2 [deg]	Nsta	Ninc	Score
860828	19.537	-155.963	C	1	12.0	3.1	198.430	11.310	309.063	85.969	24	2	1.00
861102	19.478	-155.883	A	1	13.0	2.7	114.257	15.718	276.556	74.992	18	1	1.00
870130	19.373	-155.799	A	1	10.0	2.9	358.709	74.864	166.613	15.463	31	2	.63
870303	19.456	-155.809	C	1	8.0	2.7	59.028	4.164	239.029	85.836	31	9	2.16
870403	19.532	-155.700	A	2	5.0	2.5	59.028	4.164	182.581	87.696	21	3	1.52
870404	19.350	-155.874	C	2	6.0	2.7	59.028	12.515	247.740	77.625	21	5	1.94
870918	19.314	-155.770	A	1	10.0	4.0	120.973	4.164	341.972	86.855	37	3	.50
871219	19.489	-155.818	B	1	9.0	2.5	341.300	83.898	180.001	6.440	18	2	1.00

Q is the quality factor assigned to each fault plane solution. F is the dip-slip component of fault motion: 1,normal; 2,reverse; Az1, Dip1 and Az2, Dip2 (in degrees) are the strikes and dips of the first and second nodal planes. Nsta is the number of first motions used in the determination of the fault plane solution. Ninc is the number of inconsistent first motions. Score is defined in detail in the text. Latitude and longitude are in degrees and depth is in km.

Table 2.3. Stress Tensor Directions for West Hawaii Derived from Fault Plane Solutions.

Data Set	No of	σ_1		σ_2		σ_3		Ratio	Average
	Events	PL [deg]	AZ [deg]	PL [deg]	AZ [deg]	PL [deg]	AZ [deg]	R	misfit [deg]
Entire data set	57	63	274	3	178	27	86	0.7	6.0
Area 1	29	83	312	2	203	7	113	0.9	4.5
Area 2	17	82	288	7	138	4	47	0.9	2.3
Area 3	11	48	359	3	92	42	185	0.7	2.3
Area 1*	23	83	316	3	203	6	113	0.9	4.0

PL, plunge; AZ, azimuth

*Depth $\leq$ 10 km

Table 2.4. Directions of Principal Strain for West Hawaii.

	Number of	ε_1		ε_2		ε_3		ΔM_o
	data	PL	AZ	PL	AZ	PL	AZ	10^{20}
		[deg]						[dyn cm]
Area1	29	56	244	5	341	33	75	2.9
		38	42	2	88	34	50	
Area2	17	50	259	7	160	39	65	7.1
		36	42	6	52	42	34	

Azimuth (AZ) and plunge (PL) of the principal strain directions are given with uncertainty underneath it corresponding to 2 times the standard deviation. ΔM_0 is the uncertainty of the scalar moment.

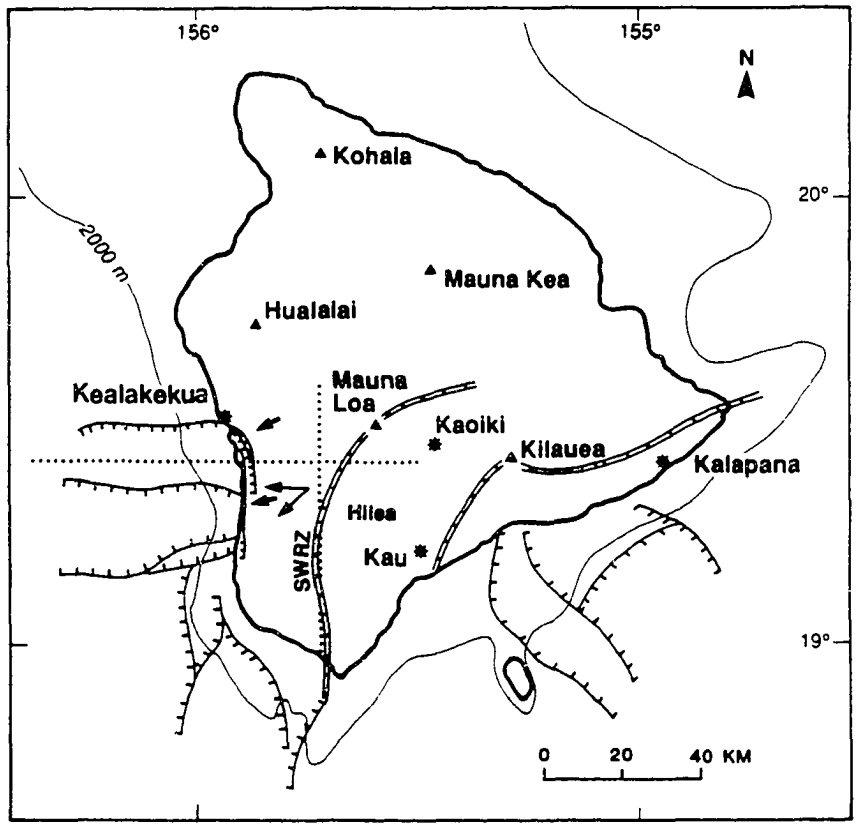

Fig. 2.1. Map of the island of Hawaii identifying the volcano summits Hualalai, Kohala, Mauna Kea, Mauna Loa, and Kilauea. Rift zones are marked with connected double lines; SWRZ, southwest rift zone. The stars are epicenters of M>6.5 earthquakes mentioned. The lines with the ticks on downthrown side marks the landslides in the west and southeast of Hawaii. The thick arrows indicate the slip direction and the thin arrows, the range of directions for the horizontal greatest principal stress. The dotted lines divide the three subregions described in Figure 2.2.

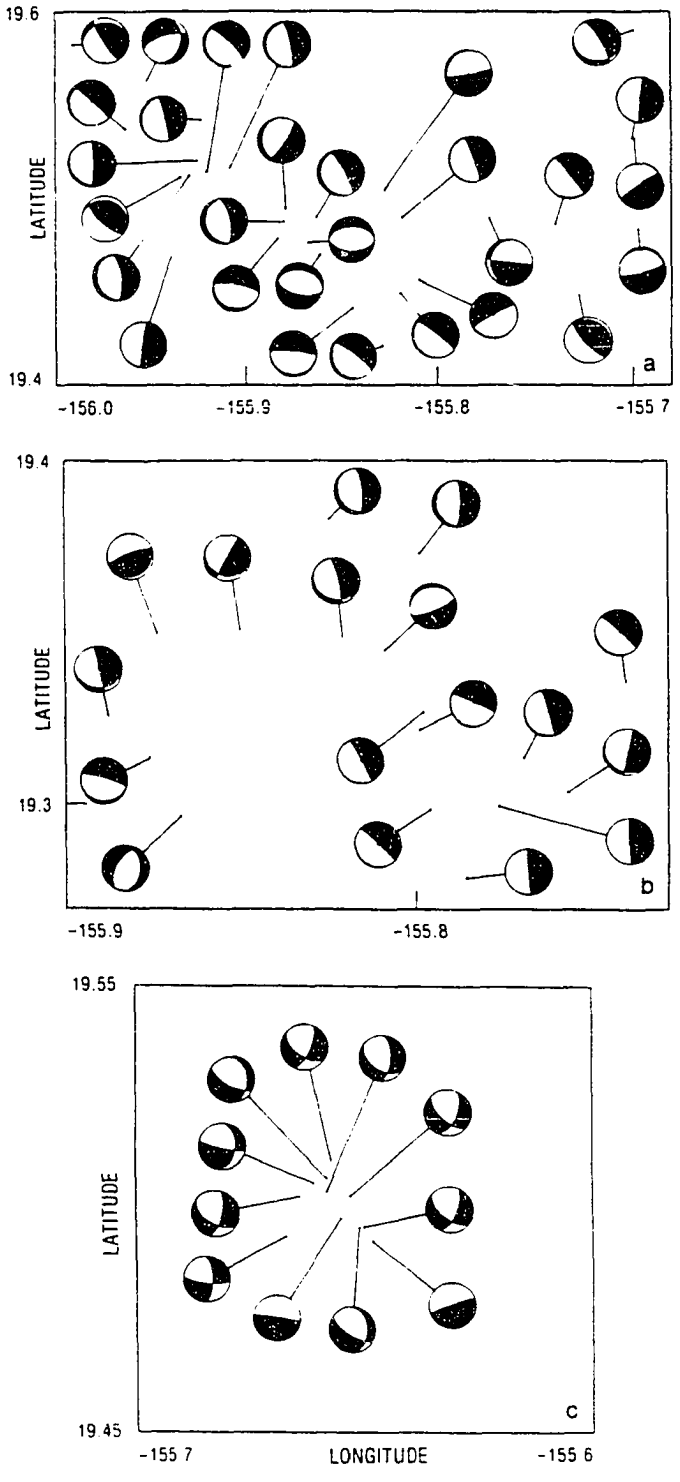

Fig. 2.2. Fault plane solutions for events (a) area 1, (b) area 2, and (c) area 3. Lower hemisphere projections with the compressive quadrants dark are used.

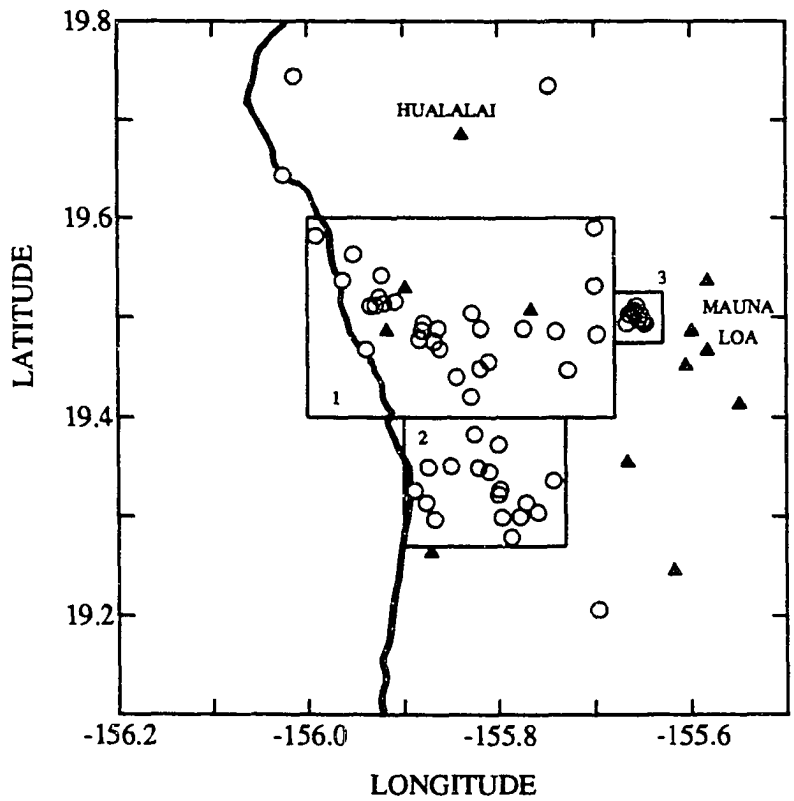

Fig. 2.3. Map of epicenters of earthquakes used in this study (open circles). The numbers (1, 2, 3) refer to three areas for which separate inversions were calculated. The four events located outside of these three areas were not used. The triangles represent the seismograph stations of the HVO network.

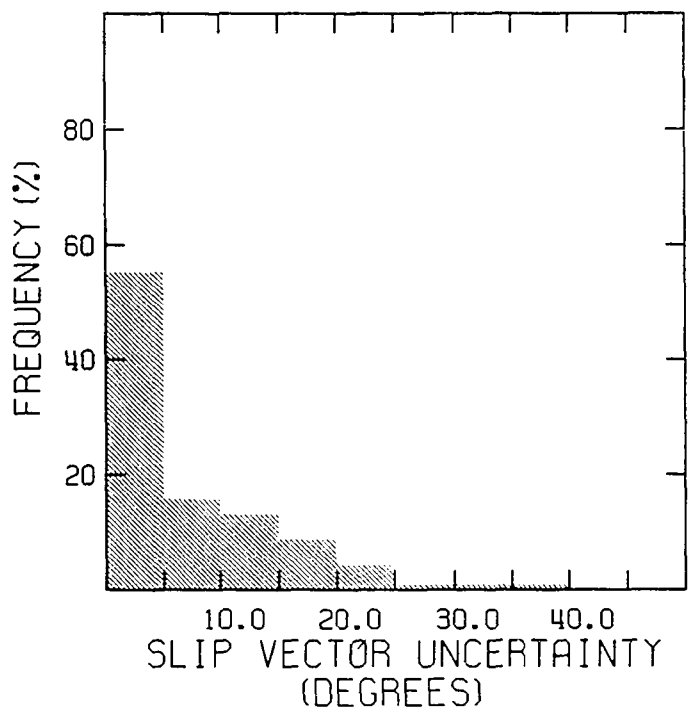

Fig. 2.4. Slip vector uncertainty of individual fault plane solutions. These values are obtained by measuring the range of angles which the slip vectors may occupy without introducing an additional violation of a first motion reading.

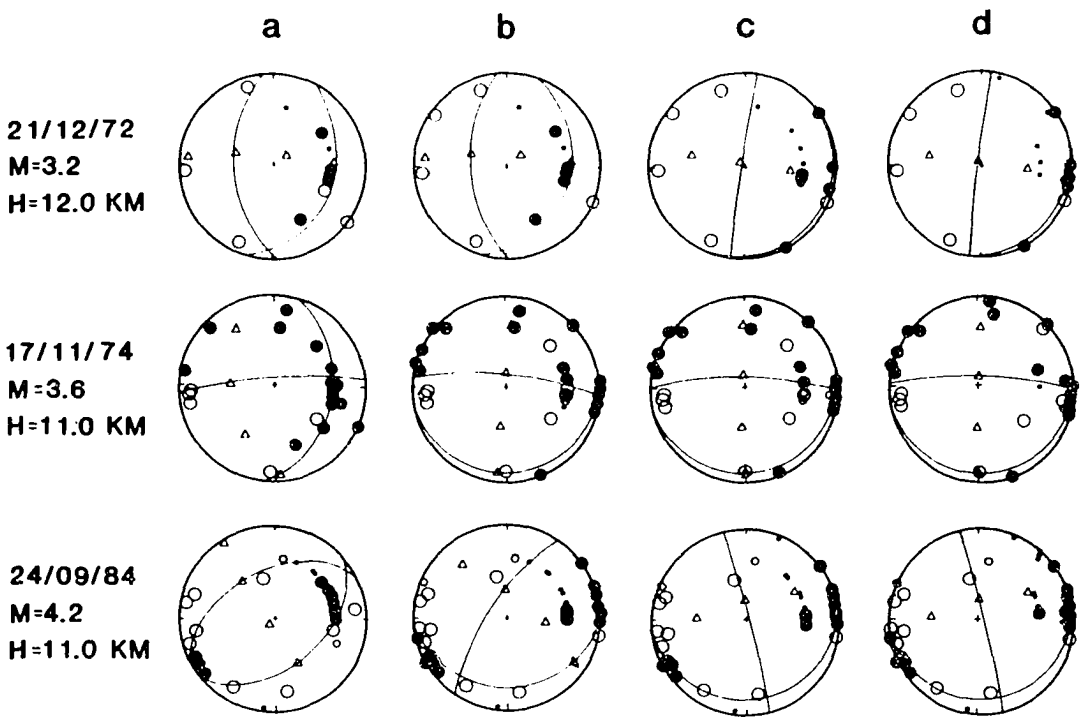

Fig. 2.5. Examples of focal mechanisms for different depths of the Moho. a) Original focal mechanisms computed from first motion data and takeoff angles as they are listed in the HVO catalog based on the model HG50 with the Moho at 16.5 km depth. b) Moho at 20.5 km. c) Moho at 21.5 km. d) Moho at 26.5 km. Lower hemisphere projections. Solid and open circles mark compressions and dilatations, respectively. Triangles are P and T axes and slip vectors. Earthquake date, magnitude, and depth are listed on the left-hand side of the fault plane solutions.

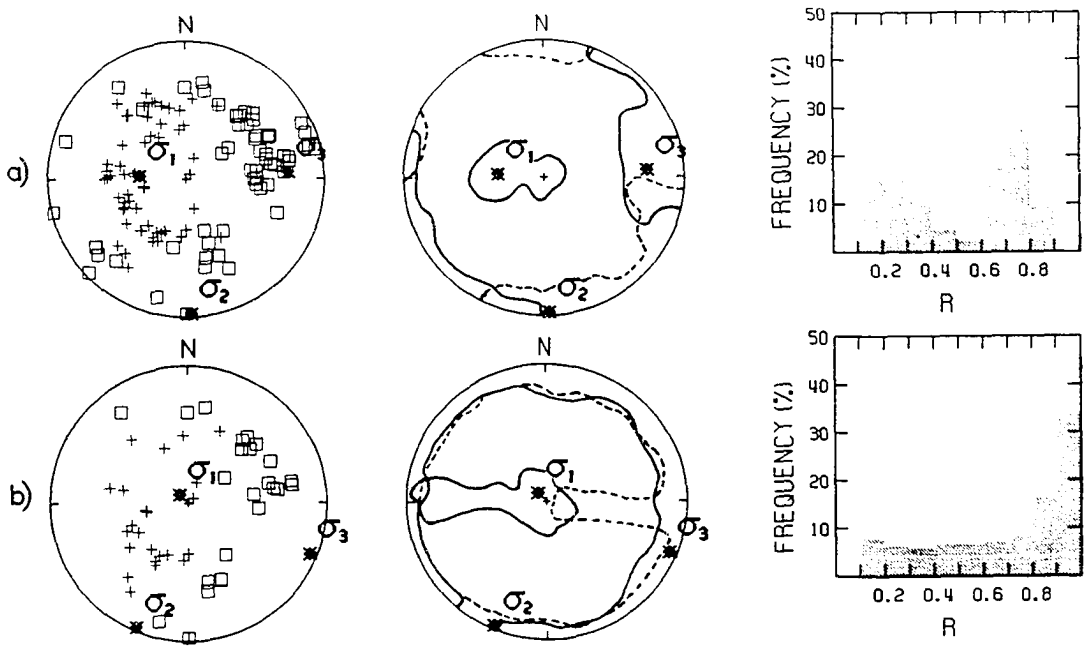

Fig. 2.6. Directions of principal stresses (stars) derived from fault plane solutions for west Hawaii. (Left) Distribution of P and T axes (crosses and squares, respectively) on the lower hemisphere stereographic projection. (Middle) 95% confidence region; the heavy contours represent the greatest and least principal stresses, and the dashed contour represents the intermediate principal stresses. (Right) Distribution of R values for the models within the 95% confidence limit. (a) For entire data, (b) for events in area 1 depth ≥ 10 km.

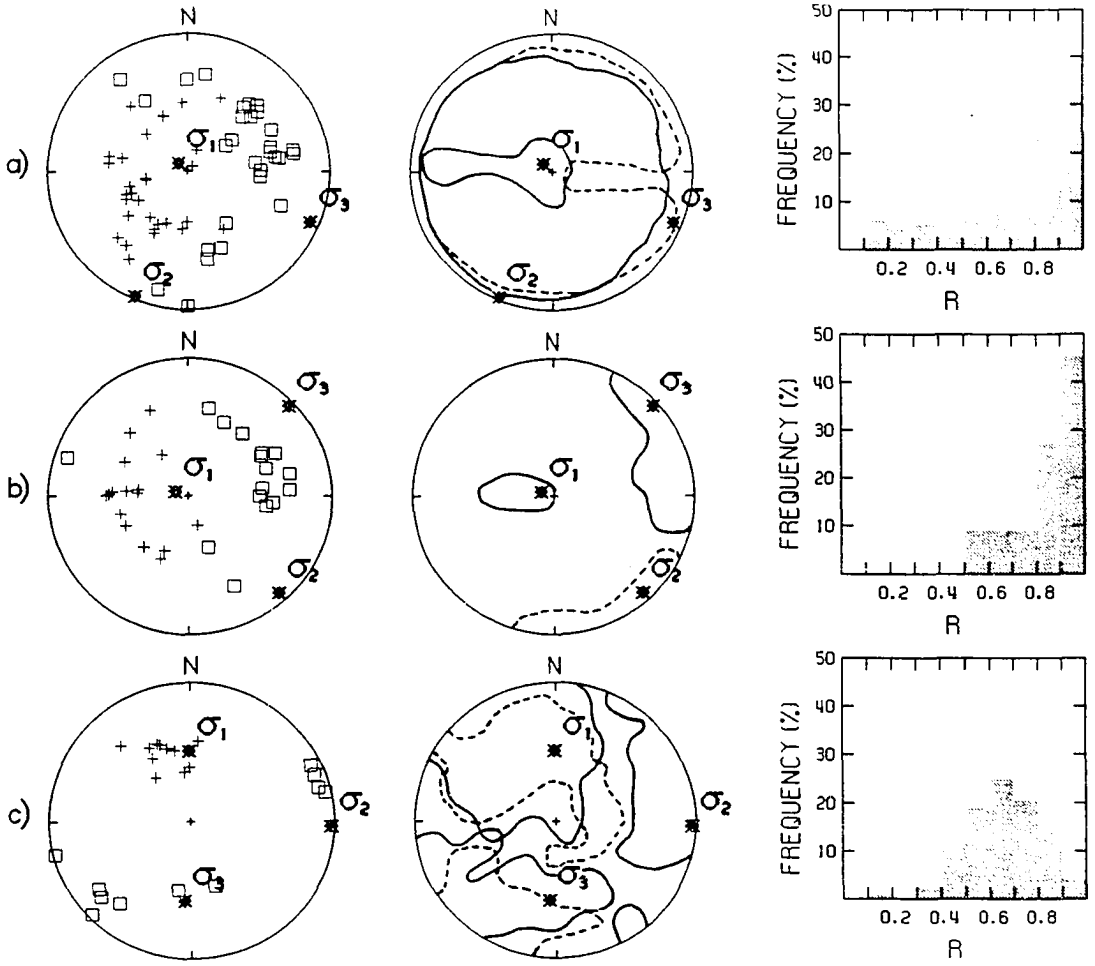

Fig. 2.7. Directions of principal stresses for subregions of west Hawaii. Same plots as Figure 2.6 for (a) area 1, (b) area 2, and (c) area 3.

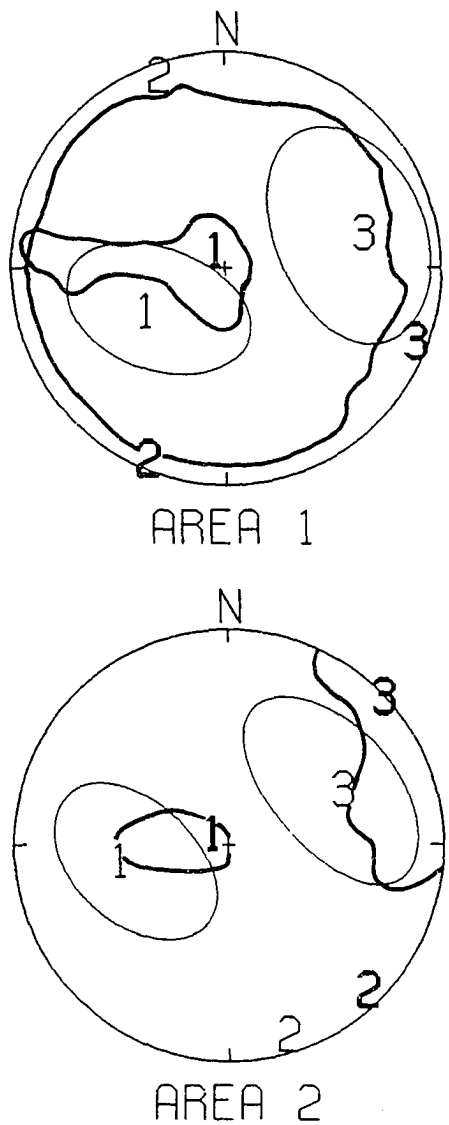

Fig. 2.8. Stereographic projections of the principal stress and strain axes for areas 1 and 2. The best fitting greatest, intermediate and least principal axes are labeled 1, 2, and 3 with bold and fine print for stress and strain, respectively. The heavy contours mark the directions of the greatest and least principal stress solutions which cannot be distinguished from the best solution at the 95% confidence level. The light contours denote the 95% confidence range of the principal strain axes (light numbers). The 95% ranges for the intermediate strain and stress axes are not drawn.

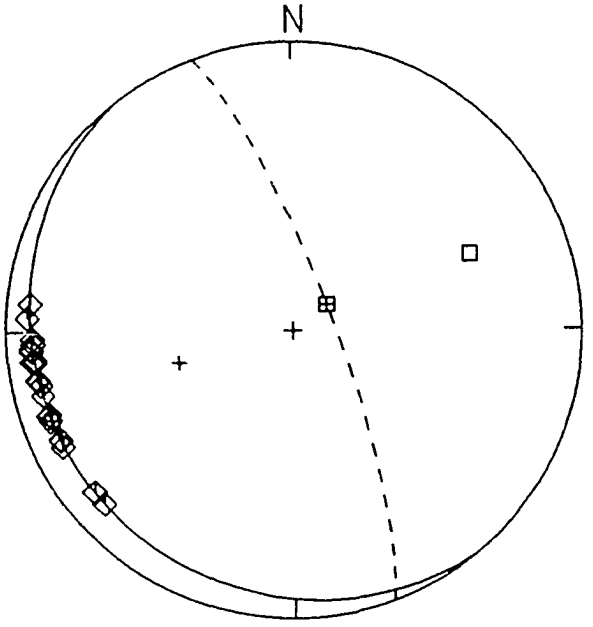

Fig. 2.9. Proposed focal mechanism for major Kona earthquakes. The plus is the P axis, the square is the T axis. The auxiliary plane is shown as a dashed line. The poles of the nodal planes are represented with a plus within a square. The diamonds represent the predicted slip vectors on the fault plane for the models within the 95% confidence region inverted from the data set of area 2.

CHAPTER 3

INVERSION FOR SOURCE PARAMETERS FROM SPARSE DATA SETS: TEST OF THE METHOD AND APPLICATION TO THE 1951 (M=6.9), KONA, HAWAII, EARTHQUAKE[1]

1. ABSTRACT

We have tested a method originally developed by *Beisser et al.* [1990] to invert teleseismic waveform data for the source parameters (strike, dip, rake and depth) of sparsely recorded earthquakes. The complete wave train of all body waves is modeled using the reflectivity method. The parameter space of strike, dip and rake is searched to find the source orientation which leads to the minimum misfit between the observed and the synthetic seismogram. The 1983 Kaoiki, Hawaii, earthquake (M_S=6.6) was chosen as a test case. The inversion of the full data set (16 stations) gave a fault plane solution similar to the best double couple moment tensor solution of Harvard (HRVD) and NEIS. These three solutions were averaged to create a standard solution. Sparse data sets were simulated by decimating the full data set and the resulting fault plane solutions were compared to the

---

[1] Chapter 3 contains the complete text and figures of the manuscript, *Inversion for source parameters from sparse data sets: test of the method and application to the 1951 (M=6.9), Kona, Hawaii, earthquake*, by M. Beisser, D. Gillard, and M. Wyss, as submitted to the *Journal of Geophysical Research*, 1992.

standard. We found that as few as one to three stations were sufficient to retrieve the focal mechanism of the 1983 Kaoiki event. We applied this technique to the 1951 Kona, Hawaii, earthquake (M_S=6.9). A total of 4 stations and 9 components were used to model the source parameters of this earthquake. The depth was estimated at 13±3 km. The fault plane solution was a decollement type with a near-horizontal plane dipping at about 15° to the south west and a near-vertical plane striking NW-SE. This observation supports a tectonic model for the Kona coast similar to that of Kilauea's south flank: the upper crust is pushed away from the center of Hawaii slipping westward along a near-horizontal plane of weakness.

2. INTRODUCTION

The focal mechanisms of historical earthquakes can provide useful information about the tectonics of an area which has not experienced any recent major earthquake. Commonly used methods to retrieve the source parameters of an earthquake require that the event was recorded by many stations covering well distributed azimuths. However, historical events in the magnitude range $6 \leq M \leq 7$ are often poorly recorded. In order to retrieve meaningful information from sparse records, *Beisser et al.* [1990] developed a method to invert teleseismic waveform data for the source parameters (strike, dip, rake, depth and scalar moment) from a single three component station. This method searches the complete parameter space of strike, dip and rake to find the source orientation, which leads to the best fit. The complete wave train of all body waves is modeled.

In this paper we use this method to model the 1951 (M_S=6.9) Kona earthquake in Hawaii. The knowledge of its focal mechanism will help to elucidate the tectonics of the western part of the island of Hawaii. Since this method has not been tested sufficiently, we will first test it on the 1983 (M_S=6.6) Kaoiki earthquake. The fault plane solution for the 1983 Kaoiki event, as well as its location and depth, are well known and the event has been recorded digitally by networks around the world. We will show that as few as one to three stations can furnish enough constraints to get unique reliable fault plane solutions, even if the azimuthal coverage is poor.

The island of Hawaii is probably deposited on an oceanic sediment layer

which may act as a zone of weakness at a depth of about 11 km. Evidence for the presence of this layer comes from fault plane solutions [*Crosson and Endo*, 1981; *Bryan and Johnson*, 1991; *Gillard et al.*, 1992], concentration of relocated earthquakes at this particular depth [*Savage and Meyer*, 1987; *Thurber and Gripp*, 1988] and identification of seismic phases reflected off the top and bottom of this low velocity layer [*Thurber et al.*, 1989]. Stress accumulates by magmatic intrusions in the rift zones and is released by earthquakes occurring along the horizontal oceanic sediment layer underlying the edifice of the island [*Dieterich*, 1988]. The slip is oriented seaward and almost perpendicular to the rift. This model has been proposed by several authors [*Swanson et al.*, 1976; *Furomoto and Kovach*, 1979; *Ando*, 1979; *Endo*, 1985; *Lipman et al.*, 1985; *Wyss and Kovach*, 1988] to explain the occurrence of the 1975 (M_S=7.2) Kalapana earthquake. Based on focal mechanisms and other seismological and geodetic evidence, these authors show that the Kalapana earthquake could be caused by the accumulation of strain energy via magmatic intrusion in Kilauea volcano and its rift zone.

In the western part of Hawaii (Figure 3.1), this tectonic model could also be valid [*Gillard et al.*, 1992]. By determining the focal mechanisms of 57 small earthquakes (M_L< 4.2) these authors found that the majority of earthquakes are of decollement type with one near-horizontal plane. The average slip direction on the decollement plane was oriented between azimuths 228° and 277° in a direction away from Mauna Loa's south west rift zone (Figure 3.1). All earthquakes studied occurred at depths between 8 km and 12 km. Based on these results, and the assumption that the sediment layer also exists under western Hawaii, *Gillard et al.*

[1992] proposed a decollement-type focal mechanism for the August 21, 1951 M_S= 6.9 earthquake (strike=142°, dip=12°, rake=-108°). No source mechanism of this major earthquake has yet been determined to confirm this hypothesis.

The 1951 Kona event is the third strongest earthquake to occur in Hawaii in historic time (since 1832) [*Wyss and Koyanagi*, 1992]. Because of the sparse seismic network at that time, only 25 world wide stations reported the directions of first motion to the International Seismological Summary. The location of the epicenter at latitude 19.5°N and longitude 155.9°W was estimated by *MacDonald and Wentworth* [1952] who also described the destructive effects of this earthquake. The magnitude of this event was M=6.9 [*Gutenberg and Richter*, 1954]. Based on the ratio of body waves and surface waves at a single station (Pasadena), *Eissler and Kanamori* [1986] estimated the depth between 25-30 km. Macroseismic data are compatible with these estimates [*Wyss and Koyanagi*, 1992].

In order to test the hypothesis that the tectonic model for the Kalapana region is also correct for the western part of Hawaii, it is important to know the source mechanism of this major earthquake. The Kona earthquake was strong enough to be well recorded at several stations. For that reason, it is possible to use the waveform inversion method developed by *Beisser et al.* [1990] to determine the source mechanism and the depth of the Kona earthquake.

3. METHOD

The method developed by *Beisser et al.* [1990] to retrieve the source parameters from one single station was modified to allow an arbitrary number of stations and components. The best fit of a data trace by a synthetic seismogram is found by a systematic grid search in the parameter space of strike, dip and rake. A synthetic seismogram is computed for every source orientation, using a five degree grid, and a correlation coefficient is obtained describing each fit. If the correlation is negative it is set equal to zero. This procedure creates a three dimensional correlation matrix for each component of the seismic record. It is also possible to compute the ratio of the maximum amplitudes of the components, if two or three components of one station are available. Thus we define another matrix that describes the misfit between the measured amplitude ratio and the computed one at every grid point. By multiplying the correlation matrices by the amplitude misfit matrix for a three or two component station, one finds the final matrix that defines the fit to the data as a function of the three fault parameters. The rake, strike and dip leading to the highest correlation value are retained as the solution. The quality of the solution can be estimated from the width of the peak in the parameter space. By visual inspection one can check the uniqueness of the solution. The computer codes of *Beisser et al.* [1990] were extended to combine the results of different three, two or one component stations by multiplying the matrices of each station.

The depth is found by modeling the P-wave group using a source orientation that matches the first onset, but is arbitrary otherwise. Because the depth controls

the duration of P-wave groups, the best matching depth can be found by visual comparison of the data with synthetics computed for different depths.

To compute synthetic seismograms we used the reflectivity method developed by *Kind* [1985] for P-SV and by *Beisser and Kind* [1988] for SH waves. The complete P-, SV- and SH-wave groups, including all depth and mantle phases like P, pP, PP, S, sS, SS etc. were computed. In order to rapidly get synthetics for different source orientations, we first computed the three so called fundamental seismograms. These are seismograms computed with the source orientations

	Strike	Dip	Rake
1st fundamental seismogram	0°	90°	0°
2nd fundamental seismogram	0°	0°	90°
3rd fundamental seismogram	0°	45°	0°

respectively. It is well known that one can compute seismograms for any arbitrary orientation by linear combinations of these three fundamental seismograms [*Ben-Menahem and Singh*, 1981]. Using this approach we were able to correlate synthetics with the data for every source orientation using a five degree grid, within reasonable computing time.

The source is a dislocation point source with the time function proposed by *Bruestle and Mueller* [1983]. The rise time of the ramp function controls the frequency of the source signal. It equals approximately the rupture duration. The maximum amplitude of the ramp function determines the amplitude level of the synthetic signal. We used the same crustal model for the receiver as for the source,

because we did not know the crustal structure under the stations. The model HG50 published by *Klein* [1981] was chosen as the velocity model in the source vicinity. This model has given good results for locating earthquakes and computing their focal mechanism in the southern and eastern part of Hawaii [*Klein*, 1981]. We found that the model HG50 produced synthetics that matched our data well enough in all cases. For depths greater than 40 km, we used the PREM model.

4. DATA

Two different data sets were used. For testing the reliability of the method, we used the digital long period data of the 1983 Kaoiki earthquake from the SRO, DWWSSN, and RSTN networks. These data are available on compact disks distributed by the National Earthquake Information Center (NEIC). For the 1983 Kaoiki event we used 16 stations with distances less than 81° (Table 3.1). The components were rotated into a ray coordinate system L, Q and T, the polarization directions of the P, SV and SH energy, respectively. The angle of rotation was measured from a plot of the particle motion of the S-phase. The same rotation angle was also used for the theoretical seismograms.

To determine the source orientation of the 1951 Kona earthquake, we gathered all available paper records. Four stations with good data quality were selected (Table 3.2): Tucson (TUC, 3 components), Arizona; Haviland (HAV, 3 components), California; Florissant (FLO, 2 components), Missouri; Matsushiro (MAT, one component), Japan. We digitized the analog paper records carefully and checked the quality of the result by overlaying the digitized data with the originals.

The digitized data are shown in Figure 3.2.

5. TEST OF THE METHOD

The test earthquake occurred on November 16, 1983 at 16:13:11 in Kaoiki, Hawaii. It was well recorded locally by 38 stations and was located by the Hawaiian Volcano Observatory (HVO) at 19° 25.8' N latitude and 155° 27.0' W longitude with a depth of 11 km. The first motion analysis of the local data indicates a strike-slip focal mechanism (Figure 3.3c). The International Seismological Center (ISC) published the Harvard (HVRD) centroid moment tensor solution (Figure 3.3a) and the NEIS moment tensor solution (Figure 3.3b) of this earthquake. The NEIS moment tensor solution is determined using the body wave moment tensor inversion method described by *Sipkin* [1982] and the Harvard solution is based on the inversion of long period body and mantle wave described by *Dziewonski et al.* [1981]. As a first task, we will compare our results to the ones produced by Harvard and NEIS. If our results are similar to the solutions computed by these standard methods, we will conclude that the method used in this paper successfully modeled the test earthquake. In the second task of the test, we will address the question whether the sparse data set, for the 1951 Kona earthquake, can adequately constrain the solution. To accomplish this task, we will consider the following three questions:

1. How sparse can the data set be and yet furnish a reliable unique estimate of the source orientation?

2. How good does the azimuthal coverage need to be to allow a unique estimate of the source orientation?
3. Are the data available for the 1951 Kona event sufficient to define a reliable unique estimate of the source orientation?

By simulating the station configuration (azimuthal coverage and available stations and components) of the 1951 event with the data of the 1983 event, we will be able to test if the known source parameters of the 1983 Kaoiki earthquake are retrievable from sparse data, and we can then estimate the quality of solution that may be expected for the Kona case.

5.1. The rise time

The frequency content of the synthetics is determined by the rise time of the ramp function that we used as a dislocation point source. A rise time of 20 seconds was needed to fit the frequency content of the Kaoiki P-wave group. Because of the shallow depth and broad pulse width the depth phases are not distinct, thus the depth could not be estimated accurately by modeling the P-wave data. Any depths within the top 12 ± 7 km led to acceptable fits. Thus we used the hypocentral depth of 11 km calculated from the local arrivals.

5.2. Modeling of the data

In order to be able to correlate the synthetic and the observed signals, the traces must be aligned on the first P-onset. Since we are modeling simultaneously P and S body waves, the S-onset of the synthetic trace should be aligned automati-

cally with the S-onset of the observed trace, if the location of the earthquake and the velocity model used to compute the synthetic seismogram were perfectly correct. For the 1983 Kaoiki earthquake (test event), we found that the S-P time of the synthetics computed with the selected velocity model were between 3 and 15 seconds shorter than the S-P time measured on the observed seismograms, indicating that the P- to S-velocity ratio of the velocity model (HG50 + PREM) is not correct. We believe that the delay of the S arrival is mainly due to an unusually low S-velocity below Hawaii, and variations in travel time may also be due to the unknown crustal properties under each station. The delay of the S-P time does not correlate with epicentral distance or the azimuth of the stations. In order to align the P- and S-onsets we proceeded by first aligning the P-onset on the L-components. Then we increased the distance between source and receiver to align the S-onset on the T-components. We used the T-component because the S-wave package is better detected on the rotated transverse component (T-component) than on the Q- or L-components. The smallest epicentral distance increase was about 52 km and the largest was 242 km (Table 3.1).

5.3. Inversion of the full data set for the 1983 Kaoiki earthquake

The next step was to compute correlation matrices for all components of all available seismic stations. Based on these we created for every station a single matrix by multiplying the matrices of the three components with the amplitude misfit matrix of this station. This procedure is demonstrated for the example of station MAJO in Figure 3.4 which shows the goodness of fit as a function of strike

and rake for a dip fixed at 25°.

The solution with the highest correlation coefficient (best solution) is represented graphically by the highest peak which has to be, according to our experience, at least 20% higher than the peak of any other solution to be considered unique. In the majority of cases, this difference is higher. The quality of the best solution is judged visually by the width of the peak. A very broad peak means that the strike, dip and rake can vary over a large range and produce the same fit to the data. The solution of the inversion of the full data set is obtained by multiplying the correlation matrices of each station together.

5.4. The standard solution for the Kaoiki test case

For judging how well we can constrain the focal mechanism from sparse data sets of the Kaoiki earthquake we need a standard, i.e. the best estimate. The difference between the local and teleseismic data (Figures 3.3a, b, c) will be discussed later, because it is not relevant to setting the standard for the "correct" teleseismic result. We will use the average of the HRVD and NEIS solutions as the best estimate, independent of our work, for the teleseismic fault plane solution

NP1: 38° / 87° / 120° (1)

Our solution using 16 stations yielded

NP1: 34° / 97° / 109° (2)

The comparison of our solution (Figure 3.3d) with the HVRD and NEIS solutions

(Figures 3.3a and b) show close agreement. All parameters are within about 11° or less from the average given in (1), except for the strike of the near-horizontal plane, which is a meaningless parameter, because the smallest change in orientation can cause great changes in strike for this geometry.

We conclude that the inversion of fault parameters using the method of *Beisser et al.* [1990] yields correct results within about 10°, when a data set with an ample number of stations and good azimuthal coverage is used. We do not know whether any of the three teleseismic solutions (Figures 3.3a, b and d) is superior to the others, thus we shall weigh them equally and use their average as the best estimate of the "correct" teleseismic result (including our work) against which we will judge the results from sparse data sets. The standard for teleseismic results therefore is the average of the three teleseismic solutions (Figures 3.3a, b and d)

NP1: 37° / 90° / 116° (3)

5.5. Inversion from single station records

We applied our technique to each available station individually and compared the resulting best fitting solutions with the standard solution (number 3). We found that 5 out of the 16 available stations (LON, COL, RSNY, GAC, CTAO) presented a unique solution similar to the standard (Table 3.3). Station AFI also had a maximum correlation for a source mechanism similar to the standard, but the broadness of the peak was too large to consider this solution as being unique. The average of the 5 unique solutions for the strike, dip and rake of the first nodal plane (NP1) is

28°, 89°, and 107°, respectively, with a standard deviation of 7°, 5° and 6° for strike, dip and rake, respectively. The remaining stations had more than one maximum with correlation values within 20% of each other. For that reason, these results were called non-unique. Nevertheless, one of the maxima for each of the station with non unique solutions, corresponded to source parameters similar to the standard solution. Thus we find that all single stations with unique solutions gave reliable solutions with fault parameters within about 10° from the standard.

5.6. Inversion from sparse multi-station data sets

Next we investigated the capability of sparse multi-station data sets to confine the results and approximate the standard solution. To accomplish this task, we decimated the data set in order to simulate the sparsity. We first tried to determine if a poor azimuthal coverage would affect the results. We combined groups of three stations with similar azimuths and take-off angles (Figure 3.5a and Table 3.4) and found that all of these combinations produce results which are similar to each other and agree with the standard solution. These solutions are all unique and the average strike, dip and rake for the first nodal plane (NP1) is 31°, 94°, and 115°, respectively, with standard deviations 6°, 6° and 9°. This result indicates that, even with a very poor azimuthal coverage, it is still possible to retrieve the final solution uniquely with a reasonable uncertainty.

In order to extend the test to any arbitrary combinations of three stations, we decimated the data set into 15 arbitrary combinations of three stations. We found very consistent results agreeing with the standard solution (Table 3.5). Each three

station combination gave a unique solution. The average for the strike, dip and rake was 212°, 84° and -107° respectively and the standard deviation for each of these parameters was 8°, 4° and 11°, respectively (Table 3.5).

The last test we conducted, was to simulate the station configuration of the 1951 Kona event, in terms of azimuthal coverage, source-receiver distance and availability of station components. The purpose was to determine, in advance, if the station combination for the 1951 event was sufficient for deriving a reliable solution. Unfortunately, only one station (Matsushiro) was working at the time of both earthquakes but with different instruments (MAJO is the station code of the Matsushiro station for the 1983 event and MAT is the one for the 1951 event). Nevertheless the stations marked with a star in Figure 3.5a are distributed in a similar fashion as the 1951 station distribution. Only the vertical component of MAT existed for the 1951 event. Therefore, for the 1983 test case, we used the vertical component of MAJO and computed source solutions with any combination of stations RSNY, ANMO, and RSSD (Table 3.6) to simulate the data set of the 1951 Kona earthquake. This test, approximating the station coverage of 1951, gives a result very similar to the standard source mechanism. The combination of the vertical component of MAJO with only one other station situated in a different quadrant of the focal sphere also gives unique solutions similar to the best solution (Table 3.6), but the standard deviation is slightly larger. In the case of combining the vertical component of MAJO with any pair of the other stations, the resulting mechanism is unique and similar to the "correct" solution (number 3 and Table 3.6).

5.7. Discussion of the test

We showed that for any decimated data set with three, 3-component stations, we can still obtain a unique, stable and reliable solution (Table 3.5). Even if the azimuthal coverage of the stations is poor, the best fitting focal mechanism can still be retrieved (Table 3.4 and Figure 3.5a). This is an important result because often historical events are not well recorded and the data present large azimuthal gaps. This problem exists for the 1951 Kona earthquake which was recorded by three stations with approximately the same azimuth and take-off angle (FLO, HAV, TUC) and one station with only one component (MAT) located in a different quadrant on the focal sphere (Figure 3.5b). The station distribution of the data we used for the 1951 Kona earthquake was simulated as close as possible with some stations of the 1983 event. The results show that if one uses the vertical component of MAT and two other three component stations, one should be able to calculate a unique reliable source mechanism(Table 3.6 and Figure 3.5a). For the Kona event, we possess two 3-component stations (HAV, TUC) and one 2-component station (FLO) in addition to the vertical component of MAT. These data are all of good quality (Figure 3.2). Therefore we feel confident that this historical event can be modeled successfully.

The results of the test demonstrate that the data set can be very sparse and still furnish a reliable solution. With any luck, one could obtain a good result from only a single 3-component station since for 5 out of 16 stations analyzed individually we obtained a unique solution similar to the final best solution (Table 3.3). The simula-

tion of the station distribution of the 1951 Kona earthquake showed that by just combining one three component station with only one component of another station (Table 3.6), one can reproduce the standard solution of the 1983 event uniquely. Stations ANMO and RSSD, when analyzed as single stations, did not provide a unique solution (Table 3.3), but their combination with only one component of MAT (Table 3.6) was enough to add the necessary constraint to obtain the "correct" solution. Consequently, it seems that the data set can be sparser than three 3-component stations and still allow successful recovery of the fault plane solution. Therefore, we conclude that we can determine the focal mechanism of an earthquake of magnitude between 6 and 7, in Hawaii, in a reliable manner using only one to three stations.

6. THE 1951 KONA EARTHQUAKE

For the 1951 Kona earthquake we digitized the data of four stations with a total of 9 components (Table 3.2) (Figure 3.2). The azimuthal coverage is poor with three stations at similar azimuths and take-off angles in the N-E quadrant of the focal sphere. Also the only station mapped in a different quadrant (N-W quadrant) (Figure 3.5b) has only a vertical component. Nevertheless we have shown above that it is still possible to obtain a unique source solution even with such a sparse data set.

6.1. The depth and rise time

For the Kona event, we found that with a rise time of 4 seconds, the resulting synthetic P-wavelet has the pulse width of the observed seismogram. Because of the narrow P-wave pulse, we were able to estimate the depth of this event. In Figure 3.6, synthetic signals computed for the depths of 5 km, 11 km, 15 km, 20 km and 25 km are compared to the data of Matsushiro. The choice of depths between 11 km and 15 km lead to the best matches (Figure 3.6). Because of the trade off between depth and rise time, the depth of 13 km that we propose for the 1951 Kona event, is not known better than ± 2.5 km. We already had computed the fundamental seismograms for a depth of 11 km and epicentral distances from 0 to 15000 km. To save computer time, we reused them to compute the synthetic signals necessary to retrieve the source orientation of the 1951 Kona earthquake. The result would not be significantly different if we had chosen a depth of 13 km for the computation of the synthetic signals.

Eissler and Kanamori [1986] proposed a depth of 20-25 km for the 1951 Kona earthquake, calculated from the ratio of body and surface waves amplitudes at the Pasadena station (PAS). We believe from our results that this event was shallower.

6.2. Inversion of the full data set for the 1951 Kona earthquake

The best result for the 1951 Kona earthquake is obtained by modeling all available components for stations MAT, TUC, FLO, and HAV. The resulting focal mechanism is a low-angle normal fault (Figure 3.5b and Table 3.7) or decollement type (dip between 0 and 30°) with a near-vertical auxiliary plane

NP1 : 316° / 78° / -81° (4)

The degree to which the solution is constrained can be seen by plotting the correlation matrix (Figure 3.7). There are two and only two maxima which occur at dip 15° and 80°, thus the best solution is unique. These maxima represent two nodal planes perpendicular to each other as expected from the double couple model of earthquake sources. One sees clearly that the fits are poor at dips between 35° and 70°. The nodal plane corresponding to the maximum at dip 80° is represented by a narrow peak with one side peak close to the maximum in the strike-rake space. This is an indication that the almost vertically dipping nodal plane is well constrained (Figure 3.7). Although the shallow dipping auxiliary plane is clearly represented by a unique maximum, many side peaks are mapped diagonally in the strike-rake space (Figure 3.7) indicating that this plane is less well constrained. This means that, for a shallow dipping nodal plane, changes in the strike do not change the waveform significantly.

The match of the data with the synthetic signals computed with the source orientation from Figure 3.5b is shown in Figure 3.8. The fit of the P-and S-waves look very good to the eyes in all cases. This is a requirement to check if the final focal mechanism is reasonable. Even PP is well match for TUC and FLO (Figure 3.8). For station HAV, the PP phase in the synthetics is too late and the observed one is more complicated than the synthetic (Figure 3.8). The lack of S energy in all components of the observed seismograms of HAV could not be modeled with the synthetics (Figure 3.8). The amplitude ratios between the components of the

same station (FLO, TUC) (Figure 3.8) agree very well with the data except for HAV (Figure 3.8). The amplitude ratios for the different arrivals in every seismogram fits also very well. In all traces, there is more energy arriving after the first S-arrival of the data than in the synthetics. This is probably due to conversion within the crust at the receiver sites.

6.3. Inversion from decimated data sets

We decimated the 1951 Kona data set in order to investigate the stability of the final solution. "Stable" means that the solution does not depend on how the stations are combined. The inversion of the source parameters was attempted using six possible combinations of two stations (Table 3.7). One of them (HAV + TUC) showed no clear maximum in the correlation matrix. Two of them did not have any unique solution, but showed two distinctive maxima. In the case of MAT+FLO these maxima represent almost the same mechanism as the best solution (4) with slightly different dip of the horizontal nodal plane. The combination of HAV+FLO presents two different solutions. One is a low-angle thrust mechanism, which is consistent with (4) and the second one is a strike-slip mechanism. The latter is not acceptable because it locates MAT on a nodal plane, which is certainly not correct according to the data.

Out of four combinations of three stations, three present unique solutions (decollement type) similar to the best solution (number 4, Table 3.7 and Figure 3.5b). The combination MAT+TUC+HAV allows two mechanisms (Table 3.7) that are also consistent with the result obtained for the combination of all four stations.

The two highest peaks are about 30° apart along the rake. For that reason, this solution was considered non-unique.

Regardless of which station combination we use, all combinations furnish a decollement type of focal mechanism with a slip in the SW direction. This is even true if the result is not unique but has two maxima. Only for one station combination was no determination of the source mechanism possible.

7. DISCUSSION AND CONCLUSION

We have successfully modeled the waveforms of the 1951, M=6.9, Kona earthquake in Hawaii and found that its focal mechanism is a decollement type with one of the nodal planes dipping at about 15° to the south-west and with a strike oriented at about 99°. This result is a confirmation of the fault plane solution proposed by *Gillard et al.* [1992] for the 1951, Kona earthquake (strike=142°, dip=12°, rake=-108°) based on averaging decollement-type focal mechanisms of local earthquakes in western Hawaii.

This study presents a new piece of evidence of the tectonic similarity between West Hawaii and the Kalapana region. The fault plane solution of the 1975 Kalapana (M_S=7.2) earthquake is a decollement type [*Ando*, 1979] and the local seismicity on the south flank of Kilauea is also characterized by earthquakes with decollement-type focal mechanisms [*Bryan and Johnson*, 1991]. Normal faults mapped at the surface are present in both regions and landslides have been identified both on land and on the sea floor (Figure 3.1) [*Lipman*, 1980; *Lipman et al.*, 1988; *Moore et al.*, 1989]. We conclude that the tectonic model proposed by

Gillard et al. [1992] is a valid model to explain the occurrence of tectonic earthquakes on the west flank of Mauna Loa volcano. This model states that accumulated stress is released along a zone of weakness, which consists perhaps of a layer of oceanic sediment buried underneath the edifice of the volcano at a depth of about 11 km. The stress is probably accumulated through repeated magmatic intrusion into the rift zone of Mauna Loa. A similar model was proposed by many authors [*Swanson et al.*, 1976; *Nakamura*, 1977; *Furomoto and Kovach*, 1979; *Ando, 1979*; *Nakamura*, 1982; *Endo*, 1985; *Lipman et al.*, 1985; *Dieterich*, 1988; *Wyss and Kovach*, 1988] to explain the 1975, Kalapana earthquake.

The 1983 Kaoiki earthquake has interesting particularities. First, the source mechanisms obtained from moment tensor solutions of long period data (HRVD, NEIS Figure 3.3a, b) and the one computed for this study as a test case (Figure 3.3d) are all consistent with each other and show a decollement type. The fault plane solution computed from the analysis of local P-wave first motion is a strike-slip type (Figure 3.3c). Furthermore this earthquake produced en echelon ground cracks extending for several kilometers within the Kaoiki seismic zone comparable to the ones produced by the 1974 Kaoiki earthquake (M_L=5.5) [*Jackson and Endo*, 1989] and consistent with strike-slip motion on a near-vertical fault plane. While the aftershocks of the 1974 event mapped out the near-vertical fault oriented NE-SW [*Endo*, 1985], the aftershocks of the 1983 event mapped out an horizontal area located at a depth of about 11 km [*Endo*, 1985; *Wyss et al.*, 1992]. These facts suggest that the 1983 Kaoiki mainshock was probably a complex event which was triggered first on a vertical plane with a strike-slip mechanism but that most of the

energy was released by one or many other events on the decollement plane. A complete and detailed model to quantitatively describe this event has not been constructed yet.

We have shown that our method of inversion of source parameters from sparse data sets works reasonably well. The results from the test, suggest that as few as one to three stations are sufficient to model the Kaoiki and Kona earthquakes.

Acknowledgments. We thank C. B. Archambeau and his group for supporting us with their computing facility, J. Taggart for his help in retrieving data and J. Gomberg for providing the digitizing software. We are also grateful for seismograms supplied by various observatories. M. Beisser was supported by the Foedor Lynen Program of the Alexander von Humboldt Foundation as well as by a Visiting Fellowship from the Cooperative Institute for Research in Environmental Sciences (CIRES), University of Colorado, D. Gillard was supported by NSF grant number EAR-9116722, and M. Wyss was supported by the Wadati endowment at the Geophysical Institute of the University of Alaska. This work was started while all authors were employed at CIRES, and finished in Fairbanks.

8. REFERENCES

Ando, M., The Hawaii earthquake of November 29, 1975: low-angle normal fault due to forceful injection of magma, *J. Geophys. Res., 84,* 7616-7626, 1979.

Beisser, M., and R. Kind, The reflectivity method for SH-waves and for different structures at source and receiver sides, *Geol. J., 42,* 137-142, 1988.

Beisser, M. , M. Wyss, and R. Kind, Inversion of source parameters for subcrustal earthquakes in the Hellenic Arc, *Geophys. J. Int., 103,* 439-450, 1990.

Ben-Menahem, A., and S. J. Singh, *Seismic waves and sources*, Springer Verlag, New-York, 1981.

Bruestle, W., and G. Mueller, Moment and duration of shallow earthquakes from Love-wave modeling for regional distances, *Phys. Earth Planet. Inter., 32,* 312-324, 1983.

Bryan, C. J., and C. E. Johnson, Block tectonics of the island of Hawaii from a focal mechanism analysis of basal slip, *Bull. Seismol. Soc. Am., 81,* 491-507. 1991.

Crosson, R. S., and E. T. Endo, Focal mechanisms of earthquakes related to the 29 November 1975 Kalapana, Hawaii, earthquake: the effect of structure models, *Bull. Seismol. Soc. Am., 71,* 713-729, 1981.

Dieterich, J. H., Growth and persistence of Hawaiian volcanic rift zones, *J. Geophys. Res., 93,* 4258-4270, 1988.

Dziewonski, A. M., T. A. Chou, and J. H. Woodhouse, Determination of earthquake

source parameters from Waveform data for studies of Global and regional seismicity, *J. Geophys. Res., 86,* 2825-2852, 1981.

Endo, E. T., *Seismotectonic framework for the southeast flank of Mauna Loa,* Hawaii, Ph.D. thesis, Univ. of Wash., Seattle, 1985.

Eissler, H. K., and H. Kanamori, Depth estimates of large earthquakes on the island of Hawaii since 1940, *J. Geophys. Res., 91,* 2063-2076, 1986.

Furomoto, A. S., and R. L. Kovach, The Kalapana earthquake of November 29, 1975; an intraplate earthquake and its relation to geothermal processes, *Phys. Earth Planet. Int., 18,* 197-208, 1979.

Gillard, D., M. Wyss, and J. S. Nakata, A seismotectonic model for western Hawaii based on stress tensor inversion from fault plane solutions, *J. Geophys. Res., 97,* 6629-6641, 1992.

Gutenberg, B., and C. F. Richter, *Seismicity of the Earth and Associated Phenomena,* Princeton University Press, Princeton, N. J., 1954.

Jackson, M. D., and E. T. Endo, Genesis of a strike-slip fault zone: the 1974 and 1983 Kaoiki ground ruptures , Mauna Loa volcano, Hawaii, *Eos Trans. AGU, 70,* 1409, 1989.

Kind, R., The reflectivity method for different source and receiver structures,*J. Geophys., 58,* 146-152, 1985.

Klein, F.W., A linear gradient crustal model for south Hawaii, *Bull. Seismol. Soc. Am., 71,* 1503-1510, 1981.

Lipman, P. W., The southwest rift zone of Mauna Loa: Implications for structural evolution of Hawaiian volcanoes, *Amer. J. Sci., 280-A*, 752-776, 1980.

Lipman, P. W., J. P. Lockwood, R. T. Okamura, D. A. Swanson, and K. M. Yamashita, Ground deformation associated with the 1975 magnitude 7.2 earthquake and resulting changes in activity of Kilauea volcano, Hawaii, *U. S. Geol. Surv. Prof. Pap., 1276*, 1985.

Lipman, P. W., W. R. Normark, J. G. Moore, J. B. Wilson, and C. E. Gutmacher, The giant submarine Alika Debris Slide, Mauna Loa, Hawaii, *J. Geophys. Res., 43*, 4279-4299, 1988.

Macdonald, G. A., and C. K. Wentworth, The Kona earthquake of August 21, 1951, and its aftershocks, *Pacific Sci., VI*, 269-287, 1952.

Moore, J. G., D. A. Clague, R. T. Holcomb, P. W. Lipman, W. R. Normark, and M. E. Torresan, Prodigious submarine landslides on the Hawaiian Ridge, *J. Geophys. Res., 94*, 17,465-484, 1989.

Nakamura, K., Volcanoes as possible indicators of tectonic stress orientation - principle and proposal, *J. Volcanol. Geotherm. Res., 2*, 1-16, 1977.

Nakamura, K., Why do long rift zones develop better in Hawaiian volcanoes: a possible role of the thick oceanic sediments, *in Proc. International Symp. Activity of oceanic volcanoes, Ser. Cienc. Nat. 3, Universidade dos Acores, Ponta Delgada*, 59-73, 1982.

Savage, M. K., and R. P. Meyer, A new model for tectonics of the south flank of Kilauea volcano, Hawaii and for the 1975 M=7.2 Kalapana earthquake:

rupture and slide zones in the old oceanic sediment layer, *Eos, Trans. AGU, 68,* 1353, 1987.

Sipkin, S. A., Estimation of source parameters by the inversion of waveform data: Synthetic waveforms, *Phys. Earth Planet. Inter., 30,* 242-259, 1982

Swanson, D. L., W. A. Duffield, and R. S. Fiske, Displacement of the south flank of Kilauea volcano: the result of forceful intrusion of magma into the rift zones, *U. S. Geol. Surv. Prof. Pap., 963,* 39 pp, 1976.

Thurber, C. H., and A. E. Gripp, Flexure and Seismicity beneath the south flank of Kilauea volcano and tectonic implications, *J. Geophys. Res., 93,* 4271-4278, 1988.

Thurber, C. H., Y. Li, and C. Johnson, Seismic detection of a low-velocity layer beneath the southeast flank of Mauna Loa, Hawaii, *Geophys. Res. Lett.,16,* 649-652, 1989.

Wyss, M., and R. L. Kovach, Comment on "A single-force model for the 1975 Kalapana, Hawaii, earthquake" by Eissler, H.K. and Kanamori, H. *J. Geophys. Res., 93,* 8078-8082, 1988.

Wyss, M., and R. Y. Koyanagi, Isoseismal maps, macroseismic epicenters, and estimated magnitudes of historic earthquakes in the Hawaiian Islands, *U.S. Geol. Surv. Bull. 2006,* 1992.

Wyss, M., B. Liang, W. R. Tanigawa, and X., Wu, Comparison of orientations of stress and strain tensors based on fault plane solutions in Kaoiki, Hawaii, *J. Geophys. Res., 97,* 4769-4790, 1992.

Table 3.1. Stations Used for Inversion of the Source Parameters of the 1983 Kaoiki Earthquake.

Station	Instrument	Distance [km]	Distance used [km]	Difference [km]	Azimuth [deg]
AFI	DWWSSN	4099	4205	106	207
LON	DWWSSN	4292	4380	88	38
COL	DWWSSN	5074	5135	61	5
SCP	DWWSSN	7571	7650	79	53
GDH	DWWSSN	8452	8670	218	21
RSSD	RSTN	5458	5520	62	48
RSNT	RSTN	5698	5795	97	23
RSON	RSTN	6368	6420	52	42
RSNY	RSTN	7799	7910	111	49
ANMO	SRO	5076	5210	134	60
SNZO	SRO	7393	7635	242	204
GAC	SRO	7699	7875	176	47
CTAO	SRO	7708	7875	167	237
TATO	SRO	8438	8670	232	292
BOCO	SRO	8917	9150	233	89

Table 3.2. Stations Used for the Modeling of the 1951 Kona Earthquake.

Station	Instrument/Component	Distance [km]	Distance used [km]	Difference [km]	Azimuth [deg]
FLO	GALITZIN/NS EW	6577	6610	33	56
HAV	GALITZIN/Z NS EW	4064	4050	-14	56
MAT	GALITZIN/Z	6603	6760	157	302
TUC	BENIOFF/Z WA/NS EW	4699	4810	111	63

WA=Wood-Anderson

Table 3.3. Fault Plane Solutions of the 1983 Kaoiki Earthquake Obtained by Modeling Individual Stations.

Station	Instrument	Solution Quality	Strike [deg]	Dip [deg]	Rake [deg]
AFI	DWWSSN	broad	205	80	-105
LON	DWWSSN	unique	200	85	-100
COL	DWWSSN	unique	25	85	115
SCP	DWWSSN	not unique			
GDH	DWWSSN	not unique			
RSSD	RSTN	not unique			
RSNT	RSTN	not unique			
RSON	RSTN	not unique			
RSNY	RSTN	unique	35	85	105
ANMO	SRO	not unique			
MAJO	SRO	not unique			
SNZO	SRO	not unique			
GAC	SRO	unique	35	85	110
CTAO	SRO	unique	205	85	-105
TATO	SRO	not unique			
BOCO	SRO	not unique			

Table 3.4. Fault Plane Solutions of the 1983 Kaoiki Earthquake for Combination of Stations with Similar Azimuth.

	Station Combinations			Fault Plane		
	1	2	3	Strike [deg]	Dip [deg]	Rake [deg]
Single	MAJO	TATO	COL	205	95	-115
Quadrant	CTAO	AFI	SNZO	205	85	-105
Combinations	GDH	RSNT	RSON	214	83	-109
	SCP	ANMO	BOCO	220	80	-130
Average				211	86	-115
Std. deviation				6	6	9

Table 3.5. Fault Plane Solutions of the 1983 Kaoiki Earthquake for 15 Arbitrary Three Station Combinations.

Station Combinations	Fault Plane I			Fault Plane II		
	Strike I [deg]	Dip I [deg]	Rake I [deg]	Strike II [deg]	Dip II [deg]	Rake II [deg]
AFI LON COL	70	14	-45	205	80	-100
ANMO RSSD RSNT	100	15	-30	219	83	-103
RSON SNZO SCP	105	20	-25	217	83	-108
GAC CTAO RSNY	97	16	-19	205	85	-105
TATO GDH BOCO	125	35	-20	232	79	-123
COL GDH RSNT	105	5	-15	200	90	-95
LON RSON GAC	83	11	-27	200	85	-100
RSSD RSNY SCP	125	10	0	215	90	-100
ANMO BOCO SNZO	113	41	-15	215	80	-130
AFI CTAO TATO	97	16	-19	205	85	-105
RSON COL RSSD	35	5	-90	215	85	-90
SCP LON RSNT	85	25	-35	207	76	-111
AFI RSNY ANMO	112	21	-14	215	85	-110
CTAO GAC GDH	97	16	-19	205	85	-105
TATO BOCO SNZO	123	35	-9	220	85	-125
Average				212	84	-107
Std. deviation				8	4	11

Table 3.6. Fault Plane Solutions of the 1983 Kaoiki Earthquake for Station Combinations Simulating the 1951 Kona Earthquake.

Station Combinations				Fault Plane I			Fault Plane II		
1	2	3	4	Strike [deg]	Dip [deg]	Rake [deg]	Strike [deg]	Dip [deg]	Rake [deg]
MAT-P	RSNY			143	16	19	215	95	-105
MAT-P	ANMO			125	50	-20	228	74	-138
MAT-P	RSSD			102	35	-9	220	85	-125
MAT-P	RSNY	ANMO		143	16	19	215	95	-105
MAT-P	RSNY	RSSD		131	10	6	215	90	-100
MAT-P	ANMO	RSSD		125	40	15	203	100	-129
MAT-P	RSNY	ANMO	RSSD	113	5	-11	215	90	-95
Average							216	90	-114
Std. deviation							9	7	14

"MAT-P" stands for the vertical component of MAJO.

Table 3.7. Fault Plane Solutions of the 1951 Kona Earthquake for Different Station Combinations.

	Station Combinations				Solution		Fault Plane I			Fault Plane II		
	1	2	3	4	Quality	Note	Strike [Deg]	Dip [Deg]	Rake [Deg]	Strike [Deg]	Dip [Deg]	Rake [Deg]
Max. 1	MAT	FLO			not unique	two Maxima	50	5	-180	320	90	-85
Max. 2							135	15	-90	315	75	-90
Max. 1	MAT	TUC	HAV		not unique	two Maxima	63	16	-161	315	85	-75
Max. 2							207	16	-19	315	85	-105
Max. 1	HAV	FLO			not unique	two Maxima	135	15	-90	315	75	-90
Max. 2							194	67	22	275	110	-155
	HAV	TUC			not unique	no Maxima				0	0	0
	FLO	TUC			unique		100	18	-123	315	75	-80
	MAT	HAV			unique		189	11	-27	305	85	-100
	MAT	TUC			unique		63	16	-161	315	85	-75
	MAT	TUC	FLO		unique		89	21	-134	315	75	-75
	MAT	HAV	FLO		unique		135	15	-90	315	75	-90
	FLO	TUC	HAV		unique		89	21	-134	315	75	-75
	MAT	TUC	FLO	HAV	unique		100	15	-125	316	78	-81
Average										314	78	-82
Deviation										4	4	9

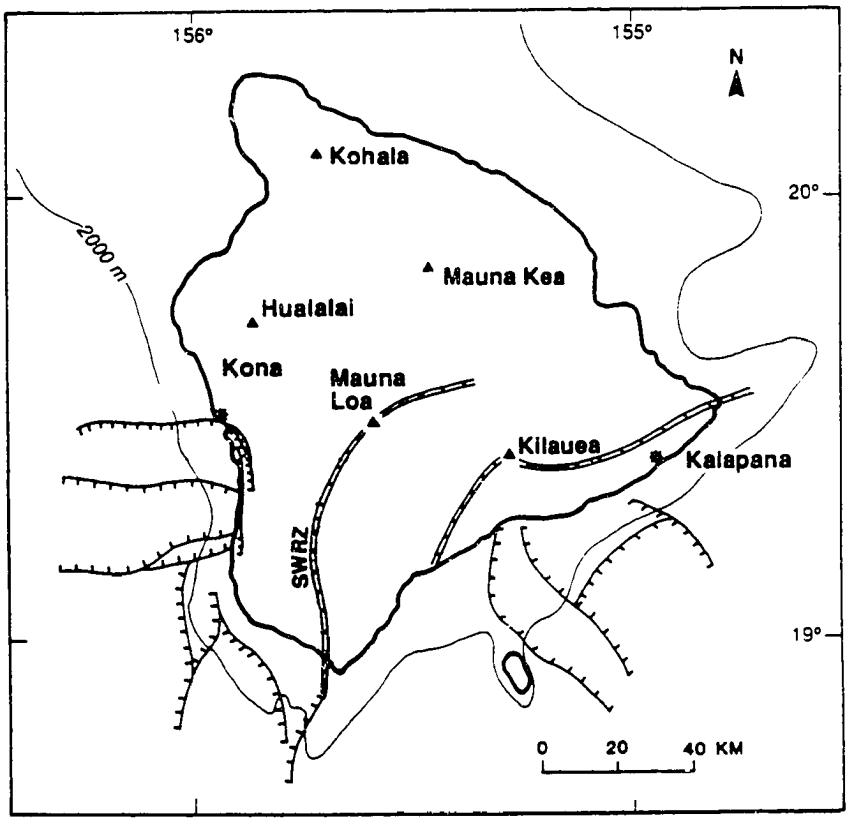

Fig. 3.1. Map of the island of Hawaii identifying the volcano summits Hualalai, Kohala, Mauna Kea, Mauna Loa, and Kilauea. Rift zones are marked with connected double lines; SWRZ, southwest rift zone. The stars are epicenters of M>6.5 earthquakes mentioned. The lines with the ticks on downthrown side marks the landslides west and southeast of Hawaii.

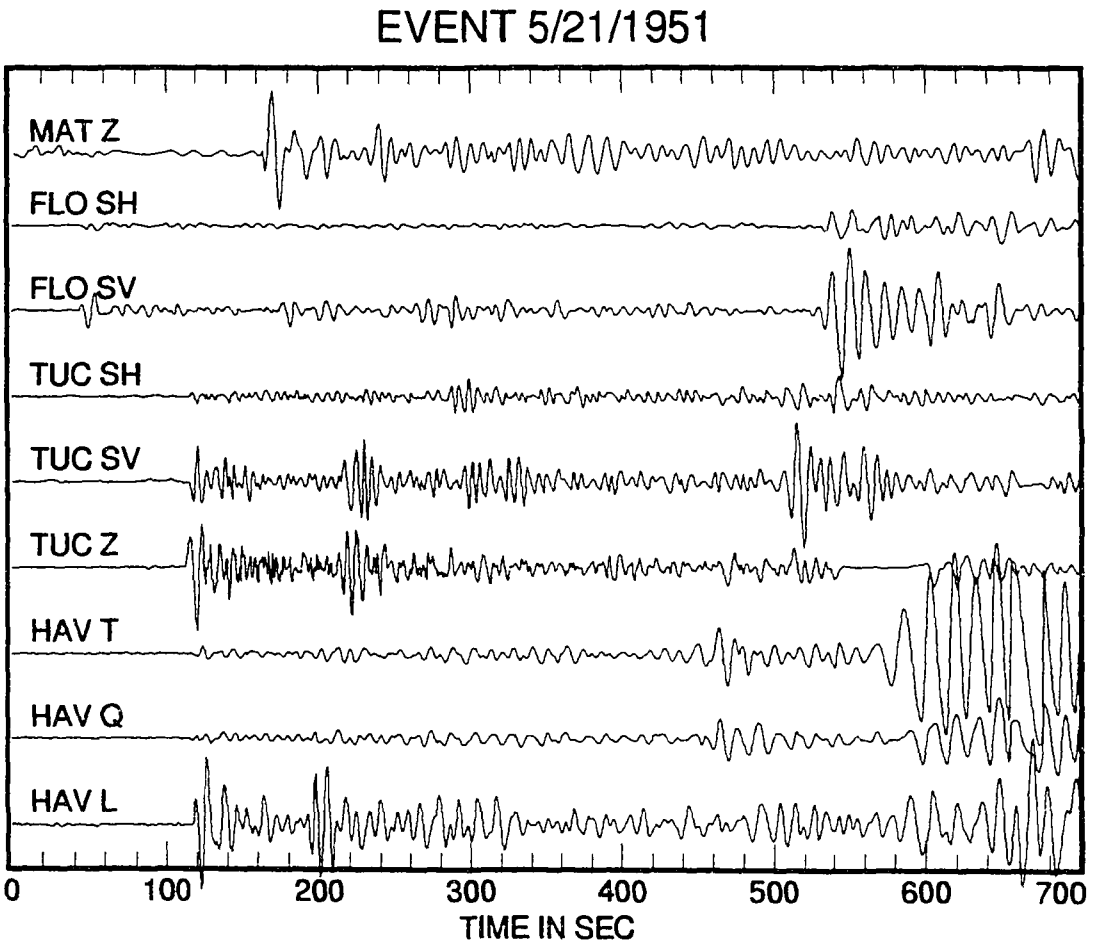

Fig. 3.2. Digitized seismograms of the 1951 Kona earthquake.

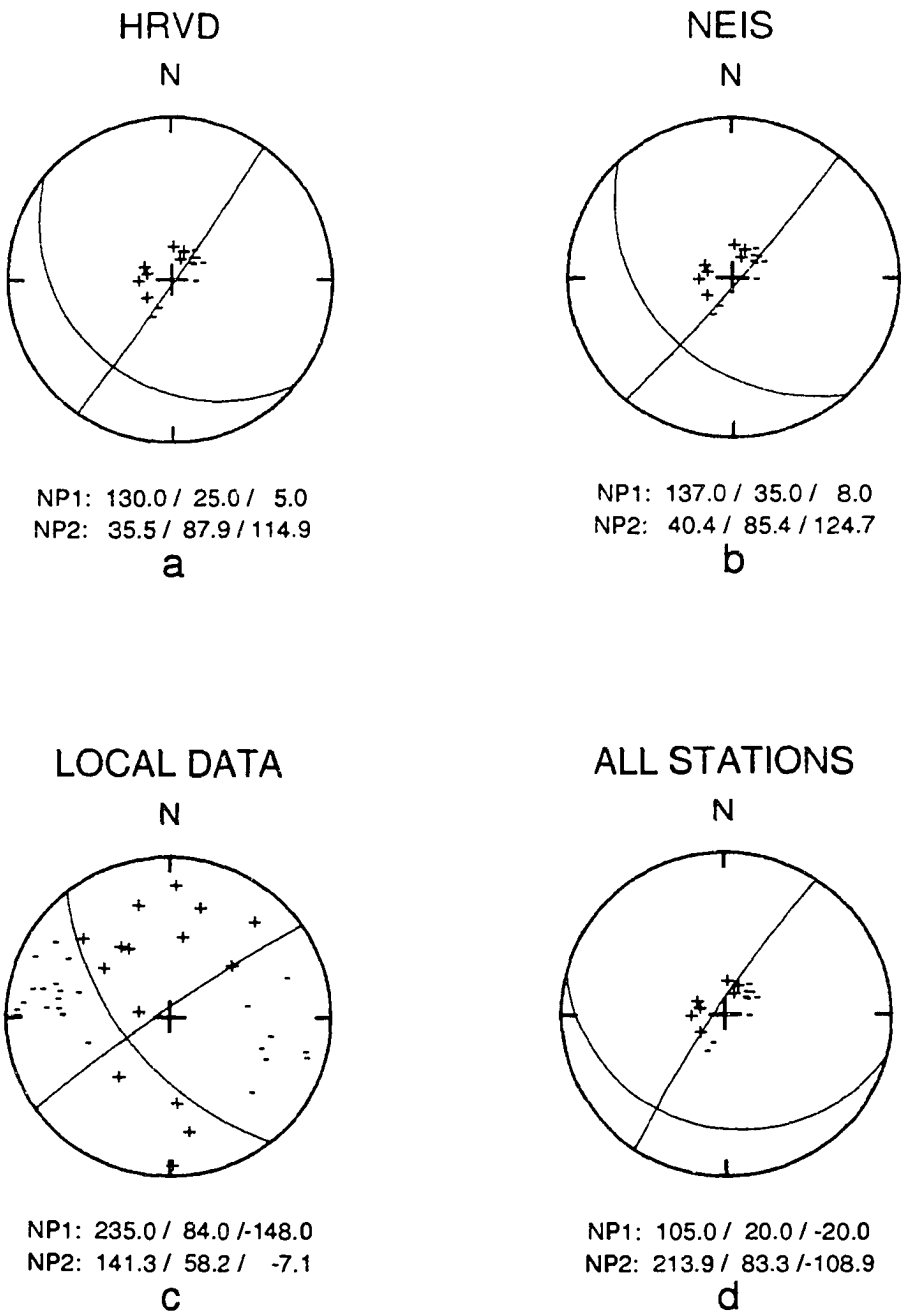

Fig. 3.3. Fault plane solutions of the 1983 Kaoiki earthquake: a) solution obtained by the Harvard (HRVD) centroid moment tensor inversion method, b) solution obtained by the USGS (NEIS) moment tensor inversion method, c) solution computed from first motions of local data, d) solution obtained from the inversion of the full data set using our method. + indicates an upward motion and - a downward motion on a lower hemisphere stereographic projection.

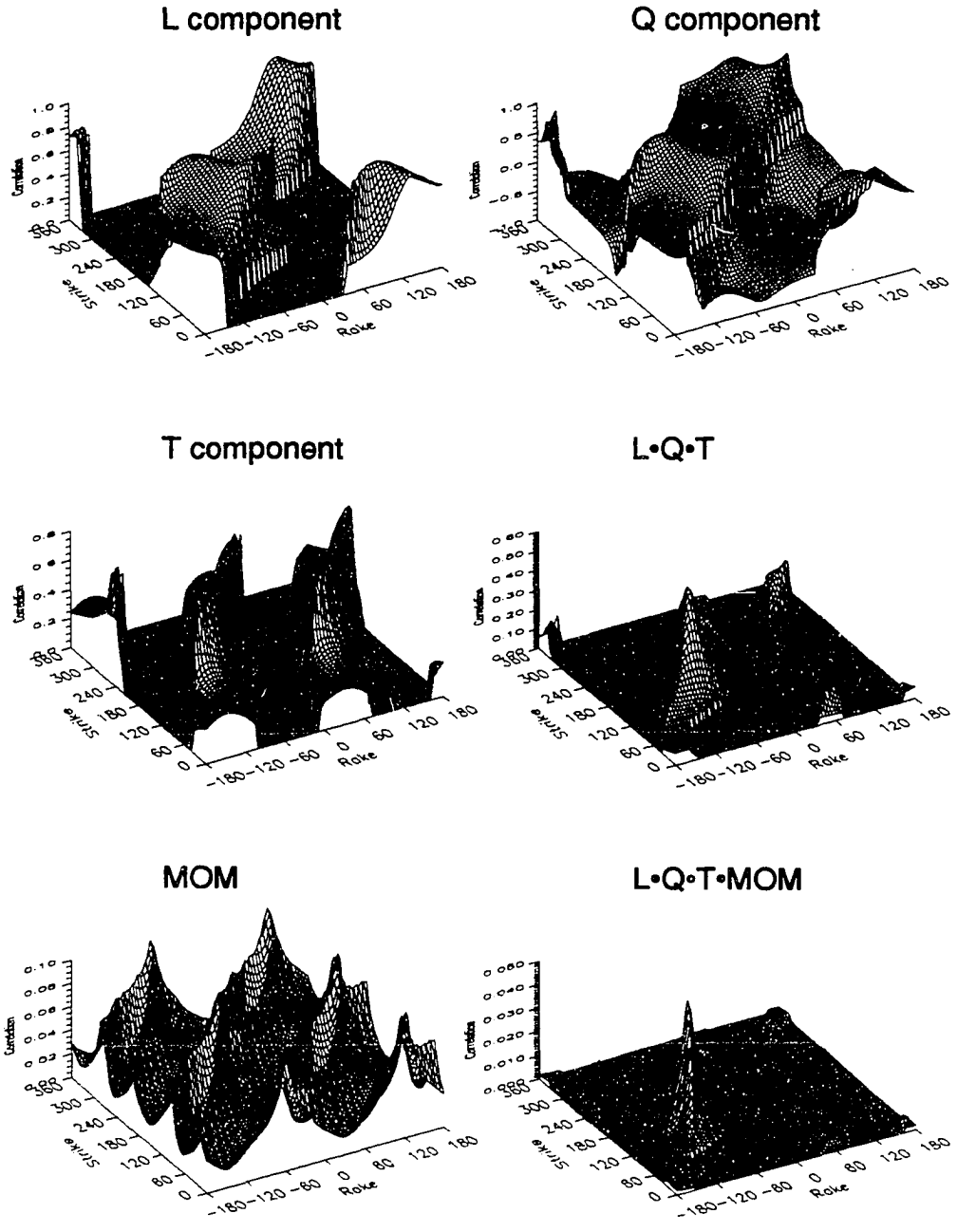

Fig. 3.4. Correlation matrices for L, Q, and T component of station MAJO. Multiplication of L*Q*T shows where the observed and the synthetic signals match for all three components at the same time. MOM shows where the amplitude ratio between the synthetic and the observed traces matches. L*Q*T*MOM is the final correlation matrix. The dip is fixed at 25°.

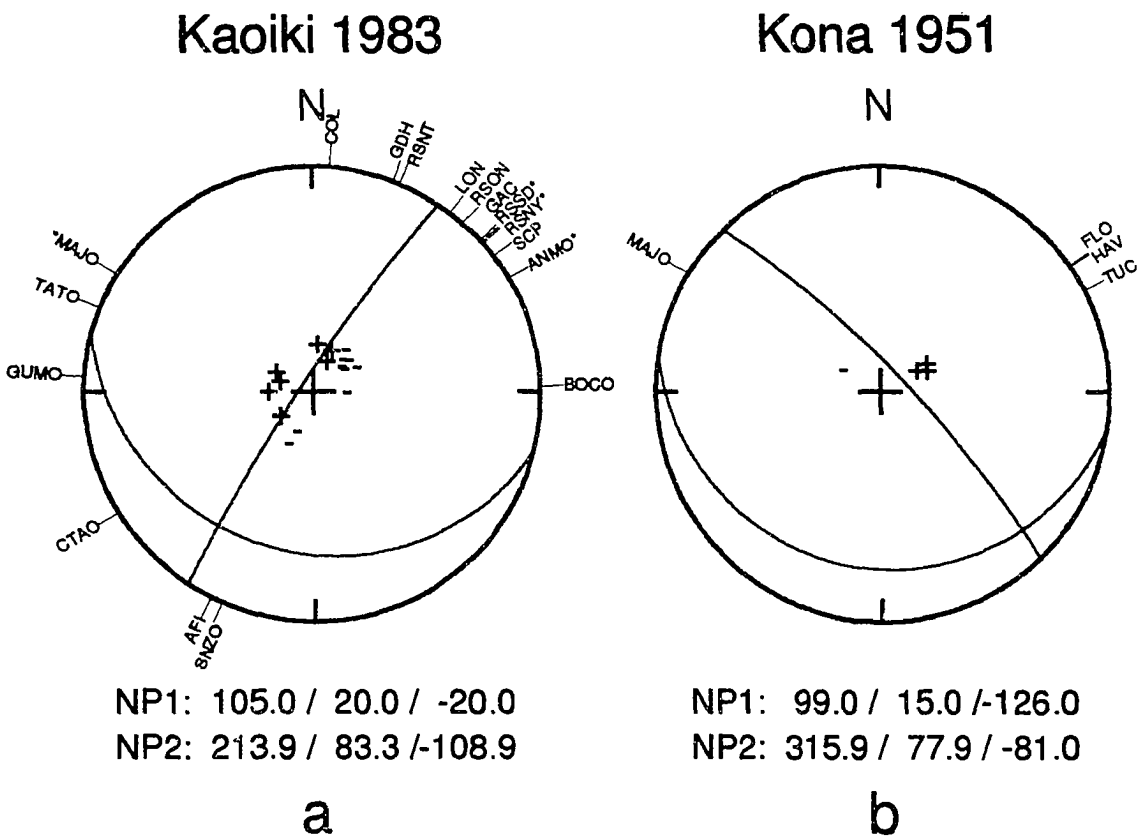

Fig. 3.5. a) Lower hemisphere stereographic projection showing the azimuthal distribution of stations for the 1983 Kaoiki earthquake, with the direction of first motions (+=up, -=down) and the nodal planes obtained from the modeling of all 16 stations. The stations marked with a star are the stations used to simulate the station configuration of the 1951 Kona event. b) Best fault plane solution for the 1951 Kona earthquake determined by modeling the seismograms of the stations FLO, HAV, MAT, TUC. + indicates an upward motion and - a downward motion.

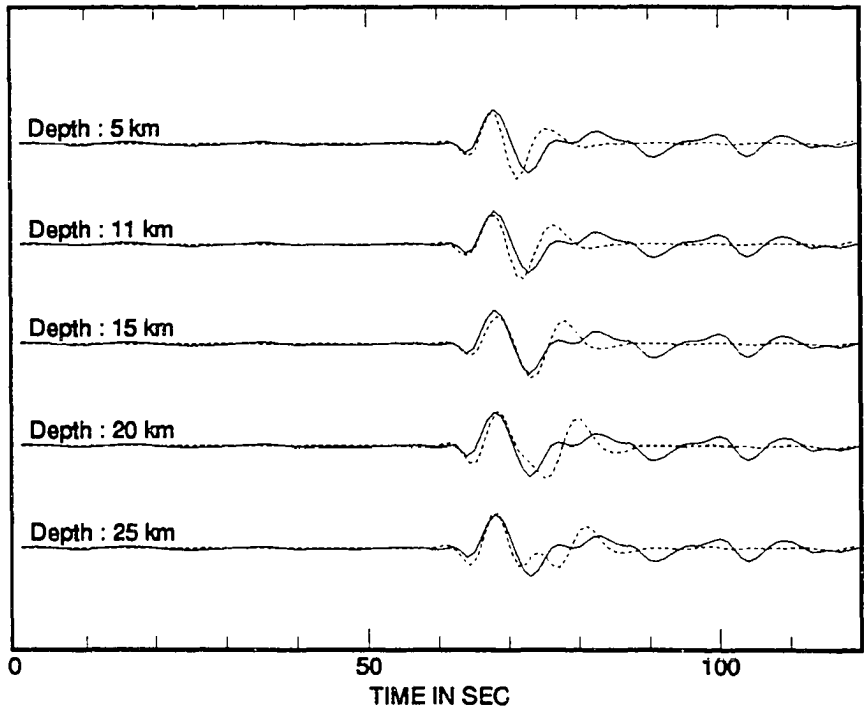

Fig. 3.6. Comparison of the observed P-wave train with the synthetics computed for different source depths at station MAT (vertical component).

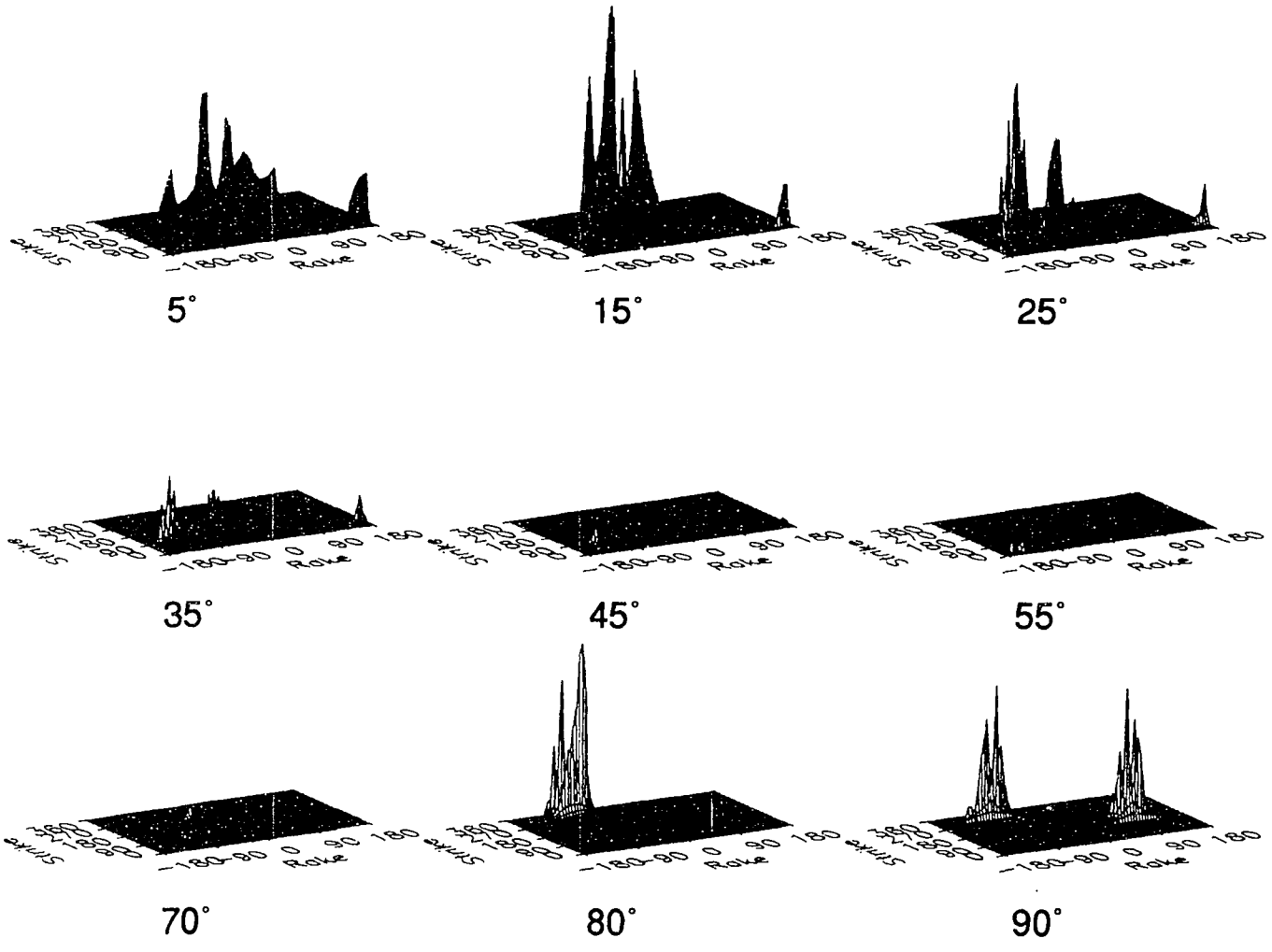

Fig. 3.7. Correlation matrices for the 1951 Kona earthquake. This is the result of the multiplication of all correlation matrices of all components of all stations HAV, TUC, FLO, MAT. The grid spacing is equal to 5° along the strike, dip, and rake. Not all dips are shown.

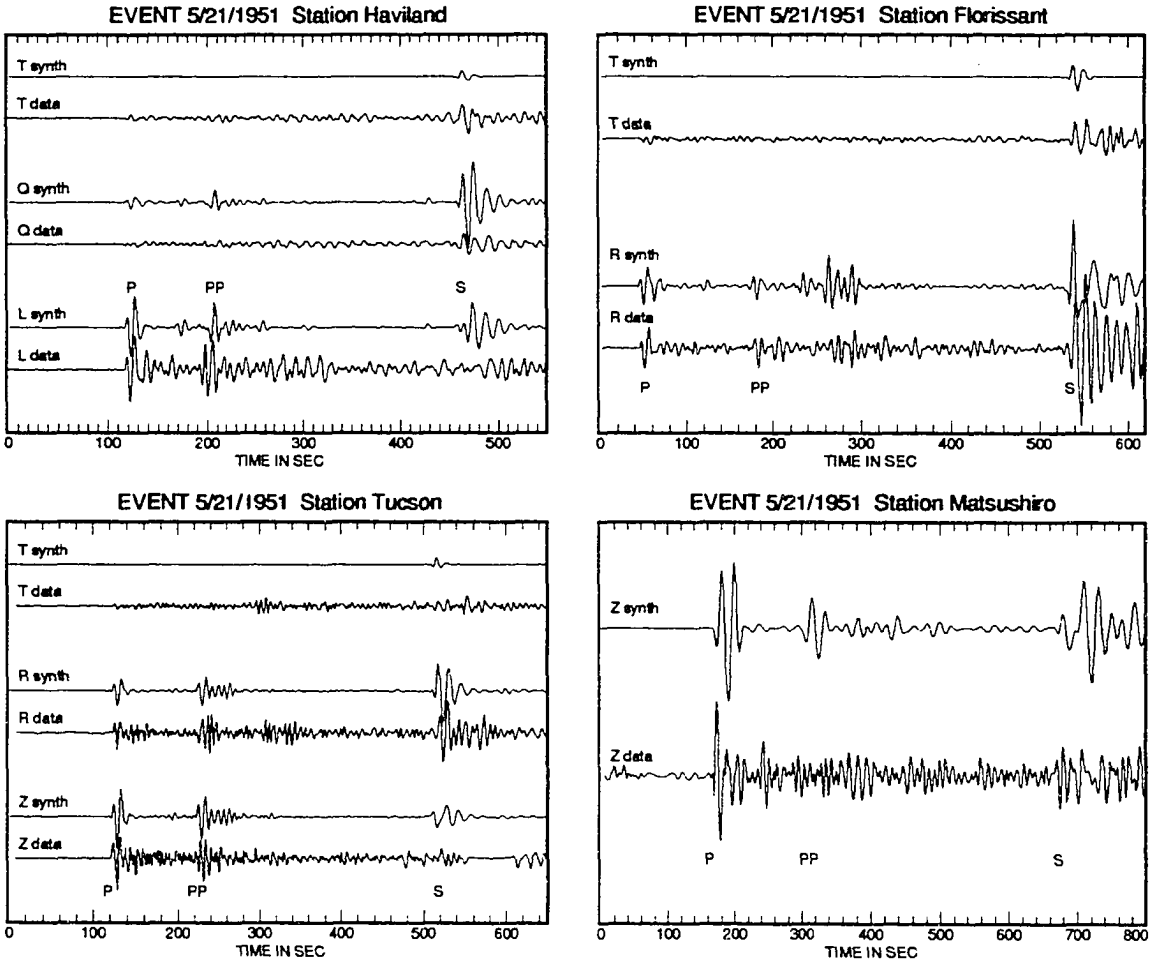

Fig. 3.8. Match of the data and synthetics computed with the source orientation of Figure 3.5b for station HAV, TUC, FLO, and MAT. Note that the instrument type which recorded the vertical component of the seismogram for station Tucson (TUC) is not the same as the one which recorded the horizontal components.

CHAPTER 4

STRESS TENSOR ORIENTATIONS IN THE SOUTH FLANK OF KILAUEA, HAWAII, ESTIMATED FROM FAULT PLANE SOLUTIONS[1]

1. ABSTRACT

Fault plane solutions of 863 earthquakes with magnitudes $M_L \geq 2.5$ which occurred between 1972 and 1992 in the south flank of the Kilauea volcano in Hawaii were determined using P-wave first motion polarities. More than 90% of these earthquakes are located south of the Kilauea east rift zone between longitude 154° 58' W and 155° 16' W and at a depth of about 10 km. The dominant focal mechanisms (53%) are decollement type with one nodal plane nearly horizontal (dip≤20°). Reverse faults and normal faults compose the rest of the fault plane solutions with 29% and 18%, respectively. The types of fault plane solutions vary as a function of time and space. The normal faults occur mainly during the aftershock period of the 1975, M_S=7.2, Kalapana earthquake, while none were observed before it. The number of reverse faults is high before 1975 and drops significantly after

---

[1] Chapter 4 contains the complete text and figures of the manuscript, *Stress tensor orientations in the south flank of Kilauea, Hawaii, estimated from fault plane solutions* by D. Gillard, M. Wyss, and P. Okubo, as submitted to the *Journal of Geophysical Research*, 1993.

1983. The decollement-type focal mechanisms are always present with a significant increase in number after 1983. Inverting for stress orientations for different subvolumes and periods, we found that in general the greatest principal stress is oriented approximately SE but the plunge changes as a function of time and space between 0° and 64°. A temporal change of σ_1 of about 20° in azimuth and 45° in plunge significant at the 95% confidence level occurred after 1979 in a volume east of longitude 155° 10' W. This change in stress orientation is interpreted as a response to the build up of stress due to magma intrusions in the southeast rift zone of Kilauea. The orientation of the strain released by the earthquakes with M<7 was calculated for the different subvolumes in the south flank. Overall the greatest principal strain is oriented SE. The dip of the strain varies from 0° to 45° as a function of space suggesting that the strain is released either on reverse faults or on the decollements but is stable as a function of time. Significant differences up to 40° between stress and strain as a function of time exist which may indicate that the strength of the crust is not homogeneous in the south flank. Most large earthquakes with magnitude M<7, slip on reverse faults striking NE at 40° and dipping SE between 60° and 70°, whereas the earthquakes with M>7 rupture the decollement plane since it is the only surface large enough to generate magnitude 7 or larger earthquakes.

2. INTRODUCTION

The south flank of Kilauea volcano is the most seismically active area in Hawaii. It is characterized by two types of earthquakes, volcanic and tectonic [*Klein et al.*, 1987]. The volcanic earthquakes are located near the summit and along the southwest and east rift zones at depths between 0 km and 5 km and are associated with the opening of cracks by magmatic intrusions [*Klein et al.*, 1987]. The tectonic earthquakes occur at depths between 5 and 14 km and at distances of several kilometers to several tens of kilometers from the volcanic earthquake activity [*Klein et al.*, 1987]. The tectonic earthquakes occur in response to the stress exerted on the crust by magmatic intrusions. Evidence for this interpretation comes from geodetic measurements which show that the crust surrounding the volcano summit and the rift zones is compressed during intrusions [*Swanson et al.*, 1976; *Dvorak et al.*, 1983, 1986; *Dzurisin et al.*, 1984]. Also, intrusions are often followed by an increase in seismicity in some crustal volume of the south flank at distances of 10 km from the rift zone [*Dvorak et al.*, 1986]. This seismicity decays with the same characteristics as an aftershock sequence [*Dvorak and Tanigawa*, 1985; *Wyss and Kisslinger*, 1989].

The largest of these tectonic earthquakes ruptured a 40 km long segment of the south flank of Kilauea on November 29, 1975, and had a magnitude of M_S=7.2. On the basis of geodetic measurements, it was shown that the strain which accumulated in the source volume for over 70 years was released in the earthquakes in agreement with the elastic rebound model [*Swanson et al.*, 1976; *Lipman et al.*, 1985].

The focal mechanism of the mainshock was a decollement type with one plane horizontal and the other vertical, striking at N53E. Most of the aftershocks had similar focal mechanisms [*Ando*, 1979; *Furomoto and Kovach*, 1979; *Crosson and Endo*, 1982; *Wyss and Kovach*, 1988]. These authors proposed a tectonic model that states that the Kalapana earthquake was produced by the accumulation of strain energy by magmatic intrusion in Kilauea volcano and its rift zones. The flank of the volcano slipped 8 m on average perpendicularly away from the rift, along a near-horizontal plane located at a depth between 8 and 11 km. This fault plane corresponds to the top of the buried oceanic sediment layer of the seafloor, upon which the edifice of the volcano is deposited and which acts as a plane of weakness. Evidence for the presence of this layer comes from refraction data [*Hill and Zucca*, 1987], from relocations of crustal earthquakes, which are concentrated at the depth of this layer [*Crosson and Endo*, 1982; *Savage and Meyer*, 1987; *Thurber and Gripp*, 1988], and from fault plane solutions, showing consistently decollement-type faulting with slip on the basal plane oriented SE [*Crosson and Endo*, 1981, 1982; *Bryan and Johnson*, 1991]. A different model based on the study of surface waves was proposed by *Eissler and Kanamori* [1987]. They proposed that the Kalapana earthquake was a landslide because it could be modeled as a single force event. This contradicts the evidence described above which is in favor of a double couple tectonic earthquake [*Wyss and Kovach*, 1988]. Recently, *Dahlen* [1993] showed that the long period radiation pattern of a shallow horizontal thrust fault is the same as that obtained from a horizontal surface point source if one uses the WKBJ approximation. Thus we favor the first interpretation since it is based on more independent evidence than

the latter, which seems to be model dependent.

The presence of the basal layer is essential for maintaining the geometry of the volcanic rift zones as shown by *Dieterich* [1988]. In his model, accommodation to dike intrusions occurs by slip on the decollement plane. This process allows the release of the compressional stress accumulated by the dike intrusions, and consequently dikes can continue to be emplaced within the rift zone. If the compressive stress was not released, the magma supply system would shut off because the resulting compressive stress would prevent further opening to create new dikes [*Dieterich*, 1988]. This model explains why, following the Kalapana earthquake, intrusion episodes occurred more frequently than average between 1975 and 1981 [*Klein et al.*, 1987]. These culminated into a major eruption at Puu'Oo (Figure 4.1) which started on January 2, 1983 and still continues as of this writing.

The above discussion indicates the importance of knowing the nature of the stress system as a function of space and time in the south flank of Kilauea. The main purpose of this study is to infer the state of stress responsible for the occurrence of tectonic earthquakes in the south flank of Kilauea volcano. Questions of particular interest are the following. How are the principal stresses oriented relative to the summit of the volcano and the rift zones? How is the stress field influenced by the occurrence of the 1975, M_S=7.2, Kalapana earthquake? Does the stress orientation in the south flank change as a function of time and in response to intrusion episodes in the rift zone?

The principal stress directions have been inferred by inversion of focal

mechanisms. The data set consists of 863 focal mechanisms from earthquakes with magnitudes M>3 which occurred in the south flank of Kilauea at least 5 km away from the rift and 10 km from the summit of the volcano (Figure 4.1). These focal mechanisms present a great diversity of types and have been classified into three groups: decollement (dip $\leq 20°$), reverse (dip $> 20°$) and normal faults.

Under the assumption that the slip on the fault plane is in the same direction as the resolved shear stress, a diversity of focal mechanisms can result from a single homogeneous stress field. This is the approach taken by *Gephart and Forsyth* [1984] whose method we have adopted in this study to determine the stress tensor. This method has been used successfully in the Kaoiki region, Hawaii, by *Wyss et al.* [1992], who found that the stress is homogeneous in most of the Kaoiki crustal volume, but, that differences between 20° to 80° of at least one of the principal stresses existed in some subvolumes. *Gillard et al.* [1992] used it to infer a tectonic model for western Hawaii. They found that the greatest principal stress is oriented near vertically in western Hawaii, which implies that the decollement plane, there, can slip under low shear stress in a similar fashion as for example the San Andreas Fault in central California [*Zoback et al.*, 1987; *Zoback and Beroza*, 1993].

Another approach to understand seismotectonic processes is to compute the strain orientation by summing the moment tensors of the earthquakes as described by *Kostrov* [1974]. The resulting moment tensor is then proportional to the average strain released by the earthquakes within a volume of the crust. We estimated the

strain orientation using Kostrov's approach and compared the principal strain orientations to the principal stress orientations. We hypothesized that these axes must be coaxial if the strength of the crust is uniform. However, if in a crustal volume, some of the earthquakes occur on a fault which is weak, the strain and stress orientations may differ. Such a situation exists in west Hawaii where the greatest principal stress and the greatest principal strain released by the earthquakes vary by as much as 30° [*Gillard et al.*, 1992]. The reason for this difference comes from the fact that a fault slips in a direction which is at 45° from the greatest principal strain released, but the shear stress resolved on this fault may be very small due to shallow or high angles between the greatest principal stress and the fault [*McKenzie*, 1969; *Kostrov*, 1974].

3. METHOD

Gephart and Forsyth [1984] developed a method to retrieve the directions of the three principal stresses ($\sigma_1>\sigma_2>\sigma_3$) and the ratio, $R=(\sigma_2-\sigma_1)/(\sigma_3-\sigma_1)$, by inverting the direction of slip on fault planes obtained from focal mechanisms. The orientations of the fault planes, and associated slip directions, given by focal mechanisms, constrain these four model parameters assuming that the stress field is uniform. The forward problem can be solved by requiring that the resolved shear stress on the fault plane is parallel to the observed slip vector and has the same direction.

The inverse problem is solved by a grid search over the entire focal sphere testing every combination of the four parameters, one by one, against all the data

[*Gephart and Forsyth*, 1984]. For each model, a misfit is determined which is defined as the smallest rotation around any arbitrary axis which brings the observed focal mechanism into coincidence with a predicted focal mechanism, in which the slip vector matches the direction of resolved shear stress on at least one of the nodal planes. Each individual observation receives two misfits, one for each nodal plane. In the absence of any objective means for identifying the true fault plane, the nodal plane with the smaller misfit is chosen as the fault plane. Then, the best fitting stress model is the one with the smallest average misfit, and one can compute the 95% confidence level using the one-norm statistics described in *Gephart and Forsyth* [1984]. Differences in the quality of the data can be taken into account by applying a weight to the misfit of each observation.

This inversion procedure, also called "exact method" [*Gephart and Forsyth*, 1984], is computer intensive, especially with large data sets. *Gephart and Forsyth* [1984] suggested the use of the approximate method to find a rough estimate of the minimum rotation needed. Instead of searching for the rotation axis giving the smallest misfit, the approximate method computes the rotation around three axes, the two axes normal to the nodal planes and the B axis (the axis defined by the intersection of the two planes) and takes the smallest angle of rotation as the misfit. This approach gives an estimate of the best stress orientation, which can be used later as a starting model using the exact method. Also, according to Gephart and Forsyth's experience and to ours, the patterns of 95% confidence level are close to the one obtained using the exact method. The only difference between the two approaches resides in the size of the average misfits. They are larger for the

approximate method and according to our experience, they can be reduced by about half using the exact method.

To test for spatio-temporal changes in the stress field, we will subdivide the data set into subsets and use the approximate method to compare the results between sets. Subsets will be regrouped together if differences between them are not resolvable at the 95% confidence level. The size of the misfit will not be a determinant criteria because it can be reduced substantially by using the exact method. The final regrouped sets will then be inverted, using the exact method and the quality of the inversion will be discussed based on the error analysis described below. If, after inversion of the final sets using the exact method, the misfit is too large to be acceptable, further subdivisions of the data set will be tested following the same procedure until a set is found with an acceptably small misfit that can be interpreted as representative of a homogeneous data set.

3.1. Misfit as a function of fault plane solution errors

We investigated the meaning of the size of the misfit, F, by perturbing the strike, dip and rake of an error free synthetic data set. We first derived the stress tensor from a set of 53 focal mechanisms corresponding to events located within area 1 (shown in Figure 4.13) at depths between 8.5 and 9 km. This stress system was then used to generate an error free synthetic set by adjusting the 53 fault plane solutions such that the slip vector on one of the nodal planes coincided with the predicted slip direction on this plane. Then we perturbed the strike, dip, and rake of each focal mechanism by adding random errors normally distributed around a zero

mean and with standard deviation of 5°, 10°, 15°, 20°, 30°, and 40°, respectively. We performed this analysis using the exact method as well as the approximate method to compare differences in misfits between the two. The perturbations of the P and T axes (second column in Table 4.1) may be the best measure of the average error introduced, because we have no other way of determining how the errors propagate when we simultaneously perturb the strike, dip and rake. The results of this error test for the exact and approximate methods are shown in Table 4.1.

For small and moderate errors that could realistically be expected in a data set (5° to 15°), the average misfits are $F \leq 6°$, and the stress orientations are retrieved within less than 20° from the correct ones. For unrealistically large perturbations of 30° and 40°, the misfits are $F > 10°$, and the correct stress directions are retrieved poorly (error 23°) to not at all (error 82°, Table 4.1). Hence, misfits of that order are likely to be representative of heterogeneity in the stress field. For the case of intermediate perturbations (20°), the misfit is still small (F=6.6°), but the stress directions are not retrieved correctly (error 77°, Table 4.1).

Based on this test, we propose that the inversion results with misfits smaller than 6° represent data from crustal volumes with relatively uniform stress tensor orientations. If the misfit is larger than 10°, we believe that the data are not from a volume where the stress state is homogeneous. Inversions that result in misfits ranging from 6° to 10° will be considered suspect, but not necessarily incorrect for data sets that could have 20° errors in the fault plane solutions and that could furnish reasonably constrained stress directions [*Gillard and Wyss*, 1993]. However, for the

high quality Hawaiian data analyzed here, it would be unrealistic to explain misfits, F>6°, by errors in the fault plane solutions larger than 15°. Therefore, we will interpret all misfits larger than 6° as indicating heterogeneity of the stress field, and thus we will subdivide these volumes in subvolumes for separate inversion. If the misfits decrease below 6° after separation from the main set, this will indicate that the main set was not homogeneous. If the misfits do not change but are less than 10°, then the conclusion will be that the size of the misfit may be affected by both the error in the data and possible stress heterogeneity.

From this analysis, one concludes also that the approximate method is capable of giving a good estimate of the best stress model because its results are always within 10° or less of σ_1 obtained from the exact method and within less than 20° of σ_3 obtained from the exact method. However, the average misfits for the approximate method are larger, by about 4° to 5° on the average, than the misfits obtained by the exact method (Table 4.1). For that reason, when using the approximate method, we will not use the size of the misfit as a criterion for deciding if a set is homogeneous or not.

4. DATA

The data consist of first motion readings and P- and S-wave arrival times of 1322 events located in the south flank of Kilauea volcano, Hawaii, within an area defined by a polygon with coordinates latitude/longitude 19.25/-155.4, 19.0/-155.46, 19.27/-154.67, 19.58/-154.67, and a depth ranging from 0 to 20 km and for a period from January 1972 through December 1991. They represent all the earthquakes with magnitude $M \geq 3$, for the period 1972-1985, and $M \geq 2.5$, for the period 1986-1991, listed in the catalogue of Hawaiian earthquakes published by the Hawaiian Volcano Observatory (HVO). We used a lower magnitude limit after 1985 because a negative artificial magnitude shift resulted from the introduction of the CUSP software which was used to generate the Hawaiian catalogue starting in 1986. The events were located using the linear gradient velocity model, HG50, determined by *Klein* [1981]. This model has given good results for locating earthquakes and computing focal mechanisms in the south flank of Kilauea [*Klein*, 1981]. All the events are located within the dense network covering most of the south flank of Kilauea (Figure 4.2).

We used the program FPFIT designed by *Reasenberg and Oppenheimer*, [1985] to compute the focal mechanisms. This program finds the fault plane solution that best matches the first motion polarities of an earthquake. The inversion proceeds by a two-stage grid search (coarse and fine) in the three dimensional parameter space of strike, dip, and rake, to find the focal mechanism that minimizes the first motion discrepancies. As an output the program gives five parameters used

to assess the quality of the solution: the minimum misfit, the uncertainty of the strike, dip and rake and the station distribution ratio. The misfit, f, which compares the observed polarities with the ones calculated for an assumed source model is weighted by the estimated variance of the data and by the theoretical P wave radiation pattern which has the effect of putting less weight on observations near nodal planes, thereby minimizing the effects of inconsistencies near nodal planes. Consequently, the minimum misfit will vary between 0, for a perfect fit with no inconsistencies, and 1, for a perfect mismatch with all the first motions polarities in the wrong quadrant. The strike, dip and rake uncertainties correspond to the total range of their possible variation within the 90% confidence limits. The station distribution ratio, STDR, is sensitive to the distribution of the first motion polarities on the focal sphere. It varies between 0 and 1. Low values (STDR < 0.4) indicate that many data points lie near nodal planes. These solutions may be less robust than solutions with higher STDR values (STDR$\geq$0.5) which represent data distributed more evenly over the focal sphere.

Multiple solutions which are defined as alternative solutions corresponding to significant relative minima are labelled by FPFIT. They are solutions with a minimum misfit within 0.04 of the best misfit and for which the distribution of P and T axes for the 90% confidence level do not overlap the one corresponding to the best solution. Thus, FPFIT is capable of identifying non-unique fault plane solutions.

The data processed consisted of all events having at least 20 first motion read-

ings. This number was lowered to 15 for the period 1972-1975 because the network was sparser. The grid point spacing for the coarse grid search over the entire focal sphere was 20°, 5°, and 20° for the strike, dip, and rake, respectively. The fine grid search was done with grid point spacing of 1° for the strike and dip, and 5° for the rake. We corrected polarity reversals using the HVO list of reversals based on compilations by *Endo* [1985], *Wyss et al.* [1992] and Klein [personal communication, 1989]. Out of 1322 events, 910 events had unique focal mechanisms and 412 events had multiple or non-unique solutions. The multiple solutions were rejected from the final data set after having been checked visually to assure that none could be used. Figure 4.3 illustrates the relationship between the fit of fault plane solutions, as measured by f, and the percentage of inconsistencies for each of the 910 focal mechanisms with unique solutions. This plot shows that most of the solutions have misfits, f, concentrated below 0.2 and percentages of inconsistencies below 20%. This figure also shows that the number of inconsistencies is not always critical in getting a solution with a low misfit. This is due to the high number of first motion readings which is about 36 per event.

The quality of the 910 remaining focal mechanisms was assessed by examining the five parameters given by FPFIT, and a grading scale from A to D was established with A being the best quality and D the poorest. These weights, A=3, B=2, C=1, D=0, were used in the inversion for stress orientations. The following scheme was adopted:

$$0.00 \leq f \leq 0.07 \text{ and } 0° \leq \delta \leq 10° \quad A$$

$0.00 \leq f \leq 0.07$ and $10° < \delta \leq 20°$	B
$0.07 \leq f \leq 0.14$ and $0° \leq \delta \leq 20°$	B
$0.14 \leq f \leq 0.20$ and $\delta \leq 20°$	C
$0.00 \leq f \leq 0.20$ and $20° < \delta \leq 30°$	C
$0.00 \leq f \leq 0.20$ and $30° < \delta$	D
$f > 0.20$	D

where δ is the largest of the uncertainties of strike, dip, and rake. Whenever the dip of one of the nodal planes is less than 20° or greater than 70°, δ is the largest of the uncertainties of the rake and the dip. This choice was made because for a nearly horizontal nodal plane, the strike is not defined and the computed error has no meaning. After applying this grading scale, we reassessed visually every focal mechanism with STDR<0.4 because such solutions are not very robust, due to the fact that the first motions concentrate near nodal planes. This happens when many first motions correspond to refracted phases, all having the same takeoff angle but different azimuths. This grading algorithm assigned an A grade to 226 solutions, a B to 492 solutions and a C to 109 solutions. 86 focal mechanisms received a D and were rejected from the final data set. Finally, we added 36 focal mechanisms with $2.5 \leq M < 3$ for 1972-1975 to increase the number of events in this period. These last events were graded following the same procedure.

We conclude that the final data set of 863 fault plane solutions is of very good quality because each is based on an average of 36 first motion readings and the fre-

quency distribution of inconsistencies is normally distributed around a mean of 4 (Figure 4.4). The average fit is 0.07 and more than 70% of the solutions have fits less than 0.1 (Figure 4.4). The distribution of STDR values indicates that the first motions are well spread on the focal spheres and that most of the solutions are robust because the average value is 0.5 and more than 80% of these values are greater than or equal to 0.5 (Figure 4.5). Finally, the distribution of uncertainties for the strike and dip indicates that the nodal planes are known in the average within 9° whereas the rake is determined within about 12° (Figure 4.6).

5. TYPE OF FAULTING

In the south flank of Kilauea, many focal mechanisms indicate motion on shallow dipping faults (0-20°) frequently referred to as decollements. Motion on these faults can be either normal or reverse. We define as decollements, focal mechanisms for which one of the nodal planes dips between 0° and 20°. Our data data set contains 440 events of this type. We also define as reverse type, any focal mechanism with a reverse component of slip and nodal planes dipping at angles larger than 20° and less than 80°. Similarly, we define as normal type, any focal mechanism with a normal component of slip and nodal planes dipping at angles between 20° and 80°. Our data set contains 263 events with reverse-type focal mechanisms and 147 events with normal-type focal mechanisms. Within each of these three types, we grouped focal mechanisms of similar orientation (similar strike and dip) and computed the average focal mechanism for each group by averaging the slip vectors. The average mechanisms for the different groups are shown in Figures 4.7 and 4.8.

No strike-slip events are contained in our data set.

During the pre-Kalapana period (before the Kalapana mainshock, 1972 through November 29, 1975), five different groups of focal mechanisms are observed. 34 decollements with a vertical plane striking parallel to the rift. 23 reverse focal mechanisms with strike parallel to the southeast rift zone and 6 with strike approximately perpendicular to the same rift zone (Figure 4.7). The nodal planes of the reverse mechanisms striking parallel to the rift, dip at angles of 33° and 58°. The mechanisms with strike perpendicular to the rift have nodal planes dipping at 45°. The normal faults are also subdivided in two groups having a common nodal plane striking at about 250° and dipping at about 64°. The other nodal planes have a similar dip but their strike is different from each other by about 120° (Figure 4.7).

In the post-Kalapana period (after the Kalapana mainshock, 1976 through 1991), a pattern of faulting similar to the pre-Kalapana period is observed: 426 decollements, 240 reverse faults and 147 normal faults (Figure 4.8). The reverse faults are subdivided in four groups with varying strikes and dips (Figure 4.8, center). Among these, the mechanism with nodal plane striking at 57° and 185°, dipping at 69° and 32° (Figure 4.8, center, circle) is the largest group with 138 events. The group represented by the focal mechanisms with both nodal planes striking approximately parallel to the southeast rift zone (N60E) has 46 events (Figure 4.8, center, diamonds). 15 events have reverse fault plane solutions transcurrent to the strike of the southeast rift zone, and their nodal planes have dips of about 45° (Figure 4.8, center, triangle). The smallest group is represented by 13 events with

both nodal planes striking EW and dipping at 53° and 38° (Figure 4.8, center, star). There are three groups of normal faults in this period (Figure 4.8, bottom). One group has both nodal planes striking approximately parallel to the strike of the south east rift zone (N60E) and their dips are 50° and 40° (58 events) (Figure 4.8, diamonds). The second group contains 49 events with one nodal plane striking approximately parallel to the rift (dip 68°) and the other striking at 136° (dip 43°) (Figure 4.8, circle). The smallest group contains 17 events and the average mechanism has one plane striking south and the other one NE with dips of 55° and 49°, respectively (Figure 4.8, star).

The diversity of faulting in the south flank of Kilauea is remarkable. In both periods, before and after the November 29, 1975, M=7.2, Kalapana earthquake, a mixture of decollement, reverse and normal faults characterized the faulting. Some differences exist between the two periods with respect to the spatial distribution of faulting. The normal faults, prior to the Kalapana event, are all located west of longitude 155° 10' W in an area along Kilauea's south west rift zone (Figure 4.7). For the post-Kalapana period, no focal mechanisms were obtained west of longitude 155° 22.5' W because few events with $M \geq 3$ occurred in this region. Normal faulting seems to occur in the post-Kalapana period east of longitude 155° 22.5' W, where no normal fault type of mechanisms were obtained prior to the Kalapana mainshock. Also, these normal fault type events seem to be located slightly NW of the events with reverse-type mechanisms (Figure 4.8). However the decollement types appear in both periods. The depth of all the earthquakes, for the pre-and post-Kalapana period, is between 8 and 12 km with an average of 10 km (Figure

4.9).

The earthquakes form patches of seismicity separated by zones of no activity. This pattern is maintained even if we plot events down to magnitude 1.5 [*Okubo et al.*, 1992]. This could indicate either that the patches of seismicity are surrounded by asperities, which are strong and never break except in large earthquakes like the Kalapana event, or by creeping fault zones. The answer to this has not been found yet.

Focal mechanisms of events with magnitude 5 and above were extracted to determine what type of faulting releases most seismic energy (Figure 4.10). Out of 10 events, 6 had a thrust-type focal mechanism similar to the mechanism marked with a circle in Figure 4.8 (center), three were of decollement type and one was a normal fault (Figure 4.10). If we add the events with magnitude down to 4.5, we obtain 10 more reverse faults, one more decollement and one more normal fault. Spatially, the majority of these events are located east of longitude 155° 10' W. The largest event, which is the 1975, M=7.2, Kalapana earthquake, has a decollement-type focal mechanism [*Ando*, 1979; *Furomoto and Kovach*, 1979; *Crosson and Endo*, 1982; *Klein*, 1981; *Harvey and Wyss*, 1986].

From the distribution of type of faulting as a function of magnitude we conclude that reverse faults are releasing about 80% of the energy for M<7 earthquakes in Kilauea's south flank. However, the single largest energy release, which exceeded the sum total of all other known seismic energy release in the south flank (November 29, 1975, M=7.2, Kalapana earthquake), occurred along the decollement

plane. The reverse faults seem to have dimensions of about 20 km, which limits the magnitude of earthquakes these faults are capable of to M≤61/2. The source length of the largest of these reverse events (26 June, 1989, M=6.2, Kilauea south flank earthquake) was estimated as 20 km [*Arnadottir and Segall*, 1991]. However, the aftershocks of this event outlined the decollement plane and extended over an area of 30 km by 7 km parallel to the rift zone [*Bryan*, 1992]. The decollement plane has dimensions equal to those of the island of Hawaii and can thus generate earthquakes with 7<M≤8 (1975, Kalapana earthquake and 1868, Kau earthquake) [*Wyss*, 1988].

6. FAULTING AS A FUNCTION OF TIME

The percentage of decollement, reverse and normal fault plane solutions within one year bins shows a strong dependence with time. We separated the data into two volumes. Volumes A and B contained all the focal mechanisms of events located east and west of longitude 155° 10' W, respectively. This separation was based on the above analysis of faulting as a function of space which showed that reverse and normal faulting were more abundant east of longitude 155° 10' W than west of it.

In volume A, prior to 1976, we found no normal faults (Figure 4.11). After 1975, normal faults appeared with a constant percentage of about 30% from 1976 till 1979 (Figure 4.11). Reverse faults dominate in percentage for the period from 1972 to 1983 with an average of about 40%. After 1983, their percentage decreases significantly. The decollement-type faults contribute a lower percentage than the

reverse faults for the period 1975-1983, but after 1983, they dominate. In volume B, the decollements are more abundant than reverse and normal fault plane solutions at all times, but their percentage seems to increase after 1980 (Figure 4.12). Reverse fault plane solutions are at a relatively high level mostly before the 1975 mainshock, and they decrease after 1983 as in volume A. Normal fault plane solutions in volume B appear mainly during a few years after 1975.

We conclude that the type of faulting along the south flank of Kilauea, varies as a function of time. Four periods with separate faulting patterns emerge. In the first period (1972-1975, prior to the Kalapana earthquake) no normal faults are ruptured in Volume A and reverse faulting is at a relative maximum in both volumes A and B. The second period extends from 1976 to 1979 (post Kalapana) and is characterized by the sudden occurrence of normal faults in the northwestern part of volume A, which are interpreted as being caused by an extensional stress regime induced by the 1975, Kalapana earthquake. The period from 1979 to 1983 contains a higher percentage of compressional events (reverse fault), which may indicate that pressure is building up within the rift zone prior to the 1983 eruptions. The last period elapses from 1983 to 1991 and shows an increase of the occurrence of events with decollement type, which seems to indicate that the south flank is now moving away from the rift along the decollement plane.

7. RESULTS OF INVERSION FOR STRESS ORIENTATIONS

We investigated the state of stress as a function of time and space in the south flank of Kilauea. The entire data set of focal mechanisms was subdivided into 5 subsets defining five different areas along the south flank (Figure 4.13). The criteria for subdivision were based on the pattern of seismicity shown by the events selected for the study. They occur in patches of seismicity separated by areas with no earthquakes (Figure 4.13). Area 1 was selected because it had no earthquakes prior to the 1975 Kalapana earthquake but many events with normal faulting type of focal mechanisms after the mainshock. The data sets contained in each area were subdivided into subsets as a function of time. We chose four periods based on the previous analysis of the type of faulting as a function of time. The first period, 1972-1975, is the pre-Kalapana period. It was selected to see if any changes in the stress orientation occurred with the mainshock. Unfortunately, not many focal mechanisms were available for this period. The second period, 1975-1979, starts just after the Kalapana earthquake and represents the aftershock period. 1980-1983 is the period preceding the eruption of Puu'Oo. The final period extends from June 1983, after the onset of the eruption, till the end of 1992.

In a first step, we used the approximate method to find the direction of principal stresses and detect any changes as a function of time within each area. In this method, the computation is much faster than in the exact method and the results are similar to the exact method in terms of orientation of stress and pattern of the 95% confidence level. However, the misfits obtained by the approximate method are not

comparable to the ones obtained by the exact method as we demonstrated above in the error analysis section. For that reason we did not use the size of the misfits obtained by the approximate method as a criterion for judging differences between subsets. Only the similarity of the orientation of the best models and the pattern of the 95% confidence level were used to judge if subsets differ significantly or not. If the 95% confidence regions of σ_1 and σ_3 for one subset did not overlap the 95% confidence regions for another subset, then the two subsets were kept separate because their stress state was judged to be different. Otherwise, if the 95% confidence regions overlapped, we decided that no significant change occurred and the subsets were joined for inversion, in a second step, using the exact method for the final result.

7.1. Area 1

No focal mechanisms were available in area 1 for the period 1972-1975 because the level of seismicity for $M \geq 3$ earthquakes was almost null. After the occurrence of the Kalapana mainshock, earthquakes appeared in area 1 (Figure 4.13). Many of these events were normal faulting events which occurred mainly in the period 1975-1979 (Figure 4.11). Inverting the focal mechanisms for each of the three periods following the Kalapana event separately using the approximate method, we found no change as a function of time within area 1 (Figure 4.14). For σ_1 and σ_3, the 95% confidence regions overlapped and their directions varied only by 15° and 23°, respectively, for the periods 1975-1979 and 1983-1992 (Table 4.2). Only 8 focal mechanisms composed the data set of period 1980-1983, making any

results poorly constrained as seen by the spread of the 95% confidence limits (Table 4.2 and Figure 4.14).

For the final result, we grouped all the focal mechanisms (110 events) of the three periods together and inverted them using the exact method (Table 4.3 and Figure 4.15). This set contained 60 normal, 18 reverse, and 22 decollement-type focal mechanisms. The average misfit was 6.0° which is at the borderline for acceptable results and may indicate that this data set is not completely homogeneous. Out of the 110 focal mechanisms, 10 had individual misfits greater than 15°, of which 9 were from the period 1975-1979. Four of these mechanisms were reverse, 5 were normal and one was decollement. A test for homogeneity as a function of depth resulted in the reduction of the size of the average misfit, but differences of stress directions could not be resolved at the 95% confidence level. Considering all aspects of the data set in area 1 we accept the stress directions estimated from the entire data set (Figure 4.15) as a reasonably reliable result, although we suspect that some degree of heterogeneity exists as a function of depth in this set.

7.2. Area 2

Using the approximate method, we found that the stress orientations vary significantly as a function of time in area 2. While the orientation of the least principal stress remained stable between 1975 and 1992, the greatest principal stress varied from being horizontal between 1972 and 1980 to plunging at an angle of 45° between 1980 and 1992 (Table 4.2, Figure 4.14). These differences were significant

at the 95% confidence level (Figure 4.14).

For the final result, using the exact method, we grouped the data for the period 1980-1992 and inverted them together (Table 4.3, Figure 4.16). We obtained a low misfit (4.5°, Table 4.3) indicating that this set was homogeneous. This set contained 155 decollement, 85 reverse, and 25 normal fault type focal mechanisms. Five focal mechanisms had individual misfits between 15° and 20°, and one had a misfit of 36°. None of these inconsistencies were normal fault type focal mechanisms. Most of the normal faults were of the type described by the diamond and circle symbols in Figure 4.8. For the reverse fault type of mechanisms, the dominant one was represented by the circle in the Figure 4.8 (middle).

We inverted separately with the exact method, the data set for periods 1972-1975 and 1975-1979 (Table 4.3, Figure 4.16). The average misfit for the data set covering the pre-Kalapana period was 3.6°, which signifies that this set is homogeneous. For the period 1975-1979, the average misfit was 6.5° which may indicate that this set is not homogeneous. The number of fault plane solutions with individual misfit larger than 15° was 14 with 5 normal faults, 6 reverse, and 3 decollement type. This data set was composed of 111 events with 68 reverse, 18 decollement, and 15 normal type of fault plane solutions. When inverting subsets separately as a function of depth, the misfit could not be reduced, and changes in stress orientation as a function of depth could not be resolved as discussed later.

7.3. Area 3

In area 3, the results of the approximate method were stable as a function of time with σ_1 and σ_3 varying on the average by less than 15° between the different periods (Table 4.2). In period 1972-1975, only 13 focal mechanisms were available and for that reason the inversion is not as well constrained as in the following years (Figure 4.14). No significant changes in the orientation of the principal stresses between the post- and pre-Kalapana periods were detected.

The inversion for the final result of all 165 events grouped together, using the exact method, gave a greatest principal stress oriented at an azimuth of 155° and a plunge of 36° (Table 4.3, Figure 4.15). The least principal stress was oriented at azimuth 338° and plunge 54°. The average misfit was 3.6°, which indicates, according to our error analysis, that the stress is homogeneous in this area.

7.4. Area 4

After inverting 4 subsets of area 4 as a function of time using the approximate method, we concluded that no significant changes in the stress orientation existed. The 95% confidence level for σ_1 and σ_3 overlapped (Figure 4.14). The number of focal mechanisms in each subset prior to 1983 was low (less than 20), which implied that the stress models obtained were not as reliable as the one obtained for the period 1983-1992, which had 60 events.

The inversion of the 88 focal mechanisms with the exact method gave a final result with a low misfit of 4.5° (Table 4.3, Figure 4.15). Based on the small size of this average misfit, we concluded that the stress field was homogeneous as a

function of time in area 4. The greatest principal stress was oriented at an azimuth of 145° and a plunge of 41° (Table 4.3, Figure 4.15). The least principal stress has an azimuth of 325° and a plunge of 45° (Table 4.3, Figure 4.15).

7.5. Area 5

In area 5, only focal mechanisms for events occurring prior to the 1975, Kalapana earthquake were available because this area has low seismicity for depths deeper than 9 km and magnitudes $M \geq 3$ after 1975. The inversion of these focal mechanisms with the approximate method gave orientations of σ_1 and σ_3 similar to the ones obtained by the exact method (Table 4.3 and 4.4). The differences were within 20° and the patterns of 95% confidence level were also similar (Figure 4.14 and 4.15). The average misfit for the final inversion with the exact method was 6.5° (Table 4.4), which suggests that this data set may not be homogeneous. It was not possible to subdivide this area any further because of the small number of events.

7.6. Stress orientations as a function of depth

We investigated the stress orientations as a function of depth in area 1 (all times considered) and in area 2 (1975-1979) because the average misfits were near 6° and above (Table 4.3), which places them into the range of suspect results, where the assumption of homogeneity within the crustal volume where these events occurred may not be fulfilled (see our analysis above).

We divided the data set in area 1 in three groups corresponding to the depth ranges, 5 to 8.5 km, 8.5 km to 9.0 km, and 9.0 to 10.5 km. These subdivisions were

chosen arbitrarily because no clear patterns exist showing that the faulting varies as a function of depth. Also, most of the events that we used for this study were located between 8 and 12 km depth. The accuracy of hypocentral depth estimates for these events is believed to be better than 2 km due to the good station coverage. However, relocations of events in the New Madrid area using three component stations to pick the S-arrival time have shown that significant difference of at least 2 km or larger exist between the relocated events and the ones located using only vertical components [*Chiu et al.*, 1992]. In Hawaii few three component stations exist. Therefore we suspect that the depth accuracy is probably not better than 2 km and it may thus be impossible to resolve stress variations as a function of depth.

We found no significant change of stress orientation from depth 5 to 9.0 km in area 1 (Table 4.4). The stress orientation was similar to that of the entire data set (Table 4.3). In the inversion of the events located at depth 9 km to 10.5 km, the azimuth of σ_1 changed by about 50° but this difference was not significant at the 95% confidence level. The average misfits decreased to values lower than 6° suggesting that perhaps the stress does vary as a function of depth.

In area 2, after making many subdivisions as a function of depth and inverting the data using the approximate method, we found that separating the focal mechanisms into two groups, one for depth 5 km to 9.5 km and the other for depth 9.5 km to 10.5 km, was most likely to show differences in stress orientations. We inverted these two groups using the exact method. The average misfits for the two depth ranges did not decrease substantially relative to the one obtained inverting for all

depths (Table 4.4). Also, the results of the two depth ranges did not differ significantly at the 95% confidence level. Because this separation did not improve the results significantly, the data set in area 2 was not separated as a function of depth.

We conclude that it is not possible to resolve stress orientation differences as a function of depth with the available data sets. The relatively high misfits obtained for area 1 and area 2 for period 1975-1979, could be due in part to differences as a function of depth or they could as well have been caused by local heterogeneities induced by the complexity of the rupture of the Kalapana mainshock.

8. STRAIN

8.1. Method of strain calculation

Earthquakes occurring within a volume of the crust will deform this volume. *Kostrov* [1974] described this process mathematically by assuming that the volume containing these earthquakes is a continuous medium and consequently calculated the deformation of the crustal volume by the earthquakes. He showed that the deformation of this volume is related to the moment tensors of the earthquakes located within this volume. Expressing the deformation of the volume in terms of strain components, the relationship between the strain and the moment tensor is given by

$$\varepsilon_{ij} = \frac{1}{2\mu V} \sum_{k} M_{ij}^{k} \qquad (1)$$

where μ is the shear modulus. The seismic moment tensor M_{ij}^k of the kth earthquake is given by

$$M_{ij}^k = M_0^k \ (u_i^k n_j^k + u_j^k n_i^k)_j \tag{2}$$

where n_i^K is a unit vector normal to the fault-plane and u_j^K is a unit vector parallel to the slip direction. These two vectors are determined by the fault plane solutions. The scalar moment M_0 is computed from the moment-magnitude relationship. The shear modulus μ can be derived from the velocity structure.

This strain tensor describes the deformation of the crustal volume resulting from the earthquakes located within this volume. Therefore, the word strain will mean the average seismic (released by earthquakes) strain in a crustal volume. This definition is necessary to avoid the confusion with the geodetic strain which corresponds to the deformation of the medium which causes earthquakes.

In this study, we are interested in comparing the orientation of the principal stresses to the principal strain directions which are the eigenvectors of the above described strain tensor. If a material is relatively uniform in strength, the principal axes of stress and strain should be coaxial, or at least close to each other. On the other hand, if there is a dominant plane of weakness with low shear strength in a volume, it is possible that slip occurs on this plane even if the greatest principal stress is not oriented at a most favorable angle. In this case the orientations of the principal stress and strain may be different because the direction of greatest principal strain and the slip direction of the fault are always at 45°, whereas the greatest principal stress can vary from being parallel to perpendicular to the fault

[*McKenzie*, 1969; *Kostrov*, 1970, 1974].

The strain calculation was applied to the different subvolumes in which the stress was uniform. The scalar moments were derived from the moment magnitude relationship for Hawaii proposed by *Zuñiga et al.* [1988]. Error ellipses representing the 95% confidence level of the orientation of the principal strain axes were computed following the procedure described in *Wyss et al.* [1992]. Errors of 10° for the strike, dip, and rake were adopted to compute the confidence ellipses. We did not consider differences in stress and strain orientations as significant at the 95% confidence level if these ranges for stress and strain overlapped. By comparing stress and strain in different subvolumes where the stress state is uniform in the south flank of Kilauea, we want to understand how the stress causing the earthquakes is related to the deformation caused by the earthquake. In other words, this comparison will show if there are zones of weakness, and how the strain is mostly released in the south flank as a function of space and in some areas as a function of time.

The inversion for stress does not weigh the data with magnitude, but the strain method does. For that reason, it is important to know if the strain orientations are significantly different within different magnitude bands if we want to compare them to the stress orientations. We found that the strain was invariant as a function of magnitude for M<7 in the five areas we investigated. The strain change due to the M=7.2, 1975 Kalapana earthquake was estimated by assuming that in each of the 4 subvolumes 1/4 of the total moment was released. The strain released by this

mainshock dominates in all volumes because of its large size but it did not affect significantly the orientation of the strain in areas, 1, 3, and 4 where ε_1 was less than 20° from the greatest principal strain computed without the Kalapana mainshock. The 95% confidence ellipses of the two calculations overlapped. However, in area 2 (period 1972-1975) and in area 5, the strain for M<8 differed significantly from the strain computed with M<7 events by about 26° and 37°, respectively. The stress results presented in Table 4.5 and Figure 4.17 correspond to magnitudes M<7.

8.2. Observed strain orientations

The principal strain orientations change as a function of space (Figure 4.17) in the south flank of Kilauea. The orientation of ε_1 and ε_3 in area 1 differ significantly from the ones in area 2, 3, and 4. In the average, the difference in ε_1 orientations between these areas is about 50°. The difference in ε_1 is most significant in the dip, which varies from being the steepest in area 1 with 65° to about 30° in areas 3 and 4, and almost horizontal in area 2 (Table 4.5). No significant difference in strain orientation exists between area 3 and 4 (Figure 4.17, Table 4.5). In area 5, the principal strain directions are not well resolved as shown by the large confidence ellipses for ε_1. Nevertheless, it is still possible to differentiate the orientation of ε_1 from the other areas at the 95% confidence level.

Area 2 is the only location where we detected significant changes in stress as a function of time. For this volume we computed the strain orientations for each subsets corresponding to the different periods. ε_3 does not change orientations

significantly as a function of time, whereas ε_1 changes azimuth by about 34° after the occurrence of the Kalapana earthquake (Table 4.5, Figure 4.17). This difference is significant at the 95% confidence level (Figure 4.17). The strain orientations in period 1975-1979 and 1980-1982, in area 2, are not significantly different.

8.3. Comparison of stress and strain tensor orientations

The stress and strain orientations are coaxial in area 1, and 3 (Figure 4.17). The coaxiality remains even after including the Kalapana event (M=7.2) as mentioned before. In area 5, the 95% confidence level for σ_1 and ε_1 overlap, and thus we conclude that the stress and strain tensor orientations are not significantly different (Figure 4.17). If one adds the Kalapana event (M=7.2), the greatest principal stress and strain differ by 37° at the 95% confidence level. In area 4, the greatest principal stress direction is different from the greatest principal strain direction by about 11° at a significant level (Figure 4.17, Table 4.5).

In area 2, it is not possible to differentiate the stress orientation from the strain orientation for the periods 1972-1975 and 1975-1979 because of the lack of resolution in the azimuthal direction of σ_1. Both ε_1 axes are almost horizontal. During the period 1980-1992, the greatest principal stress and the greatest principal strain orientations differ significantly by about 35° (Figure 4.17). This difference is measured mainly in the dip. Adding the Kalapana mainshock to the calculation of strain, introduces a difference between stress and strain of about 40° significant at the 95% confidence level.

9. DISCUSSION

9.1. Stress orientations

The stress tensor is not homogeneous in the south flank of Kilauea. Inverting all focal mechanisms of events located in the area covered by the data (50x10x10 km, Figure 4.13) gives an average misfit of 5.8° (Table 4.3). Based on the error analysis, this value is near the border line between acceptable and suspect results (6°). The entire misfit could be explained by uncertainties of 10° to 15° in the fault plane solutions, or in part by stress heterogeneity. After subdividing the entire data set into volumes of about 10 km on a side as a function of space and time, we found that the quality of the inversion was improved in many areas as reflected in the significant drop of the average misfits (Table 4.3). With confidence, we conclude that the stress is homogeneous in area 3 and 4, and does not change as a function of time (Table 4.3). However, in area 1 for period 1975-1992, and in area 2 for period 1975-1979, the average misfits are 6.0° and 6.5°, respectively, which is larger than the average misfit for the entire data set.

Because most of the larger misfits in area 1 came from focal mechanisms of events which occurred in the period 1975-1979, it is possible that stress readjustments above and below the decollement plane could have been induced by the slip along the basal plane due to the Kalapana, M=7.2, earthquake. This conjecture might be verified by analyzing the data as a function of depth. However, we found no significant change in the stress orientations as function of depth. We suspect that the accuracy of hypocentral depth estimates is not high enough to allow resolution

of differences above, at and below the decollement fault plane. We conclude that the data available do not allow the resolution of any changes of stress orientation as a function of depth. In view of the fact that the misfit is small, although near borderline, we interpret the stress orientations obtained for area 1 and area 2 (period 1975-1972) as representative of the state of stress within these crustal volumes, and we accept the observed variation as a function of time as real.

While the stress directions remain invariant as a function of time in area 1, they vary by as a much as 45° in plunge in area 2. Because the azimuth of σ_1 is not well resolved in the period 1972-1979 (Figure 4.16), we propose to take an azimuth of about 120° as the average orientation of the greatest principal stress. Therefore, the change in azimuth of σ_1 after 1980 is about 25°. These changes are significant at the 95% confidence level. The chronology of the state of stress along the south flank of Kilauea is summarized in Figure 4.18. Between 1972 and 1975, prior to the Kalapana event, the stress field is oriented radially with the greatest principal stress in the different areas pointing toward the magma chamber near the summit of Kilauea (Figure 4.18) suggesting that the source of the stress is the magma chamber near the summit. In area 2 the stress regime is compressional, with σ_1 horizontal, in accordance with the model, suggesting that, through forceful magma intrusion near the summit of Kilauea, stress is accumulated in the flank of the volcano. Geodetic measurements made on the south flank during 70 years prior to the Kalapana earthquake showed compressional strain of about $3.5x\,10^{-4}$ in a southeasterly direction [*Swanson et al.*, 1976; *Wyss et al.*, 1981; *Delaney et al.*, 1992]. Following the

Kalapana earthquake, the only change of earthquake pattern occurred within area 1 where earthquakes with focal mechanisms of normal fault type and decollements appeared, whereas no earthquakes were available for analysis before 1975. The stress in this volume was oriented in the same direction as in the adjacent volume west of it, with σ_1 plunging at 69° perpendicular to the rift (Figure 4.18).

The stress orientation in volume 2, south of area 1, did not seem affected by the Kalapana earthquake. The state of stress remained compressional and oriented in the same direction during the period 1975-1979 as prior to the main shock. We interpret this observation in the following way. The boundary between area 2 and area 1 represents the separation between the compressional and extensional quadrant induced by the decollement-type source mechanism of the Kalapana earthquake where the flank of the volcano (hanging wall) slipped in a SE direction. This mechanism induced an extensional regime in area 1 and therefore normal faults were activated in the period following the main shock (1975-1979). The extensional regime helped the emplacement of dike intrusions along the east rift zone by reducing the confining pressure perpendicular to the rift. Consequently, during the period from 1976 to 1981, the number of intrusions outnumbered the eruptions; about 24 intrusions occurred during this period and only 5 reached the surface [*Klein et al.*, 1987]. The crustal volume in area 2, south of area 1, stayed under compression after the Kalapana earthquake and during the entire period when most of the intrusions occurred 1975-1981.

Inflation and deflation periods, measured at Kilauea's summit for decades, are

taken to be indicative of changes of the stress exerted by the volcano on the crust surrounding it. The M=7.2 Kalapana earthquake started a period of deflation that lasted until 1978 when the summit began to inflate again [*Delaney et al.*, 1990; Figure 2]. The reversal of the summit tilt into a new compressive phase, starting in 1978, was closely followed in 1979 by a rotation of the stress direction in volume 2 into a direction parallel to those in the other volumes (Figure 4.18). The stress rotation in 1979 was unexpected. Instead we searched for, but did not find, rotations in 1975 and in 1983, at the beginning of the Puu'Oo eruption. Our interpretation of these observations is that the frequent intrusions in the east rift zone during 1975-1981, the renewed inflation, and the rotated stress direction starting in 1979 all indicate that stress was building up in the southeast rift zone. As the rift zone itself became the source of stress, the slip (and stress) directions in volume 2 turned perpendicular to the rift. Because the stress rotation in 1979 is demanded by our data from volume 2, and because the hypocenters range from 6 to 12 km depth, we propose that magma intrusions (in 1979 and after) in the east rift zone may have taken place below the brittle depth of the rift zone (6 km) at the depths of the earthquakes we analyzed. The existence of a deep magma body has also been proposed by *Delaney et al.* [1990] to explain horizontal extension of the summit, the uplift of the south flank, and the extension and subsidence of the axes of both east and southwest rift zones. Other evidence for the deep magma body under Kilauea's rift zones comes from the lack of seismicity at depth greater than 5 km under the rift zone [*Klein et al.*, 1987] and unusually strong attenuation of seismic intensities in the vicinity of the east rift zone [*Wyss and Koyanagi*, 1992].

After 1981, the number of intrusions decreased *Klein et al.* [1987]. The eruption of Puu'Oo that started in January 1983, and lasted for years, did not have any effect on the stress orientations. We interpret this to mean that magma was able to flow from the summit reservoir to the vent at Puu'Oo, where it reached the surface, without altering the stress conditions in the south flank adjacent to the rift. Evidence for the constancy of the horizontal compressive stress is apparent in the geodetic data, which show no strain accumulation or release after 1983 in the south flank [*Delaney et al.*, 1993].

9.2. Fault orientations

The knowledge of the orientation of the predominant active fault surfaces provides an important guideline toward establishing the appropriate tectonic model for the south flank. Gephart and Forsyth's method does not a priori require to distinguish between the fault plane and the auxiliary plane. However, their method provides a means to select the fault plane because the misfits for the two nodal planes for each earthquake are not the same. Thus, one may argue that the plane with the smaller misfit is the fault plane [e.g., *Gephart and Forsyth*, 1984; *Michael*, 1987; *Wyss et al.*, 1992]. We propose that if the two misfits differ by more than 10°, the choice of fault plane is possible for a particular focal mechanism. The 10° limit is chosen because this difference represents about twice the average misfits for acceptable inversions, and it is larger than the average error in the focal mechanisms. If, for a group of events having similar focal mechanisms, the same nodal plane is chosen as the fault plane in a significant percentage, we propose that this plane is

the predominant active fault surface.

The choice of the fault planes was tested for the most dominant group of reverse mechanisms which is represented by an average mechanism with nodal planes of strike, and dip, 185°, 32°, respectively, and 57°, 69°, respectively (circles in Figure 4.8, center), and for the group of normal faults with average fault plane solution with nodal planes of strike and dip of 238°, 50°, repectively, and 59°, 40°, respectively (diamonds in Figure 4.8, bottom), and for the decollements. The results are presented in Table 4.6.

For the reverse mechanisms, the steeper plane dipping at 69° was selected in 98% (62 events) of the cases in area 2, when a choice of fault plane was possible (Table 4.6). Overall, for the entire south flank, the steeper plane is chosen in 78% (69 events) of the cases when a choice is possible (Table 4.6). Based on this overwhelming preference for this fault plane, we propose that the steep angle plane striking approximately NE is the fault plane and we show this plane schematically as active at all times in Figure 4.19.

For the normal faults, overall, for the entire south flank, the plane striking NE and dipping at 40° was chosen in 76% (13 events) when a choice was possible (Table 4.6). However, out of 64 events, a choice was possible for only 17 events. We would be reluctant to propose that this plane is the fault plane, only on the basis of this result. However, if the NE striking plane is chosen, then slip along this fault plane is mechanically compatible with slip along the steeply dipping reverse faults in the volume south of the one where most normal faults are located (Figure

4.19). Also, this is the fault plane exposed at the surface in the Hilina Pali system which slipped during the 1975 Kalapana earthquake. Consequently, for the normal faults, we propose that the fault plane is dipping SE at 40°. This type of normal fault is shown as active in Figure 4.19 B and C.

For the decollement earthquakes, out of 372 events, a choice of fault plane was possible for only 29% (109 events) of the events. The vertical plane was chosen in 70% and the horizontal plane in 30% of the cases when a choice was possible. Hence we conclude that a choice of fault plane based on the misfits was not reliable because the latter differed by less than 10° in most cases (75%). We will however assume that the decollement plane is the fault plane in most cases, based on the following observations. The aftershocks of the 1975 Kalapana earthquake map out a horizontal plane as the rupture plane. Well located aftershocks (M>3) of the 1975 Kalapana earthquake tend to outline a horizontal plane as the rupture plane [*Thurber and Gripp*, 1988]. There is no trend of earthquake hypocenters that would outline a near-vertical fault plane, in fact no earthquakes shallower than 5 km were available for focal mechanism studies. There is no surface expression of a near-vertical fault on the south flank with the southern side upthrown, as required by the decollement focal mechanisms. Given all these facts, we are fairly confident that the model depicting the south flank as a wedge, moving seaward with slip along a decollement plane at its base [e.g. *Dieterich*, 1988] is correct. Thus, the decollement plane is shown as active at all times in Figure 4.19. It is possible that in some earthquakes near-vertical planes rupture instead of the decollement plane. This would not substantially alter our image of faulting in the

south flank. It would simply add a near-vertical fault plane, similar to the reverse fault shown in Figure 4.19.

Directly observable surface faulting was created during the 1975 Kalapana earthquake. Along the EW striking Hilina Pali fault, 1 m of normal faulting (south-side down) occurred [*Tilling et al.*, 1976]. We interpret this motion as subsidiary faulting along a shallow, aseismic fault. This type of faulting is expected in the model of a wedge under compressive stress presented by *Yin* [1993]. A contrary view is held by *Lipman et al.* [1985] who proposed that the Hilina Pali fault extends all the way down to the decollement plane. This proposal cannot be tested by analysis of earthquakes, because no seismicity occurs in the crustal volume in question (south of the Hilina fault system). A slip arrow on the Hilina fault in Figures 4.19B and 4.19D indicates that slip occurred in 1975.

9.3. The June 26, 1989, M=6.2, Kilauea south flank earthquake.

This event is the largest event in the south flank of Kilauea since the Kalapana earthquake, M=7.2, in 1975. The epicenter was located in area 2, at latitude 19.35° N and longitude 155.8° W, and the focal depth was 9.2 km (Figure 4.1). Several fault plane solutions have been published for this event. Our own solution indicates reverse-type faulting with one nodal plane of strike and dip, 183°, and 37°, respectively, and another nodal plane of strike and dip, 49° and 63°, respectively. *Bryan* [1992] using essentially the same data as ours, but employing a variety of velocity models and averaging the solutions, obtained a focal mechanism almost identical to ours. From inversion of teleseismic P and SH waves, *Chen et al.* [1990] obtained a

low angle thrust solution (decollement) with one of the nodal planes dipping NE at 16°.

Based on modeling of leveling data, *Arnadottir and Segall* [1991] found that the data could be best explained by a shallow dipping thrust located at 4 km depth. They concluded that their results did not match the seismological data because they did not include a realistic elastic structure in their modeling.

From our results above, which showed that in area 2 the steeply dipping planes are the fault planes in the case of reverse faulting, we conclude that the 26 June 1989, M=6.2, Kilauea south flank earthquake happened on a steeply dipping plane striking at 49° ± 9° and dipping at 63° ± 2°. The same conclusion was reached by *Bryan* [1992] who proposed that large Hawaiian earthquakes, may be triggered by ruptures on steeply dipping reverse faults. While it is not clear where the rupture starts in large Hawaiian earthquake like the Kalapana event (M=7.2), it is likely that the reverse faults as well as the normal faults may rupture during an M>7 earthquake and contribute to the source complexity of the mainshock. For example, *Harvey and Wyss* [1986] proposed that the 1975, M=7.2, Kalapana earthquake was composed of six subevents with focal mechanisms varying in strike and dip.

9.4. Comparison of stress and strain tensor orientations

The results of the strain analysis indicate that overall, with the exception of area 5, the axis of maximum seismic strain released is oriented approximately southeast, and nearly parallel to the strain accumulation measured geodetically before the Kalapana earthquake [*Swanson et al.*, 1976]. However, the dip of the greatest principal strain is changing as a function of space. This suggests that different types of faulting are dominant in different areas along the south flank.

In area 2, at all times, for earthquakes with magnitude M<7, the strain is released mostly on reverse faults of the type represented by the circles in Figure 4.8 (center). For M>7 earthquakes, like the 1975 Kalapana event, the strain is released by rupture on the decollement. The stress and strain are coaxial for M<7 events during 1972-1979 in this volume but after 1979 they vary by about 40° in plunge. In the remaining volumes in the south flank (area 1, 3, 4) the strain is released on the decollement and is coaxial with the stress for all magnitudes. In area 5, the resolution of both stress and strain is poor and does not allow a meaningful comparison. We conclude that the spatio-temporal differences between stress and strain in area 2 indicate that the crust is not homogeneous in strength. However we cannot conclude that the reciprocal is true for areas 1, 3, and 4 where stress and strain are coaxial.

Differences between the observed stress and strain orientations can vary as a function of time or space for a number of reasons, even if frictional properties are assumed to be invariant. In the presence of a major fault with low shear strength

the direction of strain release will be at 45° from this fault and in the direction of the slip on it, regardless of changes of the stress directions as a function of space or time. Changes of stress directions can be brought about by magma movements or by major earthquakes. Alternatively, changes of the relationship between stress and strain directions can also be caused by shifting seismic activity in a volume of diverse faulting. Assume that a crustal volume, containing several major weak faults of different orientation is under a stress with constant direction. When earthquake activity shifts from one to another of these faults, as is common, the strain release directions will change while the stress directions remain the same. We can demonstrate that both of these processes occur in area 2 of Kilauea's south flank.

The case of strain directions changing while stress remains constant happened during the 1975, M=7.2, Kalapana earthquake. This major earthquake caused a change in strain orientation in area 2, while the stress kept the same orientation. Before and after the Kalapana earthquake (1972-1970), the stress was oriented nearly horizontally (Figures 4.19 A and B). The strain was released mostly on reverse faults before 1975, and thus it was oriented approximately parallel to the stress directions (Figure 4.19 A). In the period 1975-1979 the same was true for earthquakes with M<7 (Figure 4.19 B). However, if we include the 1975 mainshock in the estimate of the strain directions, ε_1 forms an angle of 45° to the decollement plane (Figure 4.19 D). and we find that a substantial difference between stress and strain directions developed.

An example of changing relationship between stress and strain due to the

stress rotation in area 2, is illustrated in Figure 4.19. Before 1975 the greatest principal stress was oriented nearly horizontal and the strain was released on the reverse faults and consequently stress and strain were coaxial (Figure 4.19 A). In the period 1975-1979, the relationship between stress and strain did not change for earthquakes with magnitude M<7. σ_1 remained horizontal, unaffected by the occurrence of the Kalapana earthquake, and the strain released by the earthquakes with M<7 was on the reverse faults (Figure 4.19 B). In 1979, The greatest principal stress orientation changed from nearly horizontal to a plunge of 45° as a response to magma movements in the rift zone but the reverse faults kept releasing the strain, thus maintaining a constant orientation of the greatest principal strain (ε_1) nearly horizontal at an angle of 54° which is within 10° from the optimal orientation of 45° (Figure 4.19 C). We conclude that the change in stress orientation in 1979 caused a significant angular difference of about 40° between σ_1 and ε_1.

These two different cases reveal that the crust in volume 2 is not homogeneous in strength. The decollement which released the strain of the 1975, M=7.2, Kalapana earthquake, acts as a near-frictionless fault plane because prior to the mainshock the greatest principal stress was oriented nearly parallel to it (Figure 4.19 A and B). The reverse faults which released most of the strain during the 1980-1992 period, become less favorably oriented with respect to the greatest principal stress and consequently are considered also weak.

We believe that a high pore pressure, perhaps near-lithostatic, is reducing the normal stress on the decollement and allows this plane to slip freely with almost no

friction. If the pore pressure is also high in the crust surrounding the decollement where the reverse faults are located, one could explain why these faults may still slip after the greatest principal stress became reoriented less favorably with respect to the reverse faults.

In a crustal volume located in the Kaoiki region, about 30 km to the north of the volume studied here, *Wyss et al.* [1992] concluded that the pore pressure must be near-lithostatic to allow failure on strike-slip faults and decollements. *Zoback and Beroza* [1993] also showed that near-lithostatic pore pressure is required in the San Andreas fault (SAF) zone and in the adjacent crust to explain simultaneously the occurrence of strike-slip, normal and reverse faults within a uniaxial stress field acting perpendicular to the San Andreas fault. They conclude that the SAF is moving almost freely without friction. Such a conclusion can be reached for the decollement plane in Hawaii, which is able to slip while the greatest principal stress is nearly parallel to the decollement (Figure 4.19, top and center) implying that the shear stress resolved on this plane is low. If the decollement plane is frictionless, then the greatest principal stress can be oriented anywhere from horizontal to vertical. Evidence for a vertical principal stress has been shown by *Gillard et al.* [1992] in western Hawaii where major to large earthquakes also rupture the decollement plane [*Beisser et al.*, 1992]. In the south flank, the plunge of the greatest principal stress varies from nearly horizontal to a plunge of 64° as seen in this study.

10. CONCLUSIONS

1. A mixture of decollement, reverse and normal fault plane solutions characterizes the faulting in the south flank of Kilauea, Hawaii. The decollements are present throughout the south flank. Both normal and reverse fault plane solutions are mainly concentrated east of longitude 155° 10' W.

2. A single stress tensor orientation is compatible with all of the heterogeneous faulting observed in the south flank of Kilauea with an average misfit of 5.8°. However, subdividing the data as a function of space and time we find that the misfit is reduced significantly in some subsets, allowing the resolution of 20° differences in stress directions. Thus the stress field inferred from the inversion of the focal mechanism data is not homogeneous but varies as a function of time and space in the south flank of Kilauea. On average, the azimuth of the greatest principal stress is oriented approximately SE but its plunge changes as a function of time and space between 0° and 64°.

3. Average misfits between 3.0° and 6.0° were obtained in most subvolumes where inversions were performed separately, suggesting that the stress tensor was homogeneous within them.

4. The only significant temporal change of stress tensor orientation we found, occurred in 1979 and exceeded 20°. We interpret it as due to the unusually frequent intrusions in the east rift zone during 1975-1981. Based on our data, we suggest that the magma intrusions (in 1979 and after) may have extended to depths of about 10 km.

5. Changes in the style of faulting in the south flank of Kilauea were detected as a function of time. Slip on a decollement plane in the large Kalapana earthquake of 1975 (M=7.2) resulted in the appearance of normal faults in its backward quadrant where an extensional local stress regime was induced. The percentage of failure on reverse faults was higher from 1972 to 1983 than afterward. We interpret this as a consequence of a rotation of the stress tensor, starting in 1979, from an optimal to a less favorable orientation for faulting on the reverse faults. At the same time, this rotation changed the geometry for decollement faulting from unfavorable to optimal, resulting in an increase of the percentage of decollement earthquakes.

6. Based on our test of choice of fault planes and other independent observations, we propose that for the reverse faults planes oriented approximately parallel to the rift and dipping at 60° to 70° are the planes of faulting. For the normal faults, the planes approximately parallel to the rift and dipping at 40° to the southeast are proposed as the fault planes. Based on overwhelming independent observations, we proposed that the nearly horizontal plane is the fault plane for the decollement-type focal mechanisms.

7. Large earthquakes ($5 \leq M < 7$) occurring in Kilauea's south flank are almost exclusively generated on reverse faults. Based on the results of the choice of fault planes we propose that the June 26, 1989, M=6.2, Kilauea south flank earthquake happened on a reverse fault striking at 49° parallel to the rift and dipping southeast at 63°. However, the largest earthquakes ($M \geq 7$) occur on

the decollement plane. This is the only tectonic feature in Hawaii large enough to generate earthquakes with M>7.

8. The greatest principal strain released by events with magnitude M<7 is oriented southeast in most parts and at most times, but its dip changes as a function of space suggesting that different types of faulting are dominant as a function of space in the south flank. East of longitude 155° 10' W, the strain is released on reverse and decollement faults whereas west of this longitude, the strain is released mostly on the decollement. The inclusion of the Kalapana, M=7.2, mainshock in the strain calculation for each subvolume results in a maximum principal strain oriented southeast at 45° to the decollement.

9. Differences between stress and strain vary as a function of time and space in the south flank. In one crustal volume east of longitude 155° 10' W, the difference between stress and strain orientation was produced by a shift of seismic activity from reverse faults (prior to 1975) to decollement at the time of the Kalapana, M=7.2, earthquake. Before the mainshock stress and strain were nearly horizontal and parallel and the strain was released principally on the reverse faults. At the time of the mainshock, the stress did not change orientation but all the strain was released on the decollement.

10. We conclude that the reverse faults and the decollement are weak faults which can slip under low shear stress. The strain was released on the decollement during the M=7.2 Kalapana earthquake while the greatest principal stress was nearly horizontal in the volume of the crust where this event was located.

Such an unfavorable orientation for failure may imply that high pore pressure, perhaps nearly lithostatic, is prevalent within the decollement fault zone and allows near-frictionless slip by reducing the normal stress on the fault. High pore pressure may also be present in the crust surrounding the decollement where the reverse faults are located. This allows these faults to slip after they became less favorably oriented with respect to the greatest principal stress due to the change in stress orientation which occurred in 1979.

Acknowledgments. We thank John Gephart for his computer codes and advice, and H. Pulpan for his thorough review of the manuscript. D. Christensen, S. McNutt, and W. Harrison made helpful comments on the manuscript. We also thank the staff of the Hawaiian Volcano Observatory for their help and assistance in the retrieval of the data and for their hospitality during the stay of one of the author (D. G.) in Hawaii. D. Gillard was supported by NSF grant EAR-9118086 and M. Wyss was supported by the Wadati endowment at the Geophysical Institute of the University of Alaska.

11. REFERENCES

Ando, M., The Hawaii earthquake of November 29, 1975: low-angle normal fault due to forceful injection of magma, *J. Geophys. Res., 84*, 7616-7626, 1979.

Arnadottir, T., and P. Segall, A fault model for the 1989 Kilauea south flank earthquake from leveling and seismic data, *Geophys. Res. lett., 18*, 2217-2220, 1991.

parameters from sparse data sets: Test of the methdod and application to the 1951 (M=6.9), Kona, Hawaii, earthquake, *J. Geophys. Res.*, submitted, 1992.

Bryan, C. J., and C. E. Johnson, Block tectonics of the island of Hawaii from a focal mechanism analysis of basal slip, *Bull. Seismol. Soc. Am., 81*, 491-507, 1991.

Bryan, C. J., A possible triggering mechanism for large Hawaiian earthquakes derived from analysis of the 26 June 1989 Kilauea south flank sequence, *Bull. Seimol. Soc. Am., 82*, 2368-2390, 1992.

Chen, W. P., J. Nabalek, and M. A. Glennon, Source parameters of the June 26, 1989 Hawaiian earthquake, *Eos Trans. AGU, 71*, 562, 1990.

Chiu, J. M., A. C. Johnston, and Y. T. Yang, Imaging the active faults of the central New Madrid seismic zone using PANDA array data, *Seism. Res. Letters, 63*, No. 3, 375-393, 1992.

Crosson, R. S., and E. T. Endo, Focal mechanisms of earthquakes related to the 29 November 1975 Kalapana, Hawaii, earthquake: the effect of structure models, *Bull. Seismol. Soc. Am., 71*, 713-729, 1981.

Crosson, R. S., and E. T. Endo, Focal mechanisms and locations of earthquakes in the vicinity of the 1975 Kalapana earthquake aftershock zone 1970-1979: Implication for tectonics of the south flank of Kilauea Volcano, island of Hawaii, *Tectonics, 1*, 495-542, 1982.

Dahlen, F. A., Single-force representation of shallow landslide sources, *Bull. Seismol. Soc. Am., 83*, 130-143, 1993.

Delaney, P. T., R. S. Fiske, A. Miklius, and A. T. Okamura, Deep magma body beneath the summit and rift zones of Kilauea Volcano, Hawaii, *Science, 247*, 1265-1372, 1990.

Delaney, P. T., M. Wyss, P. W. Lipman, and A. T. Okamura, Comment on "Precursors to the Kalapana M=7.2 earthquake" by Max Wyss, F. W. Klein, and Arch C. Johnston, *J. Geophys. Res., 97*, 4839-4841, 1992.

Delaney, P. T., A. Miklius, T. Arnadottir, A. T. Okamura, and M. Sato, Motion of Kilauea Volcano during sustained eruption from the Puu'Oo and Kupaianaha vents, 1983-1991, *J. Geopys. Res., 98*, 17801-17820, 1993.

Dieterich, J. H., Growth and persistence of Hawaiian volcanic rift zones, *J. Gophys. Res., 93*, 4258-4270, 1988.

Dvorak, J. J., A. T. Okamura, and J. H. Dieterich, Analysis of surface deformation data, Kilauea volcano, Hawaii, October 1966 to September 1970, *J. Geophys. Res., 88*, 9295-9304, 1983.

Dvorak, J. J., and W. R. Tanigawa, Generation of earthquake swarms along the south flank of Kilauea volcano, Hawaii, *Eos Trans. AGU, 66*, 851-852, 1985.

Dvorak, J. J., A. T. Okamura, T. T. English, R. Y. Koyanagi, J. S. Nakata, M. K. Sako, W. R. Tanigawa, and K. M. Yamashita, Mechanical response of the south flank of Kilauea Volcano, Hawaii, to intrusive events along the rift zones, *Tectonophysics, 124*, 193-209, 1986.

Dzurisin, D., R. Y. Koyanagi, and T. T. English, Magma supply and storage at Kilauea Volcano, Hawaii, 1956-1983, *J. Volcanol. Geotherm. Res., 21*, 177-206, 1984.

Eissler, H. K., and H. Kanamori, A single-force model for the 1975 Kalapana, Hawaii, earthquake, *J. Geophys. Res., 92*, 4827-4836, 1987.

Endo, E. T., *Seismotectonic framework for the southeast flank of Mauna Loa, Hawaii,* Ph.D. thesis, Univ. of Wash., Seattle, 1985.

Furomoto, A. S., and R. L. Kovach, The Kalapana earthquake of November 29, 1975; an intraplate earthquake and its relation to geothermal processes, *Phys. Earth Planet. Int., 18*, 197-208, 1979.

Gephart, J. W., and D. W. Forsyth, An improved method for determining the regional stress tensor using earthquake focal mechanism data: application to the San Fernando earthquake sequence, *J. Geophys. Res., 89*, 9305-9320, 1984.

Gillard, D., M. Wyss, and J. S. Nakata, A seismotectonic model for western Hawaii based on stress tensor inversion from fault plane solutions, *J. Geophys. Res., 97*, 6629-6641, 1992.

Gillard, D., and M. Wyss, Comparison of strain and stress tensor orientation: application to Iran and southern California, *J. Geophys. Res.*, submitted, 1993.

Harvey, D., and M. Wyss, Comparison of a complex rupture model with the precursor asperities of the 1975 Hawaii M_S=7.2 earthquake, *Pageoph, 124*, 957-973, 1986.

Hill, D. P., and J. J. Zucca, Geophysical constraints on the structure of Kilauea and Mauna Loa volcanoes and some implications for seismomagmatic processes, *U. S. Geol. Surv. Prof. Pap., 1350*, 903-917, 1987.

Klein, F. W., A linear gradient crustal model for south Hawaii, *Bull. Seismol. Soc. Am., 71*, 1503-1510, 1981.

Klein, F. W., R. Y. Koyanagi, J. S. Nakata, and W. R. Tanigawa, The seismicity of Kilauea's magma system, Volcanism in Hawaii, edited by R. W. Decker, T. L. Wright, and P. H. Stauffer, *U.S. Geol. Surv. Prof. Pap., 1350*, 1019-1186, 1987.

Kostrov, B. V., The theory of the focus for tectonic earthquakes, *Izv. Acad. Sci., USSR Phys. Solid Earth, 4*, 84-101, 1970.

Kostrov, B. V., Seismic moment and energy of earthquakes and seismic flow of rock, *Izv. Acad. Sci., USSR Phys. Solid Earth, 1*, 23-44, 1974.

Lipman, P. W., J. P. Lockwood, R. T. Okamura, D. A. Swanson, and K. M. Yamashita, Ground deformation associated with the 1975 magnitude 7.2 earthquake and resulting changes in activity of Kilauea volcano, Hawaii, *U. S. Geol. Surv. Prof. Pap., 1276*, 1-45, 1985.

McKenzie, D. P., The relation between fault plane solutions for earthquakes and the direction of the principal stresses, *Bull. Seismol. Soc. Am., 59*, 591-601, 1969.

Michael, A. J., Use of focal mechanisms to determine stress: a control study, *J. Geophys. Res., 92*, 357-368, 1987.

Okubo, P., J. Nakata, A. Tomori, and W. Tanigawa, Delineation of large-scale seismotectonic structures in Hawaii, *Eos Trans. AGU, 73*, 512, 1992.

Reasenberg, P., and D. Oppenheimer, FPFIT, FPPLOT, and FPPAGE: Fortran computer programs for calculating and displaying earthquake fault-plane solutions, *U.S. Geol. Surv. Open-File Rept., 85-739*, 109 pp., 1985.

Savage, M. K., and R. P. Meyer, A new model for tectonics of the south flank of Kilauea volcano, Hawaii and for the 1975 M=7.2 Kalapana earthquake: rupture and slide zones in the old oceanic sediment layer, *Eos Trans. AGU, 68*, 1353, 1987.

Swanson, D. L., W. A. Duffield, and R. S. Fiske, Displacement of the south flank of Kilauea volcano: the result of forceful intrusion of magma into the rift zones, *U. S. Geol. Surv. Prof. Pap., 963*, 39 pp, 1976.

Thurber, C. H., and A. E. Gripp, Flexure and Seismicity beneath the south flank of Kilauea volcano and tectonic implications, *J. Geophys. Res., 93*, 4271-4278, 1988.

Tilling, R. I., R. Y. Koyanagi, P. W. Lipmann, J. P. Lockwood, J. G. Moore, and D. A. Swanson, Earthquake and related catastrophic events, Island of Hawaii, November 29, 1975: A preliminary report, *Geol. Surv. Circular 740*, 1976.

Wyss, M., F. W. Klein, and A. C. Johnston, Precursors to the Kalapana M=7.2 earthquake, *J. Geophys. Res., 86*, 3881-3900, 1981.

Wyss, M., A proposed source model for the Great Kau, Hawaii, earthquake of 1868, *Bull. Seismol. Soc. Am., 78*, 1450-1462, 1988.

Wyss, M., and R. L. Kovach, Comment on "A single-force model for the 1975 Kalapana, Hawaii, earthquake" by Eissler, H.K. and Kanamori, H. *J. Geophys. Res., 93*, 8078-8082, 1988.

Wyss, M., and C. Kisslinger, Possible reasons for differences in the aftershock decay rate, *Eos Trans. AGU, 70*, 1207, 1989.

Wyss, M., and R. Y. Koyanagi, Isoseismal maps, macroseismic epicenters and estimated magnitudes of historic earthquakes in the Hawaiian Islands, *U.S. Geol. Surv. Bull., 2006*, 1992.

Wyss, M., B. Liang, W. R. Tanigawa, and X. Wu, Comparison of orientations of stress and strain tensors based on fault plane solutions in Kaoiki, Hawaii, *J. Geophys. Res., 97*, 4769-4790, 1992.

Yin, A., Mechanics of wedge-shaped fault blocks 1. An elastic solution for compressional wedges, *J. Geophys. Res., 98*, 14245-14256, 1993.

Zoback, M. D., M. L. Zoback, V. S. Mount, J. Suppe, J., J. P. Eaton, J. H. Healy, D. Oppenheimer, P. Reasenberg, L. Jones, C. B. Rayleigh, I. G. Wong, O. Scotti, and C. Wentworth, New evidence on the state of stress of the San Andreas fault system, *Science, 238*, 1105-1111, 1987.

Zoback, M. D., and G. C. Beroza, Evidence for near-frictionless faulting in the 1989 (M 6.9) Loma Prieta, California, earthquake and its aftershocks, *Geology, 21*, 181-185, 1993.

Zuñiga, F.R., M. Wyss, and F. Scherbaum, A moment-magnitude relation for Hawaii, *Bull. Seis. Soc. Amer.*, *78*, 370-373, 1988.

Table 4.1. Relationship between Fault Plane Solution Errors and Misfit from Stress Tensor Inversion of the Perturbed Synthetic Set.

Average uncertainty of focal mechanism [deg]	Average change in P and T axes [deg]	Average misfit exact method [deg]	Average difference of σ_1 and σ_3 from best model [deg]	Average misfit approximate method [deg]	$\Delta\sigma_1$ [deg]	$\Delta\sigma_3$ [deg]
5	4	3.0	3	3.8	0	3
10	11	5.7	17	8.2	5	16
15	14	6.0	2	11.5	5	7
20	20	6.6	77	9.6	10	9
30	30	10.7	23	15.8	7	17
40	38	12.0	82	18.5	5	11

$\Delta\sigma_1$, angular difference between σ_1 of the exact and approximate method. $\Delta\sigma_3$, angular difference bewteen σ_3 of the exact and approximate method.

Table 4.2. Stress Tensor Directions Obtained with the Approximate Method as a Function of Time and Space.

Area	Time	Number of events	σ_1		σ_2		σ_3		R	Average misfit [deg]
			PL	AZ	PL	AZ	PL	AZ		
1	1975-1979	55	60	173	13	59	26	322	0.5	9.0
1	1980-1983	8	0	235	56	145	34	325	0.8	2.8
1	1983-1992	47	46	165	2	74	44	342	0.3	6.6
2	1972-1975	22	5	81	7	172	81	317	0.4	4.3
2	1975-1979	111	5	93	23	185	66	351	0.4	8.4
2	1980-1983	67	45	142	8	240	44	338	0.4	4.6
2	1983-1992	198	40	141	6	236	49	333	0.4	5.3
3	1972-1975	13	44	135	42	343	14	240	0.8	5.7
3	1975-1979	30	30	157	6	250	59	350	0.3	4.6
3	1980-1983	33	36	155	1	246	54	338	0.4	4.1
3	1983-1992	102	41	154	1	63	49	332	0.4	2.8
4	1972-1975	16	44	154	11	53	44	312	0.4	8.8
4	1975-1979	15	2	280	88	100	0	10	0.3	5.1
4	1980-1983	13	47	141	14	246	40	348	0.5	1.9
4	1983-1992	60	40	151	2	60	50	328	0.6	3.9
5	1972-1975	23	10	206	75	337	11	114	0.7	9.5

PL, plunge; AZ, azimuth in degrees

Table 4.3. Stress Tensor Directions Obtained with the Exact Method as a Function of Time and Space.

Area	Time	Number of events	σ_1		σ_2		σ_3		R	Average misfit [deg]
			PL	AZ	PL	AZ	PL	AZ		
1	1975-1992	110	64	139	4	238	25	329	0.7	6.0
3	1972-1992	165	36	155	1	246	54	338	0.4	3.6
4	1972-1992	88	41	148	2	57	49	325	0.6	4.1
2	1972-1975	22	5	86	7	177	82	320	0.4	3.6
2	1975-1979	111	7	76	33	170	56	336	0.5	6.5
2	1980-1992	265	45	145	7	242	44	338	0.5	4.5
5	1972-1975	23	7	229	82	60	1	320	0.3	6.5
Entire Set	1972-1992	784	41	150	1	241	49	332	0.4	5.8

PL, plunge; AZ, azimuth in degrees

Table 4.4. Stress Tensor Directions Obtained with the Exact Method as a Function of Depth in Areas 1 and 2.

Area	Depth	Number of	σ_1		σ_2		σ_3		R	Average misfit
	[km]	events	PL	AZ	PL	AZ	PL	AZ		[deg]
1	5.0-8.5	34	72	144	3	244	18	335	0.6	5.6
1	8.5-9.0	53	58	141	7	242	31	336	0.8	4.7
1	9.0-10.5	37	45	194	21	82	37	335	0.1	4.5
2	5.0-9.5	74	5	95	17	187	72	349	0.4	6.4
2	9.5-10.5	39	5	314	34	220	56	51	0.7	5.1

PL, plunge; AZ, azimuth in degrees

Table 4.5. Principal Strain Directions in the South Flank of Kilauea.

Data Set	Time	ε_1		ε_2		ε_3	
		PL	AZ	PL	AZ	PL	AZ
Area 1	1972-1992	61	165	6	64	28	330
Area 2	1972-1975	18	149	1	239	72	332
Area 2	1975-1979	17	115	26	213	59	356
Area 2	1980-1992	11	136	17	230	69	15
Area 3	1972-1992	26	153	14	57	60	301
Area 4	1972-1992	30	134	14	232	57	344
Area 5	1972-1975	52	204	31	62	19	320

PL, plunge; AZ, azimuth in degrees

Table 4.6. Results of Test of Choice of Fault Plane.

Number of	Area 1	Area 2	Area 3	Area 4	Total
reverse faulting	9	81	16	9	115
low angle plane	0	1	14	6	21
steep angle plane	7	62	0	0	69
decollement faulting	22	173	122	55	372
low angle plane	0	21	6	5	32
steep angle plane	5	40	19	13	77
normal faulting	43	3	8	0	64
NE striking plane	11	1	1		13
SW striking plane	3	0	1		4

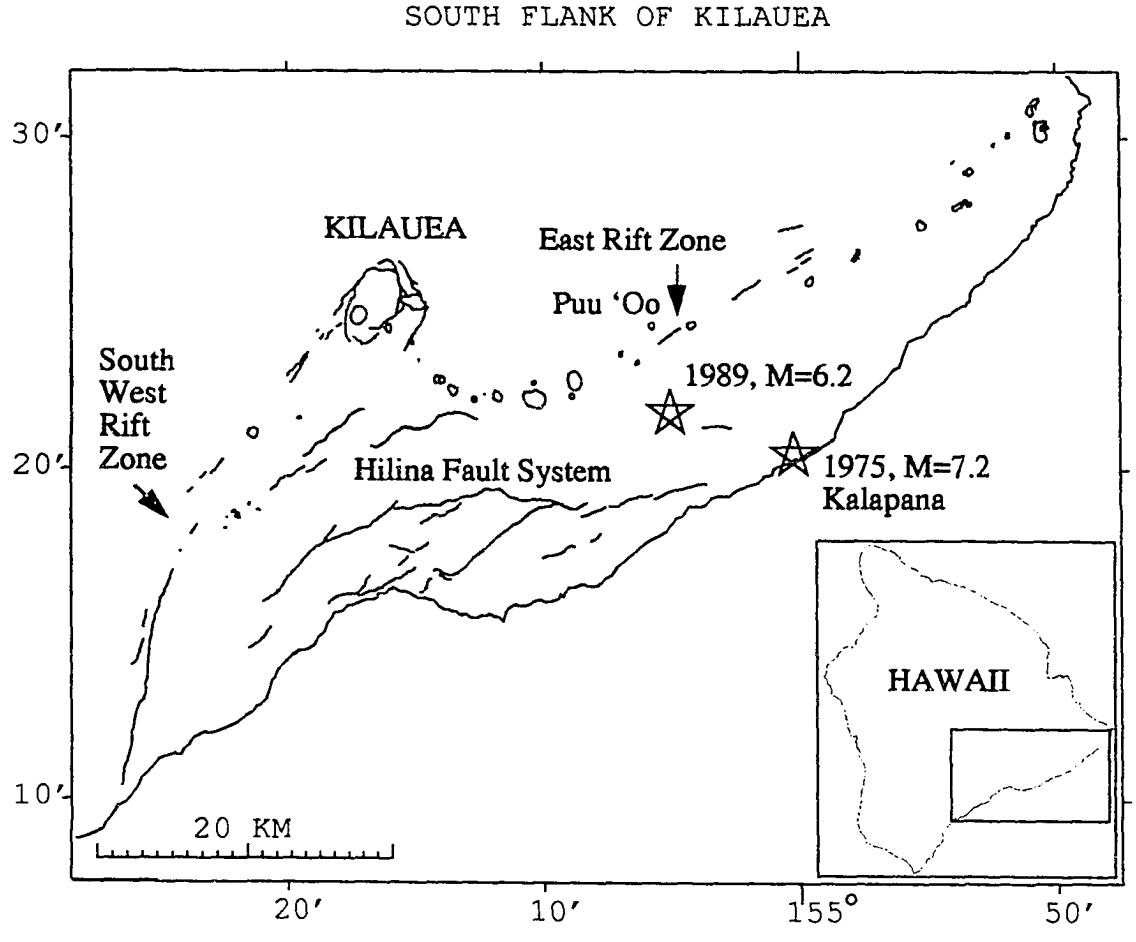

Fig. 4.1. Map of southeastern Hawaii showing the caldera of Kilauea volcano and its rift zones. The epicenters of the two largest earthquakes on Kilauea's south flank are shown by stars. An eruption lasting for many years started in 1983 at Puu'Oo. The south-facing normal fault system of Hilina showed secondary faulting in the 1975 Kalapana earthquake.

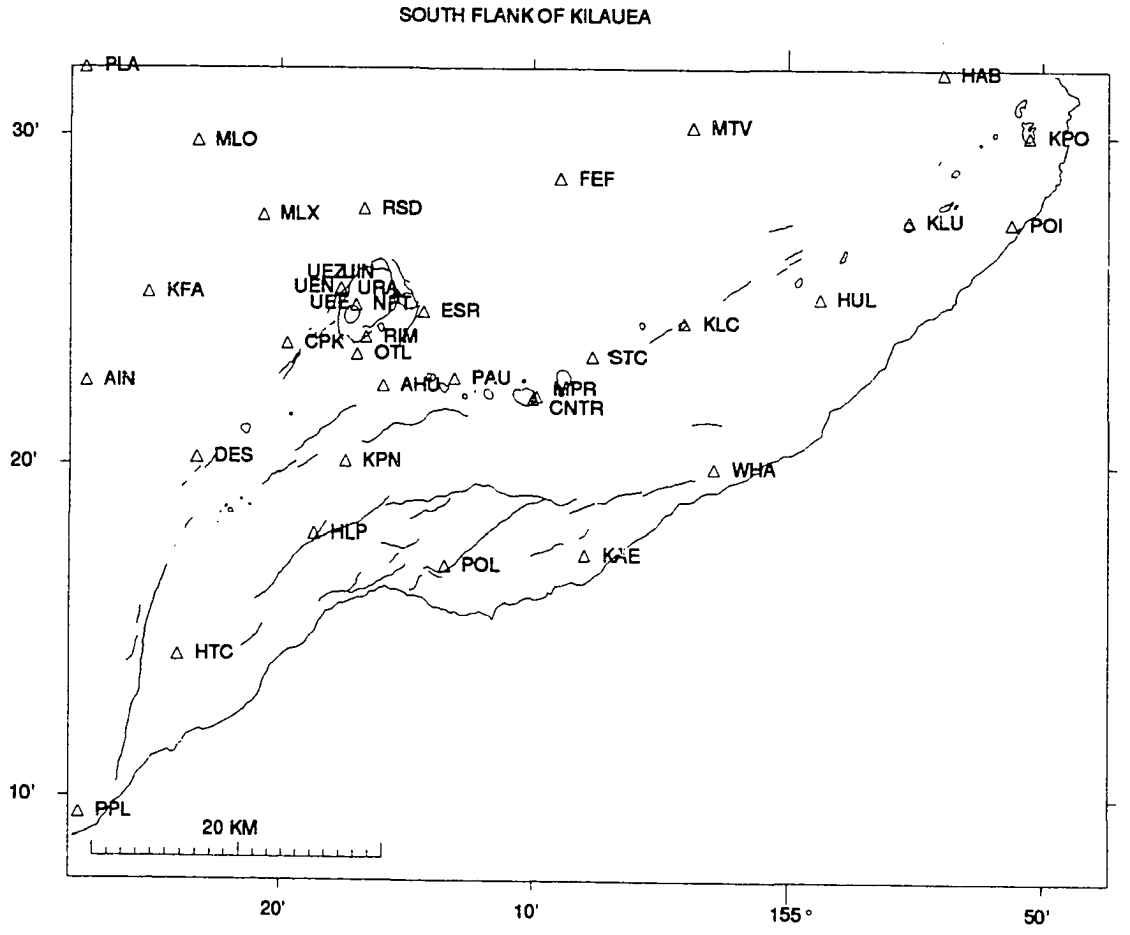

Fig. 4.2. Locations of seismic stations (triangles) on southeastern Hawaii.

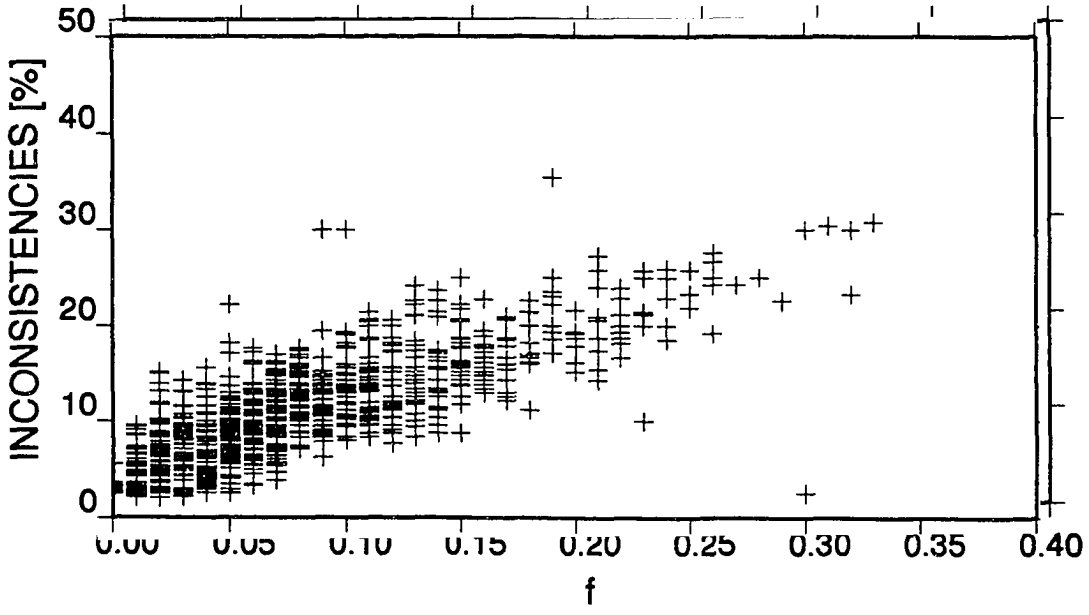

Fig. 4.3. Inconsistent station polarities for the focal mechanisms as a function of the misfit, f, computed by the fault plane solution program.

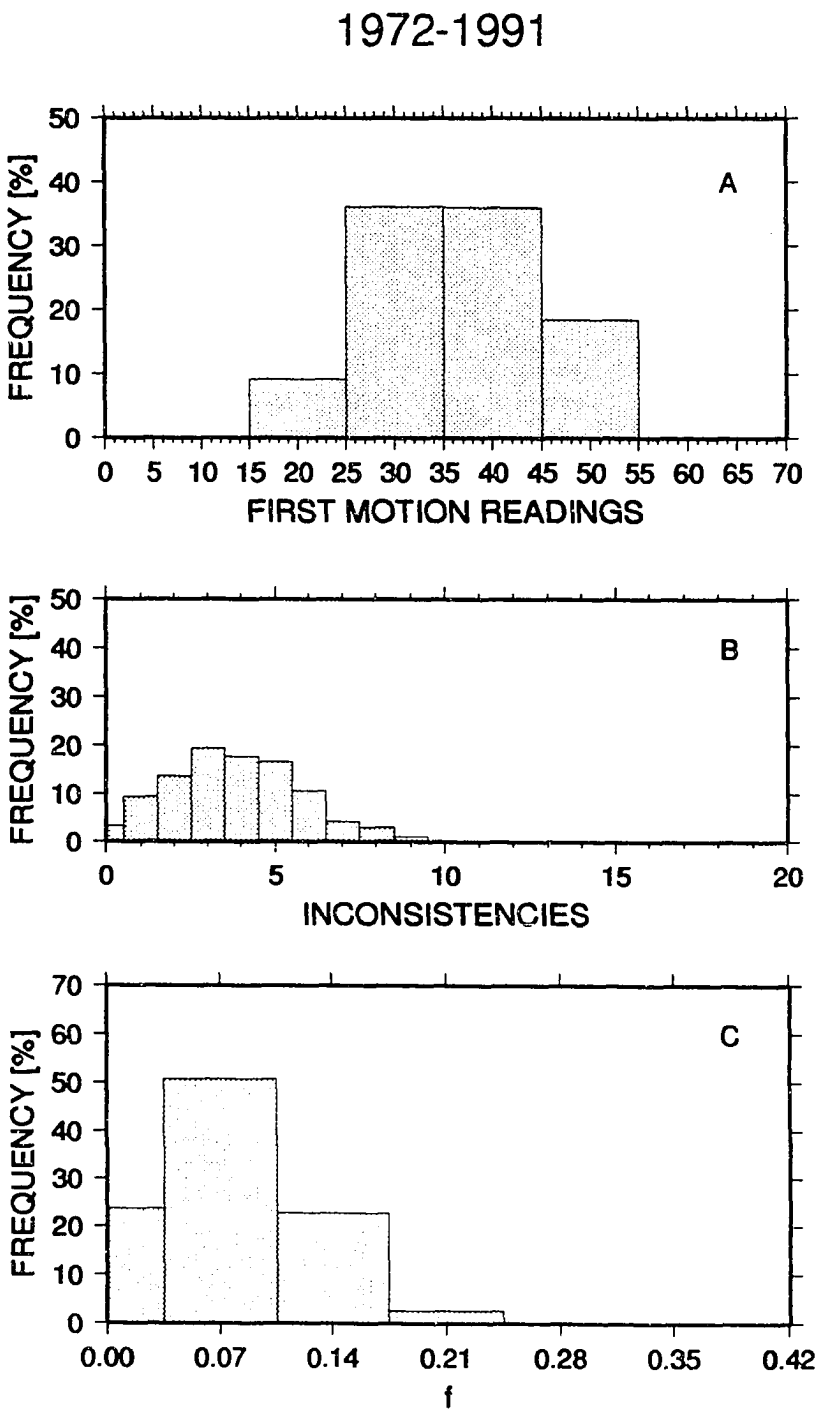

Fig. 4.4. (A) Histograms of the number of first motion readings, (B) of inconsistencies, and (C) of the misfit, f, obtained for each focal mechanism.

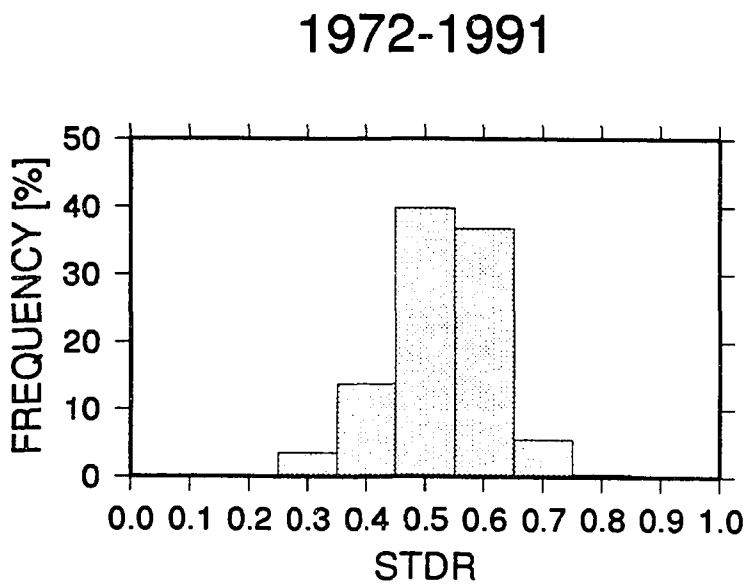

Fig. 4.5. Distribution of the parameter defined as the station distribution ratio (STDR).

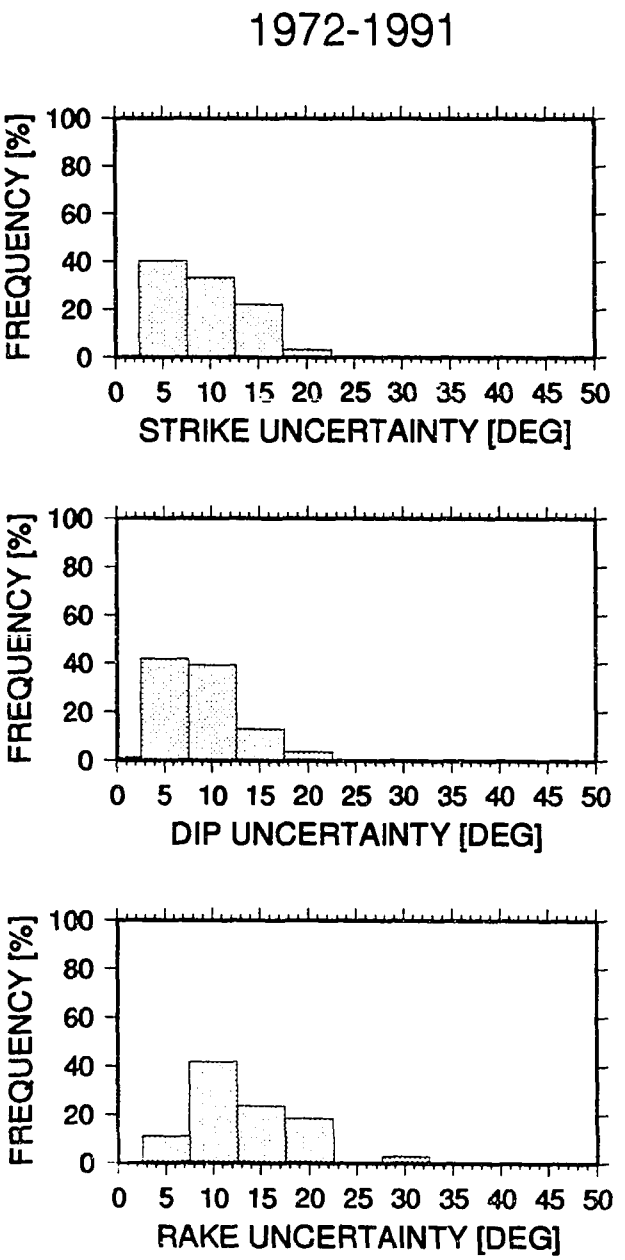

Fig. 4.6. Distribution of the strike (top), dip (center), and rake (bottom) uncertainties for the focal mechanisms.

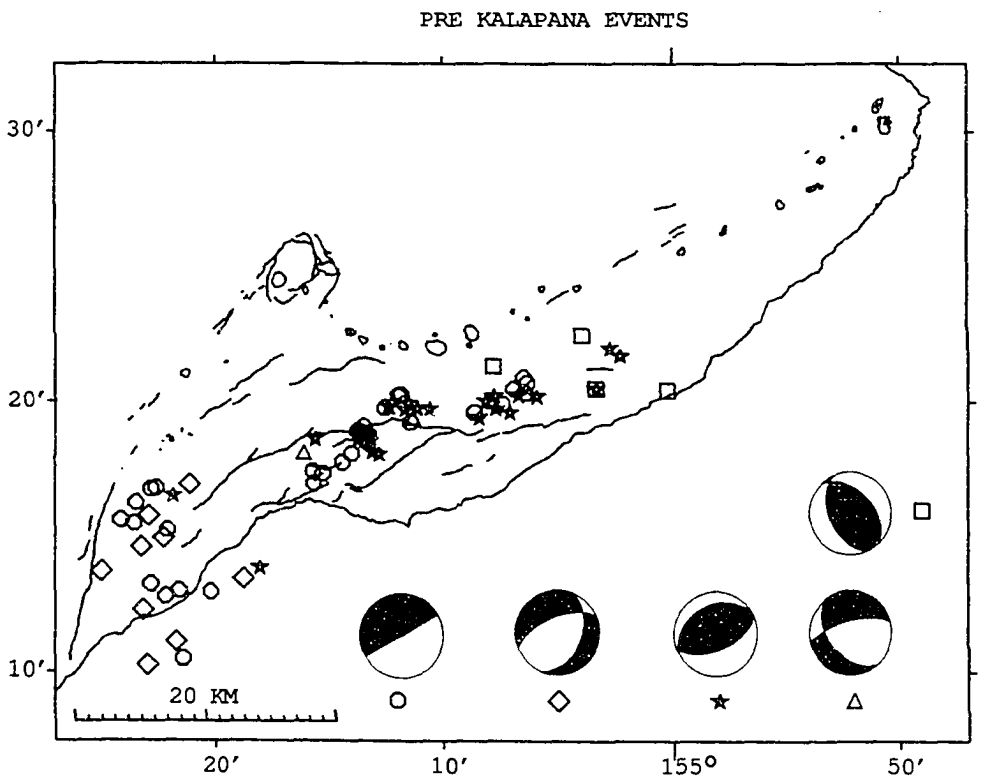

Fig. 4.7. Type of faulting in the south flank of Kilauea in the period 1972 through November 29, 1975 (pre-Kalapana period). The focal mechanisms displayed represent averages of fault plane solutions with similar orientation. A lower hemisphere stereographic projection is used, with the compressional quadrant black. Different symbols mark the epicenters of the respective fault plane solutions.

Fig. 4.8. Type of faulting for the period 1975-1992 (post-Kalapana period). Same plot as Figure 4.7. All decollement solutions are similar (A) whereas the fault plane orientations of the reverse (B) and normal solutions (C) vary. Although the epicenters of the normal faults are concentrated somewhat north of the decollement and reverse activity, all three types of solutions appear to be coeval. Given the available resolution of hypocentral depths, it is uncertain whether different faulting types are separated as a function of depth.

POST KALAPANA EVENTS WITH DECOLLEMENT FOCAL MECHANISMS

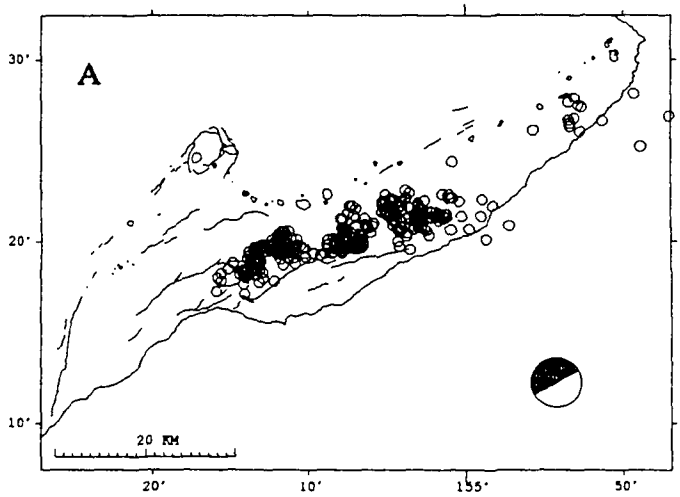

POST KALAPANA EVENTS WITH REVERSE FOCAL MECHANISMS

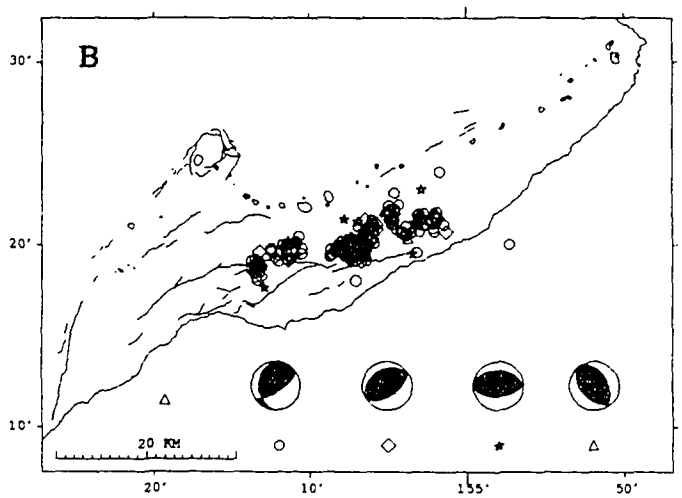

POST KALAPANA EVENTS WITH NORMAL FOCAL MECHANISMS

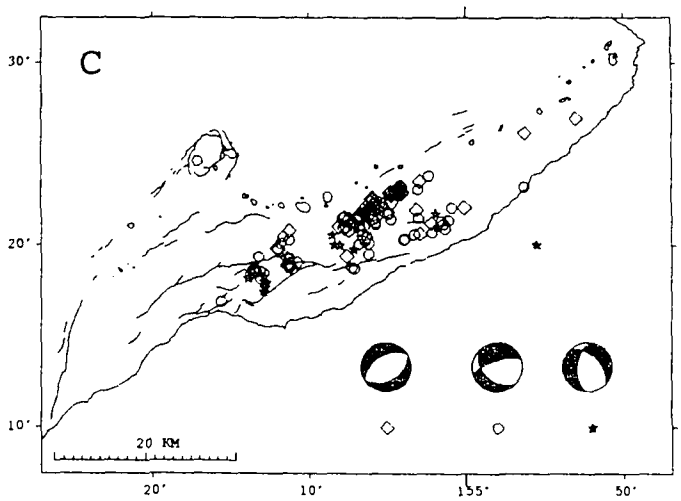

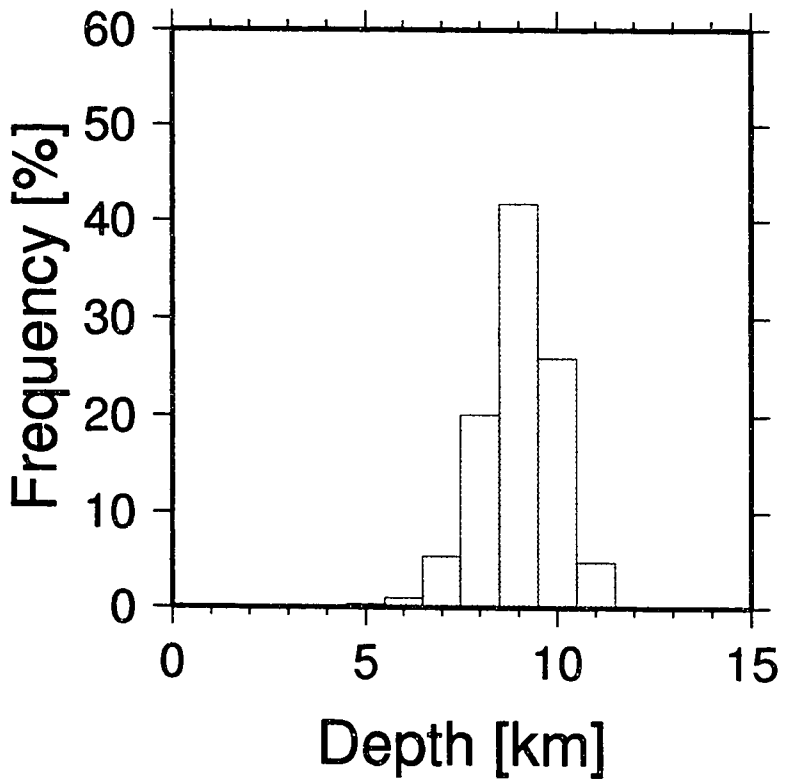

Fig. 4.9. Depth distribution of the earthquakes for which we have focal mechanisms.

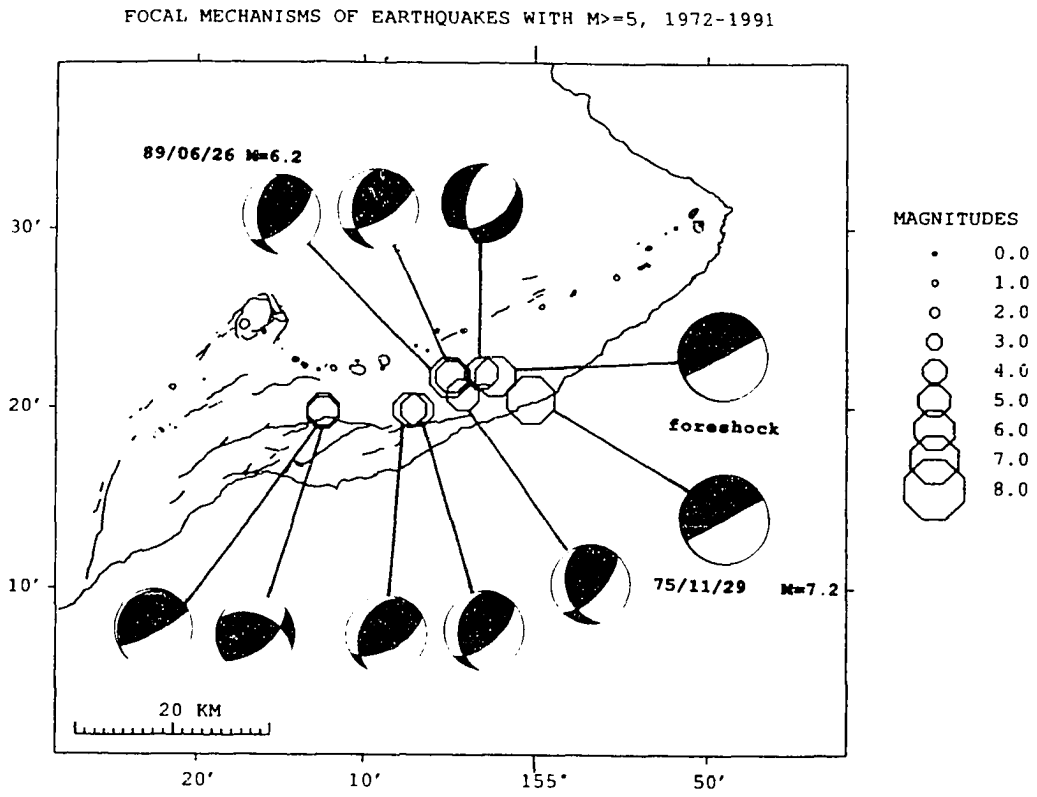

Fig. 4.10. Focal mechanisms and epicenters of earthquakes with magnitude, M≥5, which occurred in the south flank since 1972. The event labeled "foreshock" occurred 50 minutes before the 1975 mainshock.

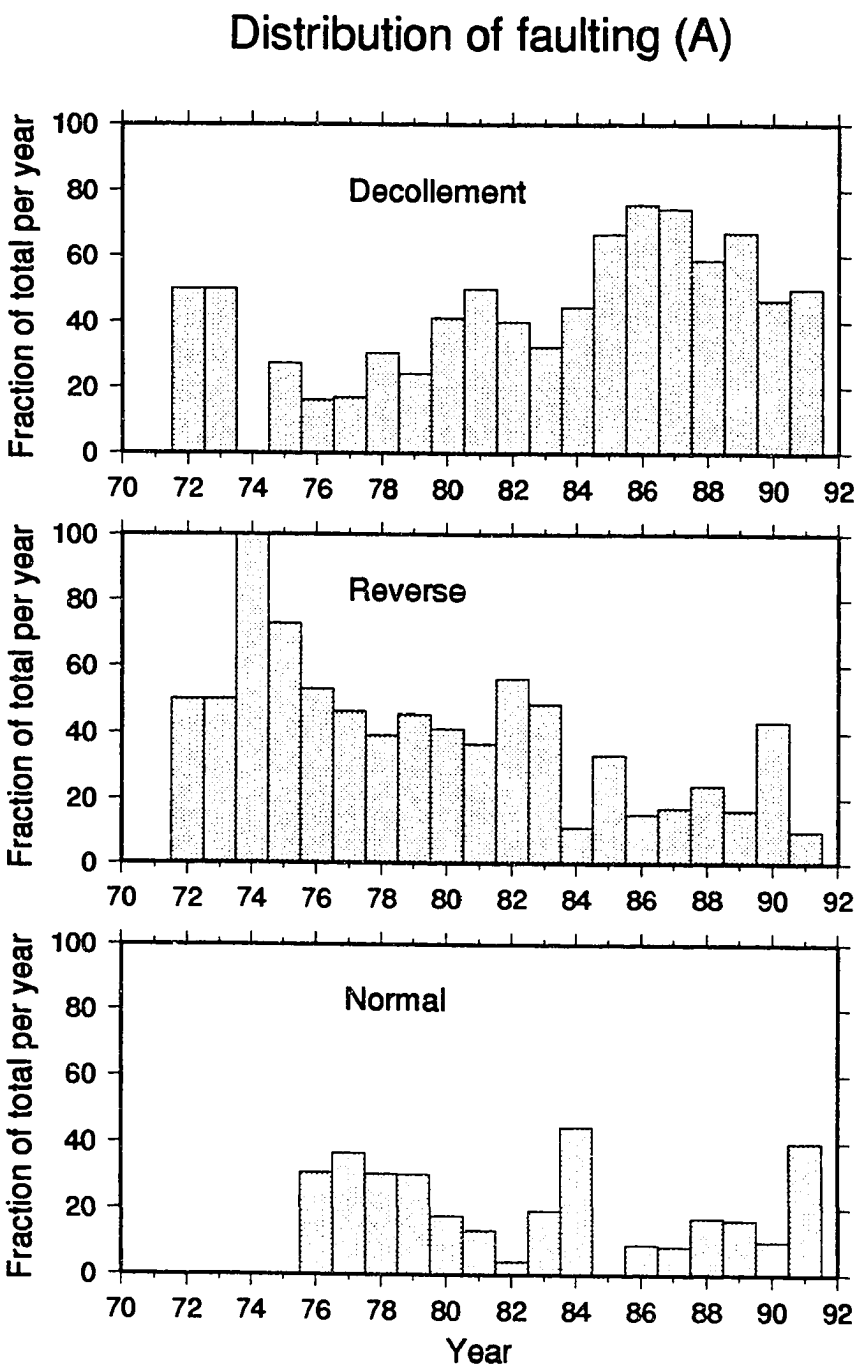

Fig. 4.11. Distribution of faulting as a function of time for earthquakes located east of longitude 155° 10' W (group A). (Top) Decollement, (center) Reverse, (bottom) normal type of fault plane solutions. The bin is one year.

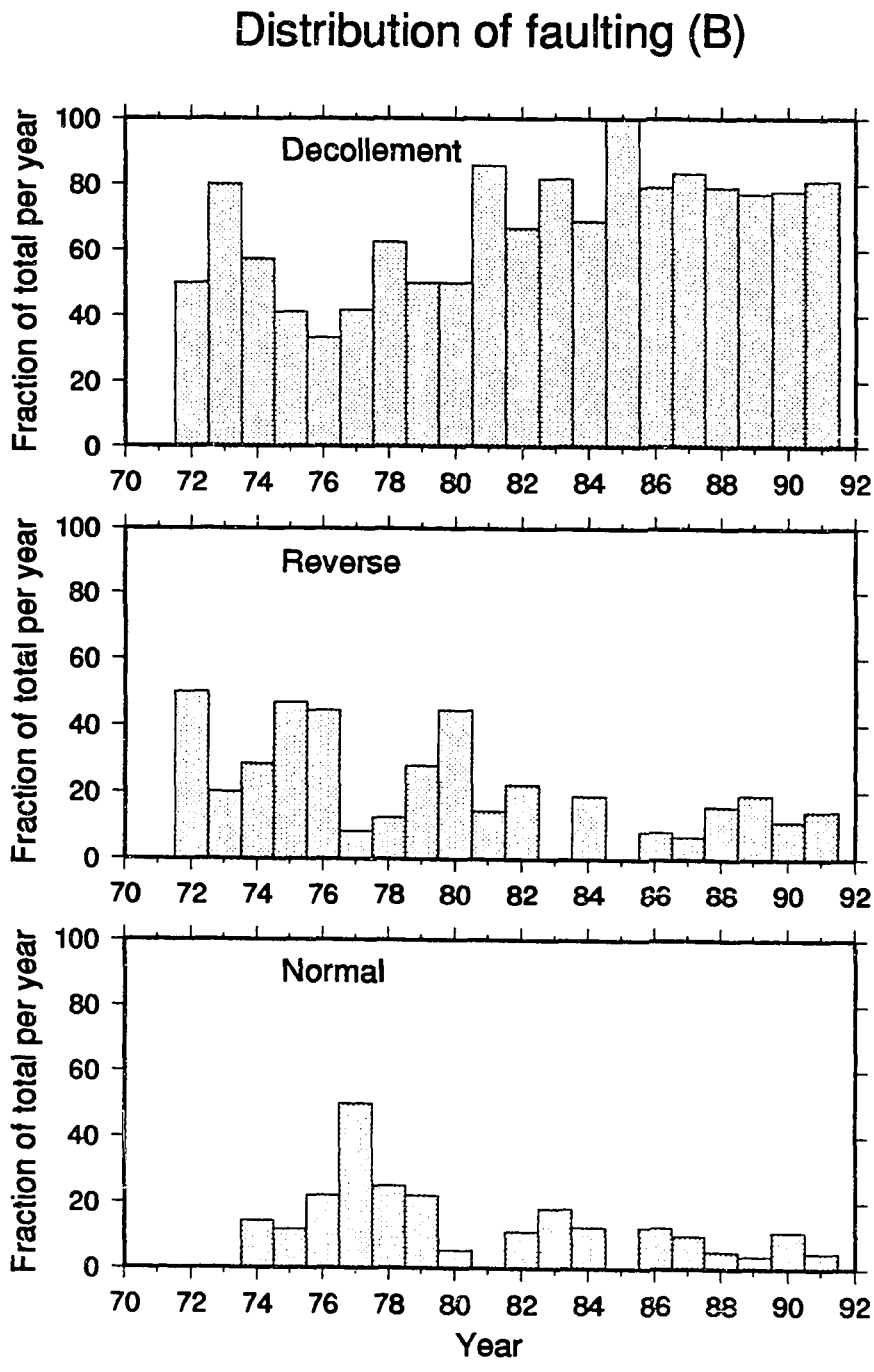

Fig. 4.12 Same plot as Figure 4.11 but for the events located west of 155° 10' W (group B).

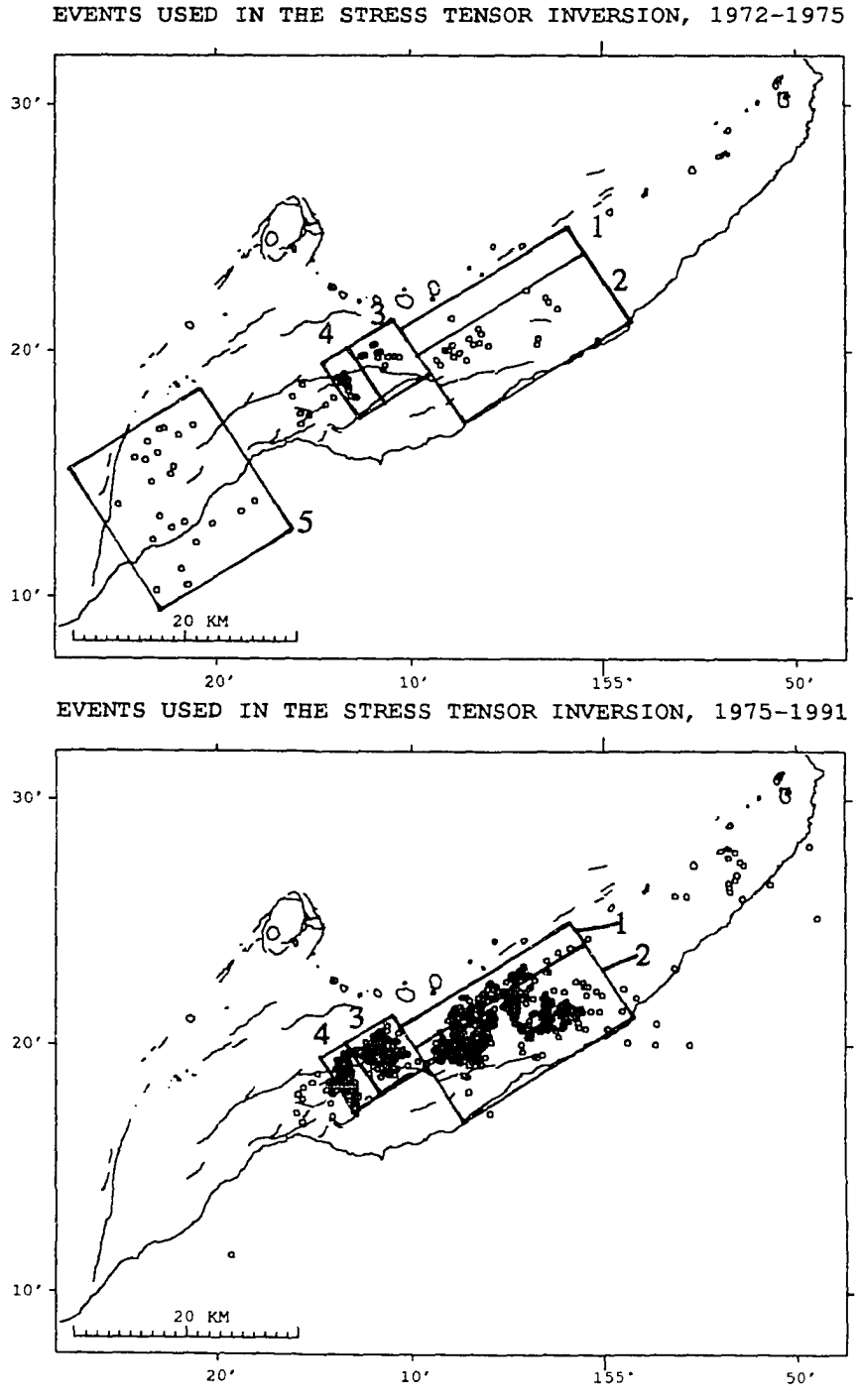

Fig. 4.13. Map of the epicenters of the earthquakes used in the inversion for stress for the period before (top) and after (bottom) the Kalapana 1975 mainshock. The rectangles define the different areas where separate inversions were performed.

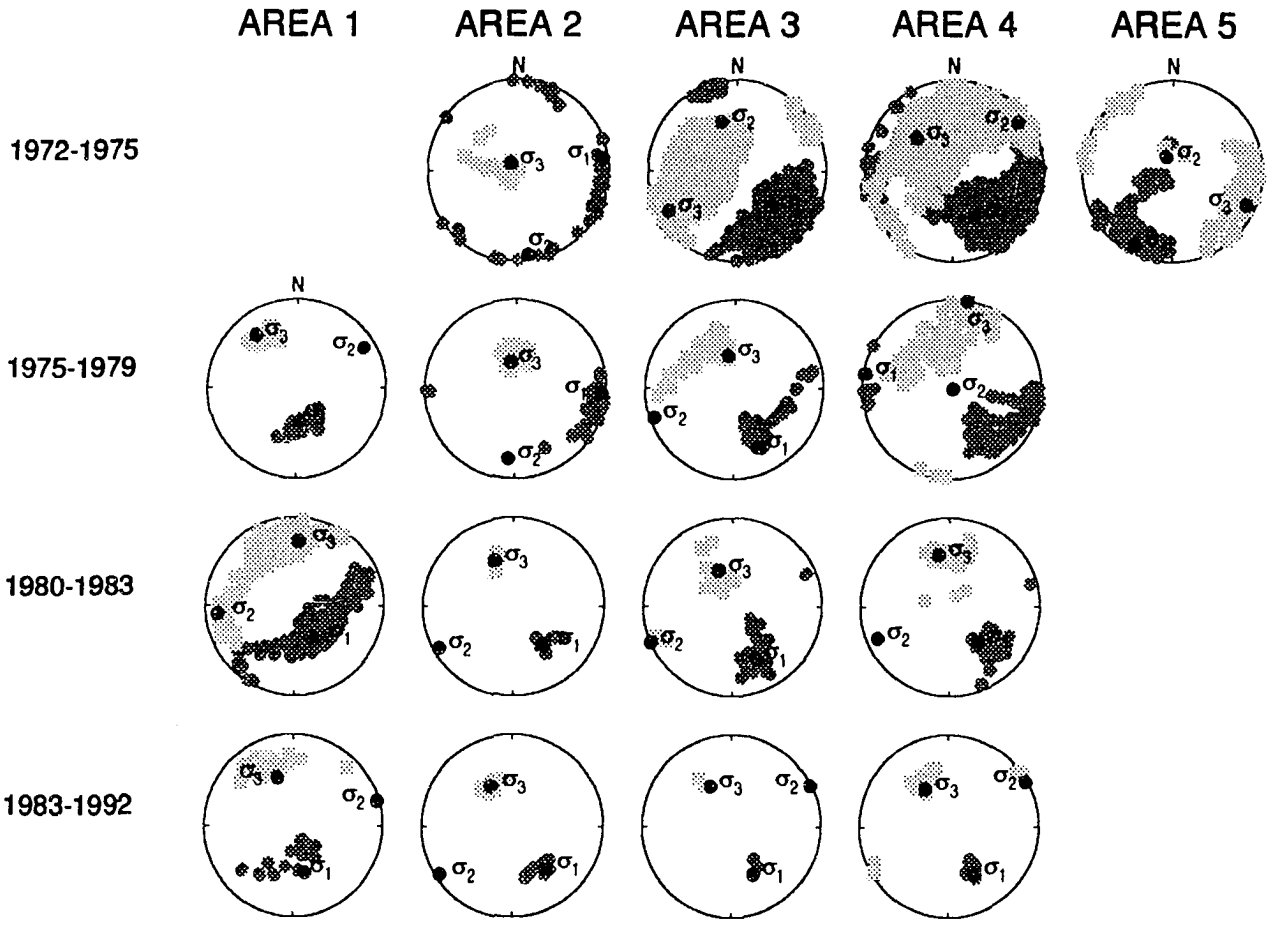

Fig. 4.14. Results of the inversion for stress using the approximate method for the different areas defined in Figure 4.13. Lower hemisphere projections of the best fitting principal stress axes, represented by a solid circle.The orientations of the stress axes falling within the 95% confidence range are shown by dark shaded circles (σ_1) and light shaded squares (σ_3). The 95% confidence limit of σ_2 is not displayed.

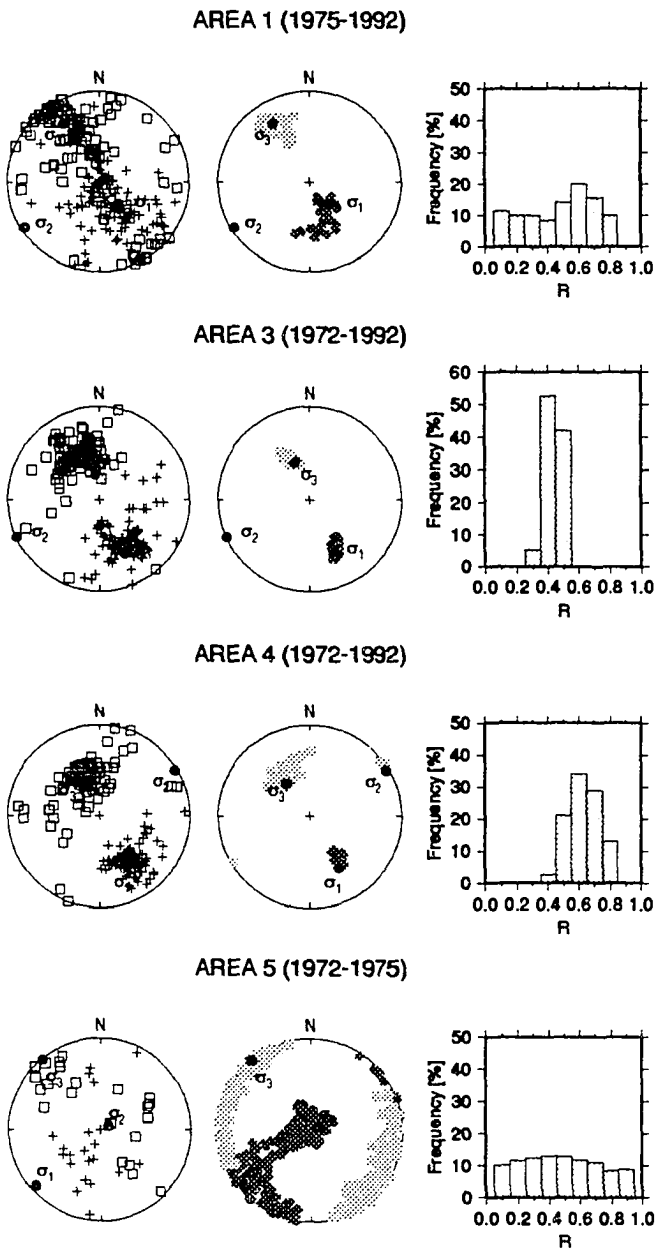

Fig. 4.15. Final results of the stress tensor inversion using the exact method for areas 1, 3, 4, and 5 (period 1972 through 1992). (Left column) Lower hemisphere projection of the P (crosses) and T (squares) axes, with the three principal stresses (dots) corresponding to the best stress model. (Middle column) 95% confidence region for σ_1 (dark gray) and σ_3 (light gray) plotted on a lower hemisphere stereographic projection with the direction of best fitting principal stresses (dots). (Right column) Distribution of R values for the stress models within the 95% confidence region.

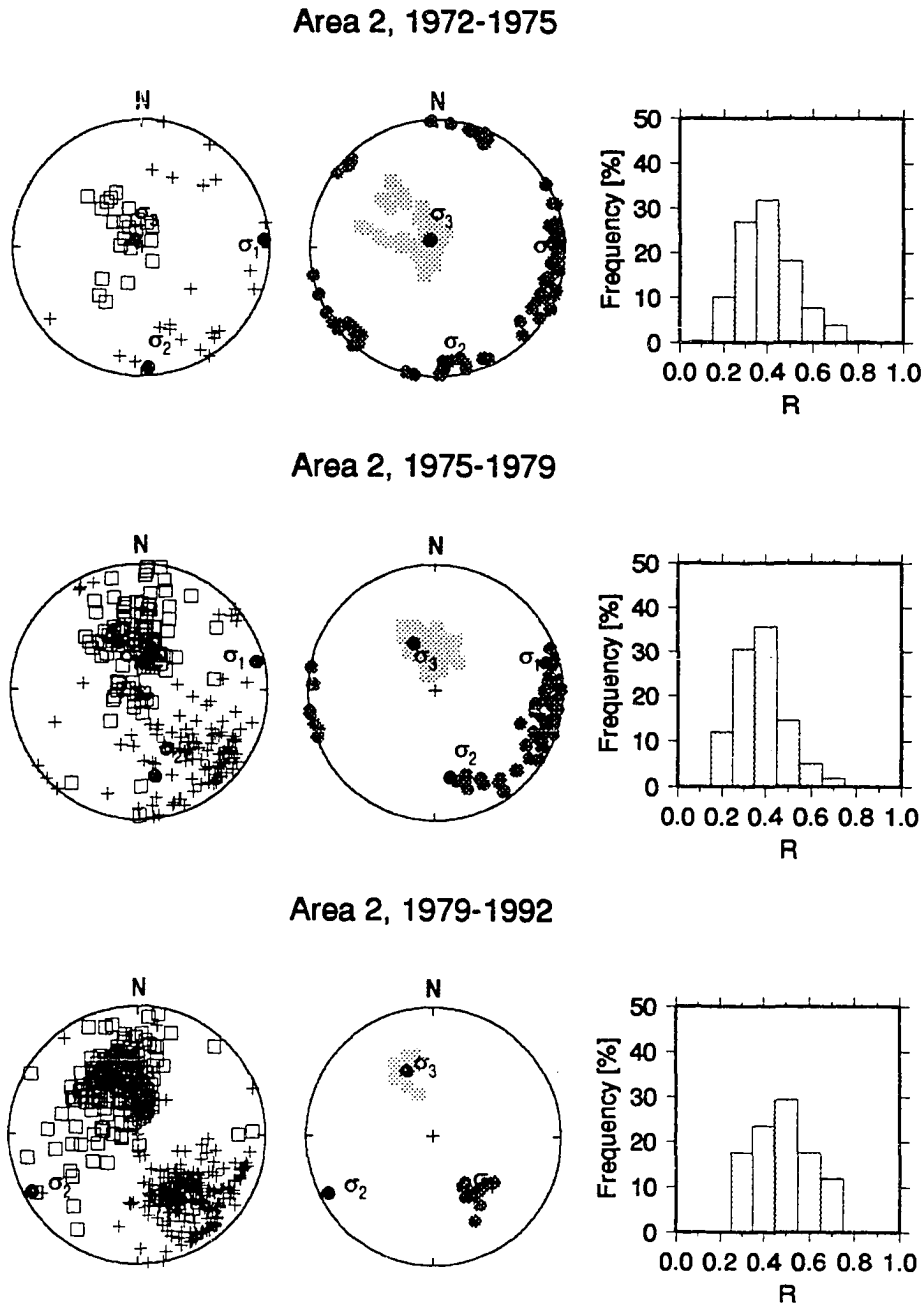

Fig. 4.16. Same plot as Figure 4.15 but for area 2 and as a function of time. Note rotation of σ_1 in 1979.

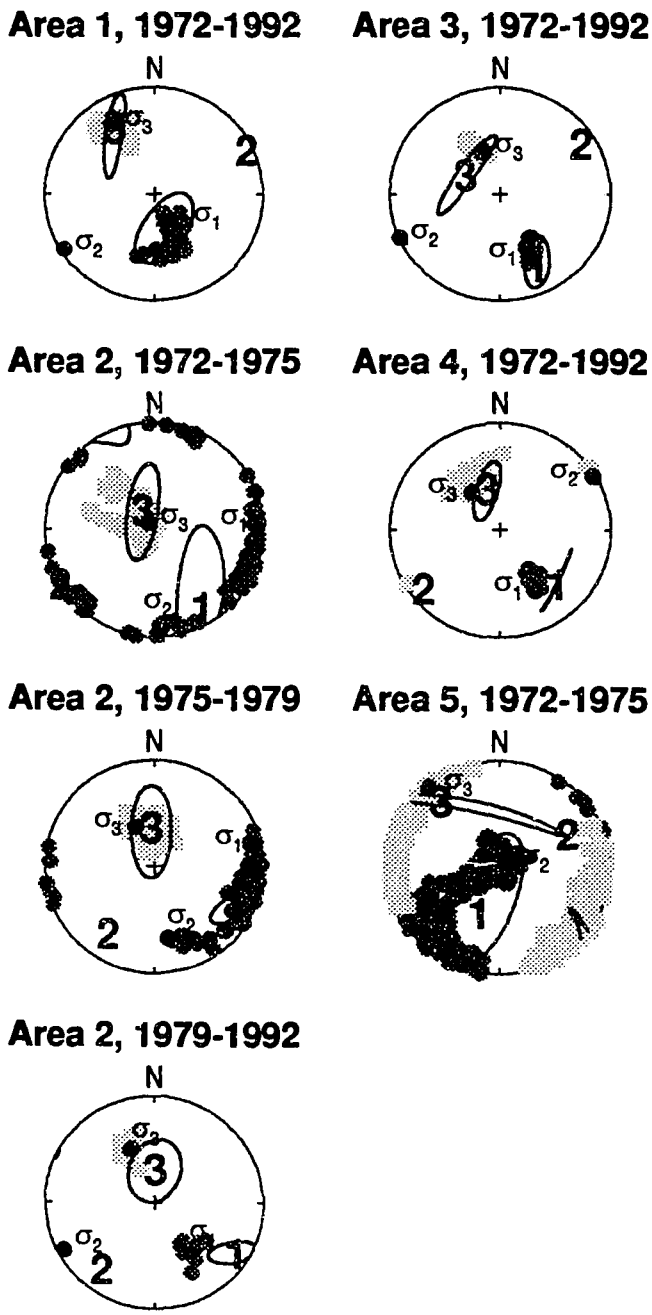

Fig. 4.17. Lower hemisphere projections of the principal strain orientations (numbers: 1=ε_1, 2=ε_2, 3=ε_3) with 95% confidence ellipses. The final results of the stress inversion are also plotted as in Figures 4.15 and 4.16.

Fig. 4.18. Summary of the orientations of the maximum horizontal stress in the south flank of Kilauea as a function of time and space. The length of the arrows is inversely proportional to the dip of the axes. (Top) Before the 1975 Kalapana mainshock the stress directions in the three active volumes point approximately toward the main magma body south of Kilauea's caldera. (Center) During the deflation period of Kilauea's summit that followed the 1975 mainshock normal faulting with slip perpendicular to the east rift zone appeared along this rift zone. (Bottom) A rotation of the stress directions in part of the south flank followed frequent intrusions in the east rift zone which were coupled with renewed inflation of Kilauea's summit. We interpret this observation as indicating an extension of the source of stress from the central magma body below the volcano to the east rift zone segment between the summit and Puu'Oo.

DIRECTIONS OF MAXIMUM HORIZONTAL STRESS

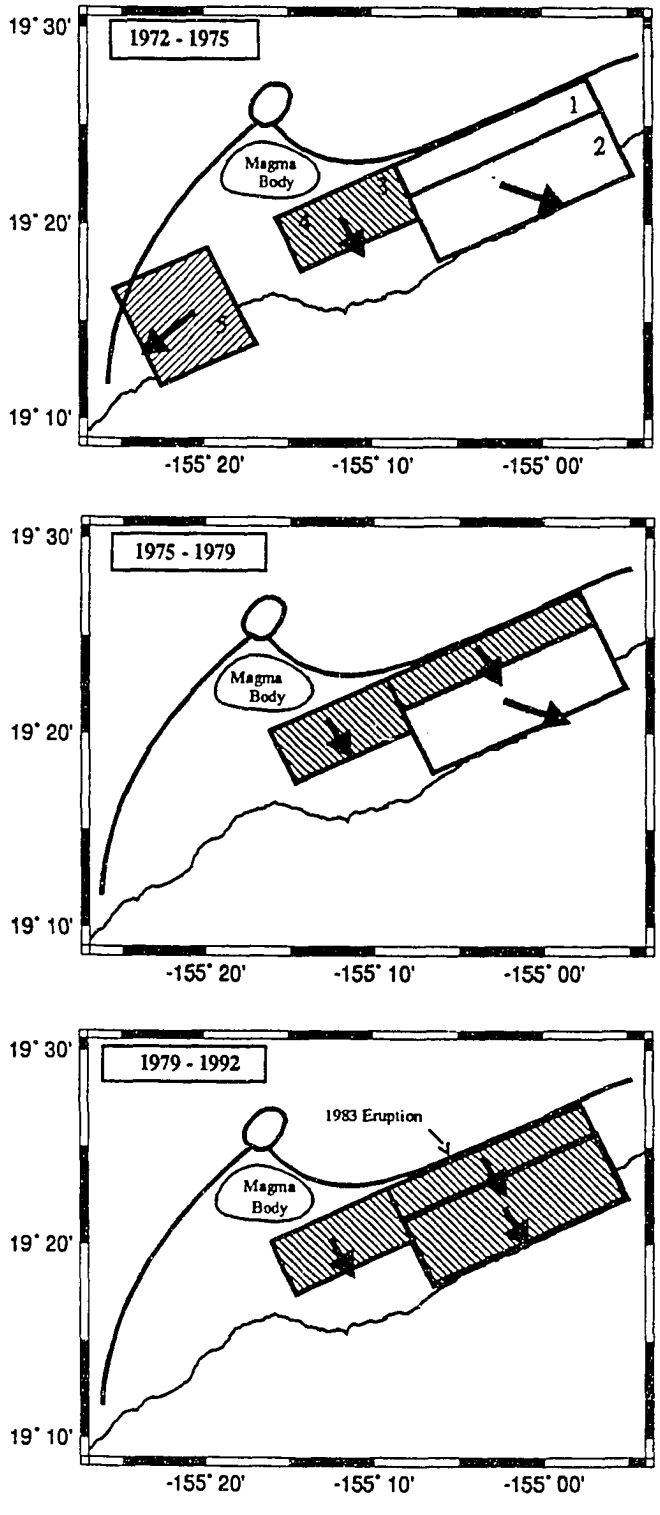

Fig. 4.19. Schematic cross section of the south flank of Kilauea with active faults and greatest principal stress (σ_1, thick arrows) and strain (ε_1, thin arrows) in volume 1 and 2 as a function of time. The strain released by the M=7.2 Kalapana earthquake in 1975 is not considered in frames A, B and C, although it is the dominant major contribution when it is considered (D). The crosses indicates the hypocenter of the Kalapana (M=7.2) earthquake of November 26, 1975. The decollement is indicated by the inclined line at the bottom of the volcanic edifice solid and dashed where faulted and unfaulted, respectively. The assumed subsurface extent of the Hilina Pali fault is marked by the curved thin line.

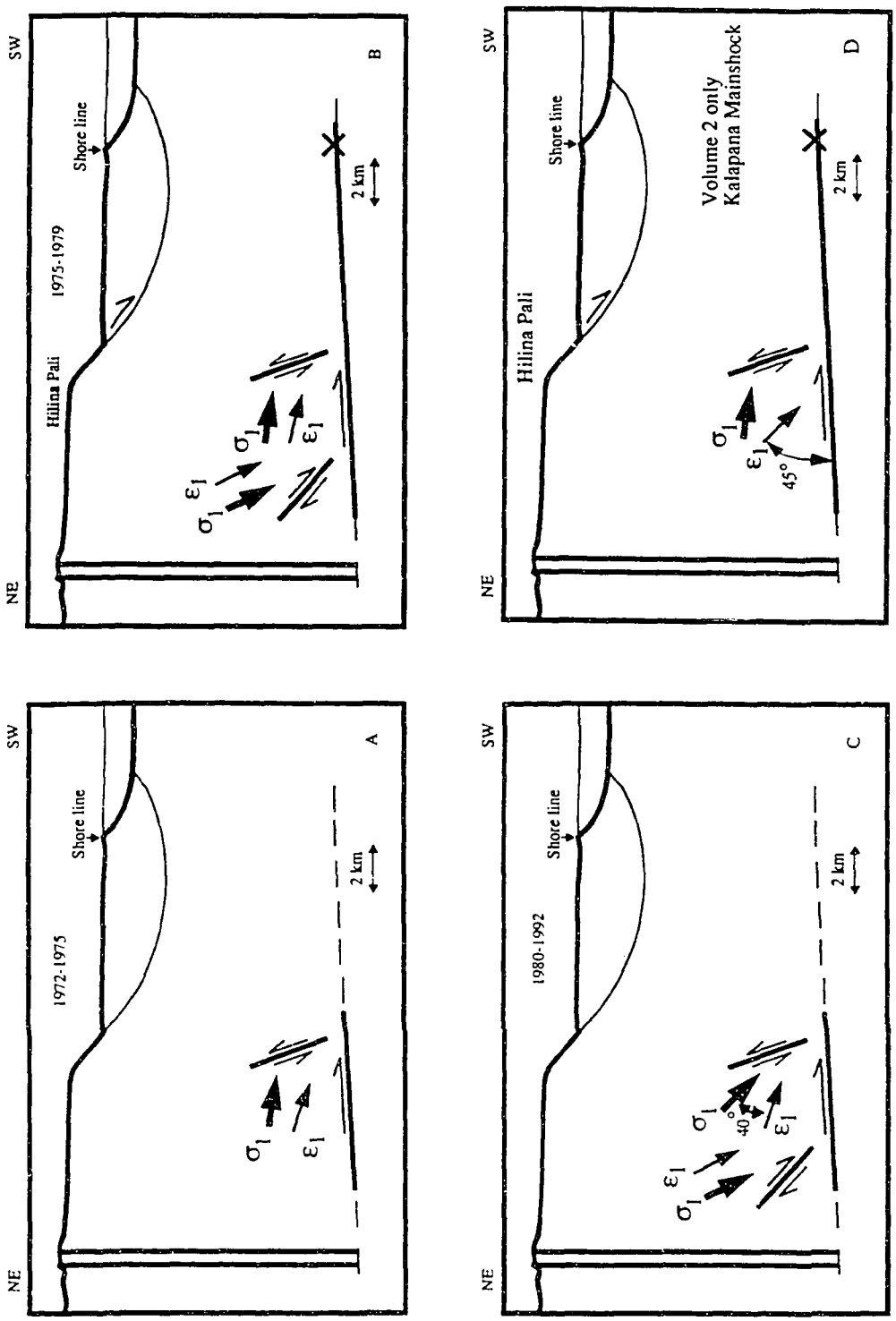

CHAPTER 5

COMPARISON OF STRAIN AND STRESS TENSOR ORIENTATION: APPLICATION TO IRAN AND SOUTHERN CALIFORNIA[1]

1. ABSTRACT

The directions of principal stress were estimated in Iran from 111 focal mechanisms of earthquakes with magnitudes $4.5 \leq M < 8$, using the inversion technique described by *Gephart and Forsyth* [1984]. Three data sets corresponding to areas of 1000 km length and 200 km width located in northern and eastern Iran, as well as Zagros were inverted. After subdividing the data as a function of space, the average misfits decreased by about 2° to values between 2° and 5°. Based on inversion of synthetic data sets, we judge the quality of inversion results as good if the average misfit is less than 6°. Thus, we conclude that the stress directions are homogeneous within the sub areas in Iran but not within all of Iran. Overall, the greatest principal stress is horizontal, approximately parallel to the direction of plate motion, and oriented SW-NE in the subsets of northern and eastern Iran and in central and west Zagros. Differences in the best fitting stress orientations up to 30°

---

[1] Chapter 5 contains the complete text and figures of the manuscript, *A comparison of strain and stress tensor orientation: application to Iran and southern California*, by D. Gillard and M. Wyss, as submitted to the *Journal of Geophysical Research, 1993*.

seem to exist between these areas, but they are not resolvable at the 95% confidence level. For each area where the stress field is homogeneous, we computed the seismically released strain tensor by summing the moment tensors of the earthquakes. We found that the strain directions are scale invariant for magnitude M<7 and coaxial with the stress directions in northern Iran and in Zagros. In eastern Iran, the strain orientations vary as a function of magnitude and the stress and strain orientations are not coaxial. If we add events with M>7 (mostly strike-slip events) to the strain computation, differences on the order of 20° to 30° seem to appear between the greatest principal stress and strain orientations although these are not resolvable at the 95% confidence level.

Focal mechanisms, published by *Jones* [1988] for five segments of the San Andreas fault (SAF) in southern California, were used to compute the strain tensor orientations which we compared to the stress directions estimated by *Jones* [1988]. These data sampled the crust adjacent to the fault within 10 km of the surface trace of the SAF. We found that the directions of principal strain form an angle of 65° with the SAF trace and are parallel to the directions of principal stress in each of the five segments analyzed. Most of the faults within 10 km of SAF are favorably oriented for faulting at an average angle of 39° with respect to the greatest principal stress orientation. Adding the focal mechanism of the 1857 great California earthquake, for which evidence of a right-lateral strike slip exist [*Sieh*, 1978], to the strain calculation introduces a difference of 20° between the greatest and least principal stress and strain orientations.

We conclude that directions of stress and released strain are parallel in crustal volumes of uniform strength and without a major dominating fault, but that they may differ by as much as 20° to 40° along major weak faults.

2. INTRODUCTION

Earthquake focal mechanisms are characterized by two types of uncertainties which have to be resolved to make tectonic interpretations based on such data. The first is that it is not possible to distinguish between the fault plane and the auxiliary plane without geological evidence of surface rupture or delineation of the fault plane by aftershocks. In some cases, the consistency of slip vector orientation in a region can provide an indication of which of the nodal planes is the fault plane. The second uncertainty is that of the orientation of the stress tensor causing the earthquakes. If they occur along faults which are preexisting planes of weakness, the greatest and least principal stresses could be oriented almost anywhere in the compressional and extensional quadrants, respectively [*McKenzie*, 1969]. Therefore it is often a poor approximation to interpret the P and T axes as the directions of greatest and least principal stresses. McKenzie approached this problem asking the question of what is the orientation and magnitude of principal stress that would produce slip in the observed direction on the pre-existing fault plane, rather than assuming that rock is freshly broken. This question can be answered by assuming that the slip on the fault plane occurs in the direction of the resolved shear stress [*Wallace*, 1951; *Bott*, 1959; *McKenzie*, 1969]. If a crustal volume contains many different planes of weakness available for faulting, the application of a single stress tensor would produce a variety of different fault plane solutions that have slips in the direction of the resolved shear stress on the fault planes. It is possible to infer the orientation of the stress tensor from fault plane solutions by assuming homogeneity of the stress tensor to explain the diversity of faulting in a volume of the

crust and by proposing that slip is parallel to the resolved shear stress on the fault planes. Based on these two assumptions many authors [e.g. *Angelier*, 1979, 1984; *Michael*, 1984; *Gephart and Forsyth*, 1984] have developed methods to estimate the direction of principal stresses and the ratio of their relative magnitudes. The results indicate that the P and T axes should no longer be used to infer the orientation of tectonic stresses. A similar conclusion was reached by *Handin* [1969] based on laboratory experiment of rock failure in the presence of pre-exisiting cohesionless surfaces.

The directions of the principal strain axes are given by the eigenvectors of the seismic moment tensor and correspond to the P and T axes [*Kostrov*, 1974]. These are always oriented at 45° to the nodal planes [*Twiss et al.*, 1993]. The axes coincide with the direction of principal stress, if and only if, the fracture area is the plane of maximum initial shear stress, which is not true in general if slip occurs along an existing break. The average seismic strain released from a volume can be computed by summing the strain released in each earthquake using the focal mechanism data and the scalar seismic moment [*Brune*, 1968; *Kostrov*, 1974] if we assume that the volume can be described by a continuum model. This is so, when the dimensions of the deforming crustal volume are large relative to the average spacing of the faults. The direction and the magnitude of the principal strain can be estimated by this method, as well as the strain rate. If the time spanned by the earthquakes is longer than the recurrence interval of the largest earthquake in the volume, one may quantitatively compare the seismic strain release rate with the rate of plate motion to infer the ratio of seismic to aseismic deformation along plate

boundaries or in continental collisions [e.g., *Brune*, 1968; *Jackson and McKenzie*, 1988; *Ekstroem and England*, 1989]. In this paper, the word "strain" will be used to mean "the average incremental seismic strain released by earthquakes in a crustal volume".

The stress tensor orientation inferred from focal mechanism data results from tectonic forces applied to a particular volume of the crust. The seismic strain released from this particular volume can be computed from the same focal mechanism data using *Kostrov*'s technique [1974]. The main purpose of this paper is to compare the orientation of the stress and strain tensors in a particular crustal volume. If a volume of material contains a dominant plane of weakness with low shear strength, the orientation of the stress and strain direction could differ significantly because slip can occur on this plane with a shear stress lower than the maximum shear stress [*McKenzie*, 1969]. In this situation, the principal strain would be oriented at 45° from this plane, independent of the strength of the fault, whereas the principal stress could be at a greater or smaller angle from the fault. Such a difference was observed in the Kaoiki area, Hawaii [*Wyss et al.*, 1992], and in Western Hawaii [*Gillard et al.*, 1992]. In a material which is relatively uniform in strength, we would expect that the stress and strain directions are close to each other and perhaps even the same. This would happen if faults present are not pronounced zones of weakness.

The areas that we have investigated in this paper are Iran and the San Andreas fault (SAF) in Southern California. There are two motivations for choosing these

areas. First, they represent two different tectonic environments where we may expect significant differences in the results of the comparison between stress and strain. Iran is an area of continental collision where no single large fault is taking up plate motion. Instead three wide (200 to 300 km) seismically active areas surrounding a zone of relatively low seismicity (Central Iran) delimit what has been proposed as the Iranian plate [*McKenzie*, 1972; *Jackson and McKenzie*, 1984, 1988] (Figure 5.1). The SAF is more comparable to an oceanic plate boundary because most of the plate motion is accommodated by it and a few large faults with a relatively narrow zone of deformation (100-200 km) [*Ekstroem and England*, 1989] (Figure 5.2). The second reason for our choice is that both areas have been studied in detailed by other authors [*Jackson and McKenzie*, 1988; *Jones*, 1988] and therefore we can use their published fault plane solutions and results in our analysis.

The deformation rate predicted from plate motions in northern and eastern Iran is mostly taken up seismically, while in the Zagros area only 10 percent or even less of the deformation can be explained seismically [*Jackson and McKenzie*, 1988]. In this paper, we will compute the stress tensor orientation following *Gephart and Forsyth*'s method [1984] using the data published by *Jackson and McKenzie* [1988] as well as additional data from the Harvard catalogue of moment tensors, and compare it to the strain orientation computed with Kostrov's method for the three major seismically active areas in Iran. If plate motion is accommodated by wide zones of deformation in continental collision rather than along one major fault, it may suggest that the strength of the crust is uniform and the faults are mostly formed by the current stress system. Thus, the strain and stress tensor orientation should be

similar.

The SAF in central California has been described by many authors [*Oppenheimer et al.*, 1988; *Zoback et al.*, 1987; *Zoback and Beroza*, 1993] as a weak fault where the greatest principal stress is horizontal and forms a high angle ($\geq 60°$) with the strike of the fault. *Jones* [1988] investigated the orientation of the stress as a function of space along the strike of the SAF in Southern California. She found that the maximum horizontal stress is at a high angle to the fault (65°) and that it changes orientation significantly (35° over 400 km) as the strike of the fault varies. She also compared the stress tensor orientation to the principal horizontal strains recorded geodetically and noticed a significant difference between the two in some areas. In a second part of our study, we will compute the strain tensor by summing the seismic moment tensors [*Kostrov*, 1974] obtained from the focal mechanisms data published by *Jones* [1988] to compare the stress and strain release orientations.

This study is also a test of how the stress tensor inversion method performs on a large scale (hundreds to a thousand kilometers). Is the assumption of homogeneity fulfilled? Are stress inhomogeneities resolvable in such large areas? How good and how stable are the results of the stress tensor computation? Answering these questions is important in assessing whether the assumptions of the method of retrieving the stress orientations from focal mechanisms are fulfilled.

3. METHODS

3.1. Inversion of stress

The stress inversion method designed by *Gephart and Forsyth* [1984] and *Gephart* [1990] retrieves from the focal mechanism data, the direction of the three principal stresses ($\sigma_1 > \sigma_2 > \sigma_3$) and the ratio R

$$R = \frac{\sigma_2 - \sigma_1}{\sigma_3 - \sigma_1} \tag{1}$$

which governs the projection of the shear stress into any given fault plane. This is possible if we assume that the slip on a fault plane is in the direction of the resolved shear stress [*Bott*, 1959]. Through a grid search over the entire focal sphere, sampling the space of the three resolvable model parameters ($\sigma_1, \sigma_2, \sigma_3,$) and varying the R value between 0 and 1, with small, constant, incremental steps, one can retrieve the stress tensor orientation with the smallest misfit. For each orientation of the stress tensor and each value of R between 0 and 1, one can compute the misfit of each nodal plane. The misfit is defined as the minimum rotation about any arbitrary axis that brings the observed focal mechanism into coincidence with any mechanism that fits the stress model in which the slip direction matches the predicted resolved shear stress direction on one of the two nodal planes. Each fault plane solution will receive two misfits, one for each nodal plane, and the smaller of the two is used in the computation of the average misfit. This procedure chooses one of the two nodal planes as the preferred fault plane in the absence of an independent means for identifying the true fault plane. The stress model with the

smallest average misfit is the optimal stress model. Confidence limits can be derived using the one-norm misfit statistics [*Gephart and Forsyth*, 1984; *Parker and McNutt*, 1980]. The confidence limit is a measure of the degree of constraint of the data set, whereas the average misfit indicates the quality of the result. As an illustration, one could imagine applying the inversion procedure to a data set composed only of one type of fault plane solutions with identical orientation along one major fault. It would certainly be possible to find a best fitting stress model with a small misfit but the confidence limits would be very large. Many stress directions would be almost equally admissible because of the lack of constraint, as with a single fault plane solution.

The constraint in this inversion procedure comes from the diversity of the type of focal mechanisms. A volume of the crust may contain faults of different orientation, producing a variety of focal mechanisms in response to the application of a single stress tensor orientation. In order to retrieve the stress directions from such a data set using the method described , it is necessary to assume that the stress tensor is spatially homogeneous. This inversion technique will give a solution which is an average if data sets from different volumes with significantly different stress tensor orientations are mixed [*Michael*, 1987]. This is a potential pitfall of the method, against which we attempt to guard by applying the following procedure. Crustal volumes of interest are subdivided for separate analysis. If the inversion leads to different results in the sub-volumes with significantly reduced average misfits, the result for the over-all volume is rejected because the assumption of homogeneity is not fulfilled. If the results for all subvolumes and the over-all volume agree and

have similar misfits, we accept them as valid, because it is reasonable to propose that the stress tensor orientation is homogeneous throughout these volumes. The criteria for subdivision are based on the distribution of epicenters. Spatial gaps in seismicity mark the limits between the different subvolumes. Tectonic fabrics, like change in the strike of a major fault, are used also to define subvolumes. The average misfit is considered "small" if it can be attributed to uncertainties in the fault plane solutions as explained in the following paragraphs.

3.2. Misfit as a function of fault plane solution errors

The meaning of the size of the misfit, F, in the inversion technique used is not well understood, except that F=0 for a perfect match. We investigated the meaning of the size of misfit, F, by perturbing the strike, dip and rake of an error free synthetic data set. Using a set of observed earthquake focal mechanisms, we created an error free synthetic set by adjusting the fault plane solution such that the slip vector on one of the nodal planes coincides with the predicted slip direction on this plane corresponding to the correct stress model. We perturbed the strike, dip and rake of each focal mechanism by adding random errors normally distributed around a zero mean and with standard deviations of 5°, 10°, 15°, 20°, 30°, and 40°, respectively. We chose the data set composed of the focal mechanisms (23 events) of Area 1 in northern Iran to generate the synthetic sets and the correct stress model is the best fitting stress model obtained from the inversion of the observed focal mechanisms in Area 1 as shown in Table 5.3.

Table 5.1a presents the results of this error test. The second column in Table 5.1a, indicates by how much the focal mechanisms changed after perturbation. By perturbing simultaneously the strike, dip, and rake, we don't know how the errors propagate. For that reason we compared the P and T axes of the perturbed and unperturbed set to have a better measure of the amount of change induced in the focal mechanism by the perturbation. The last column represents the angular difference between the correct stress model and the best fitting stress model of the perturbed set.

The correct stress model is retrieved within less than 10° for average uncertainties of focal mechanisms from 5° to 20° and average misfits less than about 6° (Table 5.1a). For focal mechanism uncertainty of 30° and 40°, the misfits are 8.5° and 7.6° respectively, and the correct model is retrieved within 11° and 23° respectively. These synthetic sets are not sensitive to perturbation because the correct model is retrievable within 11° for errors on the focal mechanism as large as 30°.

In a second experiment, two synthetic sets with radically different best fitting models but the same number of events were mixed. The two different synthetic sets represented a thrust (synthetic 1) and a normal faulting (synthetic 2) environment, respectively (Table 5.1b). The stress inversion of the mixed set gave a best model with misfit of 6.3° (Table 5.1b). This experiment together with the previous one seems to indicate that a misfit around 6° represents a critical threshold in the assessment of the quality of the inversion.

Based on these tests, we propose that the inversion results with misfits smaller

than 6° represent data from crustal volumes with approximately homogeneous stress tensor orientation. If the misfit is larger than 6°, we believe that the data are not from a volume where the stress orientation is homogeneous. We will try to subdivide volumes with misfits around 6° or above, into subvolumes such that the misfit becomes lower than 6°. If after subdivision of a data set the misfit decreases, one can conclude that the size of the misfit does not depend on the error of the focal mechanisms because the subdivision does not affect the distribution of the errors, but that the data set comes from a volume with inhomogeneous stress orientation. The results of the first test indicate that it will be difficult to resolve any difference between crustal volumes because of the stability of the stress tensor inversion of this data set. According to our experience with a similar test applied to other data sets from Hawaii (*Wyss et al.*, 1992; *Gillard et al.*, 1993) such stability in the retrieval of the correct model as the error on the data increases is not observed. This leads us to believe that the effect of the perturbation on the results of the inversion for stress orientation depends on the nature of the data set itself and for that reason the rules deduced from this analysis should be applied cautiously to other inversions of focal mechanism data in different tectonic environments. We suggest that such an error analysis should be done every time a new inversion study is undertaken.

3.3. Strain calculation

Kostrov [1974] demonstrated that the average strain ε_{ij} released in a crustal volume V containing many active faults is linearly related to the sum of the moment tensor of all the earthquakes within this volume:

$$\varepsilon_{ij} = \frac{1}{2\mu V} \sum_k M_{ij}^k \tag{2}$$

The seismic moment tensor M_{ij}^k of the kth earthquake is given by

$$M_{ij}^k = M_0^k \ (u_i^k n_j^k + u_j^k n_i^k)_j \tag{3}$$

where n_i^K is a unit vector normal to the fault-plane and u_j^K is a unit vector parallel to the slip direction. These two vectors are determined by the fault plane solutions. The scalar moment M_0 is computed from the moment-magnitude relationship appropriate for the studied crustal volume. The shear modulus μ can be derived from the velocity structure.

In this study, we are interested in the orientation of the axes of principal strain. They represent the eigenvectors of the resulting seismic moment tensor. They are independent of the volume V and the shear modulus μ. In order to compare the orientation of the principal strain axes to the orientation of the principal stress axes, it is necessary to estimate the uncertainty with which the principal strain direction can be calculated. We followed the error analysis described by *Wyss et al.* [1992] to determined the error ellipses describing the 95% confidence ranges. In order to compute the error ellipses, one needs to estimate the uncertainties of strike, dip, rake as well as M_L and M_0 assuming that they are independent of each other and

that no systematic errors are present.

3.4. Comparison of the two methods

The method of inverting focal mechanism data for stress orientation determines the direction of principal stresses by minimizing the difference between the observed and predicted slip direction. The resulting stress directions reflect the total regional stress field in a volume. Only the directions of principal stress and the ratio of their relative magnitude can be determined because this method deals with slip directions on planes and not with absolute magnitudes of stress. The stress calculation does not depend on the magnitude of the events. Each earthquake contributes the same amount in the computation of the stress tensor direction, except for a weight depending on the quality of the mechanism. Diversity in the type of faulting within the volume considered constrains the inversion and the homogeneity of the stress field is a necessary assumption.

The strain is computed directly from the observed data because the tensor of the seismic moment is completely determined by the focal mechanism and the scalar seismic moment of an earthquake. The resulting calculated strain describes the seismic deformation produced by the earthquakes occurring within a volume of the crust. From equation 3, one notices that the scalar moment M_0 weighs the summation of the seismic moment tensor of each event. Thus, if an earthquake much larger than the others is included in the data set, it will have a dominant influence on the magnitude and direction of the average strain. For that reason, one must sample all the largest earthquakes within the period considered, if one is interested

in comparing the deformation rates obtained from earthquake data with the long-term geologic rates. It can be crucial for the estimate of strain directions to include or exclude the largest event. If the largest event ruptures a major weak fault unfavorably oriented with respect to the stress directions, the strain released in the volume may not be coaxial with the stress.

The influence of the weight in the strain tensor method can be assessed by computing the strain tensor orientation for different magnitude bands within a regional data set, provided that the events within a particular magnitude band contribute more or less equally to the strain calculation (*Marrett and Allmendinger*, 1990). If the strain orientations do not change significantly as a function of magnitude, the kinematics of the fault population is scale invariant and consequently the comparison of the stress and strain becomes independent of the size of the events.

The stress inversion method assumes that the stress field is homogeneous in the crustal volume of interest and that the earthquakes located within this volume and selected for the inversion are representative of the stress field. For the strain calculation, no assumption of spatial homogeneity of the strain field is required, but testing for spatial variations of the strain field can be done also by analyzing subgroups of data and comparing their strain directions. The confidence ellipses computed following the error analysis proposed by *Wyss et al.* [1992] allows to asses the significance of any possible spatial or temporal variation of the strain field.

The results of the comparison of the two methods will show that stress and strain may be coaxial or not. If they are coaxial, one could conclude that the stress

or strain field has been successfully determined because both methods give the same answer as one would expect in a linear isotropic elastic medium. If there is a statistically significant difference between the stress and strain results, the reason may be that the crust is heterogeneous in strength or that one or both methods failed.

4. IRAN

4.1. Data

The data set of Iranian earthquakes used in this study consists of 111 events covering a period from 1909 to 1992 with magnitude $M_S \geq 4.5$, extracted from a list of 166 earthquakes with published focal mechanisms (Figure 5.1) (Table 5.2). The fault plane solutions published by *McKenzie* [1972], and *Jackson and McKenzie*, [1984, 1988] have been obtained from first motion polarity readings of long period seismograms. These authors have adjusted the velocity at the focus by trial and error and found that it was possible to fit two orthogonal nodal planes to the data using a crustal velocity of 6.8 km/s. We consider these fault plane solutions (49 events) reliable because of the careful way in which they were computed. Nevertheless, no estimate of the errors on strike, dip and rake have been proposed. The epicenters of the events instrumentally recorded are accurate to about 20 km [*Jackson and McKenzie*, 1984] but their depth uncertainty is larger because the depth determination relies only on the first P arrival and not on pP. The events recorded prior to the installation of the WWSSN network have less reliable locations and fault plane solutions, because their locations are based on macroseismic maps [*Jackson and McKenzie*, 1984]. Seven focal mechanisms are from *Jackson*

and Fitch [1981] who used waveform modelling to compute the fault plane solutions. These are the most reliable mechanisms because the depths of the events could be estimated with an accuracy of 6 km [*Jackson and Fitch*, 1981] and an average of 10 stations was used by the authors to model the P wave. We also used 16 solutions published by *Sborschichkov et al.* [1981] for which it was not possible to assess the quality. Two solutions came from *Berberian* [1982] and were judged to be of good quality. The remaining 51 fault plane solutions were obtained from the Harvard catalog of moment tensor solutions for global seismicity available on CDROM from the USGS and on the IRIS bulletin board. These solutions are computed routinely with the centroid-moment tensor (CMT) method described by *Dziewonsky et al.* [1981]. The depths derived from the CMT method also have large uncertainties because of the poor depth resolution that is available from long period seismic waves. No estimate of the accuracy of the focal mechanism is given by this method. We have given the same weight to all solutions used in this analysis because of the lack of knowledge of the errors on strike, dip and rake. Since the depth of the events is in general poorly known, we did not set a depth cutoff in selecting the data. Instead, we will test our results by removing events deeper than 40 km to observe how this affects the estimate of the orientation of the principal stress tensor direction. Results from studies of the depth of seismicity in Zagros show that few of the large earthquakes nucleate at depths greater than 15-20 km [*Jackson and Fitch*, 1979, 1981; *Jackson*, 1980; *Jackson and McKenzie*, 1984]. Because of the depth uncertainty, we assume that any events given with depth shallower than 40 km are likely to be in the crust.

We subdivided the data into three sets corresponding to the three major tectonic areas of Iran. Alborz, which is located just south of the Caspian sea, represents area 1 (Figure 5.1). The focal mechanisms of these events are composed of 15 thrust mechanisms, 6 strike slip, and 2 normal faults (Figure 5.3). Area 2, located in eastern Iran, is characterized by a mixture of 15 thrust mechanisms and 14 strike-slip events (Figure 5.1 and 5.4). The four northernmost events of area 2 are also part of area 1. The Zagros mountains, extending from the west to the south west of Iran delimits area 3 (Figure 5.1). Out of a selection of 78 events located along this seismic belt, 54 have fault plane solutions of thrust type. The remaining solutions are split into 7 normal and 14 strike-slip events (Figure 5.5). Each of these three areas will be subdivided again (area 1b, 2b, 3a-b-c) (Figure 5.1) to test the hypothesis of stress homogeneity. This task is important because the selected areas have dimensions of hundreds of kilometers and the stress field may vary within such large areas. The subdivision of the main areas into sub-areas follows the spatial distribution of epicenters without consideration of the type of focal mechanisms. The orientation and size of theses three areas coincide with the ones chosen by *Jackson an Mckenzie* [1988] for the computation of the strain tensor.

4.2. Results from the inversion for stress directions

The inversion of slip data from focal mechanisms was applied to the different subsets of data using all the focal mechanisms available. After this first computation we noticed that the fault plane solutions published by *Sborschichkov et al.* [1981] had individual misfits larger than the rest of the solutions within the set in areas 2,

3a and 3b. The size of these anomalous misfits ranged between 10° and 25°. As these authors did not discuss the quality of their focal mechanisms we suspected that this part of the data set may be inferior to the rest. For that reason, we excluded these solutions from our data. The results presented below were obtained without using the focal mechanisms published by *Sborschichkov et al.* [1981].

4.2.1. Alborz

The inversion of the 23 fault plane solutions composing the data set of area 1 gave a best model with the direction of the greatest principal stress oriented horizontally NE, and the least principal stress vertically (Table 5.3). The average misfit for the best model is 8.4° and the R value is equal to 0.4 (Table 5.3). Two focal mechanisms of normal fault type received the largest misfits (21.9° and 26.3°) and in total four had a misfit greater than twice the average misfit.

To see if the discrepancies could come from a spatially heterogeneous stress field, we inverted a subset of fault plane solutions corresponding to the events located in area 1b (Figure 5.1). The stress tensor orientation obtained from this subset is similar to the one of area 1 within about 20° (Table 5.3). The average misfit was reduced to 5.0° (Table 5.3). σ_1 is horizontally oriented NE and σ_3 quasi vertical (Figure 5.6). The 95% confidence regions cover a large area of the focal sphere (Figure 5.6). Two solutions had an individual misfit larger than 10° (10.3° and 12.7°). Only one of the normal fault solutions was present in the subset covered by area 1b, the solution with the individual misfit equal to 10.3°.

4.2.2. Eastern Iran

Two inversions were done in area 2 to test the homogeneity of the stress tensor. First, the inversion for the whole area gives an average misfit of 5.2° and a R value of 0.5. σ_1 is horizontal pointing N-NE and σ_3 is vertical (Table 5.3). The maximum misfit for a single observation is 24° and 5 fault plane solutions have a misfit larger than 10° in area 2.

The inversion for the subset of area 2b, gives an average misfit of 4.0° and the stress orientation could not be distinguished from that of the whole region 2 at the 95% level. σ_1 is horizontal and points toward NE and σ_3 is vertical (Figure 5.6). The angular difference between the principal axes of area 2 and 2b are 32° and 11° for σ_1 and σ_3 respectively. For the data in area 2b, the highest misfit is 21° and only two other focal mechanisms have misfits greater than 10° but less than 15°.

4.2.3. Zagros

We computed the orientation of the stress tensor from the three subsets of focal mechanisms (area 3 a-c) defined in Figure 5.1. In area 3a the misfit is 2.8° (Table 5.3) which is the smallest average misfit of all the inversions in this study. The largest misfit for a single focal mechanism in this dataset is 7.3°. The 95% confidence limit for σ_1 covers a band on the stereographic projection from SW-NE to SE-NW (Figure 5.7). σ_3 is also well resolved, although the 95% confidence region is somewhat larger and forms a branch toward NW on the stereographic projection (Figure 5.7). The frequency distribution of R values is wide and slightly skewed toward values smaller than 0.6 (Figure 5.7). The R value obtained for the

best model is 0.5. The greatest principal stress is oriented horizontally at an azimuth of 216° and the least principal stress is vertical (Table 5.3 and Figure 5.7).

Area 3b had 7 events listed with depth between 40 and 84 km. When we excluded from the data set of area 3b all the events with depth deeper than 40 km, the average misfit decreased from 7.2° to 6.5° (Table 5.3) and the orientation of the stress tensor did not change significantly. Further attempts to subdivide area 3b into subsets according to distribution of seismicity did not change the results but removing the data published by *Sborschichkov et al.* [1981] decreased the average misfit significantly to 4.6° (Table 5.3).

In area 3b the 95% confidence limit is tight (Figure 5.7), the R values are concentrated around 0.3. The largest individual misfit is 14.9° and 4 focal mechanisms have misfit larger than 10°. The greatest principal stress is approximately horizontal and has an azimuth of 207° and the least principal stress is vertical (Figure 5.7). The greatest and least principal stress vary by about 15° between area 3a and 3b but this difference is not significant at the 95% confidence level.

In Area 3c most focal mechanisms are similar to each other. This can be seen in the distribution of P and T axes in Figure 5.7. For that reason, the inversion is not well constrained and the 95% confidence region is very broad although the average misfit is only 4.3° (Figure 5.7 and Table 5.3). The greatest principal stress is horizontal and its azimuth is 137°. σ_3 is vertical and σ_2 is quasi horizontal and oriented at an azimuth of 41°. The R value for this best stress model is low (R=0.2) which implies, according to equation 1, that σ_1 and σ_2 have similar magni-

tudes. The mechanisms with the largest misfits are two thrust faults which received a misfit of 21.3° and 14.3° and one normal fault with misfit 22.7°. The event of 1974/12/02 (misfit=21.3°) is a thrust event with nodal planes transcurrent to the folding axis of the Zagros mountains. It was checked carefully by *Jackson and McKenzie* [1984] but they confirmed the focal mechanism as being correct. Because of its small size (M_S = 5.4) (Table 5.2) , this event may be dependent on the local stress field which may be different from the overall stress field that we are measuring.

4.3. Discussion of the stress tensor analysis

According to our error analysis, the first results of the stress inversion for the large areas (1, 2 , 1 and 2, 3a and 3b) were unacceptable because each average misfit was about 6° or larger (Table 5.3, number in parenthesis). Such average misfits are indicative of errors in the data larger than 20° or that the stress field is not homogeneous within the area. We discovered that fault plane solutions published by *Sborschichkov et al.* [1981] were responsible for the size of the average misfit in areas 2 and 3. After removing these fault plane solutions from our data sets, the average misfits decreased by about 0.4° in area 2 and 2.8° in area 3 a and b suggesting that these fault plane solutions were of poor quality.

Subdividing areas 1, 2 and 3 into smaller areas (1b, 2b, 3a , 3b, and 3c) improved the results of the stress inversion significantly. All the average misfits of the subsets are less than or equal to 5 while the average misfit for all Iran is 7.2° (Table 5.3). This indicates that the stress field is homogeneous within these areas

and that data errors are less than 15°. The solutions of the inversions are stable within each subset.

We conclude that the stress orientations are similar along all plate boundaries over length scale of a thousand kilometers. Dividing the large areas into subregions reduces the misfit and improves the results of the inversion. This implies that the stress orientations in the subsets are different from those in the larger sets. Thus the larger misfits observed in the large areas are not due to data errors but to the inhomogeneity of the stress field within these regions. The differences in stress orientations between a large set and a subset typically vary, between 15° and 20° (Table 5.3), and are difficult to resolve at the 95% confidence level by the available data.

Gephart's inversion method performs as well on a large scale (hundreds to a thousand kilometers in Iran) as it does on a small scale (ten to fifty kilometers in Hawaii) [*Wyss et al.*, 1992; *Gillard et al.*, 1992]. As in Hawaii, the misfits for the sets with homogeneous stress orientation are around 4°, the results are stable and although stress differences are not resolvable at the 95% confidence level, they can be detected. This outcome may seem surprising since over such distances (a few hundred to a thousand kilometers), the stress field is more likely to change than over short distances. On the other hand, stress heterogeneities due to fault interactions are more likely to perturb the solution at smaller scales. If the fault dimensions are much smaller than the size of the crustal volume considered, one can expect that local heterogeneities average out and their influence on the stress inversion becomes negligible. The ratio of the length of the seismic source to the length

of the studied areas is the same for Hawaii and Iran. In Hawaii, a fault length of 0.5 km for magnitude 3 earthquake in areas about 10 km long (*Wyss et al.*, 1992; *Gillard et al.*, 1992) gives a ratio of 0.05. In Iran, magnitude 6 earthquakes are used which have an estimated source length of about 20 km in areas covering distances of about 500 km, giving a similar ratio of 0.04.

4.4. Strain tensor orientations

We computed the strain in each area where the stress was considered homogeneous (misfit ≤ 5°, area 2b, 3a, 3b, 3c). We used the moment magnitude relationship derived by *Dziewonsky and Woodhouse* [1983] based on worldwide data from the Global Digital Seismic Network (GDSN), $\log M_0 = 1.5 M_S + 16.0$, to compute the moment of each earthquake. We estimated the uncertainty of the fitting process of the moment-magnitude relationship to be ±0.3. We chose the error estimate of ±0.2 for magnitude as proposed by *Dziewonsky and Woodhouse* [1983]. Using the error propagation law for products, we estimated the uncertainty on the logarithm of M_0 to be ±0.3 and the standard deviation $\Delta M_0 = 1.0 M_0$. To be conservative, we assumed 15° errors for the strike, dip, and rake of the focal mechanisms used in this study. Using these error estimates, we computed the 95% confidence limit on the greatest and least principal strain directions following the procedure described by *Wyss et al.* [1992].

The weighting effect produced by the moment was tested by determining the strain tensor orientations as a function of magnitude in four ranges for each data set; $4.0 \le M \le 5.0$, $5.0 \le M \le 6.0$, $6.0 \le M \le 7.0$, $7.0 \le M \le 8.0$. The number of events varied

within the ranges, but in the majority of them, most events contributed more or less equally to the strain calculation (Table 5.4).

In Alborz (area 1b) the least principal strain is more or less vertical for all magnitude ranges except for the two largest events. The greatest principal strain is horizontal through all magnitude bands, but azimuths vary between EW-NS. Large overlapping confidence ellipses indicate that these differences are not significant at the 95% confidence level. For $M \leq 7$ the greatest principal strain is horizontal and has an azimuth of 22° and the least principal strain is vertical (Table 5.4). If one adds the events with M>7, the strain orientations change by about 40° but this difference is not significant because the 95% confidence ellipses are large (Figure 5.8).

In eastern Iran (area 2b), the greatest principal strain is horizontal and does not change orientation significantly as a function of magnitude band (Table 5.4, Figure 5.9). It is oriented horizontally at an azimuth averaging N39E. The least principal strain orientation has a constant azimuth of about N47W through all magnitudes but its plunge is horizontal for magnitudes greater than 6 and about 45° steeper for magnitudes smaller than 6 (Table 5.4, Figure 5.9). Computing the strain orientations for $4 \leq M \leq 6$ and $6 \leq M \leq 8$ separately shows that ε_3 changes orientation significantly (Figure 5.9).

In Zagros, the directions of principal strain are invariant as a function of magnitude for $M \leq 7$ in each sub-area 3a, 3b, 3c (Figure 5.8). Differences in the orientation of ε_1 as well as ε_3 among magnitude bands are less than 15° in area 3a and 3b.

These differences cannot be resolved at the 95% confidence level (Figure 5.8). In area 3c, differences are even smaller (less than 5°). The average strain orientations in area 3a and 3b are characteristic of a thrust environment with ε_1 horizontal pointing NE and ε_3 vertical (Figure 5.8). The average principal axes differ by less than 15°. Area 3c, also has a strain field of thrust type but the greatest principal strain axis is oriented NS. The difference in strain orientation between area 3c and area 3a and 3b is about 20° and 30° respectively but they are not resolvable at the 95% confidence level. In area 3a, the strain field computed for all magnitudes corresponds to the strain produced by one event of magnitude 7.4 (Figure 5.8) and differs significantly from the strain obtained for M<7.

We conclude that the strain orientations in Alborz and Zagros are scale invariant within the magnitude range $4 \leq M < 7$ and have similar directions within 15° (area 1b and 3a and 3b) and 30° (area 1b and 3c). The largest difference cannot be resolved with the available data. However in eastern Iran, the strain directions are not scale invariant; significant differences on the order of 45° to 90° in the directions of the least principal strain are detected as a function of magnitude (Figure 5.9).

4.5. Comparison of stress and strain tensor orientations

The stress tensor orientation in Alborz and Zagros were compared to the strain tensor orientation computed for the magnitude range $4 \leq M < 7$ because within that magnitude band the strain is scale invariant. We found that the principal stress directions are approximately coaxial with the principal strain directions. None of the

differences between the two, which are in the order of 20° to 30°, are resolvable (Figure 5.8). In area 3c (east Zagros), the greatest principal stress is poorly resolved because most of the events have the same type of focal mechanism, therefore the 30° difference with the greatest principal strain is not significant. The tightness of the principal strain orientation as a function of magnitude is another indication of the lack of variety in the type of faulting in area 3c. We interpret the coaxiality of the stress and strain tensor orientation as an indication of the uniformity of the strength of the crust in Alborz and Zagros. If the largest events (M>7) are included in the strain computation, the greatest principal stress and strain differ by about 20° to 30° and the least principal stress and strain axes differ by more than 50° (Figure 5.8). The largest events in area 1b and 3a are strike-slip events (January 23, 1909, M=7.4; June 20, 1990, M=7.7) (Figure 5.1).

In area 2b, the greatest principal stress axis is approximately parallel to the greatest principal strain axis for magnitude M<7 (Figure 5.9). Significant differences appear between the orientations of ε_3 and σ_3. This difference is most significant for the largest magnitudes because two of the three largest events are strike-slip type (September, 31, 1968, M=7.3; November 27, 1979, M=7.1) (Figure 5.1) and they completely control the resulting strain field. The angular difference between σ_1 and ε_1 for 0<M<8 in eastern Iran is about 20° but this difference is not resolvable at the 95% confidence level.

4.6. Discussion

We successfully determined the stress field in Iran from focal mechanism data and we found that within large areas, hundreds to one thousand kilometers long and 200 to 300 km wide, the stress field is homogeneous. Differences of approximately 20° in the orientation of the stress as a function of space exist but they are small considering the size of the regions studied. Overall, the greatest principal stress in Iran is horizontal and oriented approximately NE-SW, and the least principal stress is vertical. This stress field is consistent with a a model of continental collisions with large forces acting at the plate boundary as suggested by *McKenzie* [1972]. Also, the greatest principal stress axes are approximately parallel to the direction of plate motion measured relative to Eurasia by *McKenzie* [1972] (Figure 5.10). The consistency in the stress orientations between Zagros, northern Iran and eastern Iran suggests that compressive stresses generated by the collision of the Arabian plate with the Iranian plate along Zagros are transmitted through the rigid central Iranian plateau to northern and eastern Iran. This interpretation has been proposed by *Ambraseys and Melville* [1982] who suggested that the buoyancy force due to the elevation of the Zagros mountains is high enough to prevent further crustal thickening and the relatively rigid central Iranian plateau is transmitting a compressive stress to northern and eastern Iran.

Comparing the stress and strain orientations in these three diffuse plate boundaries (northern Iran, Zagros and eastern Iran) can provide information on the uniformity of the strength of the crust within these regions. The coaxiality of stress and

strain may indicate that the crustal strength is uniform, while a significant discrepancy between stress and strain indicates the presence of faults with low shear strength. We found that the direction of the greatest principal strain is stable as a function of space and approximately parallel to the direction of greatest principal stress for magnitudes M<7 (Figure 5.10). For magnitude less than 7, in Alborz and Zagros, the stress and strain are coaxial suggesting that the strength of the crust is uniform. This is not the case in eastern Iran and when the strain is computed including the largest events in Alborz and Zagros. Then the greatest principal strain makes an angle of about 20° to 30° with respect to the greatest principal stress, and the least principal strain becomes horizontal. This rotation of ε_3 is due to the presence of strike-slip faults on which most of the largest events (M>7) occurred in Iran. In eastern Iran, the discrepancy between stress and strain is most pronounced through the entire magnitude range because the data set used is a mixture of half thrust and half strike slip. We conclude that the stress regime is compressional in Iran but that much of the slip is accommodated on large strike-slip faults capable of major earthquakes.

5. SAN ANDREAS FAULT IN SOUTHERN CALIFORNIA

5.1. Data

Focal mechanisms published by *Jones* [1988] in a study of the state of stress on the San Andreas Fault in southern California have been used to compute the direction of principal strain. This data set consists of 138 fault plane solutions of small to moderate earthquakes ($2.6 \leq M \leq 4.3$) that occurred between 1978 and

1985. They are located within 10 km of the surface trace of the SAF in Southern California but mostly not on the SAF itself. The fault plane solutions were obtained from P wave first motion polarities read by Jones from digitally recorded seismograms. These solutions could be determined with an accuracy of 5° in strike, dip, and rake [*Jones*, 1988]. On the basis of these mechanisms, *Jones* [1988] estimated stress directions for five segments along the SAF (Figure 5.2, modified from *Jones*, 1988) (Fort Tejon, Mojave, San Bernardino, Banning, and Indio) using *Michael*'s method [1984].

In this part of our study, we computed the strain for each of the segments defined by *Jones* [1988] using the same focal mechanisms. To compute the seismic moment from the magnitude of the earthquakes we used the moment-magnitude relationship proposed by *Thatcher and Hanks* [1973] for southern California earthquakes with local magnitudes ranging from about 3 to 7:

$$\log M_0 = 1.5M_L + 16.0 \qquad (4)$$

We estimated the uncertainty of the fitting process of the moment-magnitude relationship to be 0.3 and assumed 0.2 of uncertainty on the local magnitude (M_L). Using the error propagation law for products, we estimated the uncertainty on log M_0 to be ± 0.3 and the standard deviation $\Delta M_0 = 1.0M_0$. For the uncertainties of strike, dip and rake we used 5°. Using these error estimates, we computed the 95% confidence limit on the greatest and least principal strain directions following the procedure described by *Wyss et al.* [1992].

5.2. Results from the strain computation

The Mojave and Banning segments have virtually the same strain tensors, characteristic of a strike-slip environment with ε_1 and ε_3, horizontal, oriented NS and EW, respectively, and ε_2 vertical (Table 5.5, Figure 5.2) although the strike of the SAF is different in the two segments (Figure 5.2). These strain orientations are typical of a vertical strike-slip fault striking N45W. ε_1 is at 61° and 71° with respect to the strike of the SAF in Mojave and Banning, respectively (Table 5.6).

In the Indio segment, the strain is similar to Mojave and Banning (strike-slip type) (Figure 5.2) and the SAF strikes approximately N45W (Table 5.6). However, ε_1 is oriented N10E, at an angle of 58° with respect to the strike of the SAF (Table 5.6).

Fort Tejon is characterized by a strain tensor of thrust type (Figure 5.2) with ε_1 oriented NS as in Mojave, Banning, and almost as in Indio but with a least and intermediate principal strain totally different from all others. The angle between the strike of the SAF and ε_1 is 70° (Table 5.6).

San Bernardino, has a strain tensor of normal type with ε_3 oriented EW as in Mojave, Banning and Indio but with ε_1 almost vertical which is different from all other greatest principal strain orientation along the SAF in southern California (Table 5.5, Figure 5.2).

The strain field obtained from summing the moment tensor of all 138 events in all segments is of strike-slip type with ε_1 and ε_3 horizontal and oriented NS and EW, respectively. This overall orientation of the strain field agrees with the regional

strain orientation computed by *Ekstroem and England* [1989] in California for a 10 year period between 1977 and 1987 using a moment tensor summation.

5.3. Comparison of stress and strain directions

The principal strain directions are compared to the principal stress directions determined by *Jones* [1988] using the geologically preferred fault planes. In three adjacent segments of the San Andreas fault (Mojave, San Bernardino, and Banning) the stress and strain directions are quasi identical (Table 5.7 and Figure 5.2). In the Fort Tejon segment, the least principal strain differs from the least principal stress by 25° but this difference is not significant at the 95% confidence level. The greatest principal stress in this same segment is only 8° away from the maximum principal strain direction. In the Mojave segment, the principal strain directions are parallel to the principal stress directions if we interchange σ_2 with σ_3. This is possible because the R value obtained for the geologically preferred plane is 0.06 [Table 4 of *Jones*, 1988] which implies that the magnitude of σ_2 and σ_3 are the same.

The Indio segment presents a slight difference between stress and strain orientation. The angular difference between the greatest principal stress and strain is 18° (Table 5.7 and Figure 5.2). The azimuthal difference for the least principal stress and strain is 9°. These differences are not significant at the 95% confidence level.

5.4. Discussion

According to our starting hypothesis, the crust surrounding the SAF in southern California in each of the segments investigated, is homogeneous in strength because the principal strains and stresses are oriented in the same directions. This implies that most of the faults adjacent to the SAF in each segment are favorably oriented with respect to the greatest principal stress. This means that the angle between the greatest principal stress and the fault should be in the range of 30° to 50°. For each segment, we computed this angle averaged among all the faults within the segment and we found average angular values of 36°, 45°, 38°, 43° and 32° in Fort Tejon, Mojave, San Bernardino, Banning, and Indio, respectively. Therefore, on the average, in southern California, the greatest principal stress is most favorably oriented at an angle of 39° to the faults present in the crust adjacent to the SAF. However, except for the San Bernardino segment, the maximum horizontal stress is on the average at an angle of 65° to the local strike of the SAF. Thus, the SAF is unfavorably oriented and consequently, rupture on its surface is induced by low shear stresses implying that the fault is weak.

This can be seen using a three dimensional Mohr projection (Figure 5.11). Knowing the orientation of the principal stresses and the R value, one can construct a Mohr representation without knowledge of the individual magnitude of the principal stresses [*Jaeger and Cook*, 1979; *Gephart and Forsyth*, 1984] (Figure 5.11). For each segment the best fitting stress orientations obtained by *Jones* [1988] are used to construct the Mohr circle and the state of stress on any fault plane located within

that segment is represented by a dot plotted in the area between the circles. The state of stress on a fault plane depends on the relative magnitude of the three principal stresses and on the angle between the normal to the plane and the three principal stress axes. If the normal to the fault plane is within the same plane as σ_3 and σ_2, or σ_2 and σ_1, or σ_1 and σ_3, the location on the Mohr diagram will plot on the circle with the diameter σ_2-σ_3, or σ_1-σ_2, or σ_1-σ_3 respectively. The angle between σ_1 and the normal to the fault plane is measured around the circle with diameter equal to σ_1-σ_2 and the one between σ_3 and the normal of the fault plane is measured around the circle with diameter equal to σ_2-σ_3. For example, if σ_1 is perpendicular to the fault, the normal stress is equal to σ_1 and the shear stress is zero. If it is parallel to the fault, the normal stress becomes equal to σ_3 and the shear stress is zero.

In Figure 5.11, one can see that the normal stress resolved on the SAF is higher than for most of the fault planes in the surrounding crust for all the segments except San Bernardino where the SAF is at 43° to the maximum horizontal stress. Also, the shear stress resolved on the SAF is lower than for most of the fault planes of the adjoining crust in each segment, even San Bernardino. The Mohr circle shows graphically that most of the faults adjacent to the SAF are favorably oriented with respect to the stress field observed in the different segments, whereas the SAF, except in the Banning segment, is unfavorably oriented. This implies that the SAF is a weak fault which requires low shear stress for slip to occur and that it is surrounded by a strong crust. These results agree with the models proposed by *Rice*

[1990] and *Byerlee* [1990], which can explain the simultaneous failure of a strong crust and weak fault zone in response to a greatest principal stress oriented at an unfavorable angle (65°) to the plane of the fault zone, if the pore pressure is high (nearly lithostatic) in the crust adjacent to the fault and higher by a few percent in the fault zone [*Zoback and Beroza*, 1993].

The 1857 great earthquake with estimated magnitude, M=8 1/4, ruptured approximately 400 km of the SAF, from central California to San Bernardino [*Sieh*, 1978]. Geomorphological evidence suggests that the 1857 event was a right-lateral strike-slip earthquake [*Sieh*, 1978; *Wallace*, 1968]. If this event was included in our strain computation, it would make the contribution of the smaller events to the orientation of the principal strain negligible. Consequently, the resulting strain released by this event would have the greatest principal axis at 45° to the strike of the SAF and at 20° from the greatest principal stress.

6. CONCLUSIONS

6.1. Iran

1. The stress tensor is not homogeneous within the three broad zones of diffuse seismicity in northern Iran, eastern Iran and Zagros because after reasonable subdivisions, the average misfits of the inversion procedure decrease by about 2° and differences in stress orientations of about 20° to 30° exist.
2. The stress is homogeneous within the subregions of Iran because the results of the inversion give average misfits lower than 5°, indicative of the good quality

of the results.

3. The overall orientation of the greatest principal stress is horizontal pointing at N40E and parallel to the direction of plate motion. The least principal stress is vertical. Differences in the order of 20° exist between the sub regions but they are not resolvable at the 95% confidence level by the data available.

4. The strain tensor orientations are scale invariant for M<7 and coaxial with the stress tensor directions in northern Iran and Zagros, indicating that the strength of the crust is uniform. In eastern Iran the strain directions vary as a function of magnitude because of the mixture of thrust and strike-slip faults. This causes an angular difference between the greatest principal stress and strain of about 20° suggesting that strike-slip faults of low resistance to failure exist in eastern Iran.

5. The strain orientations are not coaxial with the stress for magnitudes larger than 7 in northern Iran, West Zagros and eastern Iran. Differences of about 20° seem to exist between the greatest principal stress and strain although they cannot be resolved at the 95% confidence level. The majority of the earthquakes with $M>7$ in Iran are strike slip. The difference between σ_1 and ε_1 suggests that the strike-slip faults rupture under low shear stress.

6. We conclude that the method of *Gephart and Forsyth* [1984] performed well on the large scale of hundreds of kilometers and furnished meaningful results. The results are stable and robust because they do not change significantly after subdividing the main dataset into subsets, nor after removing inconsistencies.

Except for east Zagros, the stress directions are well resolved because the 95% confidence limits are small. According to our error analysis, we judge the results as being of good quality because the average misfits range between 2° and 5°.

6.2. Southern California

1. In southern California, the strain is coaxial with the stress derived by *Jones* [1988] in Fort Tejon, Mojave, San Bernardino, Banning and Indio which indicates that the crust surrounding the SAF is homogeneous in strength.
2. The stress is favorably oriented in the average forming an angle of approximately 39° with the faults adjacent to the SAF. However, it has an angle of 65° with respect to the SAF which implies that the adjacent crust is homogeneous in strength and stronger than the SAF.
3. The strain released by the earthquakes changes orientation as function of the strike of the SAF.

6.3. Iran and Southern California

In southern California the direction of plate motion is not parallel to the SAF. It can be decomposed into a component perpendicular to it which is responsible for the occurrence of thrust events in the crust adjacent to the SAF, and a component along the SAF which is a strike-slip component (Figure 5.12). Along segments of the SAF which have not recently experienced large earthquakes (dormant segments), as in our study area, the stress is parallel to the strain and forms an angle of

65° with the strike of the SAF (Figure 5.12). However, in 1857, this segment experienced a great earthquake of strike-slip type. Consequently the direction of greatest principal strain would be oriented at 45° to the SAF which would be about 20° away from the greatest principal stress obtained by *Jones* [1988] (Figure 5.12). A similar situation exists along the SAF segment which was ruptured by the 1906, M_S=8 1/4, strike-slip earthquake. Along this segment, the greatest principal stress is horizontal and approximately perpendicular to the SAF [*Mount and Suppe*, 1987; *Zoback et al.*, 1987; *Mount and Suppe*, 1992; *Zoback and Beroza*, 1993]. The greatest principal strain resulting from this event would be at 45° to the greatest principal stress (Figure 5.12).

The same observation applies to Iran where the tectonic characteristics present some similarities (compressional stress regime and occurrence of thrust and strike-slip earthquakes). In Iran, slip occurs along thrust faults dipping SW at 45° (Figure 5.12). The horizontal component of slip and stress are parallel to the direction of plate motion which is NE. The stress and strain orientations are also parallel for events with 0<M<7 (strike-slip fault dormant) suggesting that, overall, the crust in Iran is uniform in strength (Figure 5.12). But, for 0<M≤8, stress and strain are not coaxial because large earthquakes occur mostly along strike-slip faults oriented approximately at 20° from the greatest principal stress (Figure 5.12). This implies that the greatest principal stress and strain are at 20° from each other (Figure 5.12) in West Zagros and eastern Iran. We conclude that the strike-slip faults in Iran as in California are weak and rupture under low shear stress.

Acknowledgments. We thank John Gephart for his computer codes and advice, and we thank D. Christensen, S. McNutt, H. Pulpan, and W. Harrison for helpful comments on the manuscript. D. Gillard was supported by NSF grant EAR-9118086 and M. Wyss was supported by the Wadati endowment at the Geophysical Institute of the University of Alaska.

7. REFERENCES

Ambraseys, M. N., and C. P. Melville, *A History of Persian Earthquakes*, Cambridge University Press, New York, 1982.

Angelier, J., Determination of the mean principal direction of stresses for a given fault population, 1, *Tectonophysics, 56*, 717-726, 1979.

Angelier, J., Tectonic analysis of fault slip data sets, *J. Geophys. Res., 89*,5835-5848, 1984.

Berberian, M., Aftershock tectonics of the 1978 Tabas-e-Golshan (Iran) earthquake sequence a documented active 'thin- and thick-skinned tectonic' case, *Geophys. J. R. Astron. Soc., 68*, 499-530, 1982.

Bott, M. H. P., The mechanics of oblique slip faulting, *Geol. Mag., 96*, 109-117, 1959.

Brune, J. N., Seismic moment, seismicity, and rate of slip along major fault zones, *J. Geophys. Res., 73*, 777-784, 1968.

Byerlee, J., Friction, overpressure and fault normal compression, *Geophys. Res. Lett., 17*, 2109-2112, 1990.

Dziewonsky, A. M., T. Chou, and J. H. Woodhouse, Determination of earthquake source parameters from waveform data for studies of global and regional seismicity, *J. Geophys. Res., 86*, 2825-2852, 1981.

Dziewonsky, A. M., and J. H. Woodhouse, An experiment in systematic study of global seismicity: centroid-moment tensor solutions for 201 moderate and large

earthquakes in 1981, *J. Geophys. Res., 88*, 3247-3271, 1983.

Ekstroem, G., and England P., Seismic strain rates in regions of distributed continental deformation, *J. Geophys. Res., 94*, 10231-10257, 1989.

Gephart, J. W., and D. W. Forsyth, An improved method for determining the regional stress tensor using earthquake focal mechanism data: application to the San Fernando earthquake sequence, *J. Geophys. Res., 89*, 9305-9320, 1984.

Gephart, J. W., FMSI: A Fortran program for inverting fault/slickenside and earthquake focal mechanism data to obtain the original stress tensor, *Computer and Geosciences, 16*, 953-989, 1990.

Gillard, D., M. Wyss, and J. S. Nakata, A seismotectonic model for western Hawaii based on stress tensor inversion from fault plane solutions, *J. Geophys. Res., 97*, 6629-6641, 1992.

Gillard, D., M. Wyss, and P. Okubo, Stress tensor orientations in the south flank of Kilauea, Hawaii, estimated from fault plane solutions, *J. Geophys. Res.*, submitted, 1993.

Handin, J., On the Coulomb-Mohr failure criterion, *J. Geophys. Res., 74*, 5343-5348, 1969.

Jackson, J. A., Reactivation of basement faults and crustal shortening in orogenic belts, *Nature, 283*, 343-346, 1980.

Jackson, J. A., and T. Fitch, Seismotectonic implications of relocated aftershock sequences in Iran and Turkey, *Geophys. J. R. Astron. Soc., 57*, 209-229, 1979.

Jackson, J. A., and T. Fitch, Basement faulting and the focal depths of the larger earthquakes in the Zagros mountains (Iran), *Geophys. J. R. Astron. Soc., 64*, 561-586, 1981.

Jackson, J. A., and D. P. McKenzie, Active tectonics of the Alpine-Himalayan belt between western Turkey and Pakistan, *Geophys. J. R. Astron. Soc., 77*, 185-264, 1984.

Jackson, J. A., and D. P. McKenzie, The relationship between plate motions and seismic moment tensors and the rates of active deformation in the Mediterranean and Middle East, *Geophys. J. R. Astron. Soc., 93*, 45-73, 1988.

Jaeger, J. C., and N. G. W. Cook, *Fundamentals of Rock Mechanics*, Chapman and Hall, London, 1979.

Jones, L. M., Focal mechanisms and the state of stress on the San Andreas fault in southern California, *J. Geophys. Res. 93*, 8869-8891, 1988.

Kostrov, B. V., Seismic moment and energy of earthquakes and seismic flow or rock, *Izv. Acad. Sci., USSR Phys. Solid Earth, 1*, 23-44, 1974.

Marrett, R., and R. W. Allmendinger, Kinematic analysis of fault-slip data, *J. Struct. Geol., 12*, 973-986, 1990.

McKenzie, D. P., The relation between fault plane solutions for earthquakes and the direction of the principal stresses, *Bull. Seismol. Soc. Am., 59*, 591-601, 1969.

McKenzie, D. P., Active tectonics of the Mediterranean region, *Geophys. J. R. Atsron. Soc., 30*, 109-185, 1972.

Michael, A. J., Determination of stress from slip data: faults and folds, *J. Geophys. Res., 89*, 517-526, 1984.

Michael, A. J., Use of focal mechanisms to determine stress: a control study, *J. Geophys. Res., 92*, 357-368, 1987.

Mount, V. S., and J. Suppe, State of stress near the San Andreas fault: implications for wrench tectonics, *Geology, 15*, 1143-1146, 1987.

Mount, V. S., and J. Suppe, Present-day stress orientations adjacent to active strike-slip faults: California and Sumatra, *J. Geophys. Res., 97*, 11995-12013, 1992.

Oppenheimer, D. H., P. A. Reasenberg, and R. W. Simpson, Fault plane solutions for the 1984 Morgan Hill, California earthquake sequence: evidence for the state of stress on the Calaveras fault, *J. Geophys. Res., 93*, 9007-9026, 1988.

Parker, R. L., and M. K. McNutt, M.K., Statistics for the one norm misfit measure, *J. Geophys. Res., 85*, 4429-4430, 1980.

Rice, J. R., Fault stress states, pore pressure distributions, and the weakness of the San Andreas fault, *in Fault mechanics and transport properties of rocks*, B. Evans and T. F. Wong, eds., Academic Press, London, 1992.

Sborschichkov, I. M., L. A. Savostin, and L. P. Zonenshain, Present plate tectonics between Turkey and Tibet, *Tectonophysics, 79*, 45-73, 1981.

Sieh, K. E., Slip along the San Andreas fault associated with the great 1857 earthquake, *Bull. Seismol. Soc. Am., 68*, 1421-1448, 1978.

Thatcher, W., and T. C. Hanks, Source parameters of southern California earthquakes, *J. Geophys. Res., 78*, 8547-8576, 1973.

Twiss, R. J., B. J. Souter, and J. R. Unruh, The effect of block rotations on the global seismic moment tensor and the patterns of seismic P and T axes, *J. Geophys. Res., 98*, 645-674, 1993.

Wallace, R. E., Geometry of shearing stress and relation to faulting, *Geology, 59*, 118-130, 1951.

Wallace, R. E., Notes on stream channels offset by the San Andreas fault, southern Coast Ranges, California, *in Proc. of Conf. on Geologic Problems of the San Andreas fault system*, W. R. Dickison and A. Grantz, Editors, *Stanford Univ. Publ., Geol. Sci., Univ. Ser. 11*, 1-21, 1968.

Wyss, M., B. Liang, W. R. Tanigawa, and X. Wu, Comparison of orientations of stress and strain tensors based on fault plane solutions in Kaoiki, Hawaii, *J. Geophys. Res., 97*, 4769-4790, 1992.

Zoback, M. D., M. L. Zoback, V. S. Mount, J. Suppe, J., J. P. Eaton, J. H. Healy, D. Oppenheimer, P. Reasenberg, L. Jones, C. B. Rayleigh, I. G. Wong, O. Scotti, and C. Wentworth, New evidence on the state of stress of the San Andreas fault system, *Science, 238*, 1105-1111, 1987.

Zoback, M. D., and G. C. Beroza, Evidence for near-frictionless faulting in the 1989 (M 6.9) Loma Prieta, California, earthquake and its aftershocks, *Geology, 21*, 181-185, 1993.

Table 5.1A. Relationship between Fault Plane Solution Errors and Misfit from Inversions of the Perturbed Synthetic Set.

Average error of focal mechanism [deg]	Average change in P and T axes [deg]	Average misfit [deg]	Difference of σ_1 and σ_3 from best model [deg]
5	8	2.9	3
10	12	4.1	0
15	18	5.8	6
20	22	5.1	3
30	36	8.5	11
40	34	7.6	23

Table 5.1B. Mixing Data Sets with Different Stress Directions.

Data set	σ_1		σ_2		σ_3		R	Misfit
	PL	AZ	PL	AZ	PL	AZ		
	[deg]		[deg]		[deg]		[deg]	[deg]
Synthetic 1	82	288	7	138	4	47	0.9	0.0
Synthetic 2	5	214	8	123	81	337	0.4	0.0
Mixed set	18	201	72	18	1	111	0.1	6.3

PL, plunge; AZ, azimuth

Table 5.2. Fault Plane Solutions of Iranian Earthquakes.

Date	Latitude [deg]	Longitude [deg]	Depth [km]	M_S	Strike1 [deg]	Dip1 [deg]	Strike2 [deg]	Dip2 [deg]	Q	Reference
090123	33.40	49.10		7.4	135	90	225	90	3	JMK88
110418	31.20	57.00		6.2	335	60	65	90	2	JMK88
410216	33.40	58.90		6.1	5	90	95	90	3	JMK88
470923	33.70	58.70		6.8	175	90	265	90	3	JMK88
481005	37.78	58.41	5m	7.3	110	5	290	85	2	M72 KD
560203	32.50	46.00		5.0	83	43	329	69	2	SBOR81
570702	36.14	52.70	10m	6.8	104	44	300	46	2	M72 NI
571213	34.35	47.65	40m	6.7	6	52	136	50	2	M72 WI
580814	34.00	47.50		5.0	57	71	327	90	2	SBOR81
580816	34.30	48.17		6.6	130	90	220	90	3	JMK88
620901	35.63	49.87	27	7.2	110	51	325	44	2	M72 NWI
640819	27.90	52.60	52iss	5.5	93	51	202	68	2	SBOR81
640819	28.00	52.60	50iss	5.2	107	48	210	76	2	SBOR81
650310	32.50	49.00	33iss	5.5	244	19	123	80	1	SBOR81
650621	28.10	55.90	40m	5.4	102	34	313	60	2	M72 ZA
660727	32.60	48.80	33	5.3mb	80	59	294	34	2	M72 ZA

Date	Latitude [deg]	Longitude [deg]	Depth [km]	M_S	Strike1 [deg]	Dip1 [deg]	Strike2 [deg]	Dip2 [deg]	Q	Reference
660918	27.90	54.30	18	5.4	82	56	270	34	2	M72 ZA
670102	30.70	50.50	60	5.2	273	20	109	70	1	SBOR81
670109	27.60	54.50	23	5.4	62	58	319	69	1	SBOR81
670111	34.10	45.70	34	5.6mb	140	50	334	40	2	M72 ZA
670129	26.50	55.30	43	5.8	249	24	67	65	1	SBOR81
680423	27.70	56.70	52	5.1	134	61	41	84	2	SBOR81
680429	39.20	44.30	34	5.3mb	59	70	320	66	2	M72 NWI
680623	29.81	51.16	8*	5.5	70	60	203	40	2	J81 ZA
680802	27.51	60.92	62m	5.7mb	266	75	118	16	1	31A SI
680831	33.97	59.02	13m	7.3	342	84	251	80	1	M72 EI
680901	34.04	58.22	15m	6.3	148	65	17	36	2	M72 EI
680904	33.99	58.24	15m	5.2	147	65	327	25	2	M72 EI
680914	28.44	53.11	33	5.6	108	60	288	30	2	M72 ZA
690103	37.13	57.90	11	5.2	132	60	321	30	2	M72 NEI
690414	27.80	54.70	50	5.0	94	71	0	80	1	SBOR81
690429	29.60	51.60	21	5.5	3	61	273	90	2	SBOR81
690621	27.50	57.50	64	5.2	246	40	9	66	2	SBOR81
690902	30.20	57.70	53	5.0	268	73	359	87	1	SBOR81

Date	Latitude [deg]	Longitude [deg]	Depth [km]	M_S	Strike1 [deg]	Dip1 [deg]	Strike2 [deg]	Dip2 [deg]	Q	Reference
691107	27.85	60.06	35m	6.7	274	82	18	30	1	31B SI
700223	27.82	54.53	20	5.6	106	46	286	44	2	22B ZA
700228	27.83	56.32	35	5.5mb	84	50	264	40	2	22C ZA
700314	38.59	44.71	23	4.8	162	90	254	60	3	14A NWI
700317	34.00	59.70	25	5.0	105	22	352	81	2	SBOR81
700401	28.00	56.70	65	5.0	183	39	348	52	2	SBOR81
700730	37.82	55.88	19m	6.6	313	68	197	42	1	28A NEI
701025	36.77	45.13	19	4.8	212	70	319	50	1	14D NWI
701109	29.52	56.85	106m	5.5mb	50	30	284	71	1	31C SI
710214	36.56	55.63	39	5.3	232	60	95	40	2	28B NEI
710412	28.31	55.60	44	5.9	81	55	261	35	2	22E ZA
710526	35.51	58.22	26	5.4	57	42	309	75	2	28C EI
710822	29.70	50.70	20	5.1	217	80	126	87	2	SBOR81
710908	29.10	60.00	10	5.6	153	71	247	79	2	SBOR81
711108	27.05	54.48	36	5.9	120	48	300	42	2	22F ZA
720410	28.43	52.83	12*	6.9	281	40	101	50	2	J81 ZA
720612	33.11	46.32	33	5.0	114	56	306	35	2	22H ZA
720702	30.10	50.85	31	5.3	132	64	312	26	2	22J ZA

Date	Latitude [deg]	Longitude [deg]	Depth [km]	M_S	Strike1 [deg]	Dip1 [deg]	Strike2 [deg]	Dip2 [deg]	Q	Reference
720806	25.07	61.23	33	5.5mb	112	70	292	20	2	31D MA
720808	25.03	61.13	41	5.0	112	70	292	20	2	31E MA
721117	27.35	59.09	65m*	5.4mb	159	80	66	70	2	32 SI
730802	37.35	56.51	9*	5.3mb	48	90	138	90	4	4 NEI
741004	26.29	66.54	33	5.9	160	50	259	80	2	31F MA
741117	32.81	55.07	43	5.2mb	65	45	278	50	2	28E CI
741202	27.99	55.82	36	5.4mb	18	50	146	52	2	22L ZA
750111	29.10	51.80	29	5.0	278	71	188	90	1	SBOR81
750307	27.50	56.26	11*	6.1	90	60	270	30	2	22M ZA
750428	33.31	54.83	42	5.3mb	149	40	329	50	2	28F CI
751224	27.01	55.54	33	5.5	80	56	260	34	2	22N ZA
760316	27.31	55.06	33	5.2	73	50	253	40	2	22O ZA
760422	28.71	52.13	24	5.5	112	50	292	40	2	22P ZA
761107a	33.80	59.16	13	6.2	0	90	90	80	3	28G EI
761107b	33.24	47.96	51	4.8	110	40	306	50	2	22Q ZA
770321	27.61	56.39	12*	6.9	258	36	78	54	2	J81 ZA
770322	27.58	56.47	15*	5.9	260	50	80	40	2	J81 ZA
770323	27.62	56.59	9*	5.4	258	36	78	54	2	J81 ZA

Date	Latitude [deg]	Longitude [deg]	Depth [km]	M_S	Strike1 [deg]	Dip1 [deg]	Strike2 [deg]	Dip2 [deg]	Q	Reference
770324	27.62	56.63	32	5.3mb	122	60	302	30	2	22R ZA
770401	27.54	56.32	12*	6.0	258	36	78	54	2	J81 ZA
770406	31.98	50.68	41	5.9	95	46	275	44	2	22S ZA
770426	32.66	48.92	47	4.8	110	62	290	28	2	22T ZA
770525	34.89	52.06	26	4.3	112	60	256	40	2	28H CI
770526	38.93	44.38	37	5.4	38	90	128	70	4	14I NWI
770605	32.64	48.09	12*	5.8	104	66	319	30	2	J81 ZA
771019	27.79	54.88	33	5.2	96	45	276	45	2	22U ZA
771219	30.95	56.47	31	5.8	58	80	322	60	2	28I CI
780211	28.21	55.42	50	4.6	96	40	276	50	2	22V ZA
780916	43.39	57.33	33	7.3	342	29	125	66	2	B82 EI
781104	37.67	48.90	34	6.0	0	70	180	20	2	28J NWI
781214	32.14	49.65	33	6.2	120	10	300	80	2	22W ZA
790110a	26.61	60.93	33	5.8	120	50	300	40	2	31L MA
790110b	26.52	61.01	33	5.9	120	56	300	34	2	31M MA
790116	33.90	59.47	33	6.7	125	64	348	34	2	28K EI
790213	33.32	57.43	33	4.8	337	34	105	67	2	B82 EI
791114	33.92	59.74	33	6.6	75	90	165	80	4	28L EI

Date	Latitude [deg]	Longitude [deg]	Depth [km]	M_S	Strike1 [deg]	Dip1 [deg]	Strike2 [deg]	Dip2 [deg]	Q	Reference
791127	33.96	59.73	10	7.1	75	90	345	90	4	28M EI
791207	34.03	59.82	31	6.0	90	72	356	80	2	28N EI
800112	33.49	57.19	33	5.9	351	33	125	66	2	28Q EI
800504	38.05	48.99	46	6.2	180	85	0	5	2	28P NWI
801219	34.59	50.65	33	5.8	129	40	255	62	2	28Q NWI
801222	34.50	50.59	41	5.2	116	60	230	56	2	28R NWI
810611	29.91	57.72	33	6.7	172	40	270	80	2	28S CI
810728	30.17	57.84	33	7.1	127	52	287	40	2	28T CI
810804	37.90	48.84	25	5.6	159	26	32	73	2	HRVD
830207	26.28	57.21	33	5.7	5	42	101	85	2	HRVD
830305	32.19	49.08	10	5.4	254	4	133	88	2	HRVD
830326	35.88	52.01	10	4.7	104	61	6	75	2	HRVD
830418	27.94	62.44	51	6.5mb	81	43	231	51	1	HRVD
830528	32.45	48.36	27	5.1	314	38	106	56	2	HRVD
830712	27.11	56.26	47	5.8	241	45	85	48	2	HRVD
840222	39.55	54.06	41	5.8	109	83	199	85	2	HRVD
840319	40.53	63.25	26	7.0	219	28	38	62	2	HRVD
840320	40.58	62.82	26	4.2	263	38	32	64	2	HRVD

Date	Latitude [deg]	Longitude [deg]	Depth [km]	M_S	Strike1 [deg]	Dip1 [deg]	Strike2 [deg]	Dip2 [deg]	Q	Reference
840806	30.84	56.92	19	5.3	72	39	282	55	2	HRVD
840814	40.44	63.40	10	4.7	56	36	241	55	2	HRVD
841222	27.51	53.68	49	4.4	115	41	303	49	2	HRVD
850202	28.22	53.48	22	5.3	114	32	284	58	1	HRVD
850327	31.65	50.54	84	5.2mb	72	31	281	62	1	HRVD
850807	27.72	52.89	15	5.2	303	39	91	55	2	HRVD
850816	36.96	59.72	10	5.0	159	26	265	82	2	HRVD
850918	31.45	49.62	11	4.4	147	36	347	55	2	HRVD
851029	36.96	54.59	15	5.9	97	31	241	64	2	HRVD
860306	40.33	51.60	35	6.3	67	5	300	87	1	HRVD
860502	28.03	53.02	15	4.9	107	47	331	52	2	HRVD
860503	27.90	53.00	15	4.5	111	33	325	62	2	HRVD
860611	40.17	51.83	50	4.7	291	43	153	55	1	HRVD
860712	29.79	51.36	33	5.6	178	81	269	82	2	HRVD
861220	29.97	51.25	15	5.0	348	70	257	89	1	HRVD
870410	37.40	57.28	15	4.9mb	292	45	180	69	2	HRVD
870429	26.99	55.93	15	5.3	273	42	62	52	2	HRVD
870512	27.95	55.32	15	4.9	278	34	80	57	2	HRVD

Date	Latitude [deg]	Longitude [deg]	Depth [km]	M_S	Strike1 [deg]	Dip1 [deg]	Strike2 [deg]	Dip2 [deg]	Q	Reference
870529	33.54	47.76	15	4.6	218	80	128	88	2	HRVD
870810	29.65	63.72	57	5.6mb	349	32	149	59	1	HRVD
870907	39.13	54.87	29	5.5	312	14	116	77	2	HRVD
871124	32.23	58.98	15	4.4	144	39	303	53	2	HRVD
871218	27.90	56.42	15	5.5	155	39	40	71	1	HRVD
880126	32.33	46.85	20	5.3	306	20	137	70	2	HRVD
880330	30.29	49.84	15	5.7	296	32	116	58	2	HRVD
880420	38.97	44.00	15	4.7	110	58	209	75	2	HRVD
880609	27.67	56.10	15	4.4	310	11	81	83	2	HRVD
880625	38.44	43.08	15	5.0	106	57	218	60	2	HRVD
880811	29.87	51.06	15	5.6	283	69	190	84	2	HRVD
880811	30.00	51.69	15	6.1	256	63	351	79	1	HRVD
880822	35.06	52.16	15	4.7	317	75	225	85	1	HRVD
880823	35.71	52.46	15	4.7	348	32	115	70	1	HRVD
880830	30.07	51.26	15	4.6	242	57	337	83	1	HRVD
881206	30.00	51.58	15	5.7	256	54	357	74	1	HRVD
890916	40.37	51.60	33	6.5	104	36	331	64	1	HRVD
890917	40.19	51.79	33	6.0	292	36	142	58	1	HRVD

Date	Latitude [deg]	Longitude [deg]	Depth [km]	M_S	Strike1 [deg]	Dip1 [deg]	Strike2 [deg]	Dip2 [deg]	Q	Reference
891120	29.81	57.69	33	5.5	240	75	148	81	2	HRVD
891207	25.94	59.00	10	5.6	142	37	305	54	2	HRVD
900120	35.82	52.92	33	5.6	357	66	91	83	2	HRVD
900315	31.61	60.23	16	4.5	100	82	190	89	1	HRVD
900325	33.69	57.05	33	4.7	223	90	313	90	3	HRVD
900620	36.96	49.41	10	7.7	200	59	300	73	2	HRVD
900621	36.65	49.81	10	5.4	204	26	351	68	2	HRVD
900624	36.82	49.42	10	4.6	234	69	138	75	1	HRVD
900706	36.82	49.31	33	4.3	94	37	359	86	2	HRVD
900803	32.80	48.24	33	4.5	96	33	318	64	2	HRVD
900926	29.09	60.91	33	5.4	189	90	279	90	3	HRVD
901011	32.82	48.31	9	4.8	128	45	308	45	2	HRVD
901015	33.67	56.79	33	4.1	114	45	335	53	2	HRVD
901106	28.23	55.46	25	6.8	274	37	73	55	2	HRVD
901216	29.05	51.31	16	5.5	332	23	144	67	2	HRVD
910522	27.42	55.81	23	4.9	98	47	311	48	2	HRVD
910724	36.50	44.08	33	5.2	335	44	116	53	2	HRVD
911006	40.90	43.43	18	4.4	32	70	123	87	1	HRVD

Date	Latitude [deg]	Longitude [deg]	Depth [km]	M_S	Strike1 [deg]	Dip1 [deg]	Strike2 [deg]	Dip2 [deg]	Q	Reference
911104	30.62	50.18	33	5.0	143	41	314	49	2	HRVD
911128	36.77	49.58	14	5.0	219	36	354	63	2	HRVD
911207	25.08	62.94	29	5.1	309	8	85	84	2	HRVD
911219	28.28	57.32	32	4.8	215	35	103	75	2	HRVD
920304	31.64	50.71	33	4.5	122	79	213	83	2	HRVD
920519	28.31	55.55	33	5.0	254	40	63	51	2	HRVD

m : mantle source velocity used in preparing the fault plane solution. * : focal depth constrained by waveform inversion. mb: body wave magnitude. iss: depth comes from International Seismological Summary. HRVD: Harvard catalogue of centroid moment tensor solution. M72 : McKenzie 1972. JMK88 : Jackson and McKenzie 1988. SBOR81 : Sborshchikov et al. 1981. B82 : Berberian 1982. J81 : Jackson and Fitch 1981. CI=Central Iran; EI=East Iran; KD=Kopet Dag; MA=Makran; NWI=North-West Iran; WI=West Iran; SI= South Iran; Q=1-normal; 2-reverse; 3-right-lateral strike slip; 4-left-lateral strike slip.

Table 5.3. Stress Tensor Directions in Iran Estimated from Published Fault Plane Solutions.

Data Set	No of Events	σ_1 PL [deg]	σ_1 AZ [deg]	σ_2 PL [deg]	σ_2 AZ [deg]	σ_3 PL [deg]	σ_3 AZ [deg]	R	Average Misfit [deg]
area 1	23	0	222	2	132	88	312	0.4	8.4
area 1b	12	15	40	18	135	66	273	0.5	5.0
area 2	27(29)	0(2)	199(232)	2(10)	109(141)	88(80)	289(333)	0.5(0.5)	5.2(5.6)
area 2b	22(24)	1(2)	231(61)	13(1)	141(330)	77(88)	325(214)	0.6(0.4)	4.0(4.6)
area 1 and 2	50(52)	0(0)	227(227)	2(2)	137(317)	88(88)	317(137)	0.5(0.4)	6.9(7.0)
area 3a	14(17)	6(5)	216(214)	9(8)	125(123)	79(81)	341(337)	0.4(0.4)	2.8(3.7)
area 3b	23(34)	19(19)	207(189)	2(0)	117(99)	71(71)	22(8)	0.3(0.3)	4.6(7.2)
area 3b*	(27)	(21)	(194)	(1)	(284)	(69)	(16)	(0.3)	(6.4)
area 3a and 3b	37(51)	17(12)	205(186)	0(0)	115(96)	73(78)	24(6)	0.3(0.2)	4.9(7.7)
area 3c	24(27)	3(3)	137(132)	9(10)	46(41)	81(79)	244(235)	0.2(0.2)	4.3(5.2)
area 3	61	17	205	0	115	73	24	0.3	5.2
all Iran	111	1	33	4	123	86	282	0.3	7.2

In parenthesis, results for data sets containing fault plane solutions published by Sborschichkov [1981]. * Depth $\leq$ 40 km. PL, plunge; AZ, azimuth.

Table 5.4. Principal Strain Directions in Iran as a Function of Magnitude Range.

Data	Magnitude	Number of	ε_1		ε_2		ε_3	
Set	Range	Events	PL	AZ	PL	AZ	PL	AZ
			[deg]		[deg]		[deg]	
Area 1b	$4 \le M \le 5$	6	28	89	16	351	57	235
Area 1b	$5 \le M \le 6$	4	10	6	12	273	74	134
Area 1b	$6 \le M \le 7$	1	2	22	8	112	82	281
Area 1b	$4 \le M \le 7$	10	2	22	7	112	83	277
Area 1b	$7 \le M \le 8$	2	9	65	49	325	39	162
Area 1b	$4 \le M \le 8$	12	9	65	47	325	42	162
Area 2b	$4 \le M \le 5$	5	4	242	41	148	48	336
Area 2b	$5 \le M \le 6$	6	9	214	50	113	40	311
Area 2b	$4 \le M \le 6$	11	9	214	50	114	39	312
Area 2b	$6 \le M \le 7$	9	2	222	84	333	6	131
Area 2b	$7 \le M \le 8$	3	7	208	80	342	7	117
Area 2b	$6 \le M \le 8$	12	6	211	81	343	7	120
Area 3a	$4 \le M \le 5$	6	6	204	5	113	82	343

Data Set	Magnitude Range	Number of Events	ε_1		ε_2		ε_3	
			PL	AZ	PL	AZ	PL	AZ
			[deg]		[deg]		[deg]	
Area 3a	$5 \le M \le 6$	6	21	205	8	112	67	3
Area 3a	$6 \le M \le 7$	2	11	200	16	107	71	324
Area 3a	$4 \le M \le 7$	13	12	200	15	107	71	327
Area 3a	$7 \le M \le 8$	1	1	180	88	288	2	90
Area 3a	$4 \le M \le 8$	14	2	181	88	245	1	271
Area 3b	$4 \le M \le 5$	7	1	215	28	124	62	307
Area 3b	$5 \le M \le 6$	15	14	215	5	306	75	55
Area 3b	$6 \le M \le 7$	3	3	194	1	104	87	3
Area 3b	$4 \le M \le 7$	23	4	195	0	285	86	17
Area 3c	$4 \le M \le 5$	6	9	175	5	84	79	327
Area 3c	$5 \le M \le 6$	16	4	176	1	267	86	7
Area 3c	$6 \le M \le 7$	4	9	170	4	79	80	327
Area 3c	$4 \le M \le 7$	24	9	171	4	80	80	328

PL, plunge; AZ, azimuth

Table 5.5. Directions of Principal Strain along the Southern San Andreas Fault.

Location	Number of Events	ε_1		ε_2		ε_3	
		PL	AZ	PL	AZ	PL	AZ
		[deg]		[deg]		[deg]	
Fort Tejon	17	10	352	39	90	49	249
Mojave	23	3	353	70	91	20	262
San Bernardino	18	62	166	28	351	2	260
Banning	40	12	176	77	332	5	85
Indio	40	35	190	54	22	5	284

PL, plunge; AZ, azimuth

TABLE 5.6. Horizontal Computed Principal Strain Directions and the Strike of the San Andreas Fault.

Segment	Azimuth of Computed Maximum Horizontal Principal Strain [deg]	Average Local Strike of San Andreas Fault [deg]	Difference [deg]
Fort Tejon	352	282	70
Mojave	353	292	61
San Bernardino	346	300	46
Banning	356	285	71
Indio	370	312	58

Table 5.7. Azimuth of Maximum and Minimum Horizontal Principal Stresses and Strains in Southern California.

Segment	Strain		Stress			
	ε_1	ε_3	σ_1	σ_3	δ_1	δ_3
	[deg]		[deg]		[deg]	[deg]
Fort Tejon	352	249	345	275	8	27
Mojave	353	262	358	267	5	9
San Bernardino	346	260	343	257	2	3
Banning	356	265	353	265	8	11
Indio	370	284	380	293	18	9

δ_1, angular difference between σ_1 - ε_1

δ_3, angular difference between σ_3 - ε_3

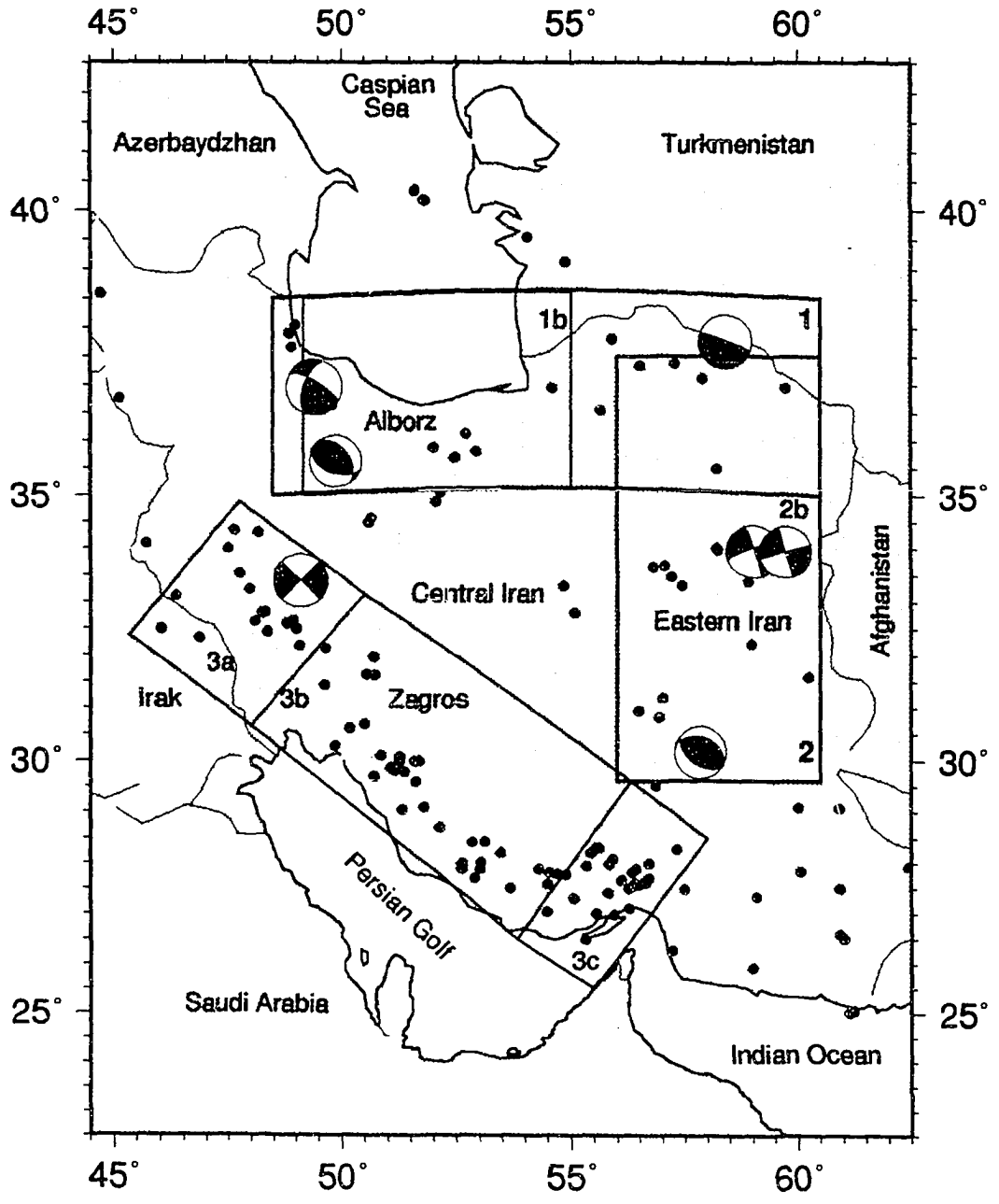

Fig. 5.1. Map of Iran with epicenters of earthquakes (dots) with known focal mechanisms. The polygons define the different areas and subareas used in the inversion of focal mechanisms for stress orientation. The focal mechanisms of events with M>7 are represented by lower hemisphere projections with the compressive quadrant shaded in black.

Fig. 5.2. Map of southern California showing the San Andreas fault (SAF) and the five segments selected for study by *Jones* [1988] as well as the stress and strain directions. The principal stress directions σ_1, σ_2, σ_3 published by *Jones* [1988] are represented by the small thin numbers, 1, 2, 3,respectively. The principal strain directions ε_1, ε_2, ε_3, computed using Kostrov's formula, are represented by the large numbers, 1, 2, 3, respectively. For the strain, only the 95% confidence ellipses for ε_1 and ε_3 are plotted.

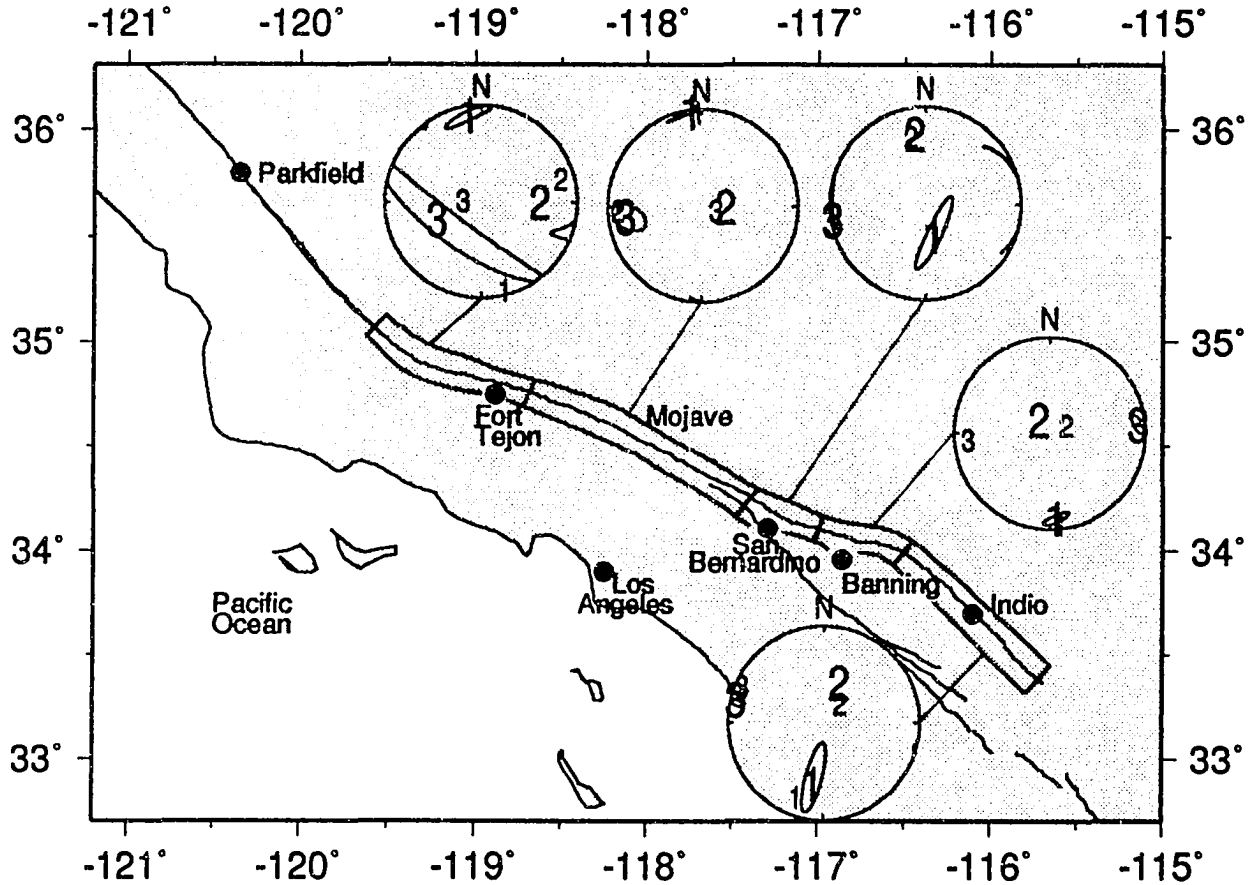

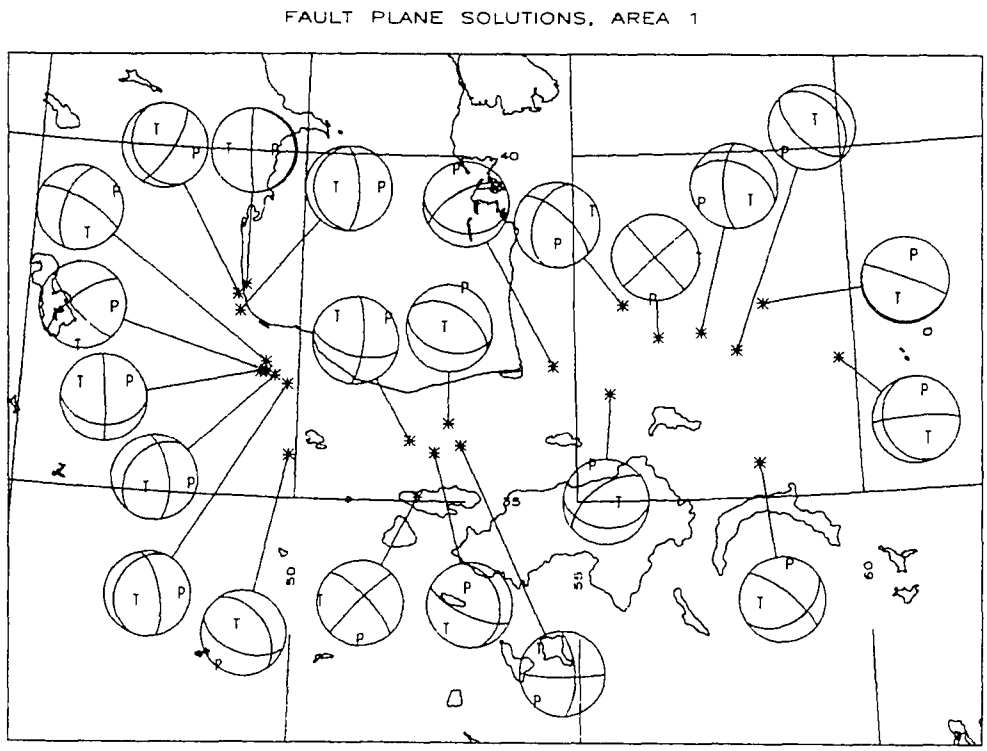

Fig. 5.3. Map of northern Iran with focal mechanisms used in the inversion for stress of area 1 (Alborz). The focal mechanisms are represented by a lower hemisphere stereographic projection. P and T axes are labelled.

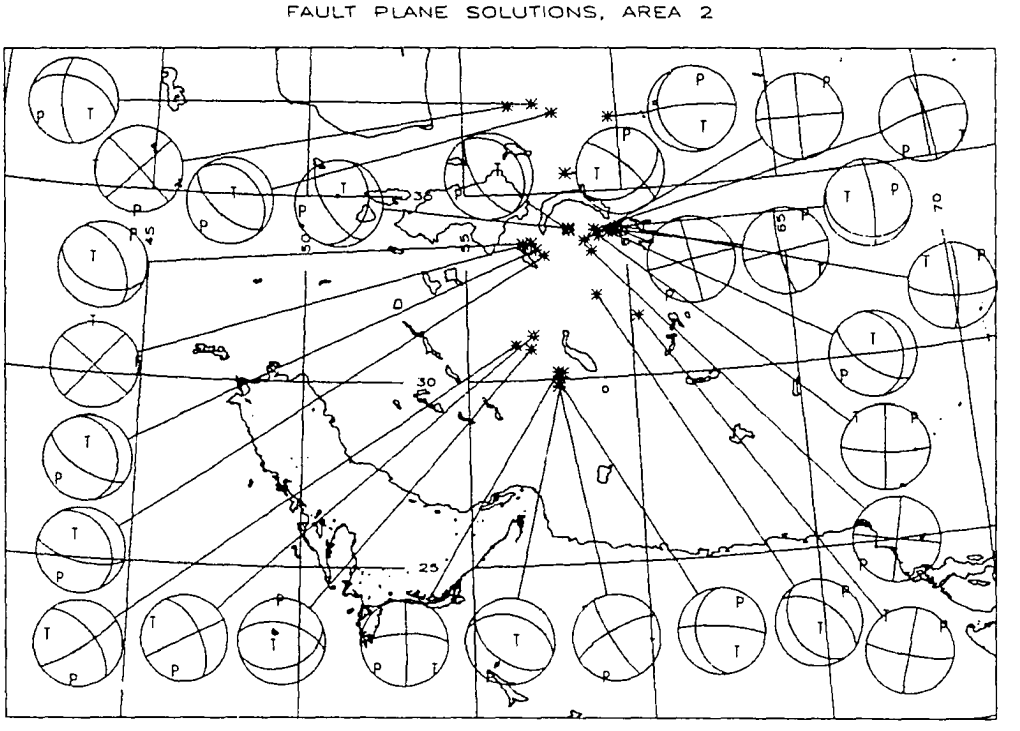

Fig. 5.4. Map of Iran with focal mechanisms used in the inversion for stress of area 2 (eastern Iran).

Fig. 5.5. Map of Iran with fccal mechanisms used in the inversion for stress of area 3 (Zagros).

FAULT PLANE SOLUTIONS IN ZAGROS 1909–1971

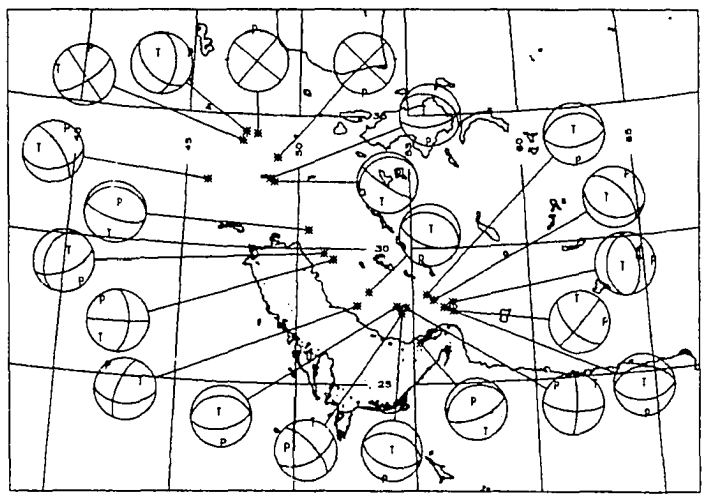

FAULT PLANE SOLUTIONS IN ZAGROS 1971–1978

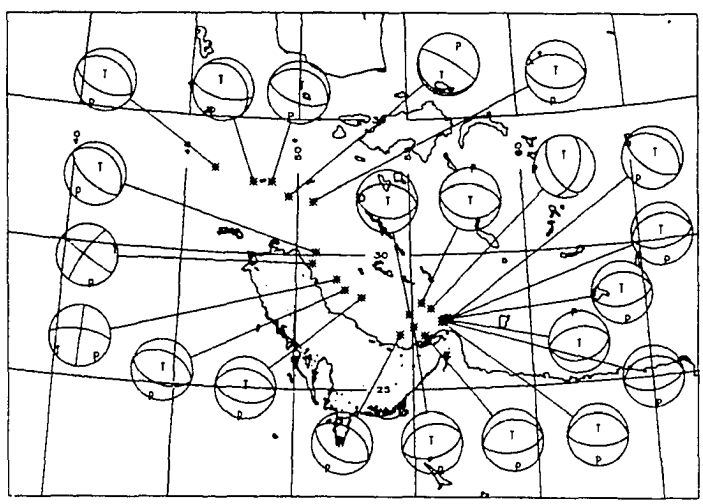

FAULT PLANE SOLUTIONS IN ZAGROS 1978–1992

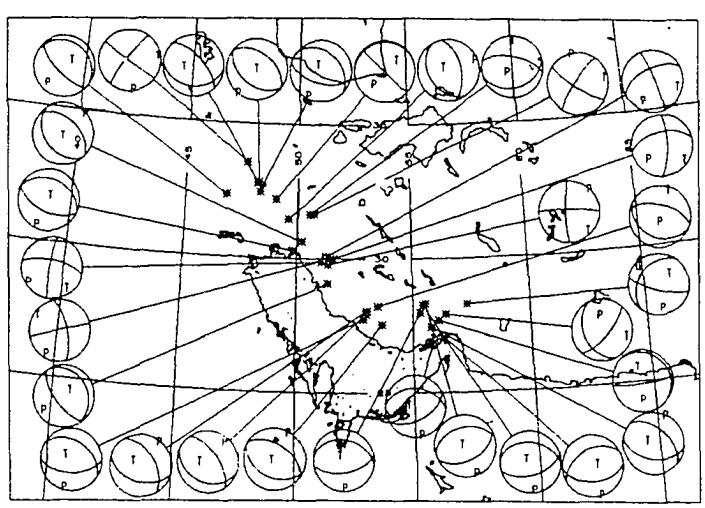

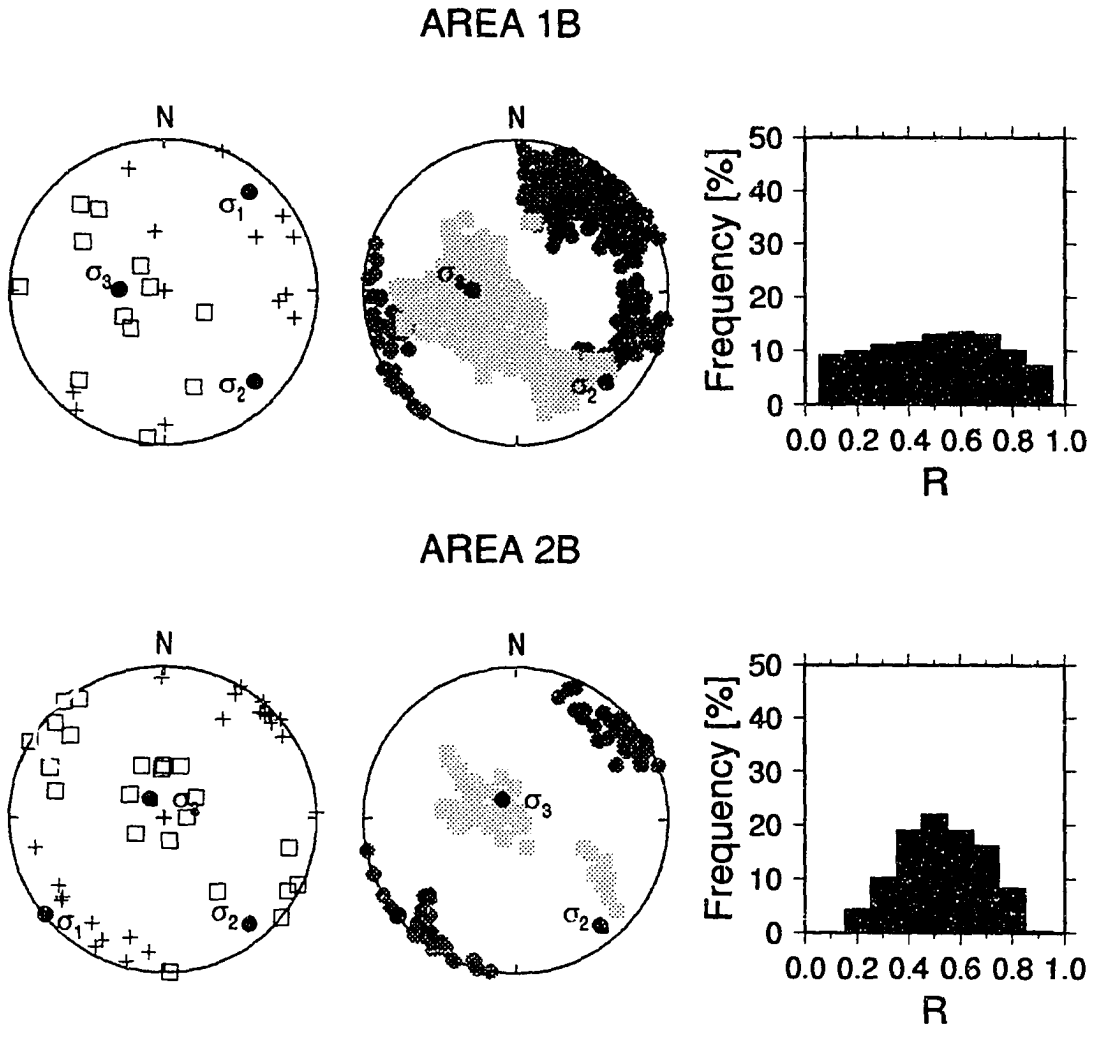

Fig. 5.6. Directions of principal stresses (dots) for subregions of northern Iran (area 1b) and eastern Iran (area 2b). (Left) Lower hemisphere projection of the P (crosses) and T (squares) axes with the three principal stresses (dots) corresponding to the best stress model. (Middle) 95% confidence region for σ_1 (dark gray) and σ_3 (light gray) plotted on a lower hemisphere stereographic projection with the direction of best fitting principal stresses (dots). (Right) Distribution of R values for the stress models within the 95% confidence region.

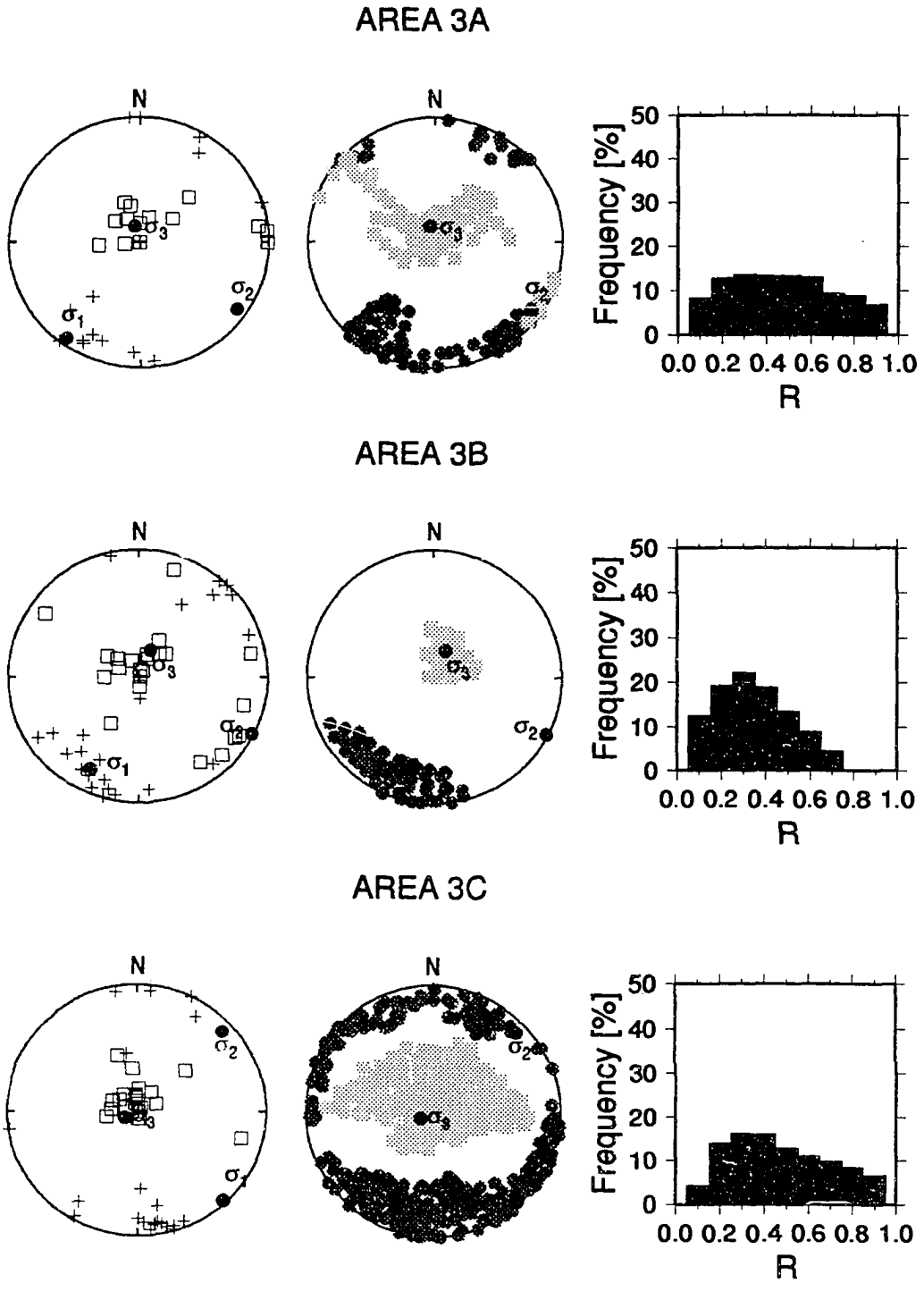

Fig. 5.7. Directions of principal stresses for subregions of Zagros. Same type of plot as Figure 5.6

Fig. 5.8. Directions of principal strain as a function of magnitude for subregions of northern Iran (area 1b) and Zagros (area 3a, 3b, 3c) plotted on lower hemisphere stereographic projections. Confidence ellipses for the greatest and least principal strain are marked with different line thickness as a function of magnitude band (first row). In the first row the numbers 1,2,3 represent the greatest, intermediate and least principal strain, respectively. Row two displayes the orientation of the principal strain directions (bold numbers) obtained for the magnitude band $4 \leq M \leq 7$ and the confidence ellipses for the greatest (1) and least (3) principal strain. Also plotted are best fitting principal stresses (fine print) with the 95% confidence regions for the greatest (dark shading) and least (light shading) principal stresses as in Figure 5.6 for area 1b, and Figure 5.7 for area 3a, 3b and 3c. Row three is the same as row 2 but the strain is computed for $4 \leq M \leq 8$. Row four is the same as row 2 but the strain is computed assuming constant magnitude.

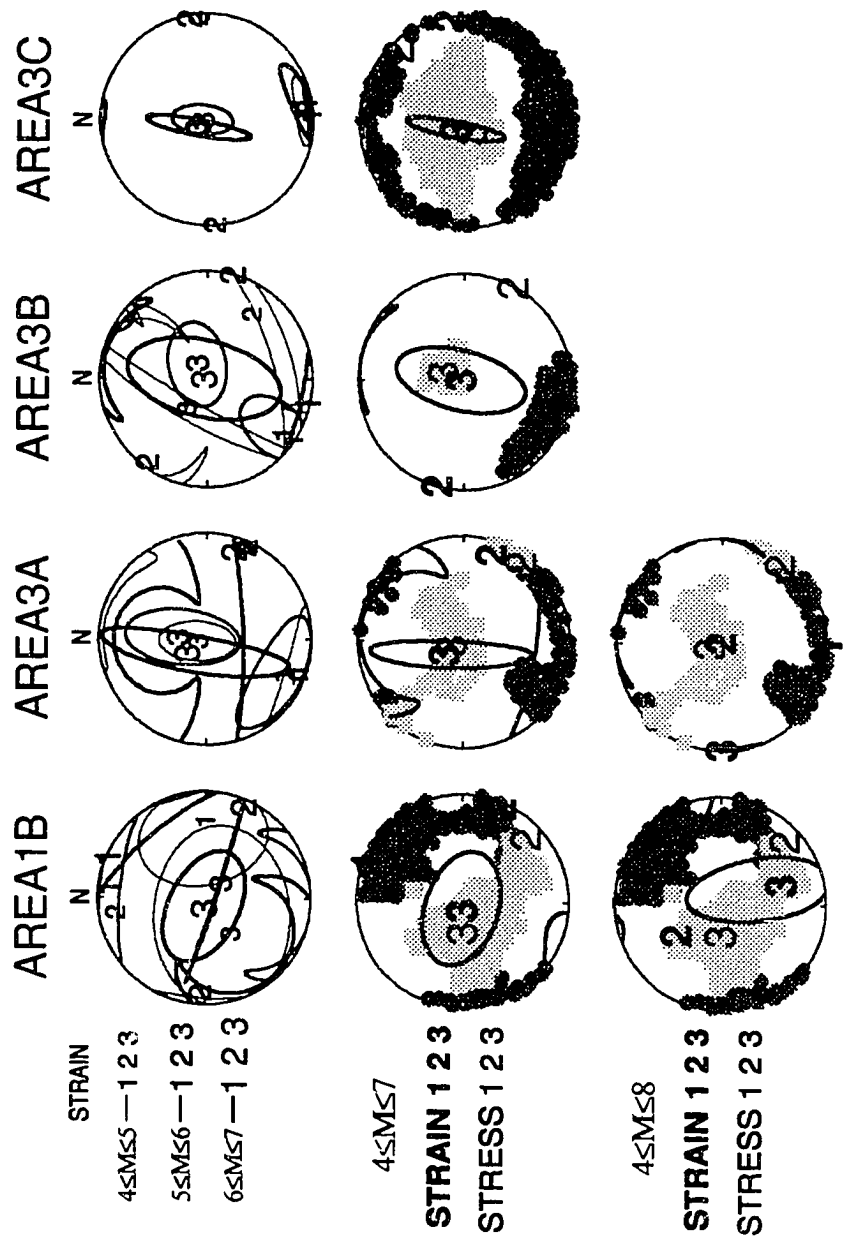

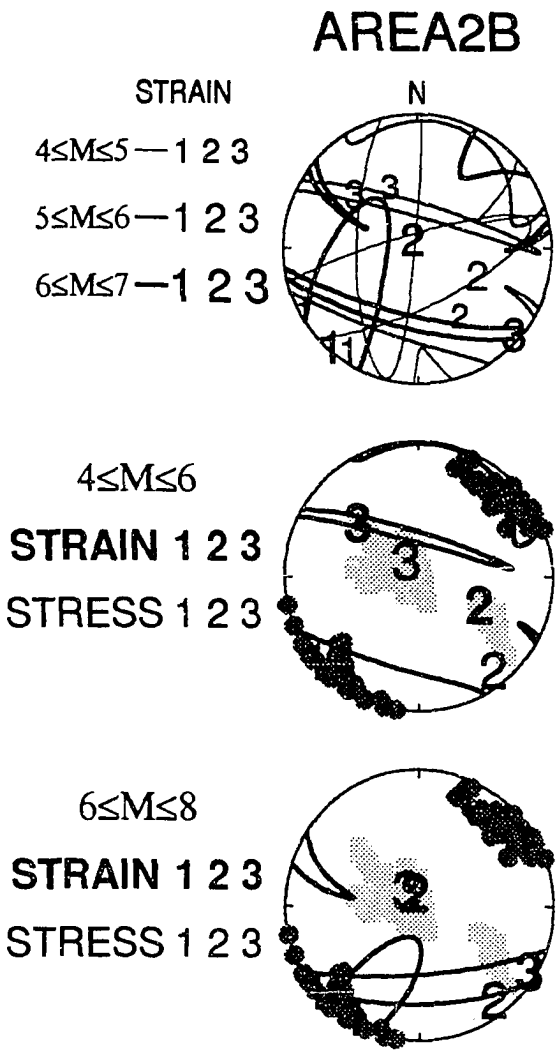

Fig. 5.9. Directions of principal strain as a function of magnitude for eastern Iran. Same plot as Figure 5.8.

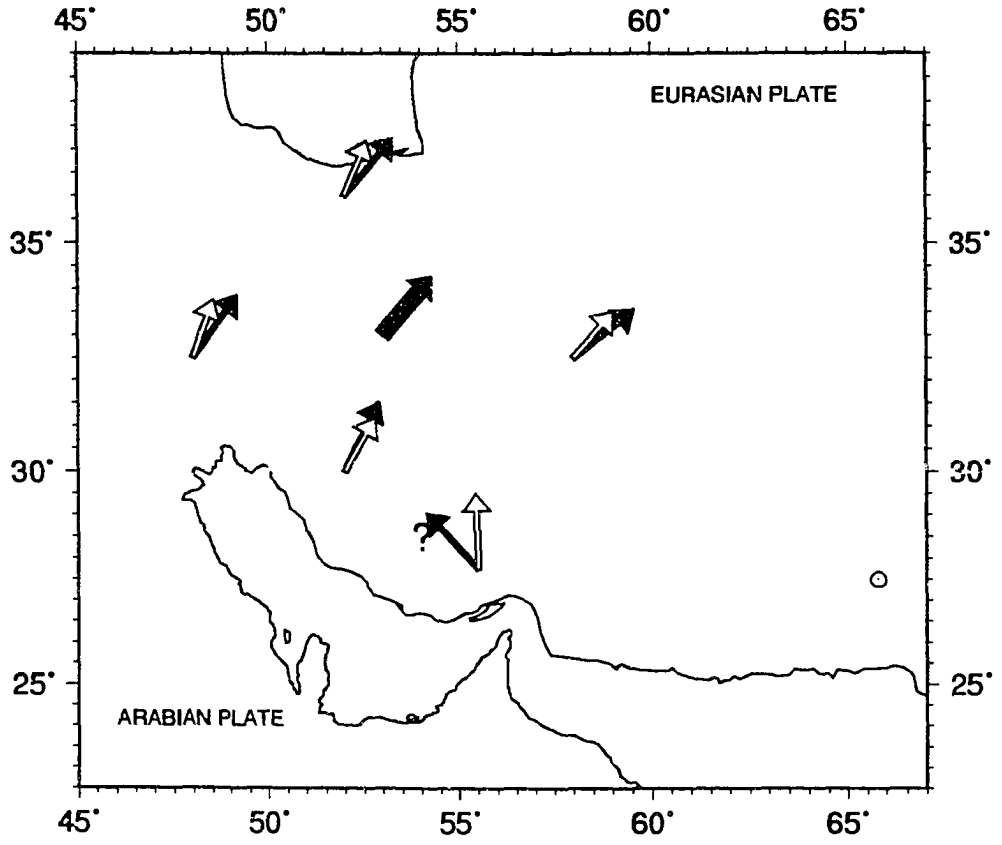

Fig. 5.10. Schematic map view of the stress and strain orientations in Iran. Thick arrow in the center represents the relative plate motion between the Iranian plate and the Eurasian plate after *Jackson and Mckenzie* [1984]. The thin black arrows represent the direction of horizontal maximum stress. The white arrows are the greatest horizontal principal strain directions for M<7. The question mark indicates that this stress direction is uncertain. The circle surrounding a point represents the Eurasian-Iranian pole of rotation determined by *Jackson and McKenzie* [1984].

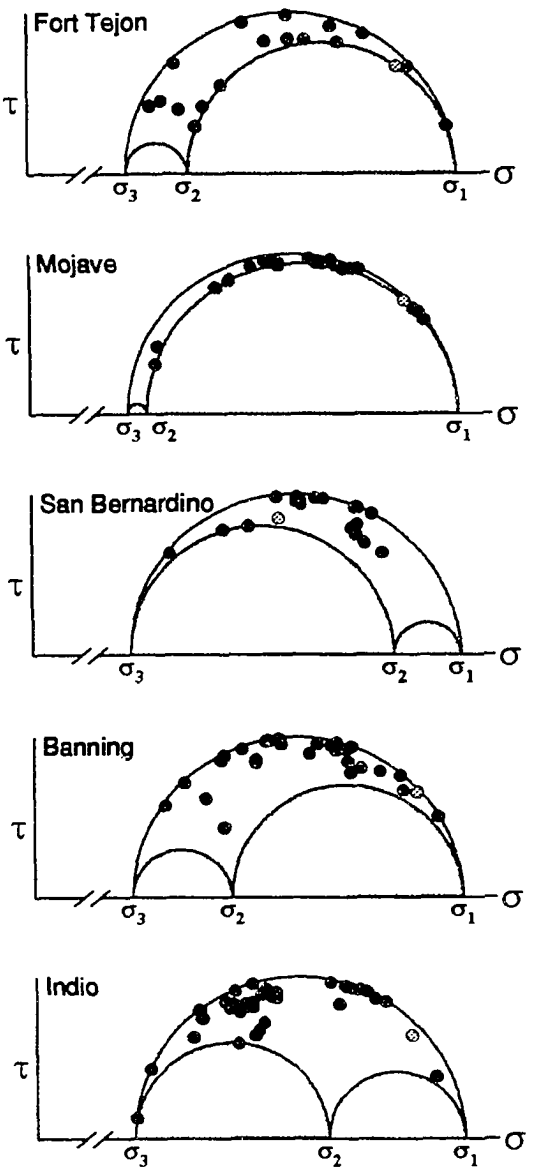

Fig. 5.11. Mohr plot representing the poles of the fault planes (dark dots) used in the stress inversion of *Jones* [1988] plotted as a function of normal stress, σ, and resolved shear stress on the faults, τ, for each segment. The horizontal axis is broken to indicate that the magnitude of the stresses are not known. The orientation of the principal stresses and the ratio of their relative magnitudes (R values) used to produce this plot come from *Jones* [1988]. The dot with the light shading represents the pole of the San Andreas fault. It is plotted as a reference point for comparison with fault planes used in the stress inversion.

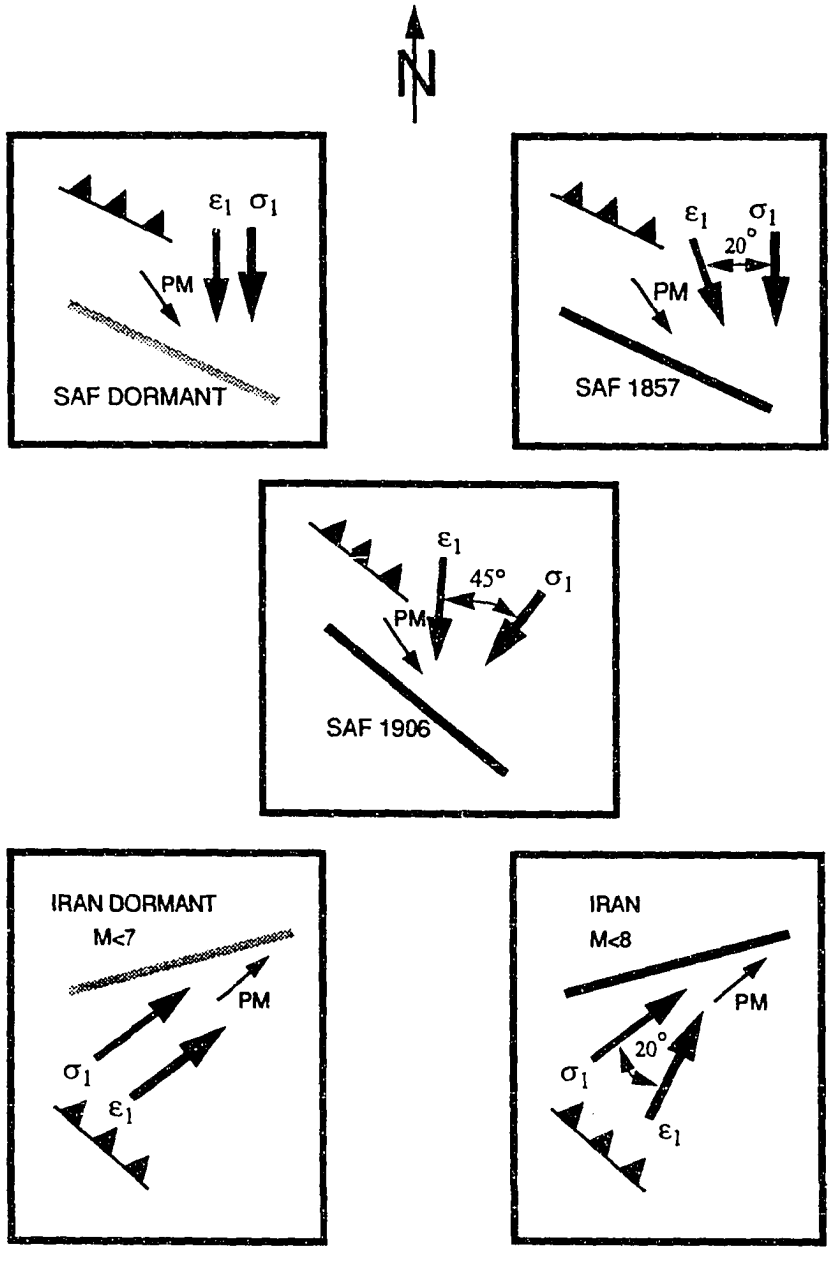

Fig. 5.12. Orientations of maximum principal stress and strain along the SAF and along strike-slip faults in Iran. The fault is "dormant" (gray shaded line) if it has not been ruptured by an earthquake with M>7. PM indicates the direction of plate motion. The black triangles along the thin line indicate thrust.

CHAPTER 6

CONCLUSION

We have studied the orientation of the stress tensor in Hawaii and Iran using a powerful method of inversion of focal mechanism data. One purpose of this study was to test this method and its assumptions in different tectonic environments and at different scales. In Hawaii the stress is generated by magmatic intrusions in the volcanoes, Kilauea and Mauna Loa, and their rift zones as well as by the load of the volcanic pile. In Iran, stresses are generated at the plate boundaries which mark the collision between Arabia and Iran forming the Zagros mountains in the south, and between Iran and Eurasia in the north.

The typical size of the crustal volumes for which inversions were performed in Hawaii were 5x10x10 km, whereas in Iran, volumes of the size 300x1000x40 km were used. Remarkably, the quality of the results was equally good in both regions. The results were robust and unaffected by expanding or reducing the number of events within individual data sets. The crustal volumes responding to a homogeneous stress field had average misfits in the range of 2° to 6° in Hawaii and Iran. From the error analysis applied to Iranian and Hawaiian data sets, we conclude that inversion results with average misfits smaller than 6° represent crustal volumes with homogeneous stress fields. In the range of 6° to 10°, the data sets should be considered suspect and further testing for homogeneity should be pursued. Our

approach of testing for stress homogeneity by subdividing data sets into subsets according to seismicity patterns and then comparing the average misfit of the subsets to the average misfit of the entire set worked well in Iran and Hawaii. In both regions, data subsets that we considered as homogeneous had average misfits significantly smaller by about 2° than the average misfit of the entire set.

When the diversity of focal mechanisms in a data set is large, the resolution of the stress tensor orientations may allow detection of changes in stress tensor orientation of at least 20° (significant at the 95% confidence level) as a function of space and time. In Hawaii, a significant rotation of the greatest principal stress of about 20° due to repetitive episodes of magmatic intrusion in the east rift zone of Kilauea volcano occurred in 1979. In Iran, differences of 20° to 30° between regions were not resolvable.

The inversion results in Iran and Hawaii agree with independent information on the expected stress directions. In Iran, the over all direction of the greatest principal stress is horizontal and approximately parallel to the direction of plate motion measured relative to Eurasia. In Hawaii, in some volumes, the maximum horizontal stress is parallel to the direction of maximum compressive strain measured geodetically.

This inversion method is strictly based on geometrical constraints and does not use a priori information about failure criteria. Faults are strictly considered as zones of weakness which can slip under low shear stress. We found that in Hawaii the decollement plane located at 10 km under the volcanic pile is a weak fault plane

because the greatest principal stress is oriented near vertically in the western part of the island (Figure 1). In the south flank, in some volumes, prior to and right after the Kalapana earthquake (1972-1979), the greatest principal stress is oriented nearly parallel to the decollement (Figure 1). These stress orientations indicate that the decollement plane which is probably present under the whole island of Hawaii is an extremely weak plane of failure which can slip almost without friction. The state of stress along this decollement plane is summarized in Figure 1 which shows a schematic cross section from the west coast of Hawaii, west of Mauna Loa's southwest rift zone, to the south flank of Kilauea. The stress orientations for the central part between the two volcanoes have been published by *Liang and Wyss* [1991]. We conclude that water may be trapped in this fault zone which is probably composed of oceanic sediments and volcanic debris which were deposited onto the ocean floor and over which the volcanic pile grew. This trapped water may be confined at near lithostatic pressure, thus reducing the normal stress on the decollement and allowing it to slip freely under the push from the volcano or its rift zone.

Comparing released seismic strain orientations to the stress orientations in a volume of the crust where some weak faults are present may reveal the strength heterogeneity of this crustal volume. In Iran, in California and Hawaii, it was observed that the stress and strain are coaxial for earthquakes with magnitude less than 7 and the strain was mainly released on reverse faults. However, for earthquakes larger than magnitude 7, the strain was released on strike-slip faults in Iran and California, and on the decollement in Hawaii causing significant angular differences between the greatest principal stress and strain from 20° to 40°. We

conclude that strength heterogeneity seems to be prevalent in a variety of tectonic environments including continental collision in Iran, transform plate boundary in California and around volcanoes in Hawaii. If the pore fluid pressure is responsible for strength heterogeneity, it should be expected to be independent of the tectonic environment.

1. Suggestions for future work

1. To understand fault properties in Hawaii and their relationship to the states of stress, one should apply a Coulomb failure analysis using a Mohr circle. It is not clear how decollement, reverse, and normal faults can be active within a similar stress state. What are the upper limits for the pore pressure to facilitate failure on these faults without creating new ruptures within the intact rock? What coefficient of friction can we expect on these faults? Are faults reactivated or newly created?
2. Recently, *Yin* [1993] gave an elastic solution for the compressional wedge problem and investigated the initiation of normal and thrust faults. Such an approach should be tested in the south flank of Kilauea which is a wedge-shaped thrust. We would try to find the model parameters (e.g. surface slope, dip of the wedge, length of the unfaulted part of the wedge called Hubbert-Rubey toes) which could explain our observations. Constraints about the pore pressure at the base of the wedge and in the wedge could also be derived.
3. The active volcanoes on the island of Hawaii (Mauna Loa, Kilauea and Hualalai) are all located south of latitude 19° 45'. We know from this study

that they are the source of stress causing tectonic earthquakes of magnitude M≥2.5 to happen in their flanks at depths of 8 to 12 km. North of this latitude, the volcanoes are inactive but magnitude M≥2.5 earthquakes are located in this region at depths between 5 and 15 km. The state of stress responsible for these earthquakes is still unknown. Is the stress governed by the load of the inactive volcanoes or are the stresses transferred through the volcanic pile from the active volcanoes to the south? Such questions should be answered to have a complete understanding of the seismotectonic of the island of Hawaii.

4. This study focused on the shallow Hawaiian earthquakes located above 15 km depth in the crust which is supposed to be decoupled from the Pacific plate. However, deep earthquakes are present under Hawaii at depths of 20 to 60 km. These earthquakes may be related to the stress field created by magma rising from the mantle and inducing brittle failure in the upper mantle or to the bending of the plate or both. The study of the focal mechanisms of these events in relation to the plate bending induced stress could help us understand how magma moves from the mantle to feed the volcanoes at the surface.

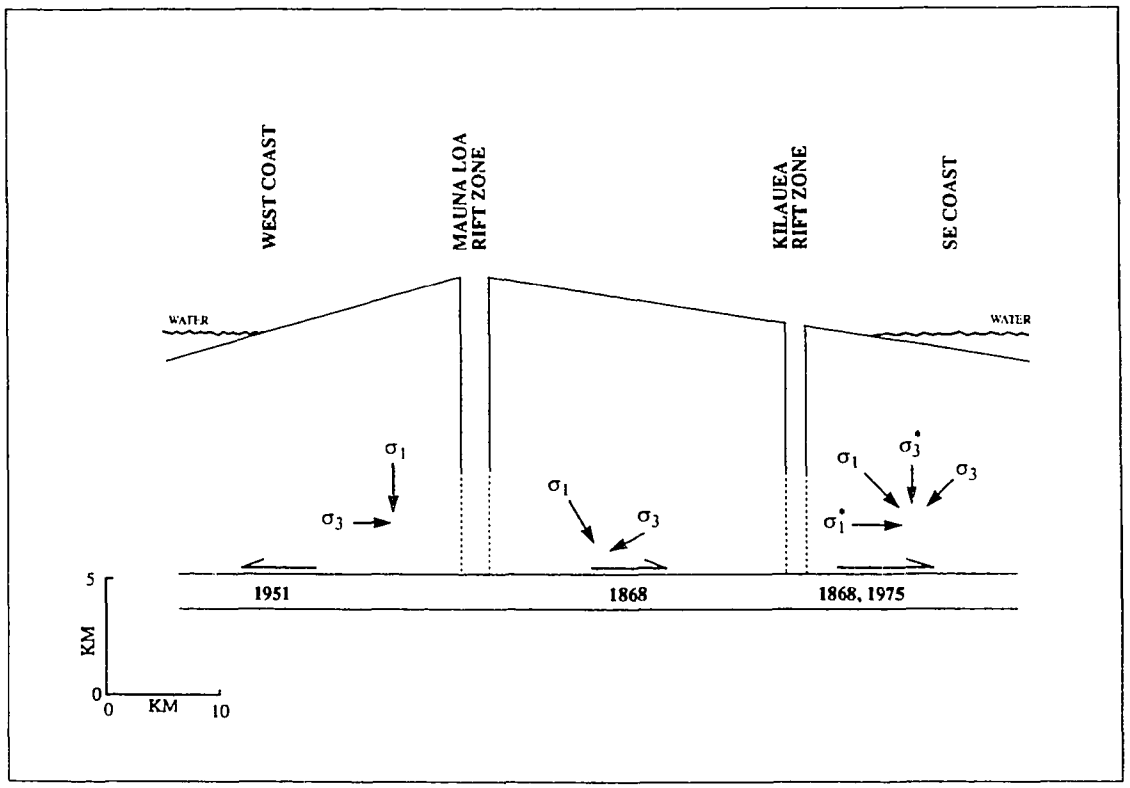

Fig. 6.1. Schematic cross section across Hawaii from the west coast to the south flank of Kilauea with stress axes and slip vectors. Full arrows indicate directions of principal stress axes ($\sigma_1>\sigma_2>\sigma_3$) as derived from fault plane solutions in this study and by *Liang and Wyss*, 1991. Half arrows are proposed slip vectors. The slip of the 1951 earthquake was derived in this study. The years of the earthquakes which ruptured individual segments of the weak decollement plane are indicated. Two stress systems corresponding to the period 1972-1979 (σ_1^*, σ_3^*) and to the overall stress regime (σ_1, σ_3) in the south flank of Kilauea calculated in this study are displayed. The decollement can slip under a greatest principal stress which can be nearly perpendicular or nearly parallel to the decollement.